

HEAT TRANSFER INVESTIGATIONS FOR OPTIMAL
HARNESSING OF ENHANCED GEOTHERMAL SYSTEMS

A DISSERTATION
SUBMITTED TO THE DEPARTMENT OF
ENERGY RESOURCES ENGINEERING
AND THE COMMITTEE ON GRADUATE STUDIES
OF STANFORD UNIVERSITY
IN PARTIAL FULFILLMENT OF THE REQUIREMENTS
FOR THE DEGREE OF
DOCTOR OF PHILOSOPHY

Esuru Rita Okoroafor

June 2021

© 2021 by Esuru Rita Okoroafor. All Rights Reserved.

Re-distributed by Stanford University under license with the author.



This work is licensed under a Creative Commons Attribution-Noncommercial 3.0 United States License.

<http://creativecommons.org/licenses/by-nc/3.0/us/>

This dissertation is online at: <http://purl.stanford.edu/br335jv9606>

I certify that I have read this dissertation and that, in my opinion, it is fully adequate in scope and quality as a dissertation for the degree of Doctor of Philosophy.

Roland Horne, Primary Adviser

I certify that I have read this dissertation and that, in my opinion, it is fully adequate in scope and quality as a dissertation for the degree of Doctor of Philosophy.

Sally Benson

I certify that I have read this dissertation and that, in my opinion, it is fully adequate in scope and quality as a dissertation for the degree of Doctor of Philosophy.

Daniel Tartakovsky

Approved for the Stanford University Committee on Graduate Studies.

Stacey F. Bent, Vice Provost for Graduate Education

This signature page was generated electronically upon submission of this dissertation in electronic format. An original signed hard copy of the signature page is on file in University Archives.

Abstract

Enhanced Geothermal Systems (EGS) offer the opportunity of exploiting the vast energy resources contained in hot impermeable rocks. In such rocks, the natural flow capacity of the system may not be sufficient to support adequate geothermal applications until it is enhanced by opening up existing fractures and propagating new fractures. Cold fluid is injected into the reservoir to exploit the energy resource, whose permeability has been enhanced. The increased permeability allows the fluid to circulate through the opened fractures to production or extraction well(s), thereby capturing and transporting the heat contained in the hot impermeable rock for power generation.

Accurate prediction of the thermal performance of EGS depends on an understanding of how the heat transport is affected by the presence of the fracture(s) – the primary flow conduit of EGS. These fractures may have aperture variability that could create channels and alter flow paths, affecting the availability of surface area for heat transfer.

The overall goal of this study was to understand the fracture topology, investigate how it can impact flow and heat transport, and demonstrate ways Enhanced Geothermal Systems can be harnessed to optimize thermal performance. To achieve the goal of this study, a systematic fracture characterization approach was used, and numerical simulation models were used to study the physical processes that govern the interaction between the fluid and the rock during heat extraction from Enhanced Geothermal Systems.

Using variogram modeling and Sequential Gaussian Simulation method, fracture apertures representing actual fractures were generated for lab-scale and field-scale investigations. Fracture characterization metrics such as the Joint Roughness Coefficient (JRC) and Hurst exponent were used in analyzing the data. Geometric anisotropy was a vital character of the generated fracture aperture distributions, which was seen to originate from the process of shearing or slip. Flow and heat transport relative to the direction of fracture shear was studied, with the perpendicular flow configuration being perpendicular

to the direction of fracture shear. In contrast, the parallel flow configuration had flow in the same direction as the fracture shear direction.

It was demonstrated in this study that the flow wetted surface area had a direct and significant contribution to the amount of heat extracted. For the lab-scale fractures, the JRC confirmed geometric anisotropy of the fracture aperture and was seen to have a direct correlation with the flow contact area. The lower the difference in JRC values between the perpendicular and parallel flow configurations, the more flow contact area expected in the perpendicular flow direction, which will lead to more heat extracted from the rock. From the variogram model parameters, it was deduced that high geometric anisotropy results in high differences in thermal drawdown and consequently a high difference in energy extracted. The thermal performance appeared to be better in the perpendicular flow configuration with a ratio of 70:30 for the lab-scale fractures.

For the field-scale fractures, it was seen that most of the fracture aperture distributions with a geometric anisotropy ratio of 2 had Hurst exponents of fracture surface aperture variability found in nature. For all the fracture aperture distributions analyzed for the field scale, the perpendicular flow configuration resulted in better thermal performance than the parallel flow configuration with a ratio of 58:42. Furthermore, for the geometric anisotropy ratio of 2, the ratio was 70:30. The perpendicular flow configuration had the injected fluid move through tortuous flow paths. These tortuous flow paths contributed to more fracture surface area being contacted by the flowing fluid, leading to an improved thermal performance in that flow configuration.

Throughout this study, temperature-dependent viscosity was used. However, a section of this study investigated the impact of using a constant viscosity in the thermohydraulic model. It was seen that for fractures with smooth, uniform apertures, for all temperature ranges and at the operating conditions being modeled, there was no significant difference between using a constant viscosity or a temperature-dependent viscosity in modeling an Enhanced Geothermal System. However, for fractures with spatial variations, it was determined that modeling with a temperature-dependent viscosity was necessary, especially for systems with high differences in reservoir and injection temperatures, and for fractures with high correlation lengths.

The impact of thermal stresses on heat extraction was also investigated. An analog Enhanced Geothermal System, the Altona Field Laboratory, was also studied for thermo-mechanical influences. It was found out that the injection of hot water into the cold rock resulted in thermal stress generation and reduction in the aperture but did not cause significant changes to the temperature profile due to the small volumetric flow rate through the system. Also, anisotropic aperture distributions were studied to determine the impact of thermoelasticity on the heat extraction of Enhanced Geothermal Systems. It was shown that when thermoelasticity is taken into consideration, the thermal drawdown could either be improved or deteriorated depending on the nature of the aperture distribution.

The impact of fracture aperture variability was investigated for Enhanced Geothermal Systems using supercritical CO₂ as working fluids. It was established that CO₂ as an EGS working fluid would result in better heat extracted from the system if the fractures are considered smooth, which agrees with related studies. However, where there is spatial variation in the fracture aperture, channeling could be detrimental to CO₂, especially at high fracture correlation lengths and high mass flow rates, due to the high mobility of CO₂.

The following are the main contributions from this study. First, it has been demonstrated that heat transport is affected by the geometric anisotropy of fracture surfaces. It was determined that in most cases, flowing perpendicular to the direction of shear or slip results in more heat extracted due to more contact of the fluid with the rock while moving through tortuous flow paths. Secondly, the conditions under which a constant viscosity can be used in modeling EGS were determined. If the fractures are known to be smooth, have low correlation lengths, or have distributed surface areas, a constant viscosity can be used in the model, especially if the difference between the reservoir temperature and the injection water temperature is small. However, for anisotropic fracture surfaces, surfaces with high correlations lengths or high tortuosity, and when the difference between the reservoir temperature and injection water temperature is large, the use of constant viscosity could result in significant computational errors from the actual.

Thirdly, it has been shown that thermal drawdown could either be improved or deteriorate when thermoelasticity is considered. This finding is different from studies previous studies that have looked into coupling thermohydromechanical processes for fractures with spatial variations and suggests that Enhanced Geothermal Systems may benefit from thermal stimulation. Finally, this work shows the first comparison between CO₂ and water at a field scale considering fracture aperture variability.

Recommended future work includes modeling of vertical fractures with spatial variations in fracture aperture to investigate how convection may impact the current findings; considering multiple fractures with spatial variations in the fracture aperture; considering non-Darcy flow in the simulation models; coupling geomechanics with the study of CO₂ on fractures with spatial variations, and developing proxy models that are quicker to perform the thermohydraulic and thermohydromechanical simulations.

Acknowledgments

It has been a life-changing experience going through the process of gaining a Ph.D. at Stanford University, Department of Energy Resources Engineering (ERE), Stanford School of Earth, Energy & Environmental Sciences. I have grown and transformed through my interactions with many and support from back home, and I would like to use this medium to express my appreciation to those who have walked this journey with me.

My deepest gratitude goes to my adviser, Professor Roland Horne. He took a chance on me. I am very grateful for his guidance, support, and availability. In addition to learning from him various technical concepts, I also learned from him coaching, mentoring, how to work with people, and other life skills that would make me a much better person. I would like to thank the other committee members, from the Chair of the committee, Professor Elizabeth Miller, to Professor Sally Benson, Professor Daniel Tartakovsky and Professor Anthony Kavscek. Professor Benson is a role model and a great mentor. Since the time I put together my proposal, her great contributions and questions spurred further ideas for my work. I am immensely grateful to Professor Daniel Tartakovsky for being very supportive during my studies. Like I have told him in the past, if all math teachers were like him, more students would get involved in mathematics and science-related courses. Many thanks to Professor Anthony Kavscek whose course on Fundamentals of Energy Processes awakened my interest in heat transfer and associated processes. I remain deeply grateful to Professor Elizabeth Miller for her willingness to be the committee's Chair. She is such an inspiration to women in the sciences. What an honor!

I am grateful for the funding from the Department of Energy Resources Engineering, at Stanford University, and the scholarship I received from Geothermal Rising to support my research. I am also grateful for the Stanford Family Grant, which made a difference between my continuing the education and leaving prematurely. I know the donors are anonymous but let it be on record that their generous donation contributed immensely to my Ph.D. journey.

I would also like to express my profound appreciation to Dr. Michael Williams of Schlumberger for his mentorship and guidance during my studies despite his busy schedule. I would also like to thank other people within Schlumberger whom I have collaborated with – Yvonne Kang, Olalekan Kenshiro, Assef Mohammed, and Qinglai Ni.

A vital part of my experience in Stanford was the education I received in class, and I am very grateful for all the Professors who contributed to passing knowledge to me. Attending those classes has provided me with standards and values for teaching and learning, which is valuable to me who is interested in knowledge sharing and mentorship. I will especially like to thank Professor Durlofsky for the opportunity to work with him as his Teaching Assistant while learning from him. I will also like to thank Professor Tchelepi, Professor Zoback, and Dr. Marco Thiele, whose classes provided fundamental concepts I have used throughout my Ph.D. Professor Battiato has been a mentor to me in this department, and I am truly appreciative of her support and encouragement in my Ph.D. journey.

My work involved a lot of numerical simulation software. I had called on Eric Liu several times when I needed help, and he was always available. I want to say thank you to Eric for ensuring I had the best support. Of course, ERE has the best staff, so I would like to thank Joanna, who was always able and available to answer questions about processes in the department; and thank you to Diane, Arlene, Thuy, Yolanda, Sam, Lyriisa, and Sandy who made my stay memorable.

I made many friends in ERE, too numerous to mention. I just want them all to know that I truly appreciate all the time I had with them within and outside of our WhatsApp group. I am very grateful for the geothermal group that I was in, which helped me grow through daily interactions, especially our “geothermal girls”, Noe, Ayaka, Halldora, and Yuran, for all the fun times we had. Thanks to Adam Hawkins for his mentorship and collaboration, Jeff, my office buddy pre-covid times, and Hannah for her special friendship. I want to mention Dr. Folake Ogunbanwo for helping me get settled in, and Negar for her extraordinary friendship. Special shout out to Dr. Wakuna, Heidi, Abby, Folasade, and Mapi, who helped me with my children while I worked towards this Ph.D.

Special thanks to Shahid Haq of Schlumberger, who constantly checked up on me and encouraged me when the going was very tough. Also, thanks to Philip Evbomoen and Kelechi Okoroafor, who would always drop off a word of encouragement at regular intervals to help lift my spirit. To my mentees, Ahmed, Rasaan and Karena, thank you for your encouragement.

I am so grateful for Muobo, Amaka Diane, Rosario, Fanyama, Odiri, Candice, Toyin, Onyinye, Ifeanyinachukwu, Akaji, Wusi and Jibola. Thank you, ladies, very much for walking this journey with me.

My family members, you all are wonderful. I am incredibly grateful to my mother for her support and belief in me and joined me at Stanford on the first day I arrived. Since then, she has provided support in the best way she could. To my two elder sisters, Chioma and Uche, thank you for your indescribable love and support. I am so blessed to have sisters like you. And to all my other siblings, especially Ogochukwu, Onyinye, and Olisehemeka, thank you for your support in everything that I did. I also want to especially thank my mother-in-law, who dedicated her time to support me, especially when the pandemic hit and I had no help. She was God-sent. Moreover, all the things that I achieved towards the end of this Ph.D., I attribute to the love and care that she gave my children and me. My children, Olachi, Nwachi, Kelechi, and Chinonye, I want to thank you for walking this journey with me, for your patience, understanding, and endurance in all of this. Thank you. And to my beloved husband, John Okoroafor, I know it has been very tough for you to be separated from your family, but you chose to allow me to fulfill my dreams because you believe so much in me. I want to say thank you so much, and I love you!

Contents

Abstract.....	iv
Acknowledgments.....	viii
1 Introduction	1
1.1 Prior Related Works	6
1.1.1 Thermal Performance Relative to Fracture Shear Offset.....	6
1.1.2 Thermohydraulic modeling of Enhanced Geothermal Systems	8
1.1.3 CO ₂ Utilization in EGS.....	8
1.2 Statement of the Problem	9
1.3 Dissertation outline	10
2 Anisotropic Effects on Lab Scale Thermal Performance.....	12
2.1 Introduction	12
2.2 Methodology	17
2.2.1 Governing Equations.....	17
2.2.2 Model Assumptions	18
2.2.3 Model Description	18
2.2.4 Fracture characterization.....	20
2.2.5 Fracture Aperture Generation	21
2.1 Numerical Simulation Model Verification.....	30
2.1.1 Validation Study – Modified Fox et al. (2015) Smooth Fracture Solution.....	31
2.1.2 Validation Study – Modified Fox et al. (2015) Solution for Fracture with Aperture Variability.....	33
2.2 Results	34
2.2.1 Thermal Performance for the original lab-scale fracture	34
2.2.2 Thermal Performance for Artificially Generated Fractures with Aperture Variability.....	38
2.3 Summary	54
3 Anisotropic Effects on Field Scale EGS Thermal Performance.....	56
3.1 Introduction	56

3.2	The Morphology of Fractures and Implications for Flow and Heat Transport...	57
3.3	Characterizing Self-Affinity in One-Dimensional and Two-Dimensional surfaces.....	58
3.4	Modeling of Enhanced Geothermal Systems	62
3.4.1	Analytical and Semi analytical Modeling of Heat Transport in Enhanced Geothermal Systems	62
3.4.2	Numerical Modeling of Heat Transport in Enhanced Geothermal Systems	64
3.5	Generation of Fracture Surface with Variable Aperture	68
3.6	Generation of Field Scale Fractures Aperture variability with Geometric Anisotropy	69
3.6.1	Upscaling histogram	70
3.6.2	Sequential Gaussian Simulation in Stanford Geostatistical Modeling Software ...	71
3.6.3	Hurst Exponent Determination	72
3.6.4	Estimating Permeability	73
3.6.5	Thermohydraulic Model	75
3.7	Results and Discussion.....	76
3.7.1	All Simulations Difference	76
3.7.2	Geometric Anisotropy Ratio of 1.5.....	80
3.7.3	Geometric Anisotropy Ratio of 2.....	84
3.7.4	Geometric Anisotropy Ratio of 3.....	90
3.7.5	Geometric Anisotropy Ratio of 4.....	93
3.7.6	Some Simulation Challenges	97
3.8	Summary	100
4	Temperature-Dependent Viscosity: Relevance to the Numerical Simulation of Enhanced Geothermal Systems	102
4.1	Introduction	102
4.2	Methodology	104
4.2.1	Description of the Enhanced Geothermal System	104
4.2.2	Relevant Temperature-Dependent Parameters.....	105
4.2.3	Determination of Aperture Distribution.....	106
4.3	Simulation Model and Software used	108
4.4	Results and Discussion.....	109
4.4.1	Constant Viscosity vs. Temperature-Dependent Viscosity: Parallel Plate Fracture Model	109

4.4.2	Constant Viscosity vs. Temperature-Dependent Viscosity: All Aperture Distributions	112
4.4.3	Constant Viscosity vs. Temperature-Dependent Viscosity: Aperture 1	115
4.4.4	Constant Viscosity vs. Temperature-Dependent Viscosity: Aperture 2	117
4.4.5	Constant Viscosity vs. Temperature-Dependent Viscosity: Aperture 3	118
4.5	Summary	123
5	Thermohydrromechanical Modeling of Enhanced Geothermal Systems	126
5.1	Introduction	126
5.2	Methodology	129
5.2.1	Formulation of the problem	129
5.2.2	Relevant Equations for the Coupled Thermohydrromechanical Process	130
5.3	Software used	133
5.4	Permeability Updating.....	134
5.5	Verification.....	136
5.1	Application of Thermohydrromechanical Modeling to the Altona Field Laboratory	137
5.1.1	The Analog Geothermal Reservoir - Altona Field Laboratory	139
5.1.2	The Altona Field Heat Transport Experiment.....	140
5.1.3	Determination of the aperture distribution.....	142
5.1.4	Modeling with Temperature-Dependent Viscosity.....	143
5.1.5	Geomechanical Model Description and simulation domain	143
5.1.6	Results and Discussion	145
5.2	Application of Thermohydrromechanical Modeling to Anisotropic Aperture Distributions	149
5.2.1	Results and Discussion	150
5.3	Summary	159
6	Comparing CO₂ and Water as Enhanced Geothermal System Working Fluids	160
6.1	Introduction	160
6.2	Methods.....	163
6.2.1	Governing Equations and Model Assumptions.....	163
6.2.2	Model Description	163

6.2.3	Relevant Properties of Water and CO ₂	165
6.2.4	Fracture characterization.....	169
6.2.5	Determination of the spatially varying fracture aperture distributions	170
6.2.6	Workflow and Metrics for Evaluation	171
6.3	Results and Discussion.....	171
6.3.1	Heat Extraction at Different Mass Flow rates – Smooth Fracture Evaluation.....	171
6.3.2	Heat Extraction at a Fixed Energy Input – Smooth Fracture	174
6.3.3	Heat Extraction at a Fixed Energy Input – Fracture with spatial variations, different correlation lengths.....	174
6.3.4	Heat Extraction at a Fixed Equivalent Energy Input – Fracture with spatial variations, different flow rates	178
6.3.5	Heat Extraction at a Fixed Energy Input – Fracture with spatial variations, comparison with a smooth fracture at a fixed rate, and fixed aperture distribution correlation length	180
6.4	Summary	183
7	Conclusions and Recommendations	185
	Bibliography	189

List of Tables

Table 2.1: Rock and fluid properties, and other parameters used in the lab-scale model	20
Table 2.2: Percentage of the fracture surface contacted by flowing fluid for the original fracture aperture distribution.....	37
Table 2.3: Summary of selected aperture distributions for further analysis	43
Table 2.4: Summary of selected aperture distributions for further analysis	43
Table 2.5: Joint Roughness Coefficients and percentage flow contact area for the selected aperture distributions	48
Table 2.6: Results of variogram modeling for the selected aperture distributions	50
Table 3.1: Number of simulation cases for different ranges and geometric anisotropy ratios (GR)	73
Table 3.2: Rock and fluid properties, and other parameters used in the model.....	76
Table 4.1: Water viscosity at different temperatures at a pressure of 101.325 kPa.....	105
Table 4.2: Statistics for the aperture distributions	107
Table 4.3: Percentage of flow wetted surface for the aperture distributions	113
Table 5.1: Parameters used in the thermohydromechanical model verification.....	137
Table 5.2: Rock and fluid properties, and other parameters used for the Altona Field Laboratory Case Study.....	145
Table 5.3: Additional parameters required for the thermohydromechanical model.....	150
Table 6.1: Rock and fluid properties, and other parameters used in the model for comparing CO ₂ and Water as EGS working fluids.....	166
Table 6.2: Thermophysical properties of CO ₂ and water at the injection and reservoir conditions	169
Table 6.3: Exit Temperature of the fluid from the production well.....	174

List of Figures

Figure 1.1: Schematic of an Enhanced Geothermal System with a doublet configuration (Yao, Shao, & Yang, 2018).	2
Figure 1.2: Map of the U.S. Geothermal Resource consisting of hydrothermal sites (black markers) and favorable enhanced geothermal system (EGS) locations in the U.S. (National Renewable Energy Laboratory, 2009).	3
Figure 1.3: Illustration of lateral direction of shear offset from Ishibashi et al. (2012).	7
Figure 1.4: Perpendicular and Parallel flow configurations relative to the lateral direction of shear offset from Co (2017).	7
Figure 2.1: Boundary conditions for the different flow configurations. Figure 2.1a is for the parallel flow configuration, while Figure 2.1b is for the perpendicular flow configuration.	18
Figure 2.2: The lab-scale three-dimensional model showing the grids. The depth (Z-axis) is not to scale. The Y and Z axes read negative with increasing values from the reference (zero in this case).	19
Figure 2.3: Cylindrical granite samples containing single tensile fractures of different sizes having either (a) no shear displacement or (b) a shear displacement of 5 mm in the lateral direction (Ishibashi et al., 2012).	23
Figure 2.4: Aperture distribution of the 50 mm x 75 mm sample generated in the work by Ishibashi et al., (2012). The lateral direction of shear offset is shown with arrows indicating the parallel flow configuration and the perpendicular flow configuration relative to the lateral direction of shear offset. The white line indicates where limit in the axial direction for the numerical simulation.	25
Figure 2.5: Example Semivariogram showing the range, sill, nugget, and lag distance (from Biswas & Si, 2013).	25
Figure 2.6: Comparison of the different variogram models with a range of 50 mm and a sill of 0.1 mm ² (from Co, 2017).	27
Figure 2.7: Comparison of the experimental variograms and the fitted model for the sheared 10 cm by 15 cm case in directions 0, 30, 60, 90, 120, and 150 degrees from the x axis (Co, 2017).	29
Figure 2.8: Histogram for the 50 mm by 75 mm fracture aperture distribution (Co, 2017).	31
Figure 2.9: Rock joint roughness profiles showing the typical range of JRC (Barton & Choubey, 1977).	32
Figure 2.10: Thermal performance at the producer – a comparison between ECLIPSE simulator and the modified Fox, et al. (2015) solution: A case of a fracture with smooth walls.	33
Figure 2.11: Fracture permeability (left) and temperature distribution (right) in the fracture (X-Y) plane.	33

Figure 2.12: Thermal performance at the producer – a comparison between ECLIPSE simulator and the modified Fox, et al. (2015) solution: A case of a fracture with spatial variations.....	34
Figure 2.13: Average temperature as a function of time, measured at the constant pressure boundary.	35
Figure 2.14: Fluid flow and heat transport on the fracture aperture after 10 minutes for the original lab scale fracture aperture distribution.	36
Figure 2.15: Filtering process done in PETREL to extract the number of grid cells that had flow above 1 cc/hr. The figure is for the original fracture aperture distribution for the parallel flow configuration.....	37
Figure 2.16: Temperature difference between the perpendicular and parallel flow directions for the 100 artificially generated fracture aperture distributions.	38
Figure 2.17: Histogram of the temperature difference between the perpendicular and parallel flow directions for the 100 artificially generated fracture aperture distributions at 0.72 minutes.....	39
Figure 2.18: Temperature difference between the perpendicular and parallel flow directions for the 100 artificially generated fracture aperture distributions at 0.72 minutes into the simulation.....	40
Figure 2.19: Temperature difference between the perpendicular and parallel flow directions for the 100 artificially generated fracture aperture distributions at 10 minutes into the simulation.....	40
Figure 2.20: Temperature difference between the perpendicular and parallel flow directions for the 100 artificially generated fracture aperture distributions at 0.72 minutes into the simulation plotted against the fracture’s flow contact surface area.....	41
Figure 2.21: Temperature difference between the perpendicular and parallel flow directions for the five selected artificially generated fracture aperture distributions.	42
Figure 2.22: Fluid flow and heat transport on the fracture aperture after 10 minutes for Realization 9 of the artificially generated aperture distributions.....	44
Figure 2.23: Fluid flow and heat transport on the fracture aperture after 10 minutes for Realization 11 of the artificially generated aperture distributions.....	44
Figure 2.24: Fluid flow and heat transport on the fracture aperture after 10 minutes for Realization 35 of the artificially generated aperture distributions.....	46
Figure 2.25: Fluid flow and heat transport on the fracture aperture after 10 minutes for Realization 56 of the artificially generated aperture distributions.....	46
Figure 2.26: Fluid flow and heat transport on the fracture aperture after 10 minutes for Realization 63 of the artificially generated aperture distributions.....	47
Figure 2.27: Variogram modeling parameters for Realization 9 of the artificially generated aperture distributions.....	51
Figure 2.28: Variogram modeling parameters for Realization 11 of the artificially generated aperture distributions.....	51
Figure 2.29: Variogram modeling parameters for Realization 35 of the artificially generated aperture distributions.....	51

Figure 2.30: Variogram modeling parameters for Realization 56 of the artificially generated aperture distributions.	52
Figure 2.31: Variogram modeling parameters for Realization 63 of the artificially generated aperture distributions.	52
Figure 2.32: Difference in the cumulative energy produced for the five selected aperture distributions, the original aperture distribution, and a smooth fracture.	53
Figure 2.33: Cumulative energy produced of the perpendicular and parallel flow configurations for the smooth fracture, Aperture 11, Aperture 35, and Aperture 63.	54
Figure 3.1: Two-dimensional synthetic self-affine surfaces with (a) an isotropic self-affine property characterized by a Hurst exponent of 0.8 and (b) an anisotropic self-affine surface with two Hurst exponents ($H_{\parallel} = 0.6$ and $H_{\perp} = 0.8$) in perpendicular directions (Candela, et al., 2009).	60
Figure 3.2: Plot of the Hurst exponents in direction (a) normal to slip and (b) parallel to it of 41 scanned fault patches (Candela et al., 2009). The average Hurst exponent is equal to 0.58 along the direction of slip and 0.81 perpendicular to it. The shaded area and dashed lines indicate 1σ and 2σ confidence intervals, respectively.	60
Figure 3.3: Geometric anisotropy ratios for mated and sheared lab-scale fractures for three fracture length scales (Co C. , 2017).	61
Figure 3.4: Workflow for field-scale fracture aperture distributions generation for thermohydraulic simulation.	70
Figure 3.5: Sample aperture distributions for the different geometric anisotropy ratios and ranges, with indications for the perpendicular and parallel flow configurations relative to the direction of slip/shear.	74
Figure 3.6: The field-scale three-dimensional model showing the grids. The Y and Z axes read negative with increasing values from the reference (zero in this case).	75
Figure 3.7: Temperature difference between the perpendicular and parallel flow directions for the 111 artificially generated field-scale fracture aperture distributions. The difference is temperature profile in the perpendicular direction minus temperature profile in the parallel direction.	77
Figure 3.8: Histogram of the temperature difference between the perpendicular and parallel flow directions for the field-scale artificially generated fracture aperture distributions at one year.	78
Figure 3.9: Histogram of the temperature difference between the perpendicular and parallel flow directions for the field-scale artificially generated fracture aperture distributions at five years.	78
Figure 3.10: Temperature difference between the perpendicular and parallel flow directions for the field scale artificially generated fracture aperture distributions at one year into the simulation. The difference is temperature profile in the perpendicular direction minus temperature profile in the parallel direction.	79
Figure 3.11: Temperature difference between the perpendicular and parallel flow directions for the 111 artificially generated fracture aperture distributions five years into	

the simulation. The difference is temperature profile in the perpendicular direction minus temperature profile in the parallel direction.....	80
Figure 3.12: Temperature difference between the perpendicular and parallel flow directions for the different cases with geometric anisotropic ratio of 1.5. The difference is temperature profile in the perpendicular direction minus temperature profile in the parallel direction.	81
Figure 3.13: Temperature difference between the perpendicular and parallel flow directions for the different cases with geometric anisotropic ratio of 1.5. The difference is temperature profile in the perpendicular direction minus temperature profile in the parallel direction.	82
Figure 3.14: Setting the filter to determine the fracture surface area contacted by the flowing fluid.....	82
Figure 3.15: Fluid flow and heat transport on the fracture aperture after one year for Aperture 1.	83
Figure 3.16: Fluid flow and heat transport on the fracture aperture after one year for Aperture 2.	84
Figure 3.17: Temperature difference between the perpendicular and parallel flow directions for the different cases with geometric anisotropic ratio of 2. The difference is temperature profile in the perpendicular direction minus temperature profile in the parallel direction.	85
Figure 3.18: Temperature difference between the perpendicular and parallel flow directions for the different cases with geometric anisotropic ratio of 2. The difference is temperature profile in the perpendicular direction minus temperature profile in the parallel direction.	86
Figure 3.19: Fluid flow and heat transport on the fracture aperture after one year for Aperture 3.	88
Figure 3.20: Fluid flow and heat transport on the fracture aperture after one year for Aperture 4.	89
Figure 3.21: Fracture aperture distribution for Aperture 4.	89
Figure 3.22: Temperature difference between the perpendicular and parallel flow directions for the different cases with geometric anisotropic ratio of 1.5. The difference is temperature profile in the perpendicular direction minus temperature profile in the parallel direction.	90
Figure 3.23: Temperature difference between the perpendicular and parallel flow directions for the different cases with geometric anisotropic ratio of 3. The difference is temperature profile in the perpendicular direction minus temperature profile in the parallel direction.	91
Figure 3.24: Fluid flow and heat transport on the fracture aperture after one year for Aperture 5.	92
Figure 3.25: Fluid flow and heat transport on the fracture aperture after one year for Aperture 6.	93

Figure 3.26: Temperature difference between the perpendicular and parallel flow directions for the different cases with geometric anisotropic ratio of 4. The difference is temperature profile in the perpendicular direction minus temperature profile in the parallel direction.	94
Figure 3.27: Temperature difference between the perpendicular and parallel flow directions for the different cases with geometric anisotropic ratio of 4. The difference is temperature profile in the perpendicular direction minus temperature profile in the parallel direction.	95
Figure 3.28: Fluid flow and heat transport on the fracture aperture after one year for Aperture 7.	96
Figure 3.29: Fluid flow and heat transport on the fracture aperture after one year for Aperture 8.	97
Figure 3.30: Boxplot of the Hurst Exponents for the different geometric anisotropy ratios.	98
Figure 3.31: Fluid flow and heat transport on the fracture aperture after one year for Aperture 9.	99
Figure 3.32: Cumulative Energy produced between the perpendicular and parallel flow directions for Aperture 9.	100
Figure 4.1: Variation of viscosity with temperature. The insert in the graph shows the trend at various pressures.	104
Figure 4.2: Description of the aperture distributions used in this study. The apertures range from 0 - 5 mm. The aperture distributions on top are the planar views, while the diagrams at the bottom are the isometric views.	106
Figure 4.3: Reservoir simulation domain showing the grids used in the model. The height (Z-axis) is not drawn to scale.	108
Figure 4.4: Temperature profile for all the aperture distributions at a reservoir temperature of 200 °C and injection water temperature of 40 °C.	112
Figure 4.5: Flow maps for all the aperture distributions at a reservoir temperature of 200 °C and injection water temperature of 40 °C.	113
Figure 4.6: Flow map for all the aperture distributions showing the area contacted by the flowing fluid at a reservoir temperature of 200 °C and injection water temperature of 40 °C.	114
Figure 4.7: Temperature profile at the producer on Aperture 1 assuming constant viscosity and temperature-dependent viscosity for different reservoir temperatures and injection temperature of 40 °C.	115
Figure 4.8: Temperature profile at the producer on Aperture 1 assuming constant viscosity, temperature-dependent viscosity for different reservoir temperatures, and injection temperature of 60 °C.	116
Figure 4.9: Temperature distribution at the fracture after five years in the X-Y plane. 13a is for constant viscosity, while 13b is for temperature-dependent viscosity. The reservoir temperature is 200 °C, while the injection water temperature is 40 °C.	117

Figure 4.10: Temperature profile at the producer on Aperture 2 assuming constant viscosity and temperature-dependent viscosity for different reservoir temperatures and injection temperature of 40 °C.....	118
Figure 4.11: Temperature distribution at the fracture after five years in the X-Y plane. 15a is for constant viscosity, while 15b is for temperature-dependent viscosity.....	119
Figure 4.12: Temperature profile at the producer on Aperture 3 assuming constant viscosity, temperature-dependent viscosity for different reservoir temperatures, and injection temperature of 40 °C.....	120
Figure 4.13: Temperature distribution at the fracture after five years in the X-Y plane. 17a is for constant viscosity, while 17b is for temperature-dependent viscosity.....	121
Figure 4.14: Temperature profile at the producer on Aperture 3 assuming constant viscosity and temperature-dependent viscosity for different reservoir temperatures and injection temperature of 60 °C.....	122
Figure 4.15: Temperature profile at the producer for Aperture 3 assuming constant viscosity and temperature-dependent viscosity for different injection temperatures and reservoir temperature of 250 °C.....	122
Figure 4.16: Difference between temperature profiles for constant viscosity and temperature-dependent viscosity models for different injection temperatures and reservoir temperature of 250 °C.....	123
Figure 5.1: Thermohydraulic workflow used in this study.	130
Figure 5.2: Interaction between the different processes in the two-way thermohydraulic coupling between ECLIPSE (thermohydraulic model) and VISAGE (geomechanical model).	134
Figure 5.3: Schematic of how the aperture is assumed to change with changes in strain. In Figure 5.3a, the rock is expanding; hence the aperture is reducing. In Figure 5.3b, the rock is contracting, leading to an increase in the aperture.	135
Figure 5.4: Comparing the thermohydraulic and thermohydraulic models for a single fracture with homogeneous and heterogeneous apertures (Guo et al., 2016).	136
Figure 5.5: Comparing the results of this study with the results from Guo et al. (2016) for three years.	138
Figure 5.6: Three-dimensional schematic of the Altona Field Laboratory (AFL) showing the spatial configuration of injection well 204 and production well 304 and three monitoring wells (104, 404, and 504) (Hawkins et al., 2017).	139
Figure 5.7: Comparison between the predicted data and the observed data for the Altona Field Heat Transport Experiment (Hawkins et al., 2020).....	141
Figure 5.8: Three-dimensional mesh for the thermohydraulic model representing the Altona Field Laboratory (AFL).	141
Figure 5.9: Schematic of the thermohydraulic model with the fracture plan exposed to show the heterogeneous permeability distribution.	142
Figure 5.10: Plot of the thermal drawdown using temperature-dependent viscosity in the model along with the observed and predicted data for the Altona Heat Transport Experiment.....	143

Figure 5.11: Fracture from the thermohydraulic (TH) model embedded within the geomechanical model. The dark color shows the degree of refinement of the model. The grids become coarser away from the TH model for the geomechanical model.....	144
Figure 5.12: Evolution of fracture aperture distribution, thermal stress, energy flow paths, and the temperature distribution for the Altona field case study. The “THM model” includes the thermoelastic effects the “TH model” does not include thermoelastic effects.	147
Figure 5.13: Production well fluid temperature for the thermohydraulic (TH) model and the thermohydraulic (TH) model along with the measured data at the Altona Field Laboratory.....	148
Figure 5.14: Grid of the thermohydraulic model. The area colored in black shows the location of the fracture embedded within the grid.	150
Figure 5.15: Original aperture distribution used for the thermohydraulic model where thermal drawdown was in favor of the perpendicular flow configuration.	151
Figure 5.16: Thermal drawdown curves of the thermohydraulic and thermohydraulic models for the perpendicular and parallel flow configuration.	152
Figure 5.17: Comparison between the aperture, temperature, and flow maps for the thermohydraulic and thermohydraulic model one month into the simulation – Perpendicular and Parallel flow configurations.	153
Figure 5.18: Comparison between the aperture, temperature, and flow maps for the thermohydraulic and thermohydraulic model one year into the simulation – Perpendicular and Parallel flow configurations.	154
Figure 5.19: Original aperture distribution used for the thermohydraulic model where thermal drawdown was in favor of the parallel flow configuration.	155
Figure 5.20: Location of the vertical wells (a) along the fracture compared to the location of the horizontal wells (b) in a perpendicular flow configuration.	155
Figure 5.21: Thermal drawdown curves of the thermohydraulic and thermohydraulic models for the perpendicular and parallel flow configuration and the vertical well.	157
Figure 5.22: Thermal drawdown curves of the thermohydraulic and thermohydraulic models for the perpendicular and parallel flow configuration only.	157
Figure 5.23: Comparison between the aperture, temperature, and flow maps for the thermohydraulic and thermohydraulic model one year into the simulation – Perpendicular, Parallel and vertical flow configurations.	158
Figure 6.1: The hypothetical EGS model showing the grids. The height (Z-axis) is not to scale.....	165
Figure 6.2: Phase behavior of water. The blue circle shows the injection conditions, while the blue star shows the reservoir conditions (Wikipedia, 2021b).....	167
Figure 6.3: Phase diagram for CO ₂ . The red circle shows the injection conditions, while the red star shows the reservoir conditions (Wikipedia, 2021c).....	167

Figure 6.4: Thermophysical properties of water and CO ₂ as a function of temperature and pressure (Huang et al., 2019).	168
Figure 6.5: Heterogeneous fracture aperture distribution for correlation lengths of 50 m, 100 m, 200 m, and 400 m.	170
Figure 6.6: Cumulative energy produced (bold lines) and net heat extracted (dashed lines) for CO ₂ and water at different mass flow rates after two years of continuous fluid circulation, smooth fracture case.	172
Figure 6.7: Energy production rate (bold lines) and net heat extraction rate (dashed lines) for CO ₂ and water at different mass flow rates after two years of continuous fluid circulation.	173
Figure 6.8: Carnot efficiencies for CO ₂ and water at different mass flow rates after two years of continuous fluid circulation, smooth fracture case.	173
Figure 6.9: Cumulative energy produced vs. cumulative energy injected for CO ₂ and water over seven years in a smooth fracture.	175
Figure 6.10: Difference between cumulative energy produced for CO ₂ and water over time for different fracture aperture correlation lengths.....	176
Figure 6.11: Temperature map at the fracture for CO ₂ and water at seven years for different fracture aperture correlation lengths.	177
Figure 6.12: Temperature difference measured at the producer for CO ₂ and water over time for different fracture aperture correlation lengths.....	177
Figure 6.13: Difference in cumulative energy produced for CO ₂ and water at different mass flow rates for a selected fracture with aperture variability with a correlation length of 200 m.	178
Figure 6.14: Evolution of the temperature distribution at the fracture plane for CO ₂ and water for the different mass flow rates.	179
Figure 6.15: Temperature difference measured at the producer for CO ₂ and water over time for different mass flow rates.	180
Figure 6.16: Temperature difference measured at the producer for CO ₂ and water as a function of time for 40 kg/s of water and 200 m fracture aperture correlation length. ...	181
Figure 6.17: Cumulative energy extracted for CO ₂ and water over time for smooth fracture and fracture with spatial variations.....	182
Figure 6.18: Energy extraction rate for CO ₂ and water over time for smooth fracture and fracture with spatial variations.....	182
Figure 6.19: Temperature map for CO ₂ and water over time for a fracture with spatial variations.....	183

Chapter 1

1 Introduction

Clean energy sources are becoming increasingly popular due to their reduced impact on the environment and growing technological innovation to support the energy transition. Geothermal energy is one of such energy sources which is generated and stored below the Earth's surface and can be harnessed as a clean energy resource. Geothermal energy is advantageous in many ways as it is considered renewable, can be used as a baseload in electricity generation, can also provide heat directly and through the use of geothermal pumps, and has a relatively low levelized cost of electricity. Being a cleaner energy source, geothermal energy can also play a significant role in decarbonizing the power sector. Although geothermal energy in today's global renewable energy mix is small, accounting for 0.3% of world electricity production and 0.2% of world heat production (REN21, 2020), there is substantial geothermal potential due to the vast amount of heat stored within the Earth. The geothermal potential is estimated to be equivalent to 44.2 terawatts-thermal (TWth) of power (Pollack et al., 1993).

The presence of fluid, heat, and permeability are essential components that make a geothermal resource suitable for utilization. Geothermal resources can be classified as conventional and unconventional. Traditionally, geothermal resources consisted of hot water reservoirs at varying temperatures and depths below the Earth's surface. Hot water or steam was tapped from these subsurface reservoirs via deep wells drilled to the depth of the resource. Such resources are referred to as conventional hydrothermal resources. Today, geothermal resources have expanded to incorporate unconventional hydrothermal resources, consisting of low-temperature resources, coproduced resources, and enhanced/engineered geothermal systems (EGS).

One of the unconventional geothermal resources fast gaining attention is the enhanced geothermal system, alternatively called engineered geothermal systems. When a resource lacks sufficient permeability and fluid to generate electricity but has adequate

heat stored in it, the concept of Enhanced Geothermal Systems (EGS) may be used. An Enhanced Geothermal System (EGS) allows heat extraction from low-permeability hot reservoirs and low-enthalpy reservoirs dominated by conductive thermal recharge. Heat extraction is achieved by first creating permeable pathways in the form of induced fractures within the rock body then injecting relatively cold fluids (e.g., liquid water) that keep the fracture(s) open and collect thermal energy from the surrounding bulk rock matrix. One or more production wells return heated injectate to the ground surface for use as a working fluid for electricity generation or direct use. Fractures are initiated by hydraulic stimulation. New tensile fractures propagate from the borehole once injection fluid pressures exceed the failure limits of the bulk rock and/or shear is induced along pre-existing fractures (e.g., McClure and Horne, 2014; Gischig and Preisig, 2015). Figure 1.1 shows an Enhanced Geothermal System with a doublet configuration.

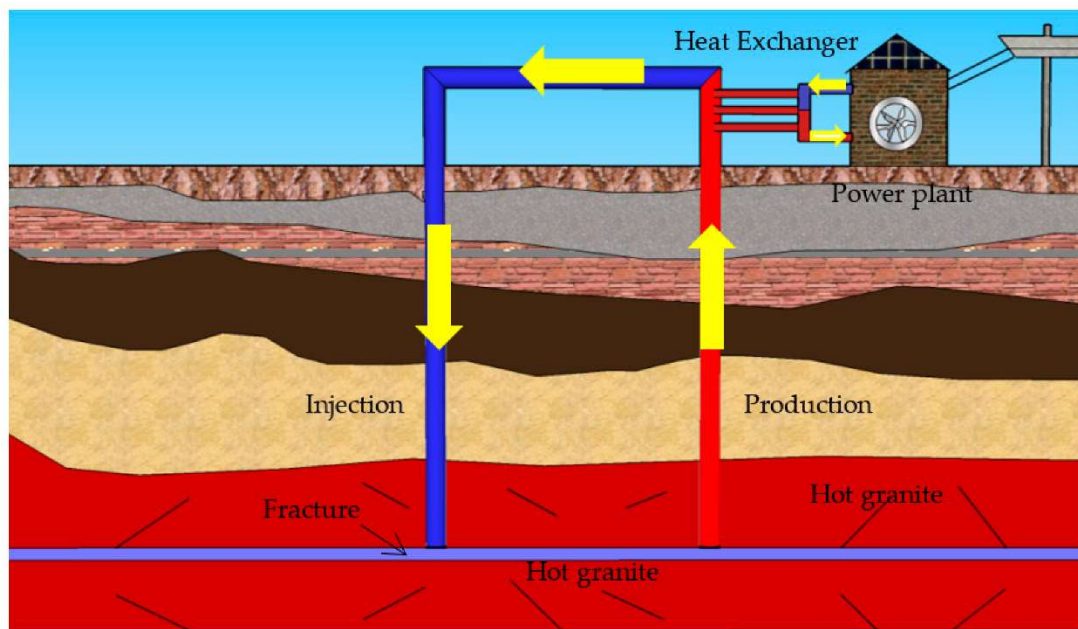


Figure 1.1: Schematic of an Enhanced Geothermal System with a doublet configuration (Yao, Shao, & Yang, 2018).

According to the Office of Energy Efficiency and Renewable Energy (Office of Energy Efficiency and Renewable Energy, 2014), EGS offers the chance to extend the application of geothermal resources to larger areas and new geographic areas. They further state that in the United States, more than 100 GWe of economically viable geothermal

capacity may be available in the continental United States, representing a 40-fold increase over present geothermal power generating capacity (Office of Energy Efficiency and Renewable Energy, 2014).

Figure 1.2 shows the overall geothermal resource map of the United States, which includes existing conventional hydrothermal sites and EGS resource potential. According to the U.S. Energy Information Administration (U. S. Energy Information Administration, 2018), this potential EGS generation capacity is approximately 10% of the current total United States electricity generating capacity.

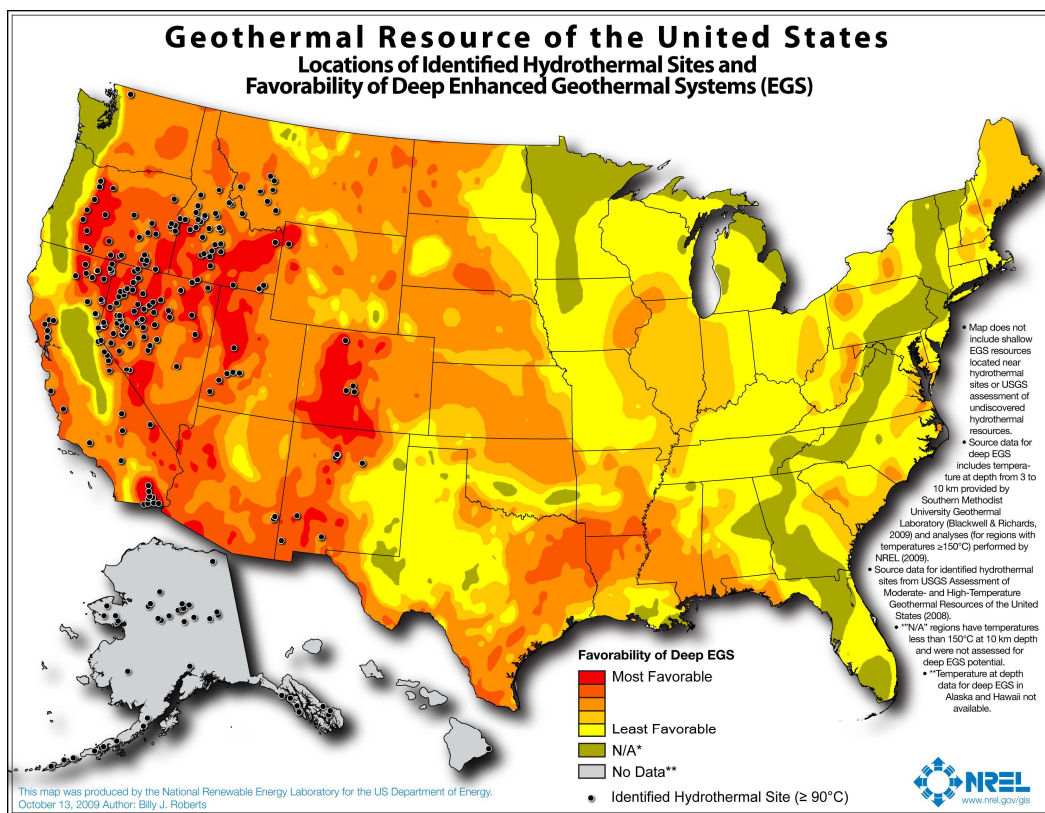


Figure 1.2: Map of the U.S. Geothermal Resource consisting of hydrothermal sites (black markers) and favorable enhanced geothermal system (EGS) locations in the U.S. (National Renewable Energy Laboratory, 2009).

The main conduit for flow in Enhanced Geothermal Systems is through faults or fractures from where heat is transported via conduction by contact between the adjacent hot rock and the cold fluid, and then convection as the fluid flows through the fault or fractures. Fractures can be stimulated by either of two mechanisms (Gischig & Preisig,

2015); (1) hydraulic fracturing where new tensile fractures are propagated from the borehole by means of a fluid pressure overcoming the minimum principal stress and perhaps the tensile strength of intact rock; (2) hydroshearing where over-pressure induces slip along pre-existing fractures that are favorably oriented in the stress field for reactivation in shear. Gischig and Preisig (2015) additionally assert that the permeability gained by hydroshearing is irreversible primarily due to the rearrangement of asperity contacts accompanied by shear dilation. Several studies have shown that the predominant mechanism in most EGS projects is hydroshearing (Pine and Batchelor (1984); Murphy and Fehler (1986); Ito (2003); Ito and Hayashi (2003); Evans (2005); Tester et al. (2006); Kohl and Mégel (2007); Bruel (2007); Dezayes et al. (2010); Cladouhos et al. (2011); Petty et al. (2013); McClure and Horne (2014); Gischig and Preisig (2015)). Thus, for the purpose of this study, the created fractures have been assumed to be created through hydroshearing.

In the methodology for estimating the U.S. EGS resource, a recovery factor of 20% was used (Augustine, 2011; Augustine, 2016). The MIT 2006 report “Future of Geothermal Energy” (Tester et al., 2006) documents a similar recovery factor of $20\% \pm 2\%$. This estimate originated from the work by Sanyal and Butler (2005), who modeled flow in fractured reservoirs using a three-dimensional finite-difference model. They examined the impact of rock temperature, fracture spacing, fluid circulation rate, well configuration, post-stimulation porosity, and permeability to estimate the recoverable heat fraction of the geothermal resource. While the simulation results by Sanyal and Butler (2005) gave a recovery factor of about $40 \pm 7\%$, the MIT report (Tester et al., 2006) showed that in early field testing, channeling, short-circuiting, and other reservoir-flow problems occur. Thus the estimated 40% recovery factor by Sanyal and Butler (2005) was revised to 20% to account for these effects.

Tester et al. (2006) also highlighted that channeling and short-circuiting of circulation fluids have been a challenge in conductive heat transfer efforts. Flow channeling is a phenomenon where liquid flow through a geologic system with a heterogeneous structure is focused along a few preferred pathways (Tsang & Neretnieks, 1998). These pathways are "paths of least resistance," where most of the flow goes (Tsang

& Tsang, 1989). These heterogeneities stem from fracture apertures (the void space between contacting rough fracture surfaces) and matrix porosities, although due to the low value of porosities in hot low permeability rocks, heterogeneities in fracture apertures are more significant.

According to Co (2017) and Mattson et al. (2018), it is often assumed that the hydraulic aperture and consequently the permeability within the fault or fracture are constant. However, real faults and fractures have rough surfaces that lead to tortuous flow pathways (Brown, 1987; Tsang & Neretnieks, 1998). Channeling of flow due to rough surfaces have been demonstrated through laboratory experiments (Hakami and Larsson, 1996; Pyrak-Nolte et al., 1997; Lee and Cho, 2002) and numerical simulations and field investigations (Abelin et al., 1991; Tsang and Neretnieks, 1998; Watanabe et al., 2008; Mattson et al., 2018; and Hawkins et al., 2020).

In Enhanced Geothermal Systems, heat production, fluid flow and heat exchange are interrelated. Heat from the rock surrounding the fracture is transferred to the production well(s) through the flowing fluid, and hence only the portion of fracture in contact with the flowing fluid provides effective heat exchange surface area. The more heat exchange surface area encountered by the flowing fluid, the more efficient is the heat extraction. The implications of a heterogeneous local aperture distribution in faults and fractures are that individual well productivity and interwell connectivity can be impacted significantly by the well locations (Abelin et al., 1991). In addition, under channeled flow conditions, relatively reduced heat transfer area can lead to inadequate heat transfer efficiency (e.g., Neuville et al., 2010) and, as a consequence, cause premature thermal breakthrough and reduced energy recovery from Enhanced Geothermal Systems (Co, 2017; Hawkins et al., 2017).

As cold fluid flows through the preferred pathways, the rock body close to them tends to cool faster than other regions of the hot, dry rock. The cooled rock body develops thermal stress that reduces the effective compressive stress acting on the preferential flow paths and thereby increases the fracture aperture (Guo et al., 2016). The consequence is that the aperture increase makes the flow more channelized, perhaps leading to further

reduced heat exchange efficiency, rapid heat production deterioration, and reduced thermal recovery.

Many studies investigating the thermal performance of enhanced geothermal systems have used water as the working fluid. With the growing need to reduce greenhouse gas emissions and the current high cost of implementing carbon capture and sequestration projects, carbon dioxide (CO₂) utilization is gaining increasing interest globally. CO₂ utilization as an alternative working fluid to water for EGS was first investigated by Brown (2000). Brown (2000) highlighted the advantageous properties of CO₂ over water, including having a higher density-to-viscosity ratio, a more significant buoyancy force, and lower salt solubility. Since then, several studies (Pruess, 2006; Luo and Jiang, 2014; Isaka et al., 2019; and Wu and Li, 2020) have built on the work of Brown (2000), with most studies confirming the findings that supercritical CO₂ provides greater power output and can simultaneously sequester CO₂. However, these studies did not consider fracture aperture heterogeneity.

Knowing that flow channeling can impact the recovery of EGS, it is imperative to model it accurately for better thermal performance estimation and forecasting while considering critical physical phenomena that occur in an EGS. Also of importance is to investigate how flow channeling can be harnessed to improve thermal performance and ultimately recovery either through the placement of wells relative to the direction of fracture shear offset or through the choice of working fluid for the EGS.

1.1 Prior Related Works

1.1.1 Thermal Performance Relative to Fracture Shear Offset

The preliminary work in this study is premised on the findings in the work by Co (2017). Co (2017) investigated the fracture flow behavior of fractures with spatial variations. Using Sequential Gaussian Simulation (SGSIM), a total of 100 artificial fracture aperture maps were generated from lab-scale fractures taken from the work of Ishibashi et al. (2012). For each fracture map generated, two flow configurations were considered. The flow configurations were assigned based on the lateral direction of the shear offset for the

sheared fractures. Thus, the perpendicular flow configuration had a pressure drop perpendicular to the lateral shear offset direction. In contrast, the parallel flow configuration had a pressure drop parallel to the lateral shear offset direction. Figure 1.3 shows what the lateral direction of shear offset implies in creating a sheared fracture either due to slip or from a mated fracture. At the same time, Figure 1.4 describes what the perpendicular and parallel flow configuration represents.

From the 100 artificial aperture maps studied, it was seen that the sheared fractures had channelized flow patterns and anisotropic flow behavior parameters. For the perpendicular flow configuration, 97% of flow occurred in 26% of the fracture area, while for the parallel flow configuration, 97% of the flow occurred in 15% of the fracture area. The geometric anisotropy, the higher degree of channeling in the parallel flow configuration, and the reduced fracture contact area in the parallel configuration, prompted the need to investigate the consequential impact on thermal performance due to fracture anisotropy.

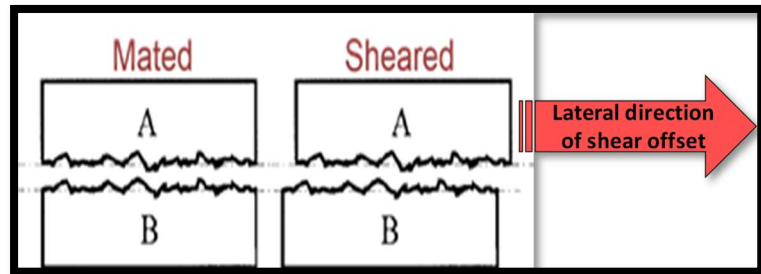


Figure 1.3: Illustration of lateral direction of shear offset from Ishibashi et al. (2012).

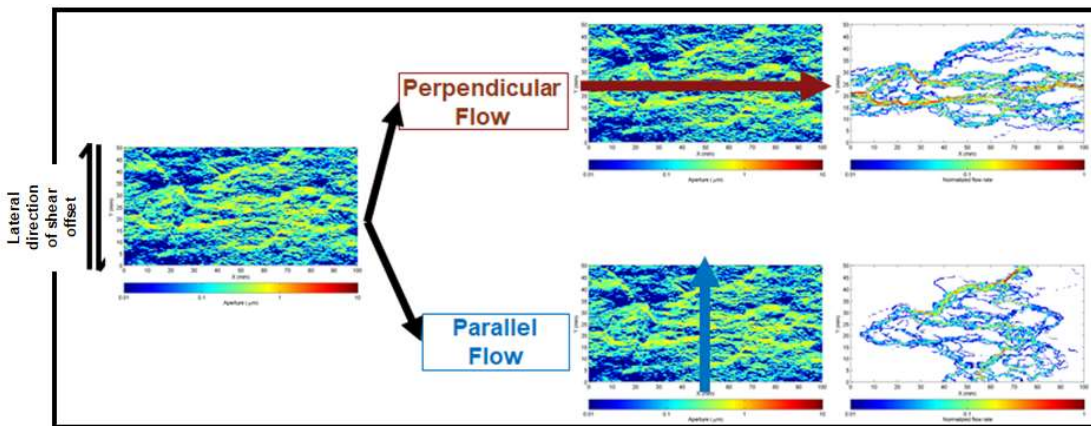


Figure 1.4: Perpendicular and Parallel flow configurations relative to the lateral direction of shear offset from Co (2017).

1.1.2 Thermohydromechanical modeling of Enhanced Geothermal Systems

With fracture aperture anisotropy impacting flow behavior and resulting in different degrees of channeling and fracture contact area, as well as the known issue of a hot rock developing thermal stress when cold fluid is injected, there is a need to investigate how fracture aperture anisotropy is impacted by a thermohydromechanical coupling of the physical processes taking place during heat exchange of the EGS. Guo et al. (2016) documents that numerous studies have shown evidence for fracture aperture/transmissivity evolution due to the thermohydromechanical (THM) processes in EGS reservoirs dominated by either a single fracture/fault or a fracture network. Findings from such studies include that the fracture flow increases due to further opening of a single fracture; only the aperture near the central part of the fracture increases over time; injection pressure decreases with an increasing water recovery percentage, indicating an increase in the overall permeability, and flow inevitably becomes more concentrated into a few channels during heat production. According to Guo et al. (2016), although THM processes significantly affected heat production in those studies, the quantitative effects of spatially heterogeneous fracture aperture on flow channeling remained poorly understood. Hence, there is a need to understand better how fractures with spatial variation and geometric anisotropy are better modeled considering a combined thermohydromechanical process.

1.1.3 CO₂ Utilization in EGS

The studies (Pruess, 2006; Luo and Jiang, 2014; Isaka et al., 2019; and Wu and Li, 2020) that followed the work by Brown (2000) comparing CO₂ to water as a working fluid for enhanced geothermal systems, showed in addition to the findings of the Brown (2000) study, that the use of CO₂ minimizes parasitic losses from pumping and cooling; reduces the use of water, and could reduce scaling and corrosion of system components due to CO₂ having a much lower tendency to dissolve minerals and other substances, compared to water. On the other hand, Pritchett (2009) considered multiphase flow effects during the heat mining and CO₂ sequestration process and found that heat sweep effectiveness

can be maximized if water is used as a working fluid in place of CO₂. The maximized heat sweep efficiency of water over CO₂ was explained as due to the development of an unstable material interface between the low-viscosity injected CO₂ and more viscous native water, resulting in the more mobile CO₂ bypassing the relatively higher viscosity regions and reducing the overall thermal sweep efficiency. These conflicting findings, combined with the absence of studies on fractures with spatial variations, motivated the need to investigate thermal performance in enhanced geothermal systems considering fractures with heterogeneity in aperture distribution.

Huang et al. (2019) carried out a field-scale investigation of the heat extraction performances of water and supercritical CO₂ as EGS working fluids. A five-spot well pattern was used. A fixed pressure drop was specified between the injection well and four production wells. They determined that supercritical CO₂ had a higher mass flow rate, higher heat extraction rate, a shorter field life, and approximately the same cumulative heat extraction compared with water for the given pressure drop. Their study, however, did not consider the possible spatial variations in fracture aperture.

Zhang et al. (2017) carried out a lab-scale investigation comparing the heat transfer behavior of supercritical CO₂ on a rough fracture and a smooth fracture at different mass flow rates and different rock temperatures. The study showed that heat transfer in the rough fracture was hindered by channeling effects. Their study, however, does not compare how water would perform in a similar situation. Moreover, the behavior of fluids varies with temperature and pressure, hence it is of interest to understand how the heat transfer on both rough and smooth fractures compares for CO₂ and water on the field scale, considering in situ conditions.

1.2 Statement of the Problem

This study addressed the gaps in the prior related work.

The study by Co (2017) demonstrated the impact of fracture geometric anisotropy on fluid flow behavior. Knowing that only the portion of fracture in contact with the flowing fluid provides effective heat exchange surface area, it is of interest to understand how the fracture and flow anisotropy affect EGS thermal performance. This work thus

investigated and provided answers on how the EGS thermal performance is impacted by the flow configuration relative to the fracture shear offset on the lab scale; how this relates to flow configuration relative to slip direction on the field scale; and how EGS thermal performance of the different flow configurations are affected when thermohydronechanical processes are coupled.

The use of CO₂ as an alternative working fluid for EGS was investigated. With different views on the suitability of CO₂ over water as an EGS working fluid, this study investigated to what extent CO₂ is a better working fluid than water. Knowing the conditions under which CO₂ is a better working fluid than water will enable decision-makers to know what factors to consider in choosing one working fluid over another to optimize heat extraction from EGS.

1.3 Dissertation outline

The overall goal of this study was to understand how enhanced geothermal systems can be harnessed, taking into account spatial variations in fracture apertures in hot low permeability rocks. Chapter 1 discusses the motivation, scope, prior related work, and intended contributions of this thesis.

Chapter 2 looks at how the problem is formulated mathematically, the proposed solution methodology, and applying the methodology to fractures on a lab scale. The goal is to understand the impact of fracture aperture anisotropy on heat extraction.

In Chapter 3, the work is extended to field-scale simulations. The process of characterizing anisotropy in field-scale simulations is outlined. The impact of geometric anisotropy on the thermal performance of fractures with spatial variations in aperture distribution is examined for horizontal fractures.

Chapter 4 describes an investigation carried out to understand the impact of assuming constant viscosity in thermohydraulic modeling of enhanced geothermal systems and compare how the thermal performance differs from a model using temperature-dependent viscosity. This simulation was carried out over different reservoir

temperatures, injection temperatures and fracture apertures with varying correlation lengths.

In Chapter 5, the thermohydraulic model used in previous chapters was coupled with a geomechanical model. The study's objective described in this chapter was to investigate how the injection of cold fluid into a hot rock through fractures with spatial variations may impact the thermal performance of the system being modeled. Experiments at the Altona Field Laboratory were used to demonstrate the coupling methodology and demonstrate to what extent the results of a model with thermoelasticity differ from a model without thermoelasticity coupled to the thermohydraulic model.

Chapter 6 describes an investigation of CO₂ as an alternative working fluid in enhanced geothermal systems. Variations in fracture aperture were accounted for in the analysis. Sensitivities were examined across different correlation lengths and different injection rates to determine to what extent CO₂ might be a better heat extraction fluid than water.

All the findings from the chapters as mentioned above, conclusions, and future work are summarized in Chapter 7.

Chapter 2

2 Anisotropic Effects on Lab Scale

Thermal Performance

2.1 Introduction

Natural fractures are typical features in many rocks, occurring at various length scales. It has been documented that these fractures have surfaces with spatial variations in aperture that lead to tortuous flow pathways (Brown, 1987; Tsang & Neretnieks, 1998). Understanding the spatial variations of fracture apertures and their impact on fluid flow is relevant for systems that rely on physical processes dependent on flow, such as unconventional reservoirs and geothermal reservoirs. Spatial aperture variation is quite often referred to as “roughness” in the literature. Thus, wherever the term roughness is used, it refers to the spatial variations in aperture.

Brown (1989) investigated the relationship between the hydraulic properties and electrical properties of fractures with spatial variations. The results indicated that the flow of fluid and the movement of electric current through fractures with spatial variations in aperture is primarily dependent on the area of contact between the fluid and the rock surface, while the details of the fracture aperture variability were of secondary import. The fracture aperture variability analyzed considered the fracture aperture distribution to be isotropic.

According to Thompson and Brown (1991), anisotropic roughness is often observed on natural fracture surfaces, and surface roughness anisotropy may also be manifest in the fracture aperture. Candela et al. (2012) examined the topographic aperture variability measurements of five exhumed faults, and 13 surface earthquake ruptures with scales ranging from 50 μm to 50 km. Using a three-dimensional Light Detection And Ranging (LIDAR) apparatus, laser profilometer, and white light interferometer, they measured the three-dimensional topography of the same objects spanning complementary

scale ranges from 50 μm to 10 m. They observed that fault aperture variability is scale-dependent, with an anisotropic self-affine behavior that is slightly anisotropic. They determined the Hurst exponent, H , to be 0.58 ± 0.07 in the slip direction and 0.81 ± 0.04 in the direction perpendicular to slip. In addition, they examined the two-dimensional aperture variability of the surface rupture of 13 major continental earthquakes. They determined that the ruptures show geometrical properties consistent with the slip-perpendicular behavior of the smaller-scale measurements.

The impact of fracture aperture anisotropy on flow properties has been studied. Thompson & Brown (1991) investigated the role of anisotropic surface aperture variability on fluid flow, solute transport, and electrical current flow in fractures. They represented the fracture surface topography in terms of fractal geometry, allowing them to use the decaying power-law power spectral density functions of the same form as fractal surfaces to model the surface aperture variability. They used the spectral synthesis method presented by Peitgen & Saupe (1988) and modified it to include anisotropy. The average fluid flow and average electric current were solved independently for a 100 cm by 100 cm fracture plane using equations of conservation of mass and conservation of charge, respectively. Their results showed that the directional characteristics of the surface were critical in determining fracture transport properties than the degree of aperture variability. They determined that aperture variability oriented parallel to the primary flow direction enhanced fluid and solute transport rates while aperture variability oriented transverse to the flow direction inhibited flow rates and delayed solute movement through the fracture.

Co (2017) analyzed flow properties of lab-scale fractures. From the study by Co (2017), it was determined that sheared fractures exhibited geometric and permeability anisotropy. Using Sequential Gaussian Simulation and the variogram from the lab-scale fractures, Co (2017) generated several artificial aperture distributions to investigate further the geometric and permeability anisotropy of the lab-scale fractures. Flow configurations were assigned based on the lateral direction of the shear offset for the sheared fractures. Thus, the perpendicular flow configuration had a pressure drop perpendicular to the lateral shear offset direction. In contrast, the parallel flow configuration had a pressure drop parallel to the lateral shear offset direction. From the

study by Co (2017), it was determined that for the perpendicular flow configuration, 97 % of flow occurred in 26 % of the fracture area, while for the parallel flow configuration, 97 % of the flow occurred in 15 % of the fracture area, implying that there was lower contact area with the parallel flow configuration.

Enhanced Geothermal Systems rely on heat extraction from the physical process of fluid flow. Cold fluid is injected into a hot rock with flow predominantly through fracture(s). Heat from the rock surrounding the fracture(s) is transferred to the production well(s) through the flowing fluid that comes in contact with the rock; hence only the portion of the fracture in contact with the flowing fluid provides effective heat exchange surface area. The more heat exchange surface area contacted by the flowing fluid, the more efficient is the heat extraction.

Several studies at the lab scale have been carried out to understand the coupled flow and heat process in Enhanced Geothermal Systems. Zhao & Tso (1993) investigated heat transfer experimentally by water flow in fractured rock. They determined that using conventional heat convection relations and assuming a smooth wall between the fractures would overestimate the heat transfer coefficients of natural fractures. They thus recommended that surface aperture variability be taken into account to quantify heat transfer from fractured rock.

Huang et al., (2016) investigated the single-phase convective heat transfer and pressure drop of water flowing through a single fracture in a cylindrical granite rock. They employed a roughness-viscosity model to account for the effects of the spatial variations in the fracture surface. Their study showed that the flow friction is raised, and the heat transfer is weakened significantly due to the large relative aperture variability.

Bai et al., (2017) combined experiments and analytical methods to evaluate the overall heat transfer coefficient (OHTC) of water flowing through a single fracture in a granite core. The cylindrical specimen was 50 mm in diameter and 100 mm in length. The fracture had a heterogeneous aperture variability distribution that was taken into account in the study. By considering the fracture aperture distribution in their study, the analytical model they formulated for determining OHTC was deemed to be more effective than some prior methods for the experimental conditions.

Ma et al., (2019) investigated the effects of the volumetric flow rate, the outer wall surface temperature, the Joint Roughness Coefficient (JRC), and the fracture apertures on the heat transfer of water flowing through fractures with spatial variations in aperture. They used 3D printing to manufacture ten samples with JRC values of the fracture surface ranging from 0–2 to 18–20. The use of 3D printing enabled them have better control of the fracture morphology. The ten fracture surfaces had lengths of 100 mm and widths of 50 mm. Their study determined that a surface fracture with higher degree in spatial variations in aperture results in greater heat extraction during the flow of the fluid through the rock surface due to a larger surface area to conduct the heat transfer under their experimental conditions.

Zhang, et al., (2020) used numerical modeling and simulation to understand how fracture aperture variability impacts heat transfer on the microscale. The fracture size studied was a 64 mm by 64 mm fracture plane. Their results showed that an increase in fracture aperture variability resulted in an increased contact area with the heat transfer coefficient decreasing with the increase in the roughness coefficient.

The studies mentioned above demonstrate that the geometry of the fracture surface has significant implications for heat transfer through the fracture. However, these studies did not consider the heat transfer implications of fracture aperture variability anisotropy.

Gao et al., (2021) studied the influence of flow direction on the heat transfer characteristics applicable to a single fracture in granite. They established a single fracture heat transfer model with a random geometry profile. The model was verified for a fracture that a smooth surface. Four cases with fracture profiles and varying angles between flow directions were set up to simulate and explore the heat transfer performance of distilled water through fractures. They used the parameter α of values 0° , 30° , 60° , and 90° for the surface flow direction. 0° was parallel to the direction of flow, while 90° was perpendicular to the direction of flow. From their study, they deduced that a model with smooth fracture surface in the flow direction exhibits a higher heat transfer capacity than that of the fracture model with varying aperture variability. Moreover, the fracture surface with $\alpha = 0^\circ$ resulted in more cooling than the fracture with $\alpha = 90^\circ$. They concluded from their study

that the angle between the fracture morphology and flow direction influences the convection heat transfer process.

The fracture surface used in the study by Gao, et al. (2021) was a pseudo-3D fracture surface that does not account for the anisotropy of the fracture aperture variability. The fracture aperture distribution thus may not represent the true morphology of real fractures. Also, only four fracture surface distributions were investigated. Hence, in this study, the impact of fracture aperture variability anisotropy on heat transfer was investigated using fracture surface aperture variability derived from real laboratory fractures and included an additional 100 artificially generated fracture aperture distributions representative of real fractures.

2.2 Methodology

2.2.1 Governing Equations

A three-dimensional single fracture model was built to study the impact of anisotropy on the heat transfer characteristics of a typical single fracture in granite at the lab scale. The model is simulated to flow cold fluid through one end of the fracture; the fluid is heated by the surrounding rock and then recovered at the other end of the fracture. The fracture is horizontal; hence gravity is not considered in the flow equation within the fracture.

The mass conservation equation for compressible fluid is given by:

$$\frac{\partial(\rho_f \phi)}{\partial t} + \nabla \cdot (\rho_f \vec{v}) = Q \quad (2.1)$$

where ρ is the fluid density; f is for the fluid; ϕ is the rock porosity; t is time; \vec{v} is the fluid velocity vector; and Q is the source or sink term.

From Darcy's law, the fluid velocity vector is given by:

$$\vec{v} = -\frac{k}{\mu} (\nabla P) \quad (2.2)$$

where k is the intrinsic permeability tensor of the rock matrix; μ is the fluid dynamic viscosity; and P is one of the independent variables, pressure.

The energy balance over the fluid phase and solid phase in the porous medium is:

$$\frac{\partial}{\partial t} (\phi \rho_f C_f T + (1 - \phi) \rho_r C_r T) + \nabla \cdot (\rho_f C_f T \vec{v}) = \nabla \cdot (K_{eff} \nabla T) + \mathbb{Q} \quad (2.3)$$

where C_f is the specific heat capacity of the fluid; ρ_r is the rock bulk density; C_r is the specific heat capacity of the rock; K_{eff} is the thermal conductivity averaged over the rock matrix and pore space; and \mathbb{Q} is a heat source/sink term.

$$K_{eff} = \phi K_f + (1 - \phi) K_r \quad (2.4)$$

No-flow boundaries and no heat flux across the boundaries are defined for the boundary conditions. To model anisotropy in heat transfer, two flow configurations were investigated. The perpendicular flow configuration had a pressure drop perpendicular to the lateral shear offset direction, while the parallel flow configuration had a pressure drop

parallel to the lateral shear offset direction (Co, 2017). The boundary conditions for the different flow configurations are shown in Figure 2.1. To solve the coupled flow and heat equation, the model is initialized with a given pressure and temperature.

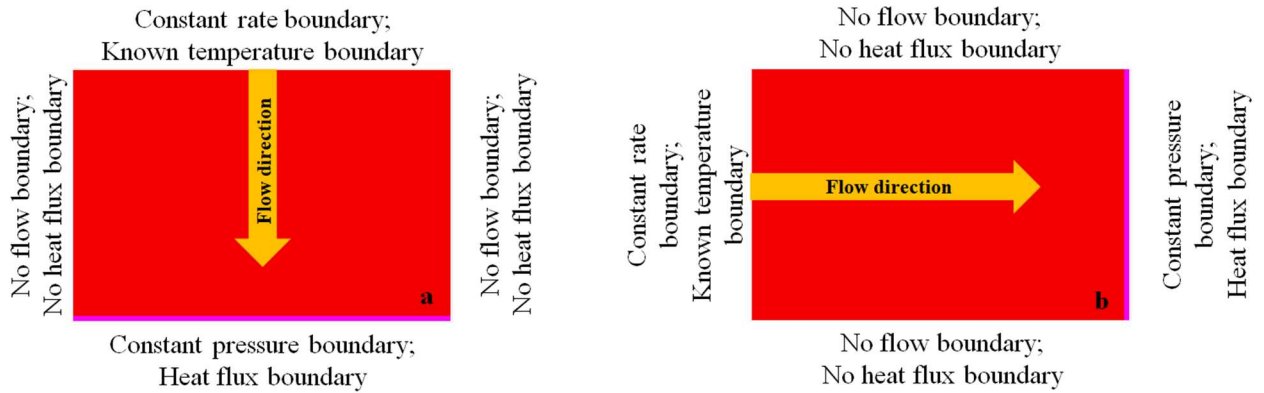


Figure 2.1: Boundary conditions for the different flow configurations. Figure 2.1a is for the parallel flow configuration, while Figure 2.1b is for the perpendicular flow configuration.

2.2.2 Model Assumptions

The following assumptions were considered in setting up the system to be modeled with water as the working fluid:

- The fluid circulating throughout the system is single-phase and remains in the liquid state throughout the duration of the simulation.
- Fluid flow is in the laminar regime, with Reynold's number low enough to allow the application of Darcy's law.
- There is no gas trapped in the rock fracture.
- Fluid-rock interaction such as chemical dissolution/deposition is minimal and can be ignored.
- Thermal stresses and changes in aperture due to injection of cold water through hot rock were ignored.

2.2.3 Model Description

The original fracture surface dimension of the lab-scale core from which flow analysis was done in Co (2017) and Ishibashi (2012) measured 75 mm x 50 mm. However, to ensure the same surface is being analyzed for heat transport, the system modeled was a

granite block with a fracture measuring 50 mm x 50 mm in the horizontal plane embedded within a relatively impermeable bulk rock matrix of height 100 mm. Hypothetical horizontal wells, one injection and one production, were placed at the edges of the fracture. The numerical model consists of a 50 by 50 by 45 grid. In the horizontal X and Y directions, the individual cells are of uniform length of 1 mm, while in the vertical Z direction, the thicknesses are very fine around the fracture and become coarse away from the fracture. Figure 2.2 shows a snapshot of the reservoir simulation domain.

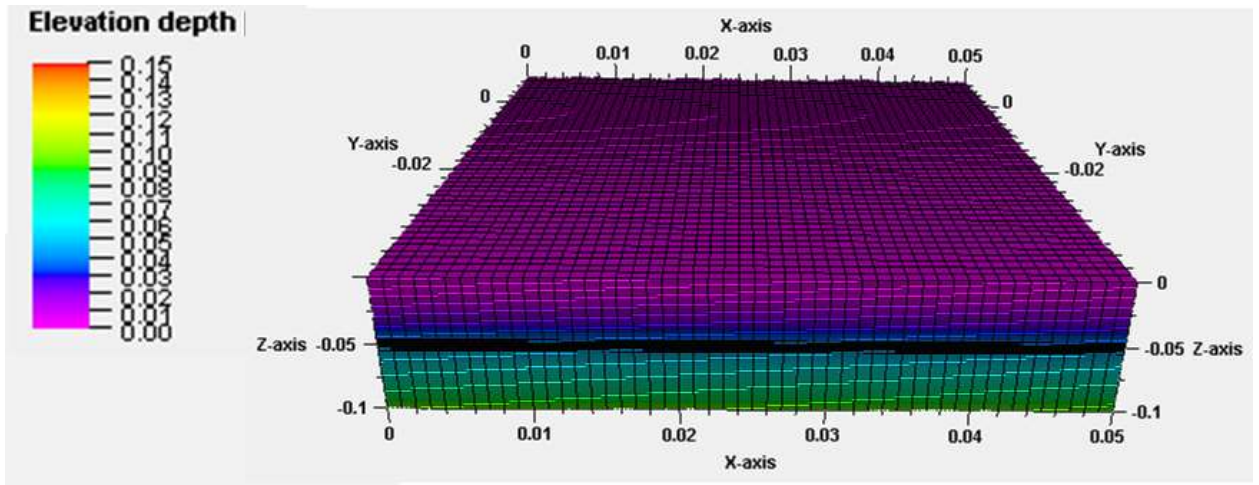


Figure 2.2: The lab-scale three-dimensional model showing the grids. The depth (Z-axis) is not to scale. The Y and Z axes read negative with increasing values from the reference (zero in this case).

The coupled flow and heat transport mechanisms were modeled with a three-dimensional compositional numerical simulator - ECLIPSE. ECLIPSE is a finite-difference simulator and was run in the fully implicit mode, with Cartesian block-center geometry in three dimensions for flow and heat transport. The Thermal option of the simulator was used. The formulation of equations used to describe thermal processes can be found in Schlumberger (2016) and has three important differences from a general compositional simulator: the addition of an energy variable and an energy equation; the presence of a water component in the gas phase as well as the water phase; and temperature dependence of properties. The thermodynamic properties of water are based on the International Association for the Properties of Water and Steam (IAPWS-IF97) (Wagner, et al., 2000) using the keyword: THSTT97. Other rock and fluid properties used in the model are presented in Table 2.1.

The initial rock temperature was 200 °C, while the injection water temperature was 65 °C. The injected fluid flow rate was 600 cc/hr. The duration of the simulation was 30 minutes. The pressure drop between the injector and the producer varied, but the pressure constraints were set to ensure the fluid remained as a single-phase liquid throughout the simulation.

Table 2.1: Rock and fluid properties, and other parameters used in the lab-scale model

Symbol	Description	Value	Units
φ	Porosity of the formation	0.01	-
k	Permeability of the formation matrix	$9.87 * 10^{-21}$	m^2
K_r	Thermal conductivity of rock	2.8	W/m/K
C_r	Specific heat capacity of rock	1000	J/kg/K
ρ_r	Density of the rock	2600	kg/m^3
μ	Dynamic fluid viscosity	0.0001303	Pa*s
P	Reference pressure for fluid viscosity	101.325	kPa
T	Reference temperature for fluid viscosity	200	°C
C_w	Specific heat capacity of fluid	4200	J/kg/K
ρ_{ST}	Reference fluid density	1000	kg/m^3
P_{ref}	Reference pressure for fluid density	101.325	kPa
T_{ref}	Reference temperature for fluid density	15.6	°C
C	Fluid compressibility	$5.00 * 10^{-10}$	Pa^{-1}

2.2.4 Fracture characterization

In this study, a comparison was made between the thermal performance of a fracture in the parallel flow configuration and in the perpendicular flow configuration. To model the fracture spatial heterogeneity, the fracture was treated as a porous medium with porosity set as 0.99 while the heterogeneous permeability is defined by the local cubic law for a fracture with spatial variations (Oron & Berkowitz, 1998), which is represented by Equation 2.5.

$$k_{f_{ij}} = \frac{b_{ij}^2}{12} \quad (2.5)$$

where k_f , i , j , and b are the effective permeability, grid number in the x-direction, grid number in the y-direction, and local fracture aperture, respectively.

2.2.5 Fracture Aperture Generation

In order to compare the thermal performance of the parallel flow configuration with the perpendicular flow configuration at the lab scale, it was necessary to generate aperture distributions typical of the lab scale. Because it was not possible to obtain several cores and determine their aperture distributions, it was essential to generate fracture aperture distributions artificially.

Hakami & Larsson, (1996), Lee & Cho, (2002), and Co (2017) demonstrated that variogram models could be used to characterize aperture distributions and quantify spatial correlations within heterogeneous fracture planes. Co (2017) extended the use of variogram models to generate aperture distributions in fracture planes. Moreover, Co (2017) showed that the sequential Gaussian simulation (SGSIM) method was an attractive approach for generating fractures with spatial variations in aperture as it uses spatial information from the variogram model of analog fractures. Thus, this section discusses variogram modeling and SGSIM, and how these geostatistical tools were used to generate artificial fractures from analog fractures. In addition, the joint roughness coefficient (JRC) is described, as it was one of the metrics used for fracture plane characterization.

2.2.5.1 Analog Fracture Aperture Distribution Determination

The analog fracture aperture distribution was obtained from the work by Ishibashi et al., (2012). In the study by Ishibashi et al., (2012), measurements of the fracture surface topography were conducted on three single fractures with sizes 50 mm × 75 mm, 100 mm × 150 mm, and 200 mm × 300 mm. The fractures were contained in cylindrical samples of Inada medium-grained granite, which is characterized by the uniaxial compressive strength between 160 and 180 MPa, the uniaxial tensile strength between 4 and 8 MPa, and the negligible small matrix permeability between 10^{-19} and 10^{-18} m² (Ishibashi et al., 2012). The rectangular fractures derived had the short side length

corresponding to the diameters of the samples while the long side length was corresponding to the length of the sample. This is shown in Figure 2.3. The lateral directions are the short side length, and the axial directions are the long side lengths of the rectangular fractures, respectively.

The cylindrical fractured samples were prepared by first inducing a tensile fracture of a larger section than the specified scale in a cubic granite block using a wedge. Fractured samples were placed so that the fracture has either no shear displacement or a shear displacement of 5 mm in the lateral direction, and the fracture was maintained by surrounding and fixing the fractured block with mortar. Because sheared fractures are more common in enhanced geothermal systems (Gischig & Preisig, 2015), sheared fractures were mimicked by adding a 5mm offset along the lateral direction (short side of the fracture) before matching the surfaces. The 5 mm shear displacement was adjusted by putting acrylic boards of 5 mm at both end planes of the fractured block. Following that, the cylindrical fractured sample was cored, and the height of the sample was adjusted by cutting the edges of the axial direction. The fracture was maintained by surrounding and fixing the fractured block with mortar.

Two-dimensional distributions of surface height were measured in a 0.25 mm square grid system with a laser profilometer. Figure 2.4 shows the resulting aperture distribution of the 50 mm x 75 mm sample generated in the work by Ishibashi et al., (2012), which was used for this section of the study. The direction of shear offset is shown in the figure, including a description of the parallel flow configuration and the perpendicular flow configuration relative to the lateral direction of shear offset. Only aperture distributions from 50 mm of the axial direction were used for the numerical modeling of this study.

2.2.5.2 Variogram modeling

The variogram is a measure of the spatial variability or aperture variability of a data set. Variogram modeling for the spatial distribution of fracture aperture has been used in several studies (Iwano & Einstein, 1993; Hakami & Larsson, 1996; Lee & Cho, 2002).

Kigobe & Kizza (2006) provide a simplified description of variogram modeling discussed below.

The variogram distance measures the degree of dissimilarity $\gamma(\mathbf{h})$ between data separated by a vector or class of vectors \mathbf{h} . If $z(\mathbf{x}_i)$ and $z(\mathbf{x}_i + \mathbf{h})$ are pairs of samples lying within a given class of distance and direction (usually in a scatterplot), and $N(\mathbf{h})$ is the number of data pairs within this class, the experimental semivariogram can be defined as the sum of the average squared difference between the components of data pairs (Goovaerts, 1997) as in the following equation:

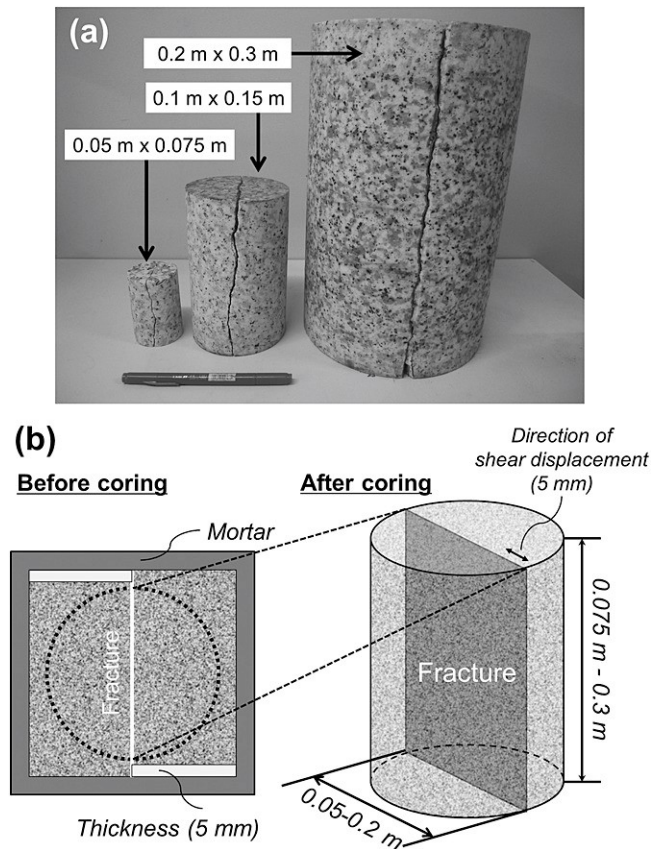


Figure 2.3: Cylindrical granite samples containing single tensile fractures of different sizes having either (a) no shear displacement or (b) a shear displacement of 5 mm in the lateral direction (Ishibashi et al., 2012).

$$\gamma(\mathbf{h}) = \frac{1}{2N} \sum_{i=1}^{N(\mathbf{h})} [z(\mathbf{x}_i) - z(\mathbf{x}_i + \mathbf{h})]^2 \quad (2.6)$$

In most literature, the semivariogram is also called a variogram; hence this term may be used interchangeably in this study though they both refer to the semivariogram as defined by Equation 2.6.

The variogram is a measure of spatial dissimilarity, that is, the further one goes along the distance x , the higher the variance. Variograms do not require knowledge of the mean (as seen in Equation 2.6) and thus are very useful in geostatistics where distributions may be skewed, and there may not be a mean.

A variogram model can be used to interpolate between the sample variogram estimations. A plot is made of the semivariogram as a function of the separation distance. The variance of the complete data set is defined as the sill, and the distance at which the model variogram meets the data set variance is defined as the range (similar to the correlation length, a term commonly used in geostatistics). The variance of the sample at a separation distance of zero is called the nugget (which accounts for random noise in the data set). The lag distance is the range for models that reach the sill asymptotically, the range is defined as the lag distance. Figure 2.5 gives an example of a semivariogram with the sill, range, and lag distance defined.

For a semivariogram to be modeled, the data functions should fulfill the mathematical condition called positive definiteness. This is a necessary condition to ensure there is a unique solution to kriging systems (a linear regression model that allows the independent variables to be linearly dependent). There is a need for models known *a priori* that meet the positive-definiteness criterion to ensure the interpolation method done on the dataset results in a unique solution. The following are examples of positive-definite theoretical semivariogram models commonly used: the nugget effect, spherical, exponential, Gaussian, and power models (Goovaerts, 1997). Their equations are presented below for one-dimensional variograms.

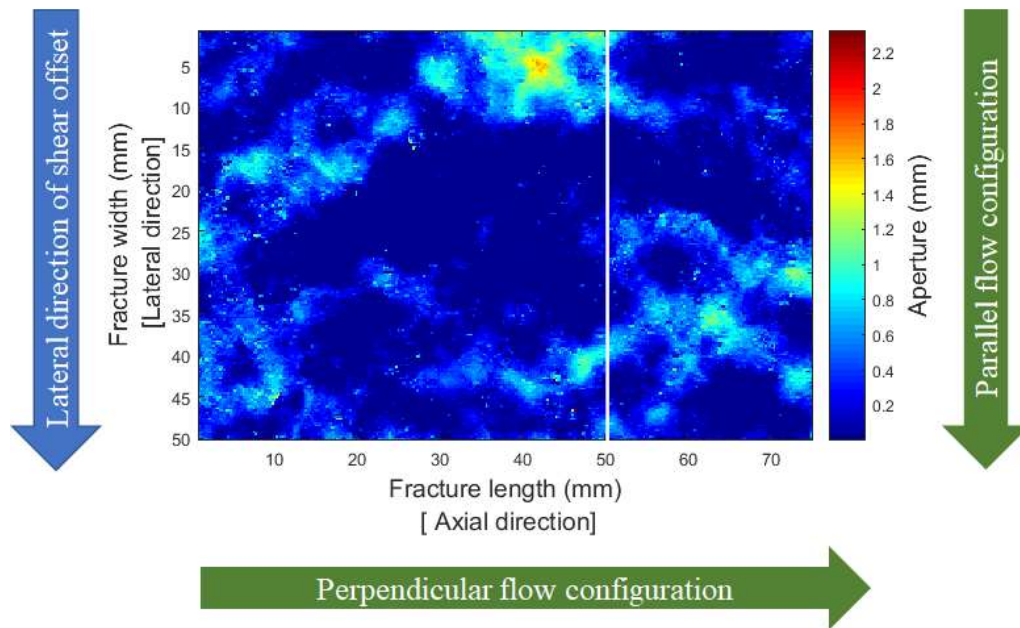


Figure 2.4: Aperture distribution of the 50 mm x 75 mm sample generated in the work by Ishibashi et al., (2012). The lateral direction of shear offset is shown with arrows indicating the parallel flow configuration and the perpendicular flow configuration relative to the lateral direction of shear offset. The white line indicates where limit in the axial direction for the numerical simulation.

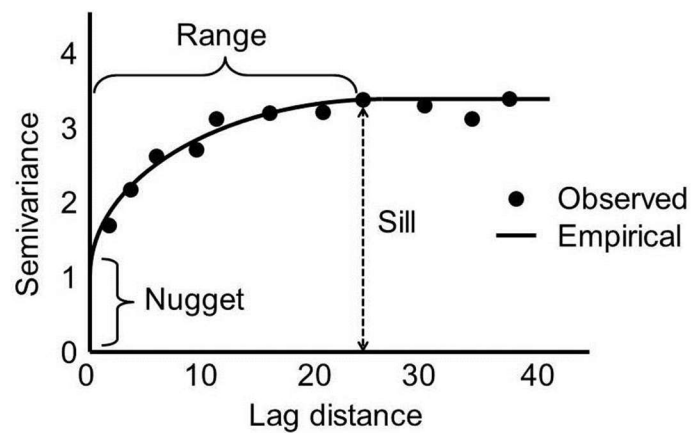


Figure 2.5: Example Semivariogram showing the range, sill, nugget, and lag distance (from Biswas & Si, 2013).

The nugget effect variogram model is given by Equation 2.7 and implies that the variogram is 0 at the origin, and everywhere else it is a straight line given by the variance.

$$\gamma(\mathbf{h}) = \begin{cases} 0, & \text{if } \mathbf{h} = 0 \\ C(\mathbf{0}), & \text{if } \mathbf{h} > 0 \end{cases} \quad (2.7)$$

The nugget effect variogram model is most useful for nested variograms where one or more variogram models are added to provide a better description of a dataset. C is the sill.

The spherical variogram model is given by Equation 2.8. It starts at 0 and the tangent to the origin is a straight line with datasets behaving linearly at the origin. Then it levels off at the range. The sill is reached when $\mathbf{h} = \left(\frac{2}{3}\right)a$, where a is the range.

$$\gamma(\mathbf{h}) = C(\mathbf{0}) * Sph\left(\frac{\mathbf{h}}{a}\right) = \begin{cases} C * \left[1.5\left(\frac{\mathbf{h}}{a}\right) - 0.5\left(\frac{\mathbf{h}}{a}\right)^3\right], & \text{if } \mathbf{h} < a \\ C, & \text{if } \mathbf{h} \geq a \end{cases} \quad (2.8)$$

In the exponential variogram model given by Equation 2.9, the variogram increases exponentially with distance, which is faster than a linear increase. As a result, the model does not really level off, and the model reaches the sill asymptotically. In reality, because of noise and sampling variances in real data, when 95 % of the sill is reached, a practical range “a” is defined.

$$\gamma(\mathbf{h}) = C(\mathbf{0}) * Exp\left(\frac{\mathbf{h}}{a}\right) = C * \left[1 - \exp\left(-\frac{\mathbf{h}}{a}\right)\right] \quad (2.9)$$

For the Gaussian variogram model represented by Equation 2.10, the behavior at the origin is such that the variogram increases slower than a linear function. The variogram is flatter at the origin and also has a practical range. The flat tangent at the origin indicates strong continuity at short distances and thus, this model may not be suitable to fit datasets with random noise.

$$\gamma(\mathbf{h}) = C(\mathbf{0}) * Gauss\left(\frac{\mathbf{h}}{a}\right) = C * \left[1 - \exp\left(-\frac{\mathbf{h}^2}{a^2}\right)\right] \quad 2.10$$

The power model, as shown in Equation 2.11 is unbounded and it is related to fractals. The behavior of the power model at the origin depends on the value of ω as shown in Equation 2.11. The behavior is approximately linear for $\omega \leq 1$ and parabolic for $\omega > 1$ (Goovaerts, 1997).

$$\gamma(\mathbf{h}) = C(\mathbf{0}) * \mathbf{h}^\omega, 0 < \omega < 2 \quad 2.11$$

Figure 2.6 is a comparison of the different variogram models with a range of 50 mm and a sill of 0.1 mm².

In this study, the exponential semivariogram model was used to fit the analog lab-scale fracture aperture data to provide an experimental variogram that could be used for further analysis. To account for variable spatial continuity in different directions, which is the geometric anisotropy, separate empirical and model variograms can be estimated for different directions in the data set. This was done in the study by Co (2017) and is shown in Figure 2.7.

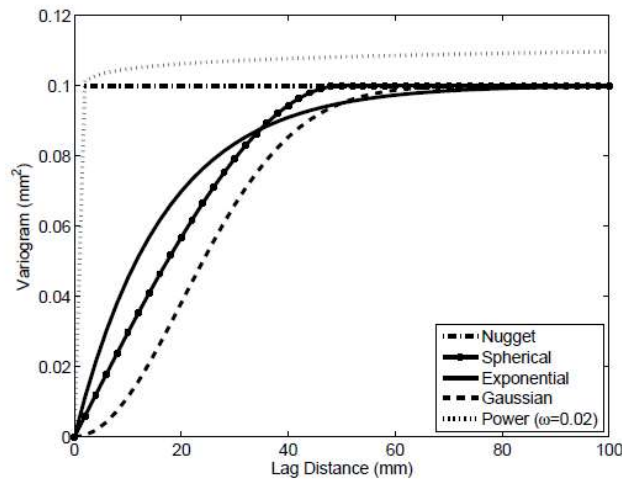


Figure 2.6: Comparison of the different variogram models with a range of 50 mm and a sill of 0.1 mm² (from Co, 2017).

2.2.5.3 Sequential Gaussian Simulation

According to Co (2017) Sequential Gaussian Simulation (SGSIM) is one method for generating the fracture aperture map using the variogram and histogram data (Remy et al., 2009). For the SGSIM method, the conditional cumulative density function (CCDF) is assumed to be multivariate normal (Goovaerts, 1997). In addition, simple kriging is used to calculate the mean and variance that are used to generate the conditional distribution function at each estimation point. At each estimation point, the distribution function is Gaussian. Simple kriging provides a way to estimate the value at a particular location vector using the data from neighboring location vectors.

The process for SGSIM is as follows: starting with a reference truth, first extract some hard data to populate the grid for which a new spatial dataset needs to be created. Secondly, choose a random location and search locally the neighborhood to perform simple kriging, which will generate a mean and a kriging variance. Third, generate a conditional Gaussian distribution function from the mean and kriging variance previously estimated. Fourth, a value is drawn from the new conditional distribution function for the chosen unknown location. Finally, a new unknown location is chosen using a random path, and steps two to four are repeated until all the unknown values have been filled. To generate a different spatial map, a new starting location is chosen on the grid. This process outlined above can be applied automatically by using the SGeMS software program.

Co (2017) used SGeMS to generate 100 artificial fracture aperture distributions using the variogram model and histogram shown in Figures 2.7 and 2.8. The artificial fracture aperture distributions were used to model flow transport in fractured planes. In this study, the 100 artificial fracture distributions were used to model heat transport in fractured planes.

2.2.5.4 Joint Roughness Coefficient JRC

Barton and Choubey (1977) performed direct shear test results for 130 samples of variably weathered rock joints (fractures dividing rocks into two sections that moved away from each other) and came up with a nonlinear shear strength criterion for rock joints given by Equation 2.12:

$$\tau = \sigma_n \tan \left(\varphi_r + JRC \log_{10} \left(\frac{JCS}{\sigma_n} \right) \right) \quad (2.12)$$

where τ is the peak shear strength of the rock with a rough surface, σ_n is the normal stress, φ_r is the residual friction angle, JRC is the joint roughness coefficient, and JCS is the joint wall compressive strength.

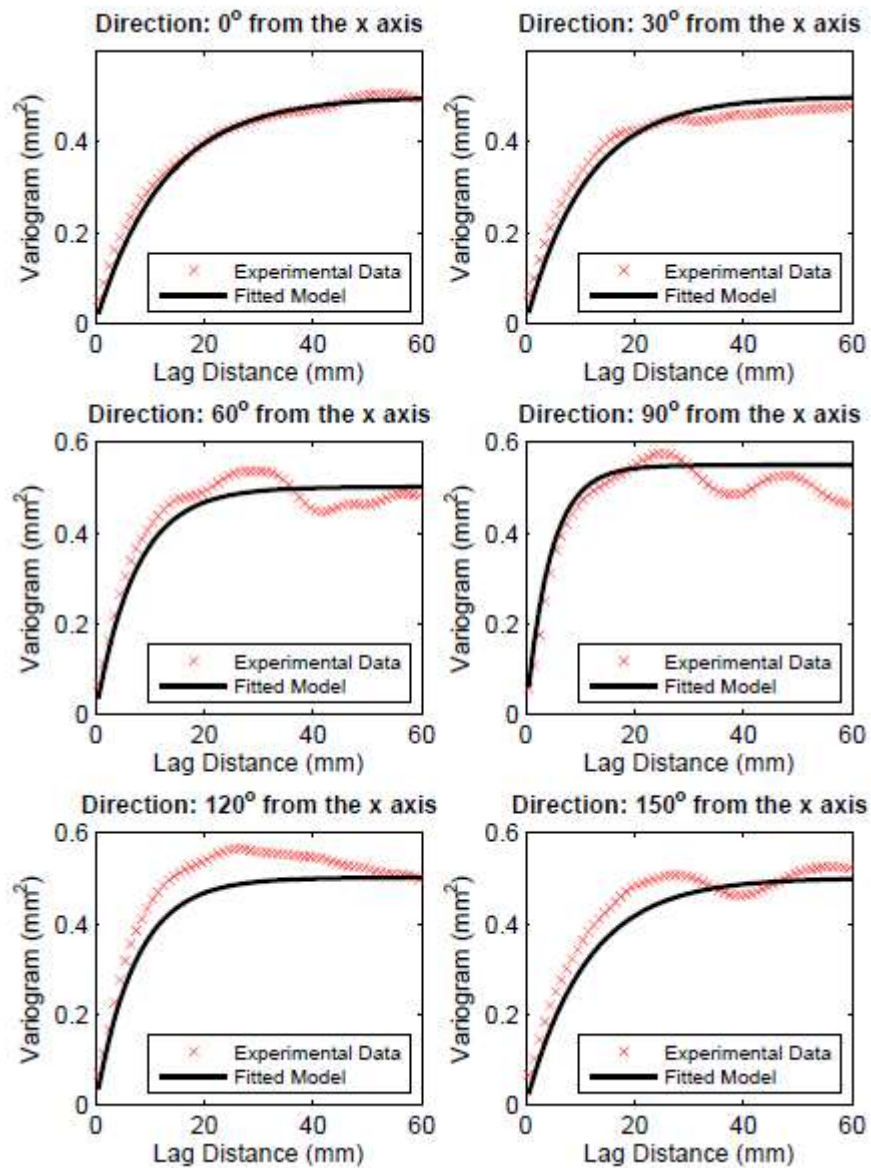


Figure 2.7: Comparison of the experimental variograms and the fitted model for the sheared 10 cm by 15 cm case in directions 0, 30, 60, 90, 120, and 150 degrees from the x axis (Co, 2017).

The joint roughness coefficient JRC is a number that can be estimated by comparing the appearance of a discontinuity surface with standard profiles such as the one published by Barton and Choubey (1977) and shown in Figure 2.9. The appearance of the discontinuity is compared visually with the profiles shown and the JRC value corresponding to the profile which most closely matches that of the discontinuity surface

is chosen. For small-scale laboratory specimens, the scale of the surface aperture variability will be approximately the same as that of the profiles illustrated.

Heinze, et al., (2021) developed a fracture surface analysis toolbox in MATLAB that can determine the JRC of two-dimensional and three-dimensional surfaces with variations in aperture. They used the equation by Tse & Cruden, (1979), which is an empirical correlation of the JRC profiles as defined by Barton & Choubey, (1977). This statistical approach uses Z_2 which is the root mean square of the first derivative of the surface aperture variability. The equation for JRC is given by Equation 2.13:

$$JRC = 32.2 + 32.47 \log_{10}(Z_2) \quad (2.13)$$

where the Z_2 parameter is calculated in the discrete form as

$$Z_2 = \frac{1}{N-1} \sum_{i=2}^N \left(\frac{z_i - z_{i-1}}{x_i - x_{i-1}} \right)^2 \quad (2.14)$$

with x_i being one of N discrete points along the profile direction and z_i the corresponding height values of the profile. The code validation procedure is outlined in the work by Heinze, et al., (2021).

2.1 Numerical Simulation Model Verification

Prior to running the simulations on the model with different fracture aperture distributions, the model was verified with published models where the fracture aperture distribution for a smooth fracture and a fracture with aperture variability were available. This was done on a field-scale model. Once the model was verified, the dimensions and other associated parameters (like flow rate and pressure) were reduced to lab scale.

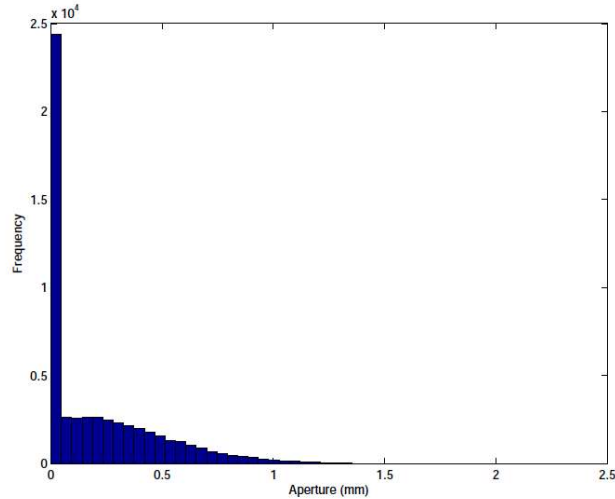


Figure 2.8: Histogram for the 50 mm by 75 mm fracture aperture distribution (Co, 2017).

2.1.1 Validation Study – Modified Fox et al. (2015) Smooth Fracture Solution

The work by Fox et al. (2015) was a hybrid finite element and boundary element method for discretely fractured geothermal reservoirs thermohydraulic model investigating the effect of spatial aperture variations on the thermal performance of discretely fractured geothermal reservoirs. They had a case of a single fracture. Before comparing the numerical simulator with their study for fractures with spatial variations, the model had to be verified for the case of a smooth fracture. Their model was modified to have a rectangular fracture. A square model of length $L = 1000$ m was used for the X-Y plane, an injected mass flow \dot{m} of 40 kg/s, and a water injection temperature of 65 °C. The initial temperature of the system was kept at 200 °C, and no effect of a geothermal gradient was considered during the simulation.

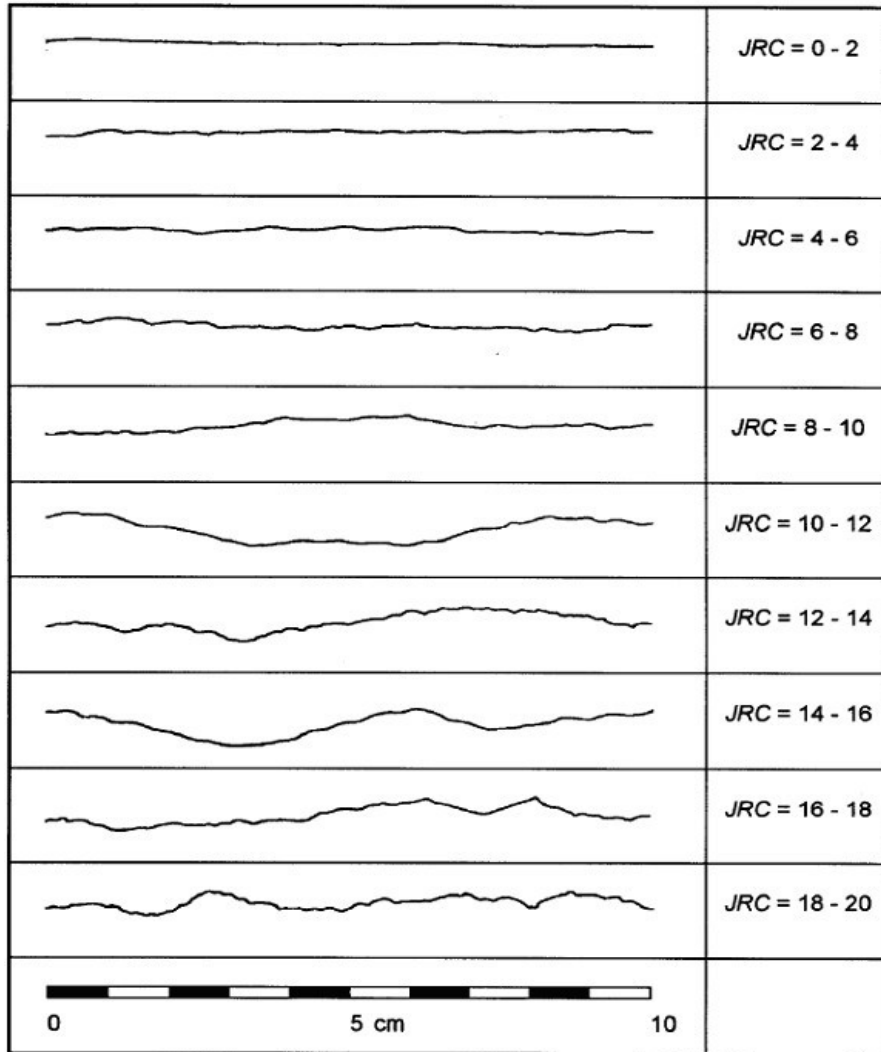


Figure 2.9: Rock joint roughness profiles showing the typical range of JRC (Barton & Choubey, 1977). The thermophysical properties include rock thermal conductivity, $K_r = 2.4 \text{ W}/(\text{m } ^\circ\text{C})$, rock density of $2300 \text{ kg}/\text{m}^3$, specific heat capacities of the rock and water, $c_r = 1000 \text{ J}/(\text{kg } ^\circ\text{C})$ and $c_w = 4184 \text{ J}/(\text{kg } ^\circ\text{C})$. The system is low permeability except at the fracture, where the permeability is very high and treated as a parallel-plate model.

The temperature at the production well as a function of time was compared between the Fox et al. (2015) solution and the numerical simulator. Figure 2.10 shows the temperature profile in the fracture after ten years. As shown in Figure 2.10, the thermal performance from the simulator agrees closely with the numerical model from the modified Fox et al. (2015) solution.

2.1.2 Validation Study – Modified Fox et al. (2015) Solution for Fracture with Aperture Variability

Fox et al. (2015) investigated several aperture distributions in their study, but for the purpose of verifying the ECLIPSE numerical model, only one of their fracture aperture maps was used. Figure 2.11 shows the fracture permeability and resulting temperature distribution after ten years in the X-Y plane. Figure 2.12 is a graph of the temperature at the production well as a function of time for the modified Fox et al. (2015) solution and the numerical simulator. Again, a close match is seen between the results of the temperature profile at the producer as a function of time.

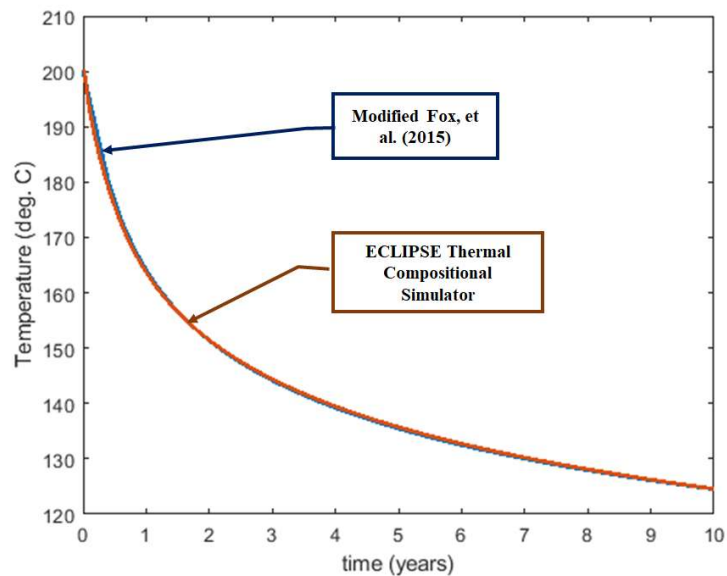


Figure 2.10: Thermal performance at the producer – a comparison between ECLIPSE simulator and the modified Fox, et al. (2015) solution: A case of a fracture with smooth walls.

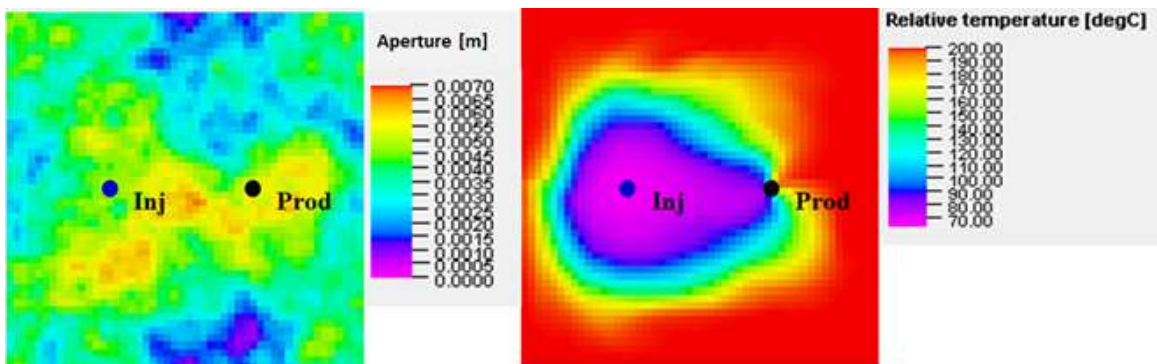


Figure 2.11: Fracture permeability (left) and temperature distribution (right) in the fracture (X-Y) plane.

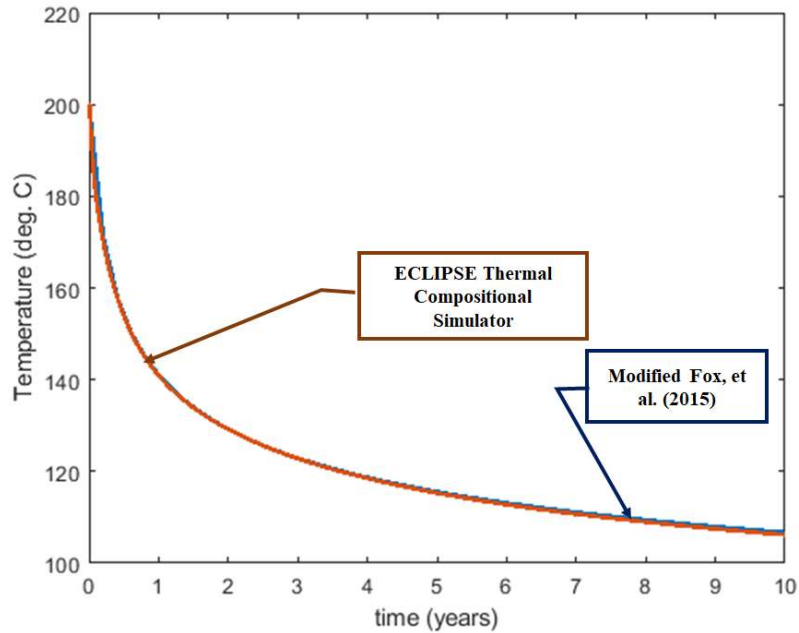


Figure 2.12: Thermal performance at the producer – a comparison between ECLIPSE simulator and the modified Fox, et al. (2015) solution: A case of a fracture with spatial variations.

2.2 Results

In this section, the results from the thermohydraulic simulation on the lab-scale fractures are presented. First, the behavior of a fracture that is parallel-walled is presented alongside the results from the original lab-scale fracture. When computing the value for a homogeneous permeability field (i.e., smooth parallel-plate fracture), the aperture value was constant at 1 mm. Subsequently, the artificially generated aperture distribution results are presented and discussed.

2.2.1 Thermal Performance for the original lab-scale fracture

Figure 2.13 shows the average temperature, measured at the outlet boundary for the perpendicular and parallel flow configurations, as a function of time. The results assuming a smooth fracture for both flow configurations are plotted. The curves for the smooth fracture overlay implying that for a smooth fracture, there is no difference between the different flow configurations, as the fracture surface is isotropic. In general, both the curves of the flow in perpendicular and parallel configurations of the fractures with spatial

aperture variability show deviation from the curves of the smooth fracture. This is in agreement with previous studies indicating that flow on a smooth fracture surface exhibits a higher heat transfer capacity than that of the fracture model with varying aperture variability (Fox, et al., 2015; Gao, et al., 2021). However, for the lab-scale fracture with spatial variations, there is only a slightly higher thermal drawdown (the drop in temperature from the initial rock temperature) in the parallel flow configuration compared to the perpendicular flow configuration.

To further understand the slight difference between the thermal drawdown in the parallel flow configuration and the perpendicular flow configuration, the flow and heat transport on the fracture plane was investigated. Figure 2.14 shows the dominant flow path of the injected water and the temperature map on the fracture plane for both flow configurations.

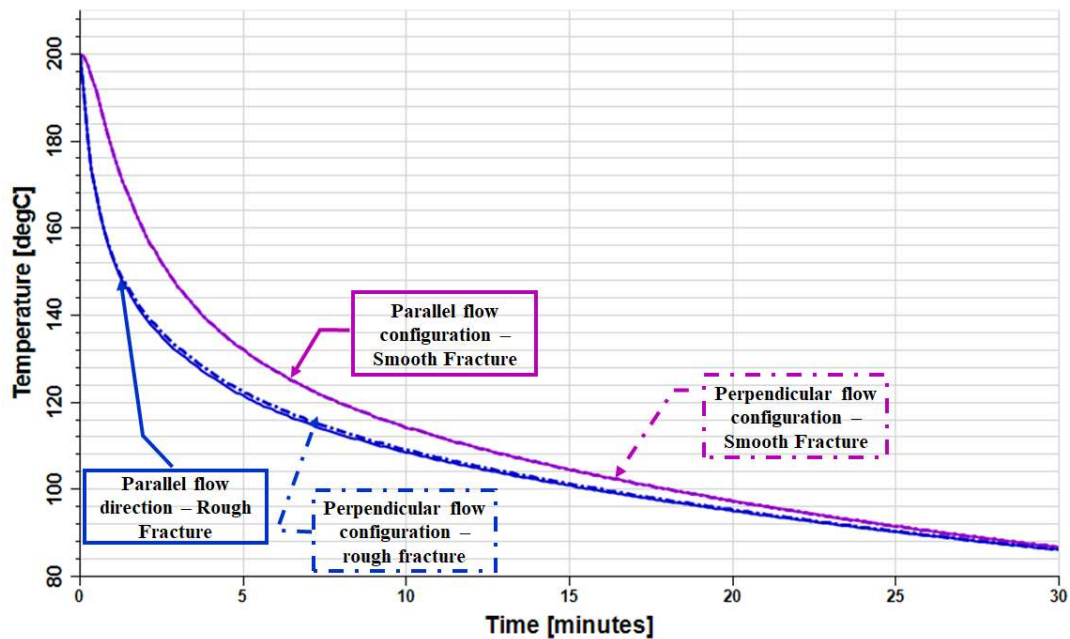


Figure 2.13: Average temperature as a function of time, measured at the constant pressure boundary.

Figure 2.14a shows the dominant flow path of the injected water in the parallel flow configuration. The direction of flow is from top to bottom of the figure. Figure 2.14b is the dominant flow path of the injected water in the perpendicular flow direction. Flow is from left to right of the figure.

The dominant flow path indicates the rock area contacted by the flowing fluid. From Figures 2.14a and 2.14b, the difference between the areas contacted by fluid in both directions does not appear to be significant.

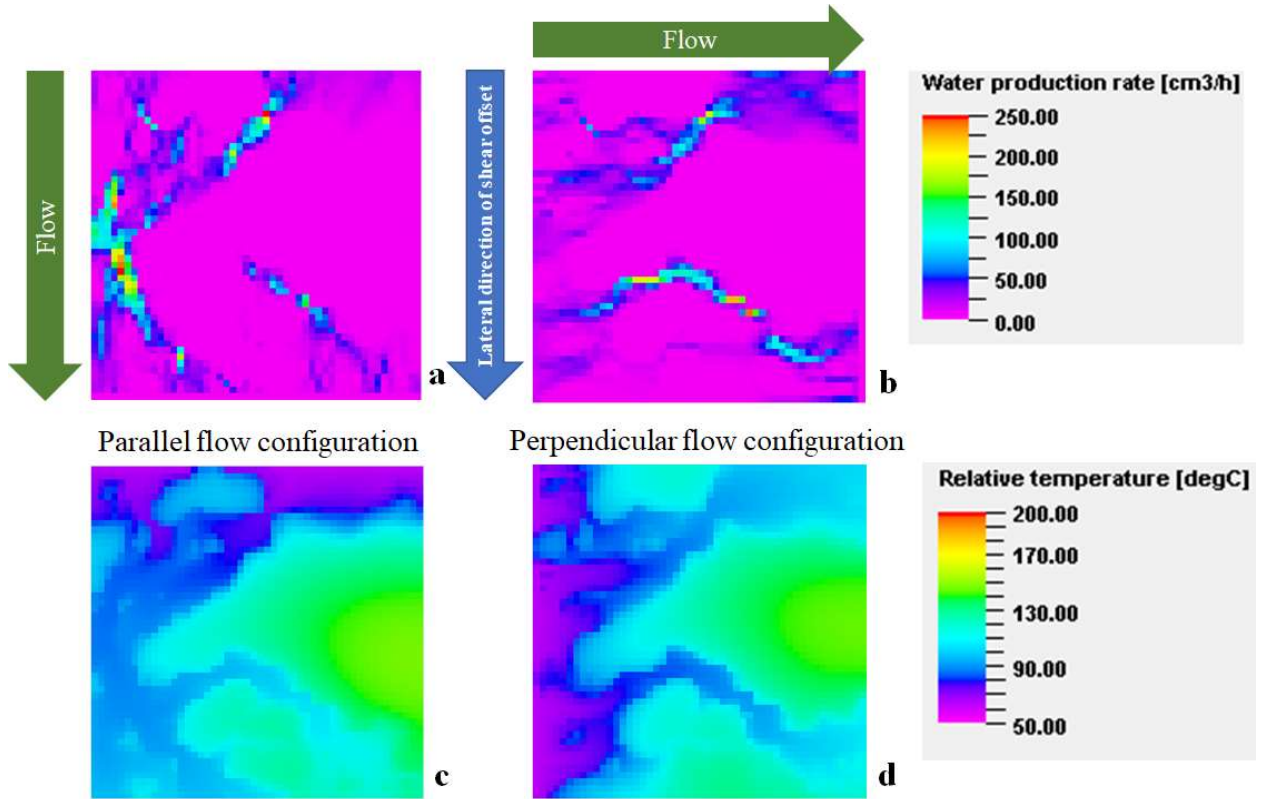


Figure 2.14: Fluid flow and heat transport on the fracture aperture after 10 minutes for the original lab scale fracture aperture distribution.

Figures 2.14c and 2.14d show the temperature map on the fracture plane of the two flow directions after 10 minutes of simulation. The temperature maps of both flow configurations give indications of channelized thermal sweep. The consequence of the channelized thermal sweep seen in the temperature map is that not all areas of the rock adjacent to the fracture contribute to heat transfer to the fluid at the given time, supporting the behavior seen in the thermal drawdown curves of Figure 2.13. The area that has not received significant cooling by the injected water is slightly larger in the parallel flow configuration than in the perpendicular flow configuration. This result is however qualitative. To quantify the area of the fracture that was in contact with the rock, a filter

across the fracture plane was applied in the simulation post-processor (PETREL) to provide a count of the grid cells in which water flow rate was measured above 1 cc/hr. Figure 2.15 shows a snapshot of the filtering process. The results of the percentages of the contact area are shown in Table 2.2.

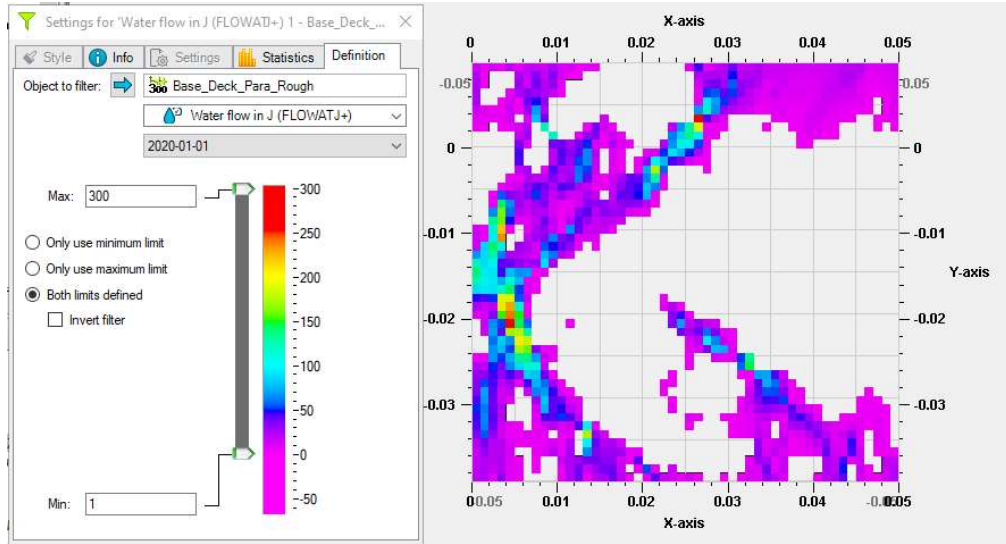


Figure 2.15: Filtering process done in PETREL to extract the number of grid cells that had flow above 1 cc/hr. The figure is for the original fracture aperture distribution for the parallel flow configuration.

Table 2.2: Percentage of the fracture surface contacted by flowing fluid for the original fracture aperture distribution

Aperture Distribution	Number of cells with fluid contact	Total number of cells	Percentage of fracture area contacted (%)
Original fracture aperture - Parallel flow configuration	1014.00	2500	40.56
Original fracture aperture - Perpendicular flow configuration	1113.00	2500	44.52

The data in Table 2.2 show that more area is contacted by the fluid flowing in the perpendicular flow configuration. Though the difference in thermal drawdown between the two flow configurations is small, the larger contact area in the perpendicular flow configuration could explain why the perpendicular flow configuration has a lower thermal

drawdown, as more heat is extracted due to the flowing fluid in contact with more rock surface area.

Having looked at the thermal performance on the original lab-scale fractures, a similar analysis was done for the artificially generated fractures with aperture variability.

2.2.2 Thermal Performance for Artificially Generated Fractures with Aperture Variability

The thermohydraulic model was run with the fracture characterized by the 100 artificially generated fracture aperture distributions. Figure 2.16 is a plot of the difference in thermal drawdown between the perpendicular flow direction and the parallel flow direction for all 100 simulations. All plots above the zero horizontal line indicate that the temperature measured at the extraction end of the fracture was higher in the perpendicular direction than in the parallel direction. Similarly, all plots below the zero line indicate that the temperature measured at the extraction end of the fracture was higher for the parallel flow configuration resulting in lower thermal drawdown in that flow configuration.

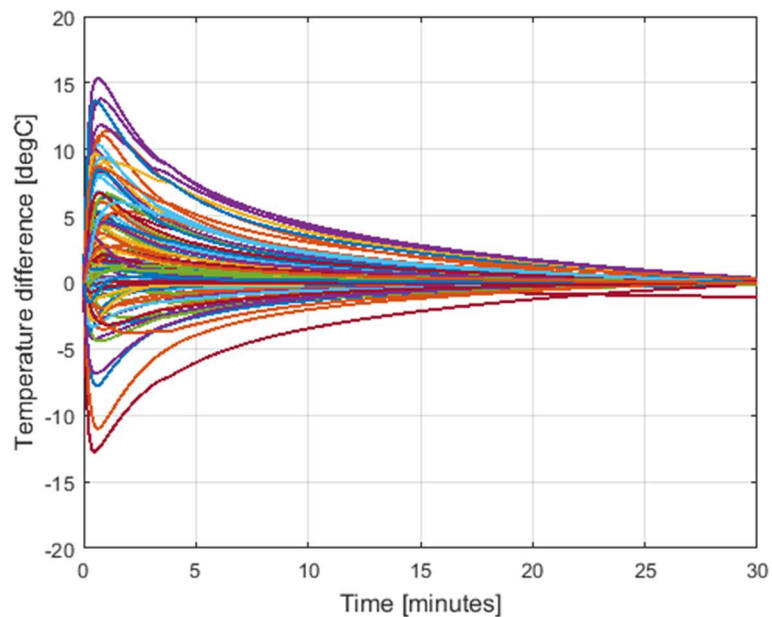


Figure 2.16: Temperature difference between the perpendicular and parallel flow directions for the 100 artificially generated fracture aperture distributions.

From Figure 2.16, it can be seen that the highest temperature differences occurred between 0.6 and 0.8 minutes into the simulation. Hence a histogram of the temperature differences at 0.72 minutes was plotted as shown in Figure 2.17. The data in Figure 2.17 indicates that most of the temperature differences are above 0, and the temperature difference values with the highest frequency lie between 1.25 °C and 2.5 °C.

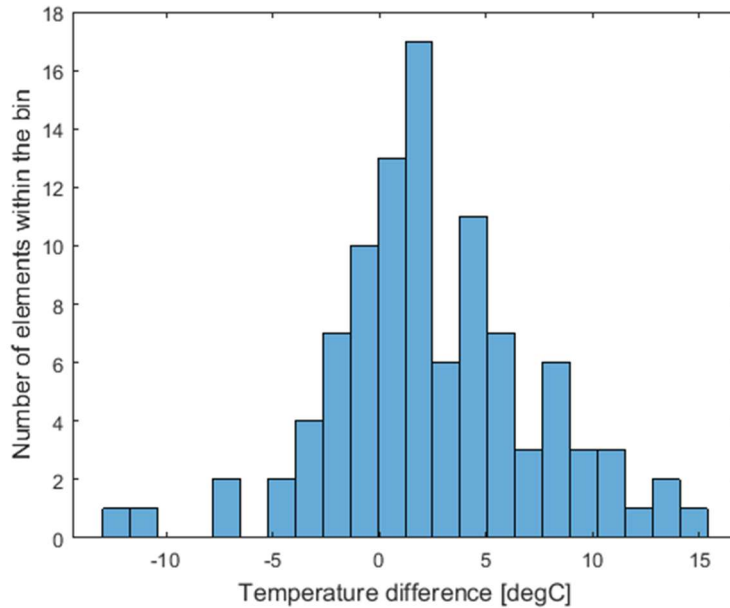


Figure 2.17: Histogram of the temperature difference between the perpendicular and parallel flow directions for the 100 artificially generated fracture aperture distributions at 0.72 minutes.

To quantify the percentage of the artificially generated fracture aperture distributions that resulted in the perpendicular flow configuration with lower thermal drawdown than the parallel flow configuration, the data was sorted and a count was performed. Figure 2.18 shows the sorted data at 0.72 minutes of simulation while Figure 2.19 show the sorted data at 10 minutes of simulation. At 0.72 minutes of simulation, the percentage of fracture aperture distributions that resulted in the perpendicular flow configuration having lower thermal drawdown (and higher temperature at the extraction end of the fracture) was 70 %. By 10 minutes of simulation, the value was 71 %. These results indicate that on average, there is a 70 % chance that the perpendicular flow configuration will result in a lower thermal drawdown than the parallel flow direction.

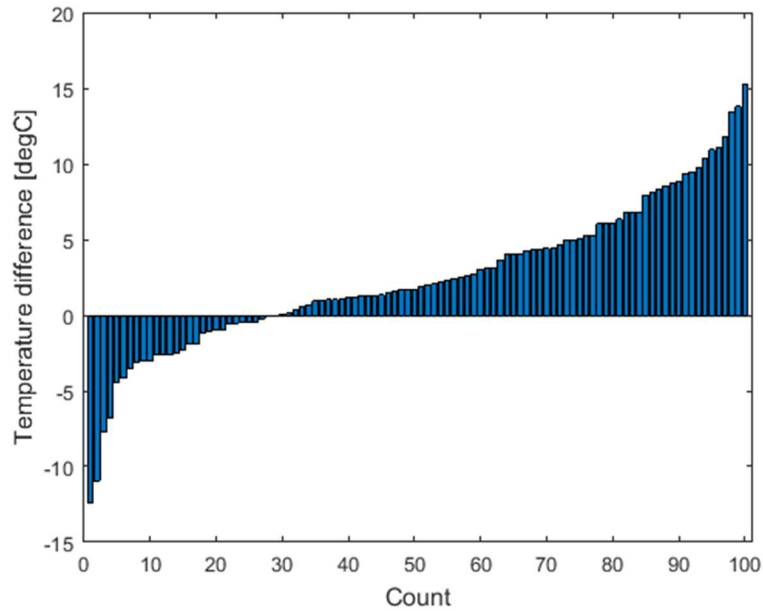


Figure 2.18: Temperature difference between the perpendicular and parallel flow directions for the 100 artificially generated fracture aperture distributions at 0.72 minutes into the simulation.

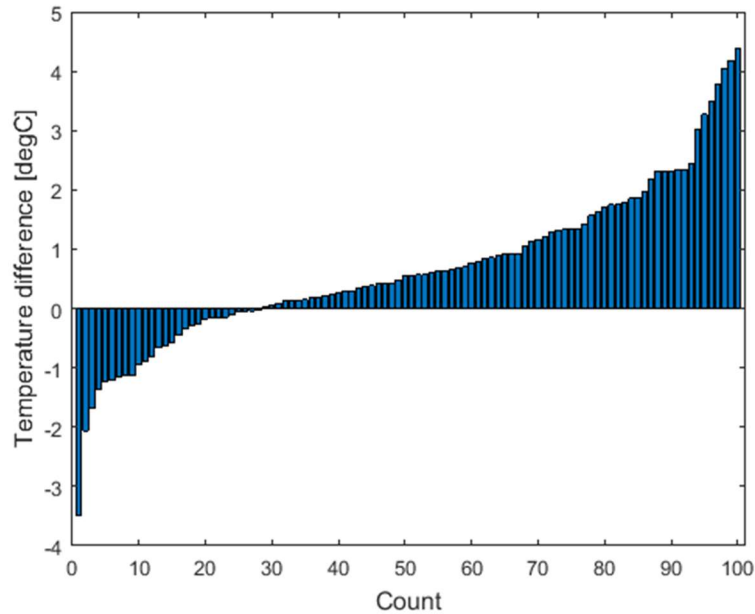


Figure 2.19: Temperature difference between the perpendicular and parallel flow directions for the 100 artificially generated fracture aperture distributions at 10 minutes into the simulation.

The temperature difference between the perpendicular and parallel flow directions for the 100 artificially generated fracture aperture distributions at 0.72 minutes was plotted against the difference in the fracture area contacted by the flowing fluid. The plot is shown

in Figure 2.20. The data in the plot indicates a linear relationship between the temperature difference between the flow directions and the difference in the fracture surface area contacted by fluid. Thus, the higher the difference in the flow wetted surface area, the higher the difference in temperature between the flow configurations.

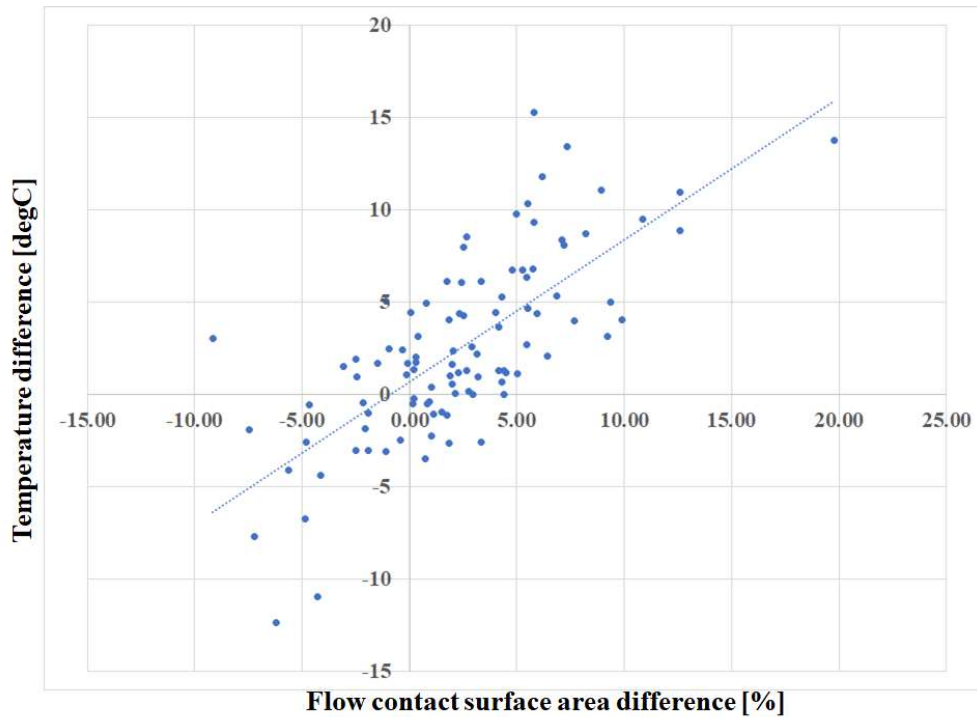


Figure 2.20: Temperature difference between the perpendicular and parallel flow directions for the 100 artificially generated fracture aperture distributions at 0.72 minutes into the simulation plotted against the fracture’s flow contact surface area.

A few aperture distributions were selected for further analysis to understand more the impact of anisotropy on the thermal performance of the lab-scale fractures. Figure 2.21 shows the temperature difference plot of the chosen aperture distributions, while Table 2.3 is a list of the selected aperture distributions with remarks to support why they were chosen. These aperture distributions were analyzed based on their flow and temperature maps at the fracture, contact area, joint roughness coefficient (JRC), and anisotropy of the ranges from variogram modeling. The objective was to understand if there were specific characteristics of the fracture surface that favored heat transport for a given flow configuration.

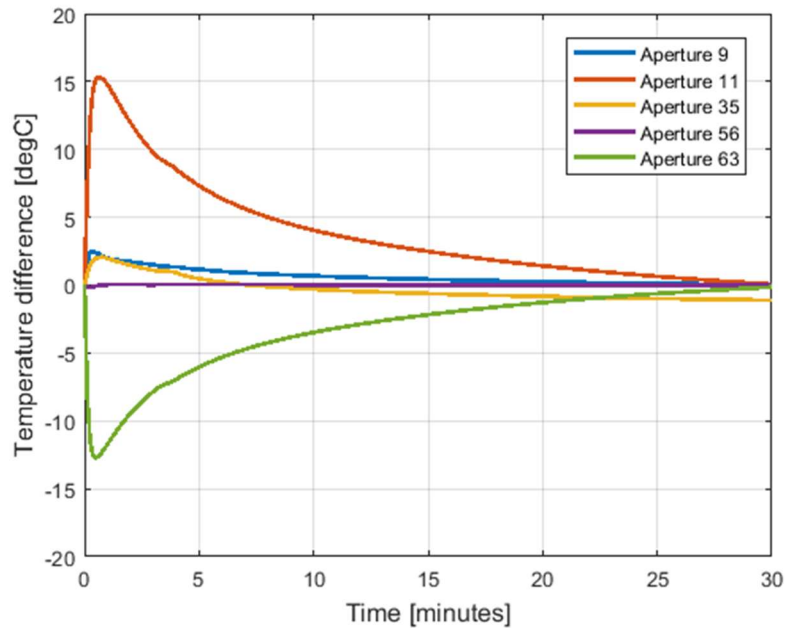


Figure 2.21: Temperature difference between the perpendicular and parallel flow directions for the five selected artificially generated fracture aperture distributions.

2.2.2.1 Flow and Temperature Map Analysis

Figures 2.22 to 2.26 show the flow and temperature maps at the fracture surface for the selected aperture distribution at 10 minutes into the simulation. Table 2.4 summarizes the percentage of the fracture area covered during flowing conditions for all the selected aperture distributions. For Aperture 9, which is one of the aperture distributions with temperature difference in the range of most of the simulations, though the temperature difference indicates that the perpendicular flow configuration is more favorable, this does not stand out in the flow and temperature maps, as shown in Figure 2.22. An estimation of the area contacted by the flowing fluid for Aperture 9 shows that the perpendicular flow configuration contacts 3.26 % more area than the parallel flow configuration (Table 2.4), thus justifying the higher extracted temperature in the perpendicular flow configuration.

Aperture 11 had the highest temperature difference recorded from the simulations. From the flow map of Figure 2.23, flow is seen to be more channelized in the parallel flow configuration (Figure 2.23a) than in the perpendicular flow configuration (Figure 2.23b). As a result, less area (5.84 %) is contacted in the parallel flow configuration than in the perpendicular flow configuration (Table 2.4). From the temperature map, the less cooled

area is larger in the parallel flow configuration (Figure 2.23c) compared to the perpendicular flow configuration, contributing to why more heat is extracted in the perpendicular flow configuration.

Table 2.3: Summary of selected aperture distributions for further analysis

Aperture Distribution No.	Temperature difference at 0.72 minutes	Remarks
9	2.40	Falls in the range of temperature difference with the highest frequency
11	15.29	Had the highest temperature difference
35	2.09	Had a unique trend of going from positive temperature difference to negative temperature difference
56	-0.01	Had almost no difference in temperature
63	-12.39	Had the lowest temperature difference

Table 2.4: Summary of selected aperture distributions for further analysis

Aperture Distribution No.	Percentage of fracture area contacted (%)		
	Parallel flow	Perpendicular flow	Difference (Perpendicular - Parallel)
9	55.56	58.72	3.16
11	45.12	50.96	5.84
35	66.56	72.96	6.40
56	63.32	67.72	4.40
63	49.00	44.00	-5.00

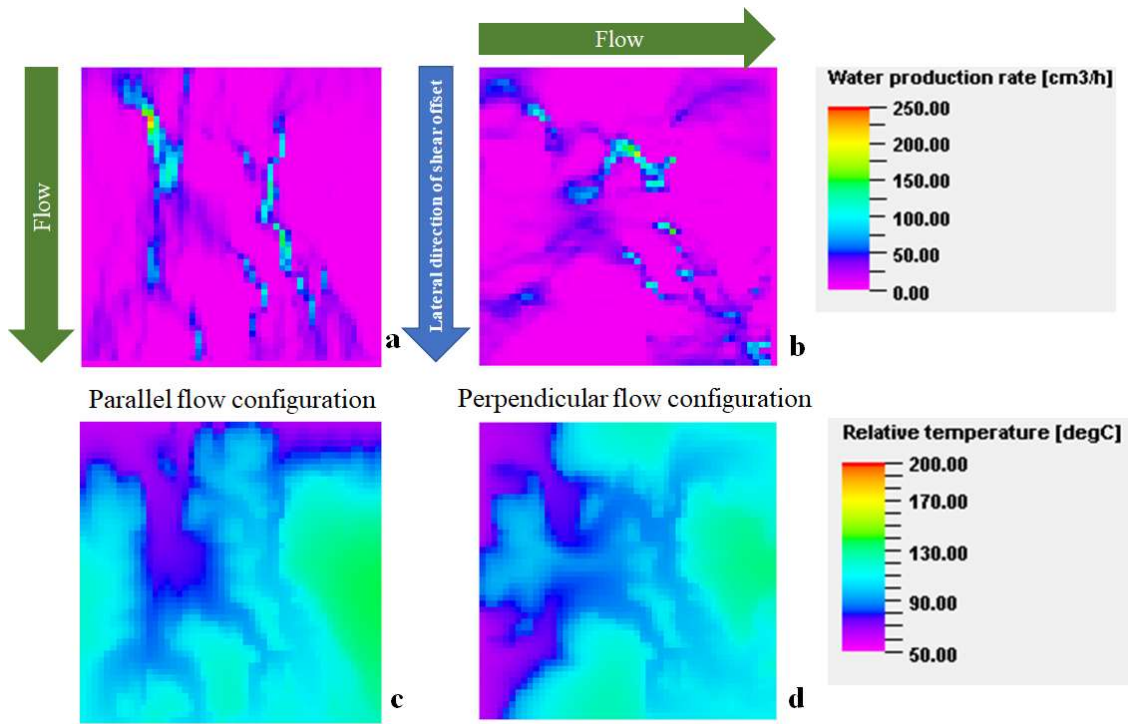


Figure 2.22: Fluid flow and heat transport on the fracture aperture after 10 minutes for Realization 9 of the artificially generated aperture distributions.

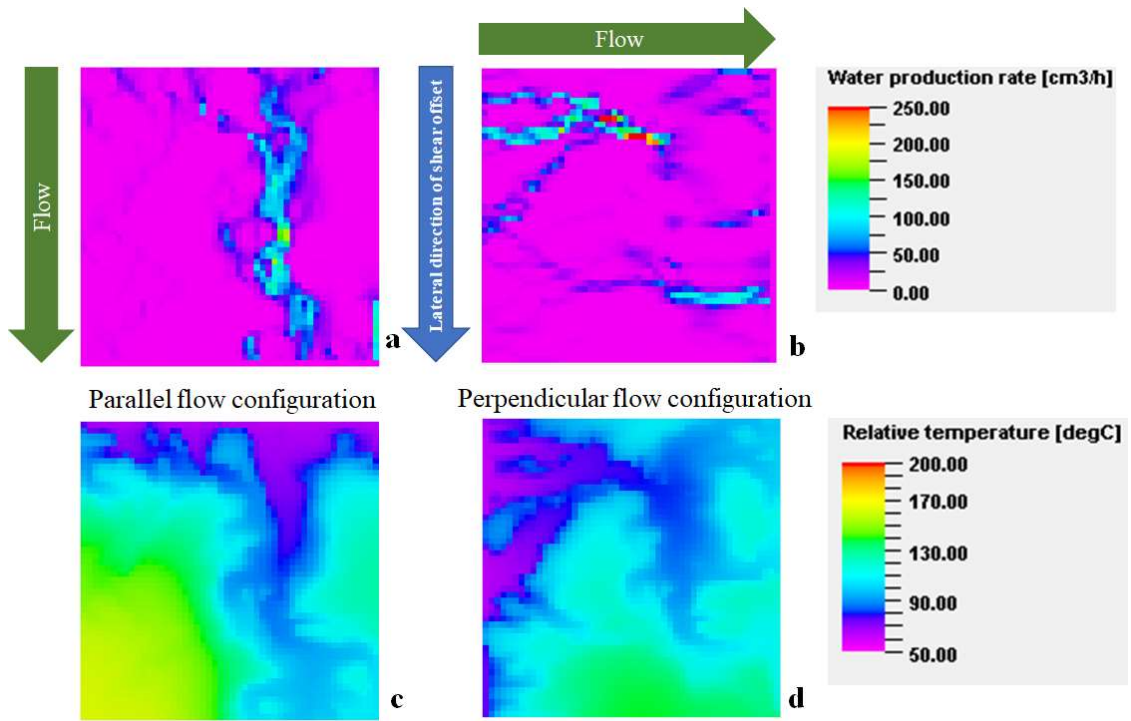


Figure 2.23: Fluid flow and heat transport on the fracture aperture after 10 minutes for Realization 11 of the artificially generated aperture distributions.

Aperture 35 starts out having higher temperature difference between the perpendicular flow configuration and the parallel flow configuration, and after about 6 minutes into the simulation, the trend changes (Figure 2.21). An observation of the flow and temperature maps (Figure 2.24) indicate that the flow and thermal sweep follow a stripy pattern in the perpendicular flow configuration whereas the flow and thermal sweep do not have a strongly stripy pattern. This would imply that in the longer term, the fluid flow would remain within the stripes of the perpendicular flow configuration, resulting in poorer thermal sweep, which would result in less heat extraction, as seen in Figure 2.21 after 6 minutes.

Aperture 56 was selected due to the minimal difference between the temperatures of the perpendicular and parallel flow configuration (Figure 2.21). From Table 2.4, the difference in area contacted by the different flow configurations is 4.4 %, higher than Aperture 9 which was 3.16 % in contact area difference and had a temperature difference of about 2.4 °C. An observation of the flow maps (Figure 2.25a and Figure 2.25b) show that though there may be higher contact area in the perpendicular flow configuration, there was more volumetric flow rate within some sections of the channels in Figure 2.25a for the parallel flow configuration. Thus, this additional flow volume may have compensated for the lower contact area of the parallel flow configuration and evened out heat extraction in that flow configuration compared to the perpendicular flow configuration.

Aperture 63 had the highest temperature difference in favor of the parallel flow configuration to the perpendicular flow configuration with the parallel flow configuration having a higher temperature of about 12.39 °C by 0.72 minutes into the simulation. The flow map and temperature map at the fracture is shown in Figure 2.25. A qualitative inspection of the flow map shows more flow areas in the parallel flow configuration than in the perpendicular flow configuration (Figures 2.26a and 2.26b). From Figure 2.26c, it can be seen that more of the fracture surface area is cooled in the parallel flow configuration compared to the perpendicular flow configuration (Figure 2.26d). There is evidence of an area in the latter temperature map that has not been adequately cooled relative to the parallel flow configuration.

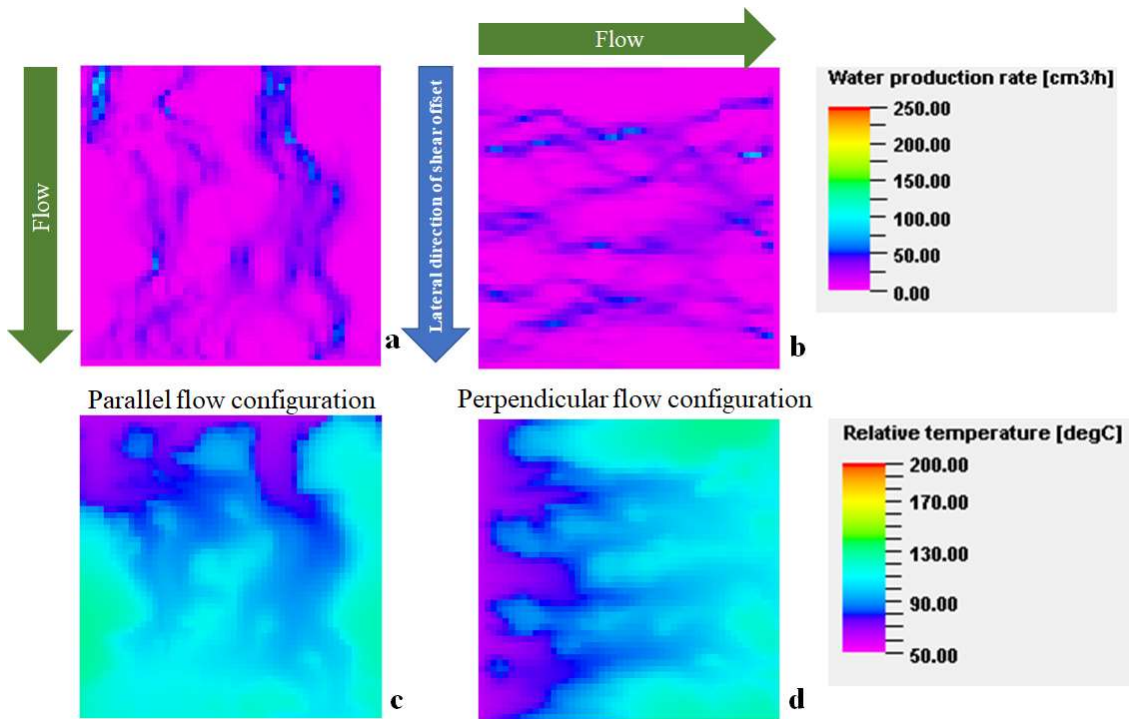


Figure 2.24: Fluid flow and heat transport on the fracture aperture after 10 minutes for Realization 35 of the artificially generated aperture distributions.

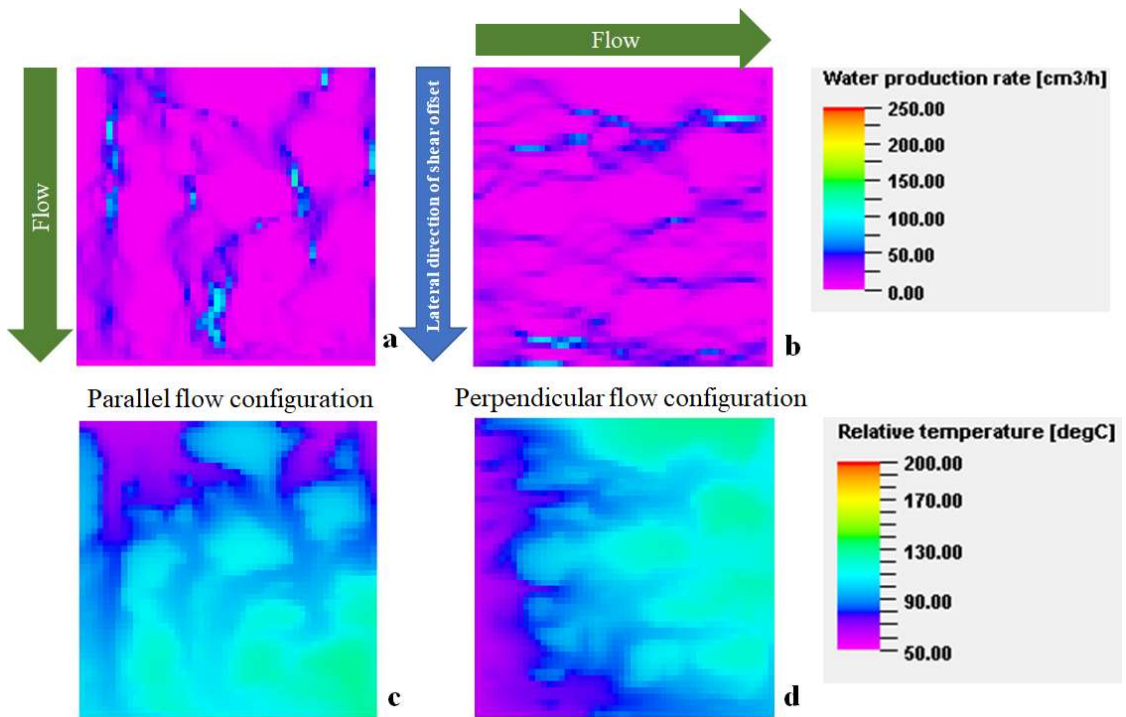


Figure 2.25: Fluid flow and heat transport on the fracture aperture after 10 minutes for Realization 56 of the artificially generated aperture distributions.

The percent flow contact area in the parallel flow configuration was 5 % more than in the perpendicular flow configuration for Aperture 63 (Table 2.4). This further supports the observations that the higher surface area in contact with the fluid, the higher the heat extraction from the rock.

In general, fractures with variation in aperture distribution will result in less heat extracted from the rock compared to a smooth fracture. Also, the flow contact area is a significant contributor to how much heat can be extracted from a surface that has spatial variations in aperture. Moreover, within a channel or preferential flow path, more heat is extracted from the rock if the flowrate is high. To understand if the degree of aperture variability contributes to flow wetting, flowrate or heat transport, metrics such as the joint roughness coefficient and geometric anisotropy from variogram modeling were investigated and discussed in the sections that follow.

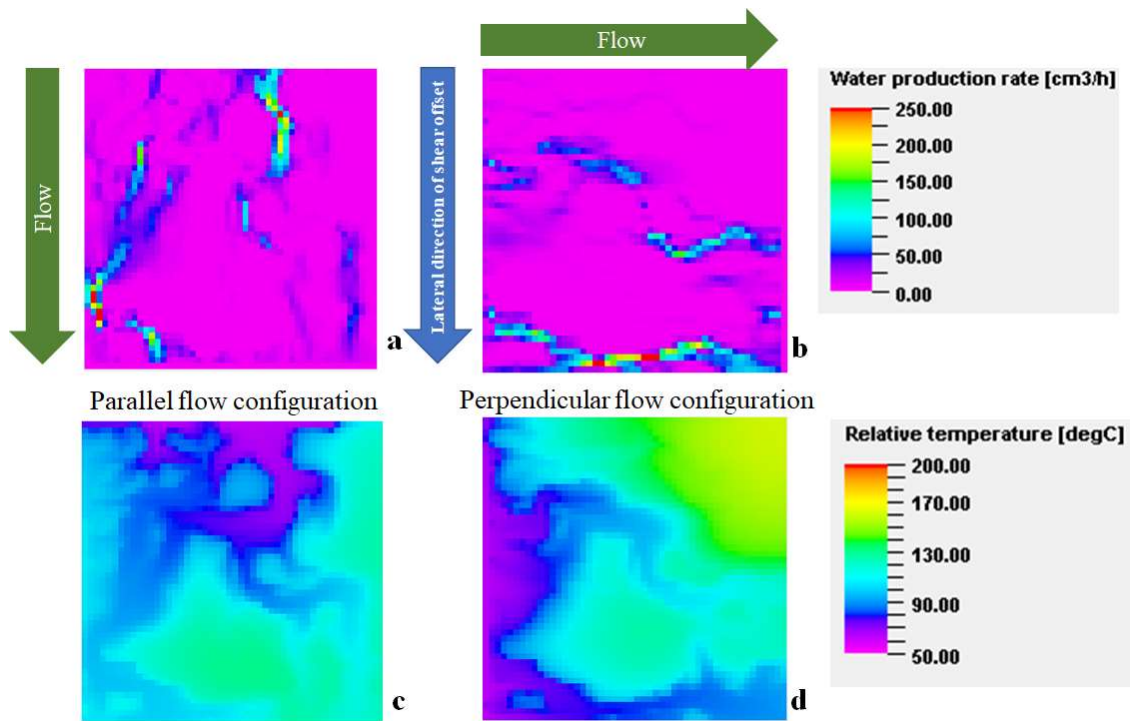


Figure 2.26: Fluid flow and heat transport on the fracture aperture after 10 minutes for Realization 63 of the artificially generated aperture distributions.

2.2.2.2 Joint Roughness Coefficient and Flow Contact Area Analysis

The preceding analysis using the flow map, temperature map, and percentage of flow contact area does not explain why a given flow configuration would be more favorable to flow surface wetting and heat extraction. To gain insights to the morphology of the fracture surface and if they contribute to channeling and heat extraction, the joint roughness coefficients were analyzed and compared with the flow contact area, since it has been deduced that the flow contact area is a significant contributor to how much heat is extracted from the rock.

An estimated value of the joint roughness coefficient (JRC) is compared with the 10 standard roughness profiles defined in the work by Barton and Choubey (1977), and as shown in Figure 2.9, to give an indication of a sheared surface's roughness. The higher the JRC, the higher the spatial aperture variability of the surface will appear. Table 2.5 shows the estimated JRCs for the selected aperture distributions in the parallel and perpendicular flow directions, placed adjacent to the percentage flow contact area for the respective flow directions.

Table 2.5: Joint Roughness Coefficients and percentage flow contact area for the selected aperture distributions

Aperture Distribution No.	JRC			Percentage of fracture area contacted (%)		
	Parallel flow direction	Perpendicular flow direction	JRC Difference (Perpendicular - Parallel)	Parallel flow	Perpendicular flow	Difference (Perpendicular - Parallel)
9	18.01	13.43	-4.58	55.56	58.72	3.16
11	16.90	11.76	-5.14	45.12	50.96	5.84
35	18.12	14.38	-3.74	66.56	72.96	6.40
56	17.14	14.25	-2.89	63.32	67.72	4.40
63	14.14	11.44	-2.70	49.00	44.00	-5.00

In analyzing the JRCs alongside the percentage of flow contact area, it was observed that the JRCs in the parallel flow direction were higher than the JRCs in the

perpendicular flow configuration. This information gives an indication of anisotropy of the fractured surface, and is in agreement with studies that suggest that there is anisotropy in the aperture variability of fractured surfaces (Thompson & Brown, 1991; Candela, et al., 2012; and Co, 2017).

Another observation from the data was that there is a strong correlation between the JRC in the perpendicular flow direction and the flow contact area in the perpendicular flow configuration. The higher the JRC, the higher the flow contact area. While this relationship is true for some of the aperture distributions in the parallel flow configuration, using these results would have to be done specifically for a given flow configuration, as a JRC of 14 in the parallel flow direction may result in a low flow contact area whereas a JRC of 14 in the perpendicular flow direction may result in a high flow contact area.

For the aperture distributions analyzed, a low difference in the JRC value between the perpendicular flow configuration and the parallel flow configuration correlates with a high difference in percentage of flow contact area. Thus, the lower the difference in JRC values, the more flow contact area expected in the perpendicular flow direction, which will in turn lead to more heat extracted from the rock.

These findings suggest that the morphologies of the fractured rock have characteristics that could support preferential flow and consequently heat transfer in a given flow configuration, though the information has to be used relative to the flow configurations and not in isolation.

2.2.2.3 Variogram Modeling

Having examined how the joint roughness coefficient could impact flow and heat transport, a variogram modeling was performed to understand if there were spatial characteristics of the fracture surface that could contribute to improved flow and heat transfer for a given flow configuration.

Table 2.6 shows the interpreted variogram parameters for the selected aperture distributions, while Figures 2.27 to 2.32 show the experimental variograms for the aperture distributions. Only two angles were analyzed for the variogram model – the 0° and the 90° angles.

Table 2.6: Results of variogram modeling for the selected aperture distributions

Aperture Distribution No.	Variogram Model Results				
	Long Range (mm)	Short Range (mm)	Sill	Nugget	Long/Short Range (Ratio)
9	28.62	19.87	0.37	0.02	1.44
11	12.72	8.35	0.17	0.02	1.52
35	15.11	12.32	0.28	0.02	1.23
56	9.56	7.55	0.25	0.02	1.27
63	17.49	10.73	0.20	0.02	1.63

Geometric anisotropy is said to exist when the ranges of the variogram model vary as a function of direction. As all the aperture distributions are stochastic realizations of the original lab-scale fracture aperture distribution, which had geometric anisotropy (Figure 2.7), it was expected that the artificial aperture distributions would also have geometric anisotropy.

From the variogram modeling, the nuggets for all the aperture distributions were found to be the same at 0.02. However, there were differences between the sills and the ranges across the different aperture distributions. The long range is 90° from the x axis, and corresponds to the parallel flow configuration, while the short range is 0° from the x axis and corresponds to the perpendicular flow configuration.

From the variogram model parameters, it was observed that Aperture 11 and Aperture 63, which had the highest differences in temperatures between the flow configurations, also had the highest geometric anisotropies (1.54 and 1.63 respectively from Table 2.6) and had lower sills compared to the other aperture distributions. On the other hand, Aperture 35 and Aperture 56, which had low differences in temperatures for the flow configurations (including changing from favoring the perpendicular flow configuration to favoring the parallel flow configuration), had low anisotropy. Hence it can be deduced that high geometric anisotropy results in high differences in thermal drawdown, though these values do not indicate which direction will give a higher thermal drawdown.

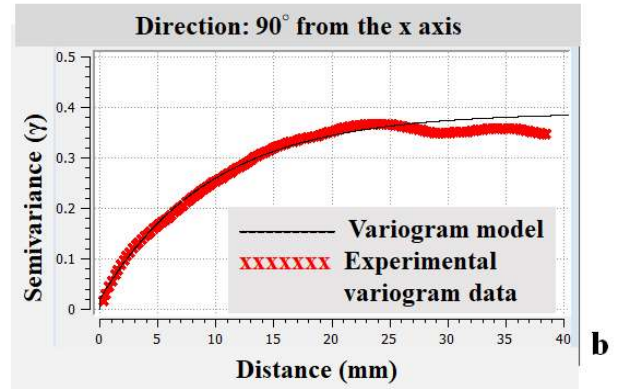
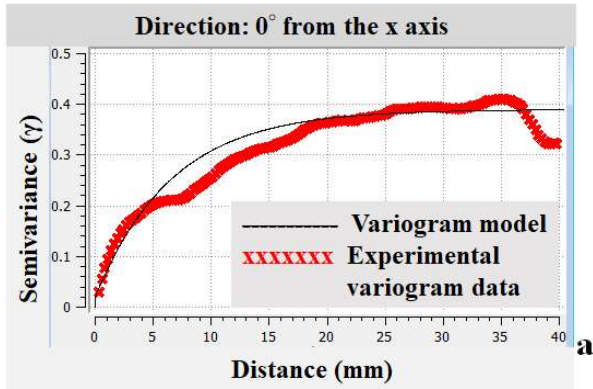


Figure 2.27: Variogram modeling parameters for Realization 9 of the artificially generated aperture distributions.

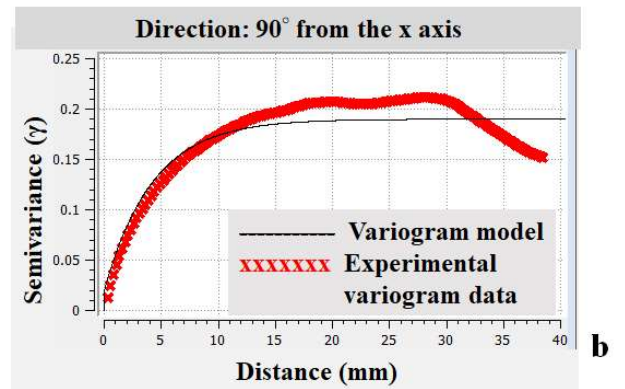
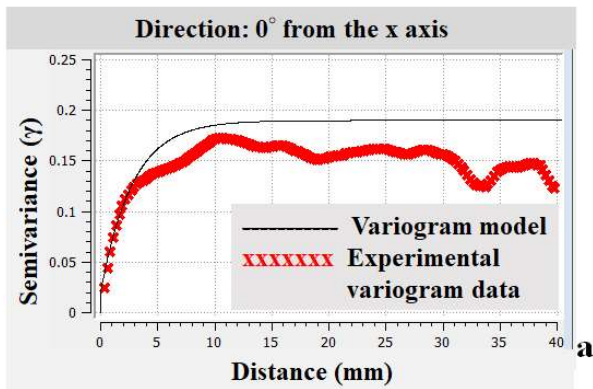


Figure 2.28: Variogram modeling parameters for Realization 11 of the artificially generated aperture distributions.

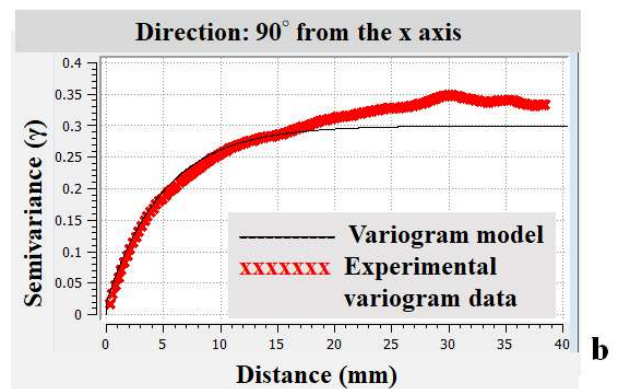
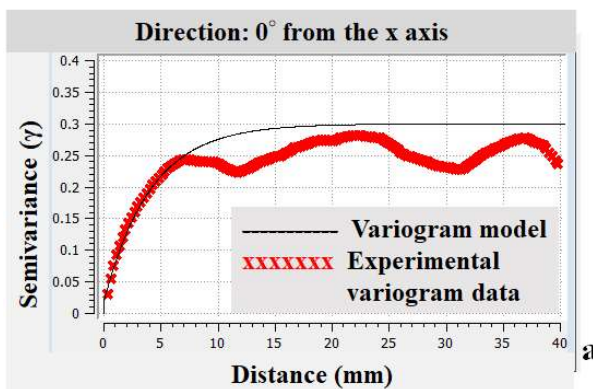


Figure 2.29: Variogram modeling parameters for Realization 35 of the artificially generated aperture distributions.

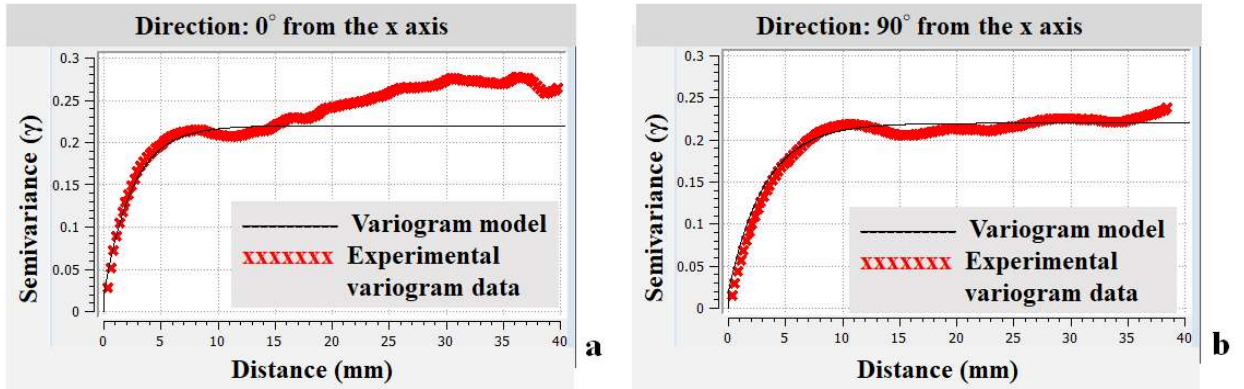


Figure 2.30: Variogram modeling parameters for Realization 56 of the artificially generated aperture distributions.

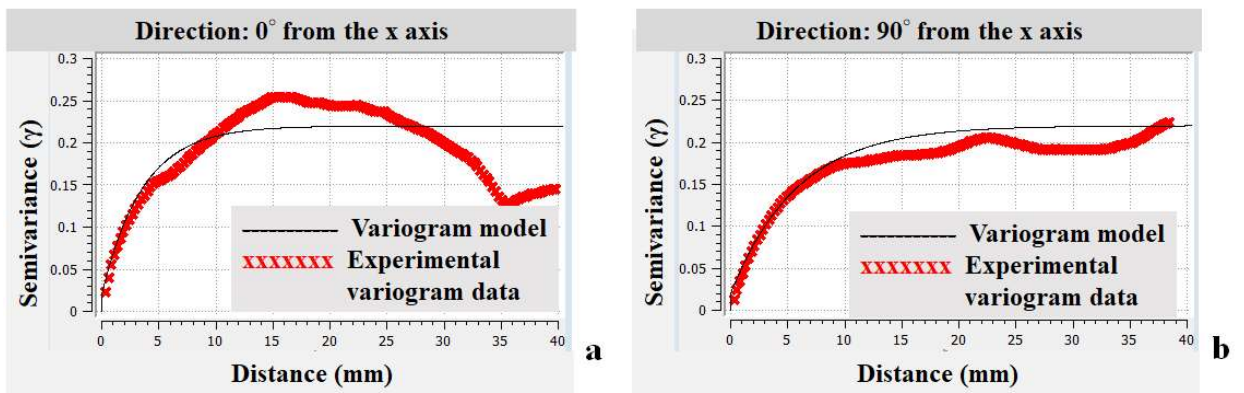


Figure 2.31: Variogram modeling parameters for Realization 63 of the artificially generated aperture distributions.

2.2.2.4 Cumulative Energy Produced

Having examined the fracture aperture variability and spatial characteristics, it was useful to evaluate how the heat extracted for the different flow configurations translates to energy produced. The cumulative energy produced is determined from the solution to the energy balance given in Equation 2.3. In Figure 2.31, the difference between the cumulative energy produced of the two flow configurations is plotted for the five selected aperture distributions, the original aperture distribution and a smooth fracture. Similar to the trend seen in Figure 2.20 for the temperature difference between the perpendicular and parallel flow directions for the five selected fracture aperture distributions, Aperture 11 resulted in the largest difference in energy produced while Aperture 63 resulted in the lowest difference in energy produced. Aperture 56 and the model with a constant fracture aperture had zero difference in the energy produced.

The absolute values of the energy produced as a function of time are shown in Figure 2.33 for the smooth fracture defined by a constant fracture aperture, Aperture 11, Aperture 35 and Aperture 63. The results for the different flow configurations are plotted. The smooth fracture results in the highest cumulative energy extracted. Aperture 35, which had higher temperature difference in favor of the perpendicular flow configurations in the first six minutes of the simulation then had the parallel flow configuration with higher temperatures afterwards, resulted in higher energy extracted in the perpendicular direction. This can be attributed to the fact that the system's temperature was hotter at the initial time, and after the temperature of the system had dropped, not much heat could be extracted though the perpendicular flow configuration had higher thermal drawdown after six minutes into the simulation. Aperture 11 had higher energy extracted in the perpendicular direction, while Aperture 63 had higher energy extracted in the parallel direction, in agreement with the results in Figure 2.31.

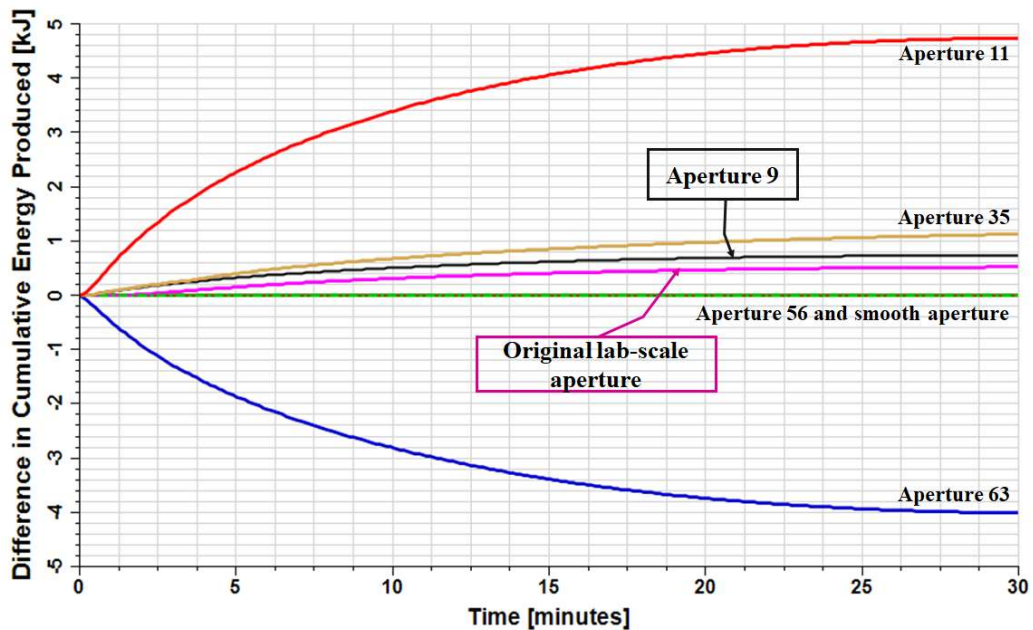


Figure 2.32: Difference in the cumulative energy produced for the five selected aperture distributions, the original aperture distribution, and a smooth fracture.

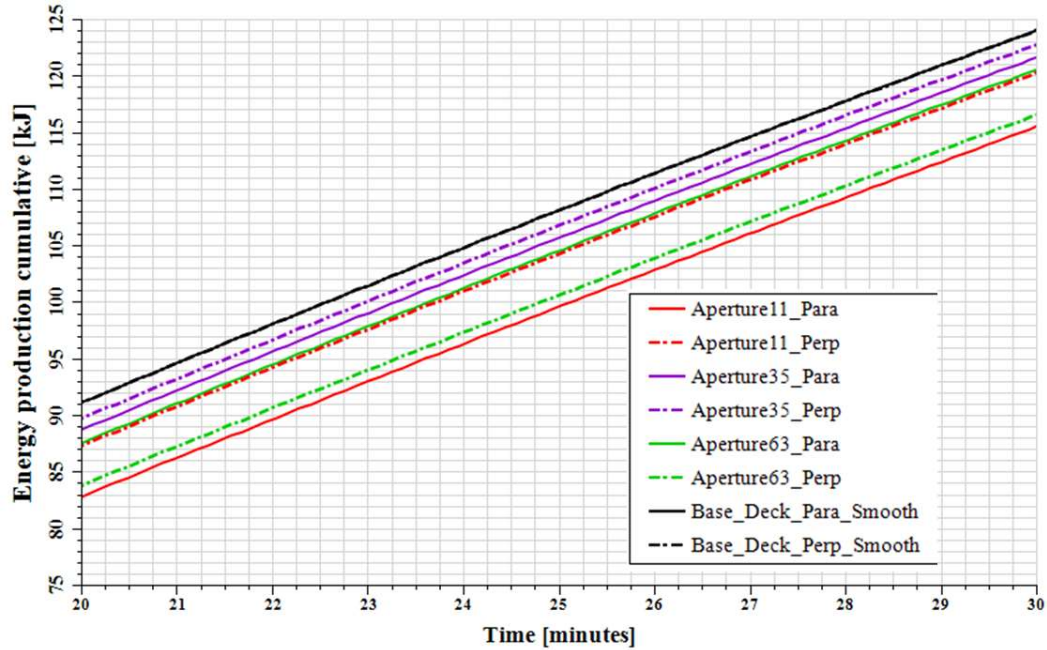


Figure 2.33: Cumulative energy produced of the perpendicular and parallel flow configurations for the smooth fracture, Aperture 11, Aperture 35, and Aperture 63.

2.3 Summary

In this part of the study, the effect of fracture geometric anisotropy on thermal performance was investigated by examining heat transport in parallel and perpendicular flow configurations defined by applying a pressure gradient relative to the direction of the fracture shear offset. A thermohydraulic model was run at the lab scale on the fracture aperture distribution determined for a 50 mm by 50 mm sheared fracture. Subsequently, the thermohydraulic model was run on 100 artificially generated aperture distributions.

The results indicate that flow on a smooth fracture surface would result in lower thermal drawdown than a fracture with spatial variations in aperture. Also, the extracted heat for a smooth fracture was independent of flow direction.

The results of the thermohydraulic modeling of the system having fractures with spatial variations, either from the original lab-scale fracture aperture distribution or the artificially generated aperture distributions, show that fracture aperture variability and consequently channeling results in higher thermal drawdown compared to the smooth surface.

Of the 100 artificially generated fracture aperture distributions used in this study, 70 % had temperatures as a function of time higher in the perpendicular flow configuration compared to the parallel flow configuration. This result is in agreement with the findings by Gao et al. (2021) where the fracture surface with $\alpha = 0^\circ$ (parallel flow configuration) resulted in more cooling than the fracture with $\alpha = 90^\circ$ (perpendicular flow configuration).

It was also observed from this study that the flow wetted surface area had a direct and significant contribution to the amount of heat extracted, i.e., the larger the surface area in contact with the flowing fluid, the more heat is extracted.

Geometric anisotropy was observed in the datasets joint roughness coefficient (JRC) and variogram modeling parameters. The JRC was seen to directly correlate with the flow contact area though the absolute JRC values are meaningful when looking at a specific flow configuration, as a high JRC in the perpendicular direction might be a low JRC in the parallel direction. However, the difference in JRC between the perpendicular and parallel flow configurations had an inverse relationship with the difference in the percentage of flow contact area for the aperture distributions analyzed. Thus, the lower the difference in JRC values, the more flow contact area expected in the perpendicular flow direction, which will in turn lead to more heat extracted from the rock.

From the variogram model parameters, it was deduced that high geometric anisotropy results in high differences in thermal drawdown and consequently high difference in energy extracted, though the values of the geometric anisotropy do not indicate which direction will give a higher thermal drawdown.

Having examined the performance on the lab scale, the next phase was to investigate the impact of fracture geometry anisotropy on the field scale, which is the focus of Chapter 3.

Chapter 3

3 Anisotropic Effects on Field Scale EGS

Thermal Performance

3.1 Introduction

Enhanced Geothermal Systems (EGS) are created artificially using hydraulic pressure to stimulate preexisting fractures in a hot host rock, thereby causing the rock to slip. This stimulation results in fractures that are self-propped from the slippage with mismatched asperities on each side of the fracture. This process of stimulation, known as hydroshearing or shear stimulation, results in improved permeability of the reservoir that is irreversible primarily due to the rearrangement of asperity contacts accompanied by shear dilation (Gischig and Preisig, 2015). The improved permeability allows for heat to be extracted from the rock to the working fluid circulated throughout the system. Several studies have suggested that the predominant stimulation mechanism in most EGS projects is either hydroshearing or mixed-mode (Pine and Batchelor (1984); Murphy and Fehler (1986); Ito (2003); Ito and Hayashi (2003); Evans (2005); Tester et al. (2006); Kohl and Mégel (2007); Bruel (2007); Dezayes et al. (2010); Cladouhos et al. (2011); Petty et al. (2013); McClure and Horne (2014); Gischig and Preisig (2015)).

Because the predominant stimulation mechanisms in Enhanced Geothermal Systems involve shearing, in this study, an investigation was carried out to understand how flow relative to the directions of slip or shear can impact heat transfer and heat extraction. Before presenting the results of this investigation, the morphology of fractures is discussed. A review of methods to model field scale Enhanced Geothermal Systems was carried out, including how fractures are modeled and characterized for heat transfer investigations.

3.2 The Morphology of Fractures and Implications for Flow and Heat Transport

Flow channeling is a phenomenon where liquid flowing through a geologic system with its heterogeneous structure is focused along a few preferred pathways (Tsang & Neretnieks, 1998). These pathways are "paths of least resistance" where most of the flow goes (Tsang & Tsang, 1989). These heterogeneities stem from fracture apertures (the void space between contacting fracture surfaces with aperture variability) and matrix porosities. However, due to the low value of porosities in Enhanced Geothermal Systems, heterogeneities in fracture apertures are more significant.

Kolditz & Clauser (1998) have suggested that differences between heat models and field observations could be due to channeling induced by the fracture aperture variability or the fracture network. Tester et al. (2006) also highlighted that channeling and short-circuiting of circulation fluids have been a deterrent in conductive heat transfer efforts.

Channeling of the fluid flow due to fracture aperture variability has already been observed experimentally and studied (Méheust & Schmittbuhl, 2000, Plouraboué et al., 2000, Schmittbuhl et al., 2008, Tsang & Tsang, 1998). Channeling of flows due to surfaces with spatial variations in aperture have been demonstrated through laboratory experiments (Hakami & Larsson, 1996; Pyrak-Nolte et al., 1997; Lee & Cho, 2002; Ishibashi et al., 2012), and numerical simulations and field investigations (Abelin et al., 1991; Tsang & Neretnieks, 1998; Watanabe et al., 2008; Mattson et al., 2018; Hawkins et al., 2018).

To understand the cause of channeling, there is a need to understand the nature of the fracture surface. The topology of natural fracture aperture variability has been examined at field scale and has been demonstrated to have aperture variability characterized by a scale-invariant property with a self-affine geometry (Candela et al., 2009). Self-affinity is a fractal feature whose pieces are scaled by different amounts in the x- and y-directions (Wikipedia, 2021a). Fractals are subsets of Euclidean space that exhibit similar patterns at increasingly more minor scales, such that if this replication of patterns is the same at every scale, it is called affine self-similar.

A visual inspection of the fracture surface studied in Candela et al. (2009) shows that there are striations across the fracture surface. These striations were observed to be

aligned in the direction of slip or shear. Candela et al. (2009) determined a roughness scaling exponent close to 0.8 for fracture aperture variability profiles oriented in a direction perpendicular to the striations observed on the fault plane. In addition, the influence of slip was also quantified, and it was demonstrated that the fault surfaces have smaller aperture variability amplitude along the slip direction than perpendicular to it.

Candela et al. (2012) examined the topographic roughness measurements of five exhumed faults and 13 surface earthquake ruptures with scales ranging from 50 μm to 50 km. They observed that fault aperture variability is scale-dependent, with an anisotropic self-affine behavior that is slightly anisotropic. They determined the aperture variability scaling exponent to be 0.58 ± 0.07 in the slip direction and 0.81 ± 0.04 in the direction perpendicular to slip. In addition, they examined the two-dimensional aperture variability of the surface rupture of 13 major continental earthquakes. They concluded that the ruptures show geometrical properties consistent with the slip-perpendicular behavior of the smaller-scale measurements.

The finding of the studies mentioned above corroborates the lab-scale findings of Thompson & Brown (1991) and Co (2017) that sheared fractures exhibit anisotropy. In the previous chapter, it was seen that flow in the direction perpendicular to shear resulted in improved thermal performance over the parallel flow configuration with a ratio of about 70:30 at lab-scale. Hence, it is of interest to understand how anisotropy impacts heat transfer at the field scale and if the process of shearing or well placement can be modified to better harness heat from Enhanced Geothermal Systems.

3.3 Characterizing Self-Affinity in One-Dimensional and Two-Dimensional surfaces

Mandelbrot (1983) and Voss (1985) proposed self-affinity as a general scaling transformation that can be used for the quantitative description of fault aperture variability. According to Meakin (1998), a self-affine one-dimensional profile remains unchanged under the scaling transformation $\delta x \rightarrow \lambda \delta x$, $\delta z \rightarrow \lambda^H \delta z$ for one-dimensional profiles extracted from a surface (Figure 3.1). In this scaling transformation, δx is the coordinate along the profile, and δz is the roughness amplitude. For a self-affine profile, the scaling

exponent H , referred to as the Hurst exponent, lies in the range $0 \leq H < 1$. Self-affinity implies that a profile appears smoother as the scale increases. An enlarged portion of the profile will appear statistically identical to the entire profile if different magnifications are used in the x and z directions.

This self-affinity property can be defined for two-dimensional surfaces using sets of one-dimensional parallel profiles extracted from the surface. Furthermore, if the surface is striated along a given orientation, H could vary for different directions in the surface plane, leading to anisotropic scaling behavior. According to Candela et al. (2009), an anisotropic self-affine surface $Z(x, y)$ with coordinates (x, y) obeys the property:

$$Z(\lambda^{1/H_{\parallel}}x, \lambda^{1/H_{\perp}}y) = \lambda Z(x, y) \quad (3.1)$$

where λ is a positive dilation factor, H_{\parallel} is the Hurst exponent defined along a direction parallel to slip or shear, and H_{\perp} is the Hurst exponent defined along a direction perpendicular to slip or shear. An example of an anisotropic self-affine surface is shown in Figure 3.1b.

The Hurst exponent is valuable for determining the fractal dimension of a surface with spatial variations in aperture, which has been found to be superior to the Joint Roughness Coefficient for quantifying surface aperture variability (Ge et al., 2014). The fractal dimension D is related to the Hurst exponent H through the Euclidean dimension E as given by Equation 3.2:

$$D = E - H \quad (3.2)$$

where $E = 2$ for a one-dimensional profile and $E=3$ for a surface.

The study by Candela et al. (2012), having examined surface topographic roughness measurements of faults and fractures with scales ranging from $50 \mu\text{m}$ to 50 km , determined the roughness scaling exponent to be 0.58 ± 0.07 in the slip direction and 0.81 ± 0.04 in the direction perpendicular to slip (Figure 3.2). The different values of Hurst exponent with a difference in direction suggests anisotropy of the fracture surface.

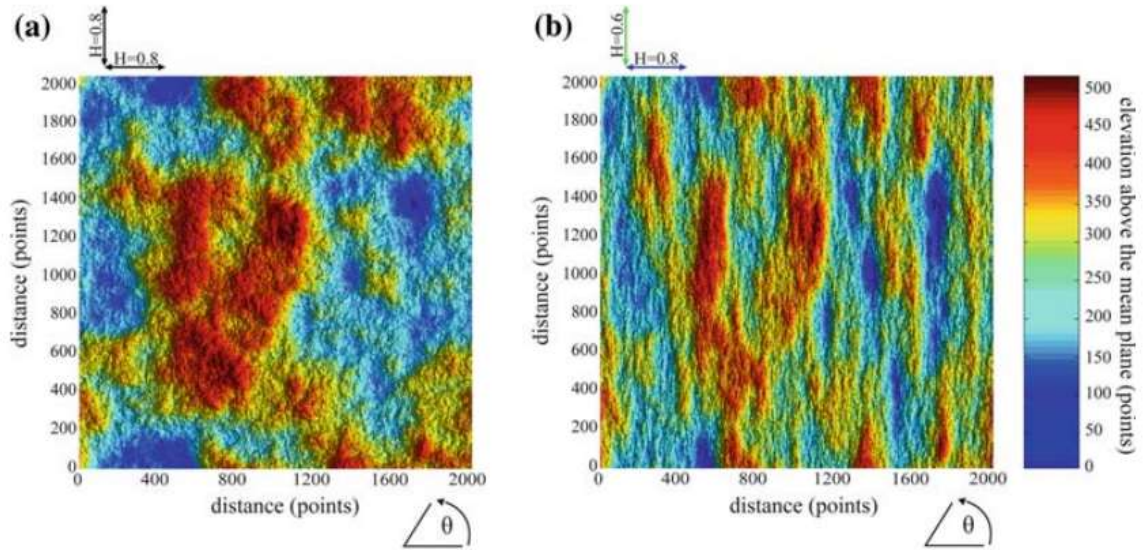


Figure 3.1: Two-dimensional synthetic self-affine surfaces with (a) an isotropic self-affine property characterized by a Hurst exponent of 0.8 and (b) an anisotropic self-affine surface with two Hurst exponents ($H_{\parallel} = 0.6$ and $H_{\perp} = 0.8$) in perpendicular directions (Candela, et al., 2009).

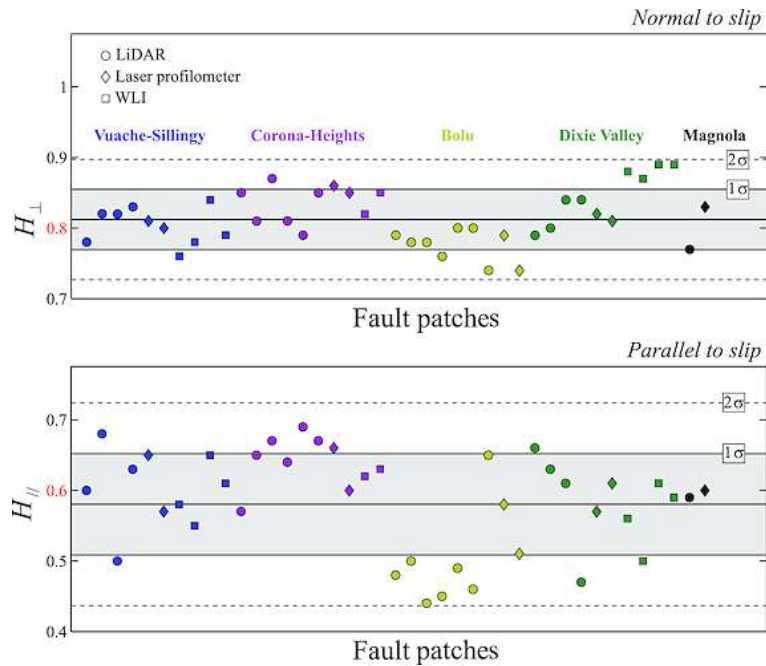


Figure 3.2: Plot of the Hurst exponents in direction (a) normal to slip and (b) parallel to it of 41 scanned fault patches (Candela et al., 2009). The average Hurst exponent is equal to 0.58 along the direction of slip and 0.81 perpendicular to it. The shaded area and dashed lines indicate 1σ and 2σ confidence intervals, respectively.

Geometric anisotropy exists when there is variable spatial continuity in different directions. When variogram models are used to determine geometric anisotropy, the

geometric anisotropy ratio is the ratio of the range in the x-direction to the range in the y-direction from a given variogram model. Co (2017), using variogram modeling, determined geometric anisotropy ratios for sandstone and granite fracture distributions generated using the displacement discontinuity boundary element method. The sandstone fracture anisotropy values were between 3 to 3.5, while the granite anisotropy values were between 4 and 4.5. These values were constant across different stress conditions. Co (2017) further determined the anisotropy ratio of the three lab-scale fractures from the study by Ishibashi et al. (2012), which had length scales of 75 mm x 50 mm, 150 mm x 100 mm, and 300 mm x 200 mm. The geometric anisotropy ratio was found to be one for mated fractures, suggesting isotropy of mated fractures, and ranged from 2 – 3 for the sheared fractures (Figure 3.2). In Chapter 2 of this study, selected lab-scale artificially-generated aperture distributions were analyzed to derive variogram parameters, resulting in geometric anisotropy ratios between 1.23 to 1.63.

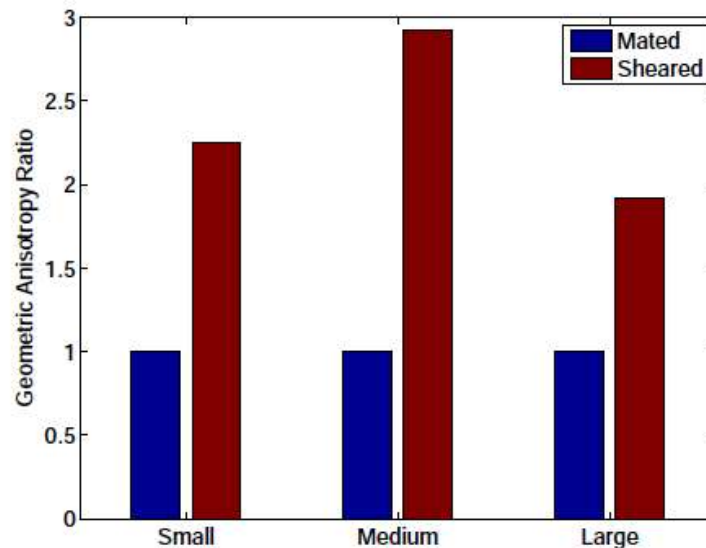


Figure 3.3: Geometric anisotropy ratios for mated and sheared lab-scale fractures for three fracture length scales (Co C. , 2017).

The information from the Hurst exponent and geometric anisotropy ratio can give indications of variable spatial continuity in different directions. Thus, in this study, self-affinity was characterized by the Hurst exponent and geometric anisotropy ratio from variogram modeling.

3.4 Modeling of Enhanced Geothermal Systems

3.4.1 Analytical and Semi analytical Modeling of Heat Transport in Enhanced Geothermal Systems

Several models exist to describe heat transport in Enhanced Geothermal Systems. The physical processes in this system consist of heat conduction by contact between the rock and fluid, then advection/convection (which is the transport of the heat through the flowing fluid), and mass transport in the fluid (from injecting in and extracting out the fluid). This section looks at the analytical and semi analytical heat transport models in Enhanced Geothermal Systems.

Gringarten et al. (1975) presented a theory for heat extraction from a fractured hot, dry rock based on the assumption of the infinite and uniform apertures of parallel vertical fractures. Coldwater enters through the bottom of each fracture, and heat is transferred from the hot rock to the water in the fractures via heat conduction. Their mathematical model provided a framework for comparing the energy extracted from single fractures vs. multiple fractures. It provides a simplified model for understanding heat transfer in fractured hot, dry rocks.

Gringarten & Sauty (1975) presented a mathematical model for describing the transient behavior of the pumped water and aquifer temperatures during reinjection of a fluid. Their solution for the water temperature within a stream channel was obtained from Lauwerier's one-dimensional solution (Lauwerier, 1955). Their results were helpful for designing a geothermal heat extraction system in an aquifer with a uniform regional flow.

Bödvarsson & Tsang (1982) presented a model similar to Gringarten & Sauty (1975), but they considered horizontal fractures in their model.

Kolditz (1995) examined the heat transfer in the fractured rocks when mining the heat energy from a hot, dry rock. The dimensional effect of heat diffusion in the rock matrix and its impact on the heat conductivity where the heat is transported from a hot, dry rock was investigated. The dimensional effect on heat transfer was done by comparing a two-and-a-half dimensional to a three-dimensional analytical model. The fully 3D model

reflected the nature of the spatial heat propagation in the geological formations, could predict the minimum borehole separations, and demonstrated the need to consider three-dimensional modeling.

Cheng et al. (2001) demonstrated that the heat conduction in the unbounded domain could be handled using the Green's function approach. They transformed the governing equations of heat extraction from a single fracture embedded in an infinite geothermal reservoir into an integral equation, eliminating the need to discretize the reservoir. They solved a one-dimensional and two-dimensional problem representative of flow through an infinite enhanced geothermal system. The two-dimensional problem, however, required a numerical solution. Cheng et al. (2001) demonstrated that there were significant differences in thermal performance prediction between a one-dimensional and two-dimensional representation of the system. Thus the use of correct reservoir geometry could be significant in predicting the life of an Enhanced Geothermal reservoir.

Ghassemi et al. (2003) emphasized the three-dimensional heat conduction effect in hot, dry rock. The physical mechanisms considered were limited to the advective heat transport in the fracture by fluid flow and the heat exchange with the reservoir. The numerical difficulty of modeling a three-dimensional, unbounded domain was overcome by utilizing the integral equation formulation and the three-dimensional Green's function for heat conduction. The need for discretizing the reservoir was eliminated, and the final numerical solution system involved only the two-dimensional fracture plane. The three-dimensional heat conduction effect was investigated against its one-dimensional simplification. The study showed that the simplification of reservoir heat flow to one dimension could significantly underestimate the extraction temperature and reservoir life.

Yang & Yeh (2009) developed a mathematical model describing the heat energy extracted from a hot, dry rock in a multiwell system. They accounted for a geothermal gradient in a geothermal reservoir, and their solutions for the water temperature were given in the Laplace domain, and computed by numerical inversion using the modified Crump method. They determined that the geothermal gradient affects only the early time heat extraction effectiveness significantly but directly impacts the water temperature for all times if the vertical thickness of the geothermal reservoir is large.

Martínez et al. (2013) developed analytical models for heat transfer in a single fracture surrounded by an infinite matrix. These models accounted for advection and hydrodynamic dispersion in the fracture, longitudinal and transverse conduction in the matrix, and a two-way coupling between heat transfer in the fracture and matrix. They also handled distributed or localized heat sources of arbitrary duration. The analytical models were first derived in the Fourier-Laplace space. In their most general form, the solutions were given by their Fourier and Laplace transforms and required numerical inversion, but in specific cases could be inverted using inverse Fourier and Laplace transforms.

Abbasi et al. (2019) examined the problem of water injection into a fractured geothermal reservoir in Cartesian coordinate. They developed an exact analytical solution that can describe the transient temperature distribution and advancement of the thermal front generate due to the transient temperature of heat-depleted water in a coupled fracture-matrix system at the scale of a single fracture. The solution was able to capture convective heat transport in fractures, conductive heat transfers in matrix block, and heat flux transfer between rock matrix and fracture.

The fractures have been treated as parallel plates without spatial heterogeneities across the fracture plane in the modeling methods described above. Analytical and semi analytical models are limited to simple problems and simple geometries. More sophisticated modeling methods are required when complexities exist, such as nonlinearities in the governing equations or boundary conditions. Hence, with complexities in the partial differential equations and boundary conditions and heterogeneities in geothermal reservoirs, numerical methods were introduced to understand the behavior of the heat and fluid transport mechanisms that occur in such Enhanced Geothermal Systems.

3.4.2 Numerical Modeling of Heat Transport in Enhanced Geothermal Systems

More rigorous models exist to capture better the fracture network and physical processes in Enhanced Geothermal Systems.

Li et al. (2013) explained what is involved in numerical modeling of the coupled thermo-hydraulic problem of enhanced geothermal systems. According to Li et al. (2013), the development of a heat transfer model starts with a fracture model, followed by a fluid flow model, and finally, the heat transfer model. They stated that the models to simulate fractures could be grouped into two categories (Fracture Continuum Models (FCM) and Discrete Fracture Models (DFM)), and the conceptual approaches to model fluid flow in fractured rocks fall into the same two categories: continuum approach and discrete fracture approach. They further explained that the continuum approach idealizes the fractured rock mass as a porous medium when the rock mass scale is sufficiently large relative to the fracture geometry. In contrast, the discrete fracture approach conceptualizes the rock mass as a set of impermeable blocks separated by systems of fractures that are idealized as networks of planar conduits. Each fracture is treated separately, producing the locations, orientations, dimensions, and connections.

Moreover, Li et al. (2013) explained that after the fracture and flow models are set up, the heat transfer models can be built accordingly. For the FCM, the heat transfer process is governed by Fourier's law of heat conduction, wherein one thermal conductivity coefficient is used to take into account both the rock and fluid heat conductivity. On the other hand, the heat transfer between fluid flow and rock is mainly governed by explicit heat convection equations in the DFM. A proper heat convection coefficient would be chosen to represent each fracture's dimensions and flow state.

Three-dimensional, double-porosity, finite-difference numerical models have been used to simulate enhanced geothermal systems (Sanyal & Butler, 2005; Pruess & Narasimhan, 2012; Stacey & Williams, 2017). O'Sullivan et al. (2001) document that dual-porosity representations of fractures have been used extensively in geothermal simulations because of lower computational requirements and the general uncertainty in fracture network characterization.

Bataillé et al. (2006) performed a systematic numerical study of the coupling between forced and free convective flows in the Soultz-sous-Forêts, France, Enhanced Geothermal System. They considered an extensive range of injection rates and Rayleigh numbers. The simulations showed that if there is weak or no free convection in an EGS

reservoir, economic exploitation of the system will rapidly end because of a decrease in produced fluid temperature.

Jiang et al. (2014) developed a three-dimensional transient model for the EGS subsurface thermohydraulic process, which was solved using a finite-volume numerical method. They employed the local thermal equilibrium theory, which focuses more on the overall heat transfer effect and assumes the solid matrix and the fluid locally have the same temperature always. The heat reservoir was considered to be an equivalent porous medium, which was characterized by a single porosity and a finite permeability. The fluid properties, viscosity and density, were independent of temperature and pressure. They demonstrated that the local thermal equilibrium model is adequate to predict EGS production temperature.

A finite-difference simulator was employed in the geothermal assessment of Italy's Pisa plain (Feng et al., 2017). In this case, the field was not an enhanced geothermal reservoir. Still, the numerical model allowed for a realistic description of the processes occurring at the injection and production wells, and set the baseline for assessing the long-term behavior of a geothermal doublet in the Pisa plain.

Recent developments in numerical simulation of enhanced geothermal systems employ finite element methods to account for the complexities of fracture networks (Xing et al., 2015). However, for the system investigated in this study, which is a single fracture embedded in a rock mass, a finite element method would not be required. Despite these recent developments, many models do not account for possible spatial variations within the fractures. The failure to account for spatial variations in the fracture aperture is not surprising as the flow equations and heat transport equations need to be modified to take cognizance of the aperture variations.

Neuville et al. (2010) investigated the effect of aperture heterogeneities on thermal performance with uniform base flow through a rectangular fracture. They assumed the surrounding rock to remain at the original reservoir temperature and only considered the heat transfer in the fracture. Such a model does not describe the thermal behavior of a geothermal reservoir over a long period of time. Thus, a more representative approach

would be to model coupled convective or advective heat transport in the fracture with that of the conductive heat transport in the surrounding rock.

Hawkins & Becker (2012) performed an experiment to evaluate the effect of channelized flow on fluid/rock heat transfer. Hot water was circulated between two wells in a single bedding plane fracture, and the elevation of rock matrix temperature was measured using fiber optic Distributed Temperature Sensing (DTS). Between wells with good hydraulic connection, heat transfer appeared to follow a classic dipole sweep pattern. Between wells with poor hydraulic connection, heat transfer was skewed toward apparent regions of higher transmissivity. The findings suggested that flow channeling could significantly impact heat transfer efficiency even in single planar fractures.

Fox et al. (2015) studied the effect of spatial aperture variations on the thermal performance of discretely fractured geothermal reservoirs. They selected a dipole flow in circular fractures between a single injector and producer to determine the effect of fracture surface variations on fluid flow and a reservoir's thermal performance. For simplicity, effects like temperature-dependent properties and buoyancy were not considered. Fractures with self-affine aperture fields where long-range correlations dominate over short-range correlations were generated. The results showed that spatial aperture variations most frequently lead to a diminished thermal performance due to the presence of flow channels that reduce the heat transfer area. Fox et al. (2015) added that an enhanced thermal performance occurred in the less common cases when the aperture was small in the region between the wellbores, causing fluid flow to sweep out more significant areas of the fracture and extract heat from a larger area.

The studies by Neuville et al. (2010), Hawkins & Becker (2012), and Fox et al. (2015) demonstrate that spatial variations in fractures can be accounted for in field-scale thermohydraulic modeling of Enhanced Geothermal Systems. These studies, however, do not account for anisotropy in the fracture surface. In Chapter 2 of this study, it was seen that flow in the direction perpendicular to shear resulted in improved thermal performance over flow in the direction parallel to shear. Moreover, Raleigh et al. (1974) suggested that geothermal wells be drilled perpendicular to the expected orientation of fractures. Though their objective was to generate multiple vertical cracks from a single well, because this

direction of placing wells was deemed to result in an increased economic life of EGS through a series of parallel, vertical cracks, it is of interest to know if this well configuration would result in improved energy extracted with fracture aperture variability taken into account. The pertinent question addressed in this section of this study is if the behavior at the lab scale reflects the behavior at the field scale and the implications for the direction of shear and well placement.

3.5 Generation of Fracture Surface with Variable Aperture

Different approaches have been used to determine fracture aperture distributions to characterize the spatial heterogeneity of fracture surfaces. This section outlines the various methods that can be used to generate synthetic fracture surface with variations in aperture.

Mandelbrot (1983) showed that surface profiles along a line in the fracture plane exhibit decaying power-law power spectral density functions of the same form as fractal surfaces. A method to compute the power spectral density function is to take the Fourier transform of the topography with details of the procedure outlined in Bendat & Piersol (1971). Peitgen & Saupe (1988) developed a spectral synthesis method to generate computer models of isotropic fractal surfaces using the methodology of Bendat & Piersol (1971). Thompson & Brown (1991) modified the methods of Peitgen & Saupe (1988) to account for anisotropy of the fracture surface aperture variability. Candela et al. (2009, 2012) used a Fourier-based method to simulate a matrix scaling random Gaussian field on a two-dimensional grid, where an anisotropy matrix was introduced when calculating the two-dimensional Gaussian random field. The eigenvalues of the matrix corresponded to the inverse of the two aperture variability exponents in the parallel and perpendicular direction relative to slip.

Méheust & Schmittbuhl (2001) used random seeding, and Fast Fourier Transforms to generate isotropic fractures with a self-affine aperture field. This method was adopted by Fox et al. (2015) and modified for circular fractures.

According to Tsang et al. (1988), Tsang & Tsang (1989), and Tsang & Neretnieks (1998), the aperture of a typical rock fracture can be statistically represented by a spatially

autocorrelated random field. The spatial autocorrelation characteristics are described by the variogram and correlation length λ . According to Guo et al. (2016), the semivariance curves of the spherical, exponential, and Gaussian variogram models do not significantly differ from each other when the correlation length is the same or when they are fitted to the same set of geostatistical data. Thus in their study, they used the spherical variogram model, which was assumed to be spatially isotropic on the fracture, with a nugget of zero. The algorithm to generate the heterogeneous aperture field was Principle Component Analysis (PCA), with the generated data following a lognormal distribution. The same procedure was used by Wu et al. (2021) to create heterogeneous fracture aperture distributions for heat and flow transport investigations.

Co (2017) used Sequential Gaussian Simulation to generate artificial aperture distributions. An exponential variogram model honoring the statistics of a lab-scale variogram model was used. Anisotropy in the aperture distribution was taken into consideration.

While all the methods described could provide representative fracture surface aperture variability for investigating heat and flow transport processes, in this study, the Sequential Gaussian Simulation was selected to have control on the correlation lengths and ensure input from an actual fracture surface was considered in generating the field-scale aperture distribution.

3.6 Generation of Field Scale Fractures Aperture variability with Geometric Anisotropy

To model the impact of fracture anisotropy on thermal performance at the field scale, synthetic fracture aperture maps had to be generated. This section describes the procedure used in generating field scale fracture apertures with spatial variations. The workflow is shown in Figure 3.4. The 75 mm x 50 mm lab-scale aperture distribution from Ishibashi et al. (2012) was the starting point to generate the field-scale aperture distribution. First, the maximum aperture for the field scale was determined using scaling correlations. Using the calculated maximum aperture, the aperture distribution was adjusted to match the maximum aperture for the field scale. A variogram model was also determined from the

lab-scale data. Subsequently, synthetic fracture aperture maps were generated using Sequential Gaussian Simulation (SGSIM). The main input data sets for the SGSIM runs were the adjusted aperture distribution and the aperture variogram model. Then the aperture distributions were checked to determine if their Hurst exponents were in the range found generally in nature. In this study, Hurst exponents used for selecting the aperture distribution were 0.6 ± 0.1 in the slip direction and 0.85 ± 0.1 in the direction perpendicular to slip. Once an aperture distribution met these criteria, its permeability was estimated for input into the thermohydraulic model. The details of each step of the workflow are described in the following sections.

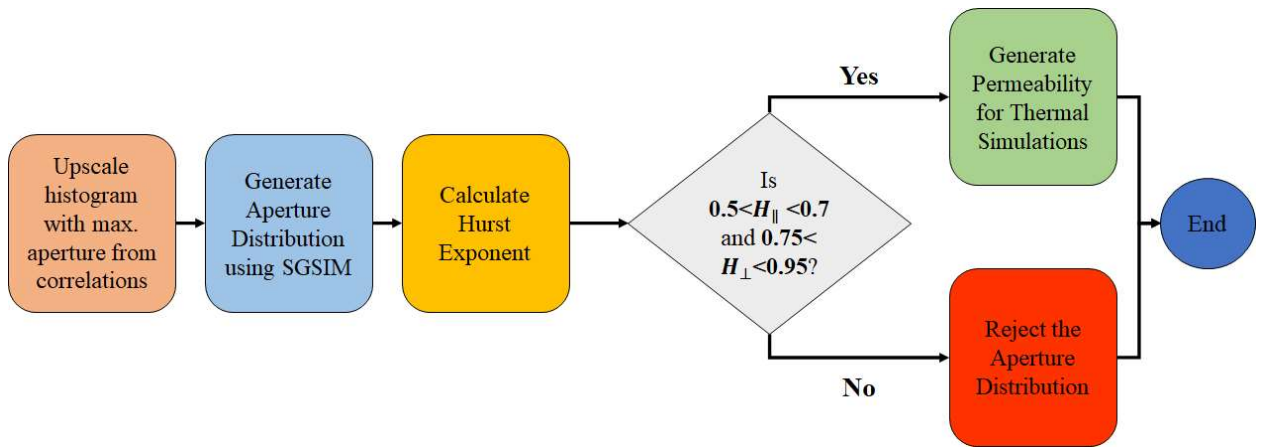


Figure 3.4: Workflow for field-scale fracture aperture distributions generation for thermohydraulic simulation.

3.6.1 Upscaling histogram

The first step in generating fracture aperture maps with spatial variations at the field scale was to adjust the aperture distribution of the lab-scale fracture. The adjustment was to ensure the aperture values represent the field scale. In literature, there are two main methods used to account for aperture to length scaling – the linear (Vermilye & Scholz, 1995; Scholz, 2010) and power law (Olson, 2003; Olson & Schultz, 2011) correlations. Co (2017) applied the two methods for upscaling the aperture distribution of the smaller length scale from the work by Ishibashi et al. (2012). The upscaled aperture distributions were compared with distributions of the medium and larger length scale from the study by Ishibashi et al. (2012). Co (2017) observed that the power-law correlation provided the

best overall fit, providing more consistent and accurate aperture distribution values for the medium and large-scale fractures. Thus, for this study, the power-law correlation with coefficients from Co (2017) was used.

According to Olson (2003), the maximum aperture to length can be described with a power-law equation of the form:

$$b_{max} = CL^e \quad (3.3)$$

where b_{max} is the aperture, L is total fracture length, C is the preexponential constant (with units of length^{1-e}), and e is the power-law scaling exponent.

Co (2017) found C to be 0.005 and e to be 0.005, thus leading to the power-law correlation used in this study as:

$$b_{max} = 0.005L^{0.005} \quad (3.4)$$

Once the maximum aperture distribution was determined, the aperture distribution was determined by a linear scaling of the Ishibashi et al. (2012) small length scale aperture distributions to match the maximum aperture distribution of the field length scale, where $L = 1000\text{m}$.

3.6.2 Sequential Gaussian Simulation in Stanford Geostatistical Modeling Software

Co (2017) demonstrated the suitability of Sequential Gaussian Simulation (SGSIM) for generating synthetic aperture distributions. For this study, the aperture distributions were represented statistically by a spatially autocorrelated random field, as this is common in literature (Tsang & Neretnieks, 1998). Thus, the method of Sequential Gaussian Simulation (SGSIM) within the Stanford Geostatistical Modeling Software (SGeMS) (Remy et al., 2009) was used to generate the aperture distributions. A complete discussion on the SGSIM method and variogram modeling can be found in Goovaerts (1997) and in Chapter 2 of this study. The spatial autocorrelation characteristics were described by the variogram model and the range (correlation length) λ of the apertures. The target histogram was the upscaled histogram of the lab-scale fracture aperture distribution from the work by Ishibashi et al. (2012). The distribution of the fracture aperture was lognormal.

A Gaussian variogram model was used for all the aperture distributions in this study. The variogram was taken to be spatially anisotropic on the fracture, with a nugget of zero.

According to Tsang & Tsang (1987) and Tsang et al. (1988), the ratio of correlation length λ to the characteristic flow length of a system L can lie between 0.05 and 0.40 for typical hydrological applications. The system is modeled with a characteristic flow length of 1000 m, translating to correlation lengths between 50 m to 400 m. Hence, in selecting the ranges to ensure anisotropy, it was essential to consider the limits of 50 m to 400 m. Because geometric anisotropy ratios were found to range from 1.5 to 4, different anisotropy ratios were also considered in selecting ranges to characterize the anisotropic aperture distribution. Table 3.1 summarizes the ranges, geometric anisotropy ratios, and the number of simulation cases used for this study. Figure 3.5 shows sample aperture distributions for the different geometric anisotropy ratios and ranges and provides indications for the perpendicular and parallel flow configurations. The shorter ranges (the range in the y-direction) were 50 m, 60 m, 75 m, and 100 m. The selected geometric anisotropy ratios were 1.5, 2, 3, and 4. A total of 110 cases of aperture distributions were generated.

3.6.3 Hurst Exponent Determination

Several methods are available to compute the Hurst exponent of a surface with spatial variations in aperture. These include the roughness-length method (Malinverno, 1990), the RMS correlation function, the Fourier power spectrum, and the wavelet power spectrum (Schmittbuhl et al., 1993, Candela et al., 2009), variograms (Develi & Babadagli, 2015), and maximum-minimum height difference (Heinze et al., 2021). Heinze et al. (2021) developed a fracture surface analysis toolbox in MATLAB that can determine the Hurst exponent and fractal dimensions of two-dimensional and three-dimensional surfaces with aperture variability. The method calculates the Hurst exponent and the fractal dimension based on the work by Schmittbuhl et al. (1993).

In the method by Schmittbuhl et al. (1993), a profile of length L is split into bands, with a bandwidth, db , that changes with each iteration. The mean value amplitude difference between the highest peak and the lowest valley (maximum-minimum height

difference, MM) is determined for each bandwidth. As the bandwidth increases, this value (MM) also decreases. The maximum-minimum height difference follows a power law with the bandwidth, db, and an amplitude parameter, A [1/m], through the following equation:

$$MM = A * db^H \quad (3.5)$$

A linear trend can be distinguished in a log-log plot over a bandwidth range. The slope of this line in the log-log plot is the Hurst exponent, which is related to the fractal dimension D by $D = E - H$ according to Equation 3.2.

Table 3.1: Number of simulation cases for different ranges and geometric anisotropy ratios (GR)

	GR=1.5		GR=2		GR=3		GR=4	
Range in y-direction (m)	Range in x-direction (m)	# of cases	Range in x-direction (m)	# of cases	Range in x-direction (m)	# of cases	Range in x-direction (m)	# of cases
50	75	7	100	16	150	6	200	2
60	90	9	120	14	180	8	240	4
75	112.5	13	150	14	225	4	300	2
100	150	5	200	3	300	2	400	1
	TOTAL	34	TOTAL	47	TOTAL	20	TOTAL	9

3.6.4 Estimating Permeability

Local aperture can be defined as the point-wise variation in aperture along a fracture (Oron & Berkowitz, 1998). The local cubic law model is a variant of the cubic law model applied to local apertures and has been used widely to characterize the fracture's hydraulic aperture and, in some cases, the permeability (e.g., Tsang (1984); Brown (1987); Tsang & Tsang (1989); Huo & Benson (2014)). The fracture is modeled as a two-dimensional, variable-aperture medium having local parallel-plate segments, with negligible fracture surface undulation in the third dimension. The fracture plane is subdivided into equal-sized grid blocks. The cubic law is assumed to apply locally, and each grid block is assigned a permeability based on the local fracture aperture value. In flow simulations, the internode transmissivities are calculated from the harmonic mean of the apertures

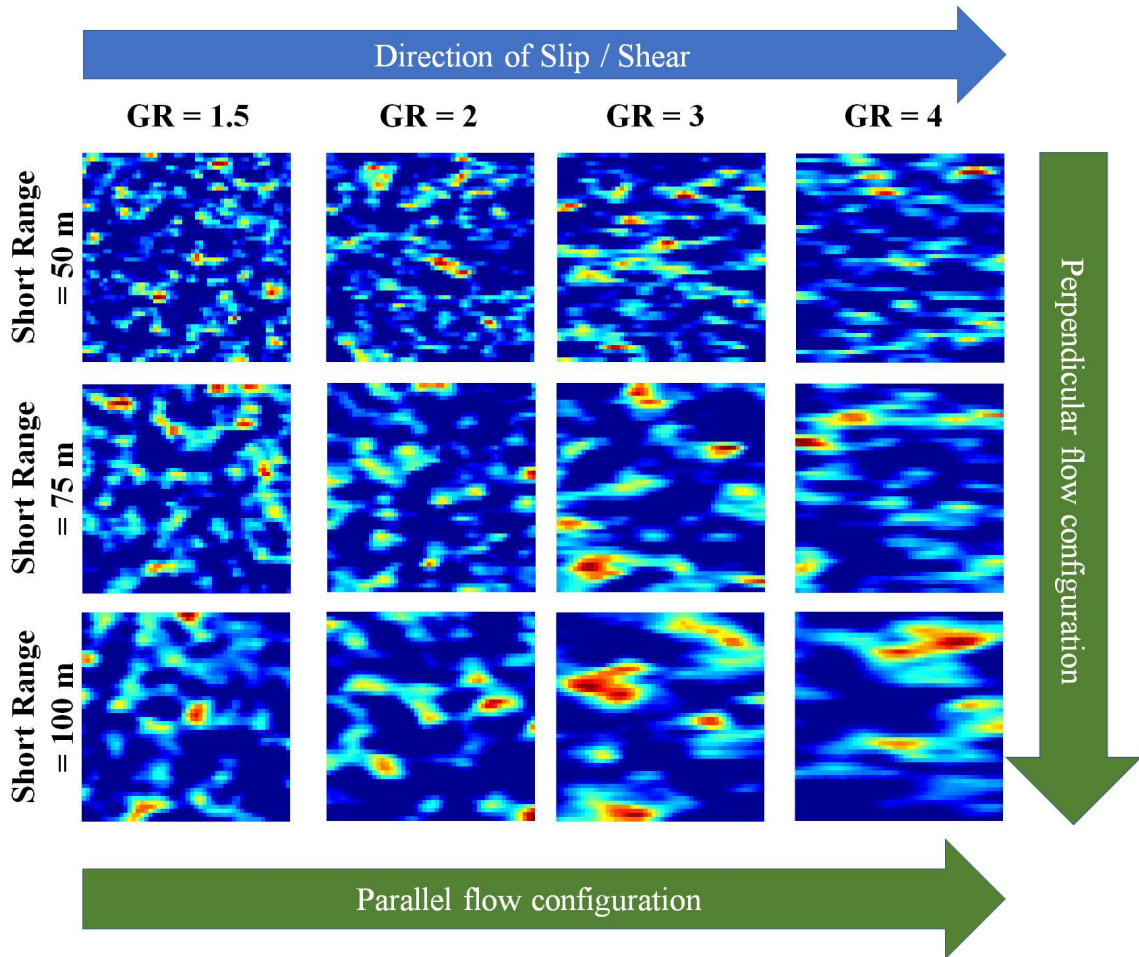


Figure 3.5: Sample aperture distributions for the different geometric anisotropy ratios and ranges, with indications for the perpendicular and parallel flow configurations relative to the direction of slip/shear.

To model the fracture's spatial heterogeneity, the fracture was treated as a porous medium with the porosity set as 0.99. At the same time, the heterogeneous permeability is defined by the local cubic law for a fracture with spatial variations (Oron & Berkowitz, 1998), which is represented by Equation 3.6.

$$k_{f_{ij}} = \frac{b_{ij}^2}{12} \quad (3.6)$$

where k_f , i , j , and b are the effective permeability, grid number in the x-direction, grid number in the y-direction, and local fracture aperture, respectively.

3.6.5 Thermohydraulic Model

The governing equations and assumptions used in the thermohydraulic model were described in Chapter 2. In Chapter 2, the dimensions were for a lab-scale system. In this part of the study, the model's dimensions are field scale.

The system modeled was to simulate a typical granitic reservoir with a fracture measuring 1000 m x 1000 m in the horizontal plane of the impermeable rock. One horizontal injection well and one horizontal production well were placed at the fracture edges for each flow direction. The numerical model consists of a 50 by 50 by 45 grid. In the horizontal x and y directions, the individual cells are of a uniform length of 20 m. In contrast, in the vertical z direction, the thicknesses are very fine around the fracture and become coarse away from the fracture. The height of the reservoir within the simulation domain is 190 m. Figure 3.6 shows a snapshot of the reservoir simulation domain.

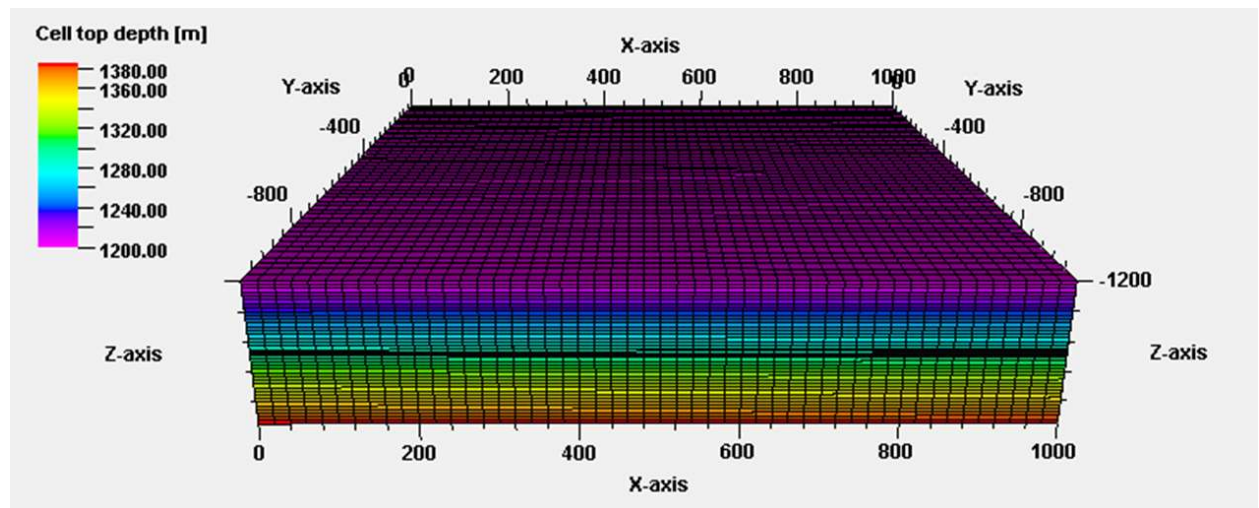


Figure 3.6: The field-scale three-dimensional model showing the grids. The Y and Z axes read negative with increasing values from the reference (zero in this case).

The initial rock temperature was 200 °C, while the injection water temperature was 40 °C. The injected fluid flow rate was 25 kg/s. The duration of the simulation was seven years. The injection pressure was 150 bar, and the producer bottom hole pressure was allowed to vary. However, the pressure constraints were set to ensure the fluid

remained as a single-phase liquid throughout the simulation. Other rock and fluid properties used in the model are presented in Table 3.2.

Table 3.2: Rock and fluid properties, and other parameters used in the model

Symbol	Description	Value	Units
φ	Porosity of the formation	0.01	-
k	Permeability of the formation matrix	$9.87 * 10^{-21}$	m ²
K_r	Thermal conductivity of rock	2.8	W/m/K
C_r	Specific heat capacity of rock	1000	J/kg/K
ρ_r	Density of the rock	2600	kg/m ³
μ	Dynamic fluid viscosity	0.0001303	Pa*s
P	Reference pressure for fluid viscosity	101.325	kPa
T	Reference temperature for fluid viscosity	200	°C
C_w	Specific heat capacity of fluid	4200	J/kg/K
ρ_{ST}	Reference fluid density	1000	kg/m ³
P_{ref}	Reference pressure for fluid density	101.325	kPa
T_{ref}	Reference temperature for fluid density	15.6	°C
C	Fluid compressibility	$5.00 * 10^{-10}$	Pa ⁻¹

3.7 Results and Discussion

This section presents the results from the thermohydraulic simulation on the field scale artificially generated fractures. First, an analysis was done, consolidating all the simulation results together. Subsequently, an analysis was done by geometric anisotropy ratio.

3.7.1 All Simulations Difference

The thermohydraulic model was run with the fracture characterized by the 110 artificially generated fracture aperture distributions. Figure 3.7 is a plot of the difference in thermal drawdown between the perpendicular flow direction and the parallel flow direction for all

110 simulations. All plots above zero indicate that the temperature measured at the extraction end of the fracture was higher in the perpendicular direction than in the parallel direction. Similarly, all plots below zero indicate that the temperature measured at the extraction end of the fracture was higher for the parallel flow configuration resulting in lower thermal drawdown in that flow configuration.

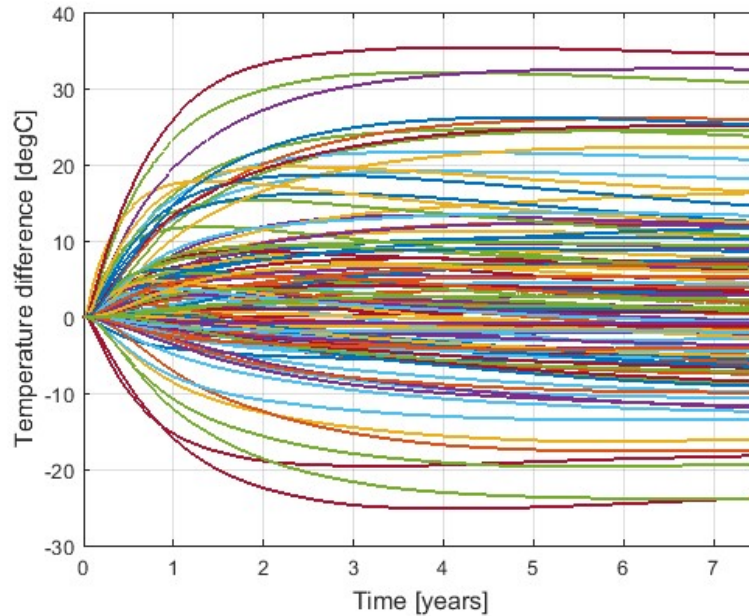


Figure 3.7: Temperature difference between the perpendicular and parallel flow directions for the 111 artificially generated field-scale fracture aperture distributions. The difference is temperature profile in the perpendicular direction minus temperature profile in the parallel direction.

A histogram of the temperature differences at one year and five years into the simulation was plotted, as shown in Figures 3.8 and 3.9. The data in Figure 3.8 indicates that most of the temperature differences are above 0, as the data are skewed to the right, and the temperature difference values with the highest frequency lie between 0 °C and 5 °C. By five years, the temperature difference values with the highest frequency are between 0 °C and -5 °C, indicating that more heat is extracted in the parallel direction for a few of the simulation cases after some time (Figure 3.9).

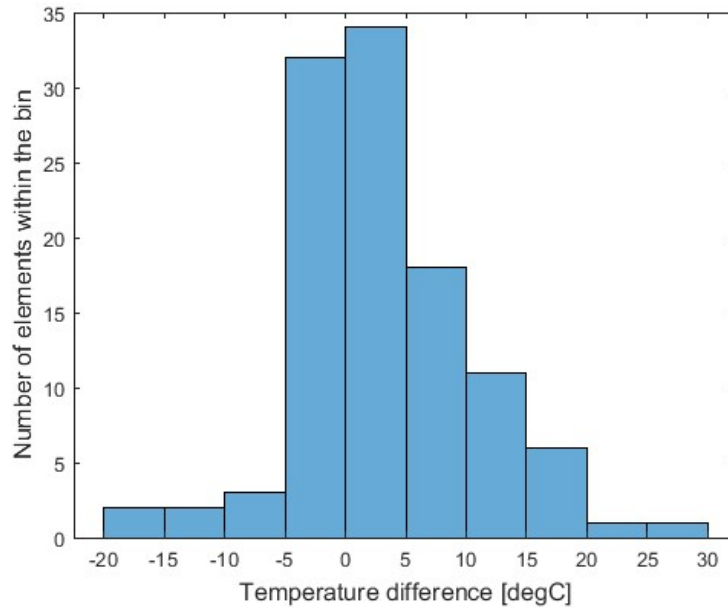


Figure 3.8: Histogram of the temperature difference between the perpendicular and parallel flow directions for the field-scale artificially generated fracture aperture distributions at one year.

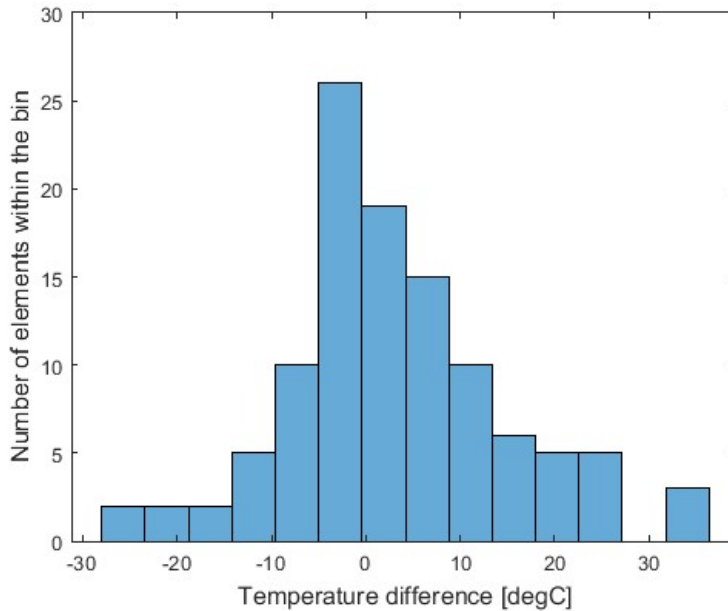


Figure 3.9: Histogram of the temperature difference between the perpendicular and parallel flow directions for the field-scale artificially generated fracture aperture distributions at five years.

To quantify the percentage of the artificially generated fracture aperture distributions that resulted in the perpendicular flow configuration with lower thermal drawdown than the parallel flow configuration, the data was sorted, and a count was

performed. Figure 3.10 shows the sorted data one year into the simulation, while Figure 3.11 shows the sorted data five years into the simulation. At one year of simulation, the percentage of fracture aperture distributions that resulted in the perpendicular flow configuration having lower thermal drawdown (and higher temperature at the extraction end of the fracture) was about 64.5 %. This percentage was calculated based on the data in Figure 3.10. The number of cases below the 0 line is 39; hence the percentage was calculated as $\frac{110-3}{110} \times 100$. The value was about 56.3 % (deduced from Figure 3.11) five years into the simulation. These results indicate that there might be differences in which flow configuration is better at different times in the life of an Enhanced Geothermal System.

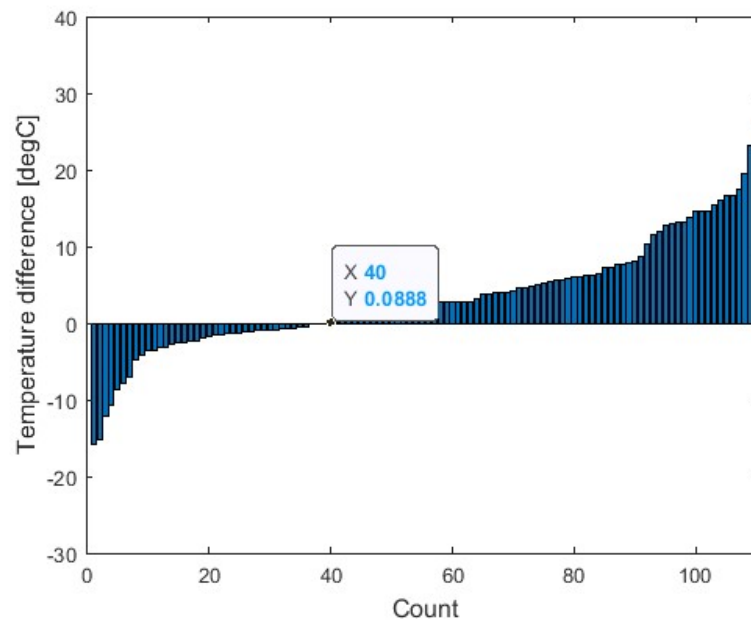


Figure 3.10: Temperature difference between the perpendicular and parallel flow directions for the field scale artificially generated fracture aperture distributions at one year into the simulation. The difference is temperature profile in the perpendicular direction minus temperature profile in the parallel direction.

Another deduction that can be made from Figures 3.7 to 3.11 is that the temperature difference in favor of the perpendicular flow configuration is, on average, higher than the temperature difference in favor of the parallel flow configuration. To understand the characteristics of the aperture distributions that contribute to the high

temperature difference for each flow configuration, further analysis was carried out for each geometric anisotropy ratio. For each geometric anisotropy ratio, the flow map and the temperature map were presented for selected cases: one with a significant temperature difference in favor of the perpendicular flow configuration and another with a temperature difference in favor of the parallel flow configuration. The percentage of flow contact surface areas was computed for the selected aperture distributions.

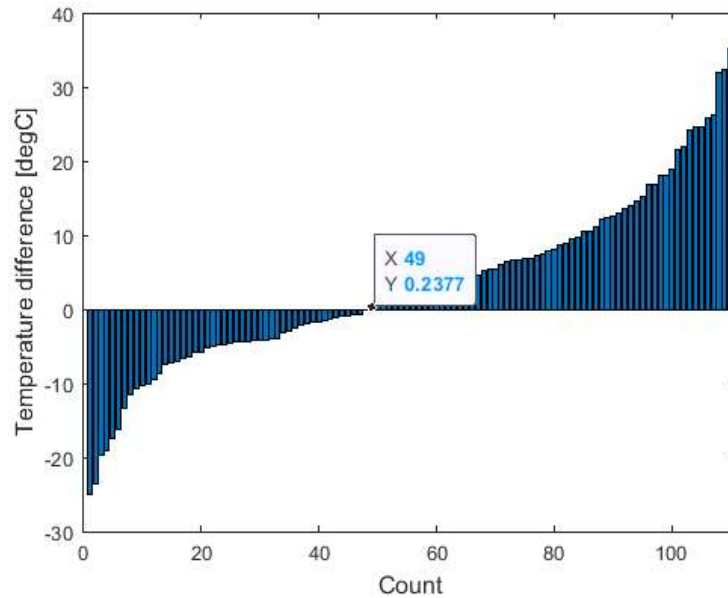


Figure 3.11: Temperature difference between the perpendicular and parallel flow directions for the 111 artificially generated fracture aperture distributions five years into the simulation. The difference is temperature profile in the perpendicular direction minus temperature profile in the parallel direction.

3.7.2 Geometric Anisotropy Ratio of 1.5

For the y-direction range values of 50 m, 60 m, 75 m, and 100 m, the geometric anisotropy ratio of 1.5 imply an x-direction range of 75 m, 90 m, 112.5 m, and 150 m.

Figure 3.12 shows the temperature difference between the perpendicular and parallel flow directions for the different ranges in the y-direction for the geometric anisotropic ratio of 1.5. There is no evident preferred flow configuration from the figures except for the aperture distributions with a short range of 100 m and a long range of 150 m, where most of the curves are above the zero line. Figure 3.13 shows the sorted count of the temperature difference between the perpendicular and parallel flow directions for

the different cases with geometric anisotropic ratio of 1.5 taken at one year into the simulation. This geometric anisotropy ratio had a total of 34 aperture distributions. For this geometric anisotropy ratio, about 58.8% of the aperture distributions favored the perpendicular flow configuration (Figure 3.13).

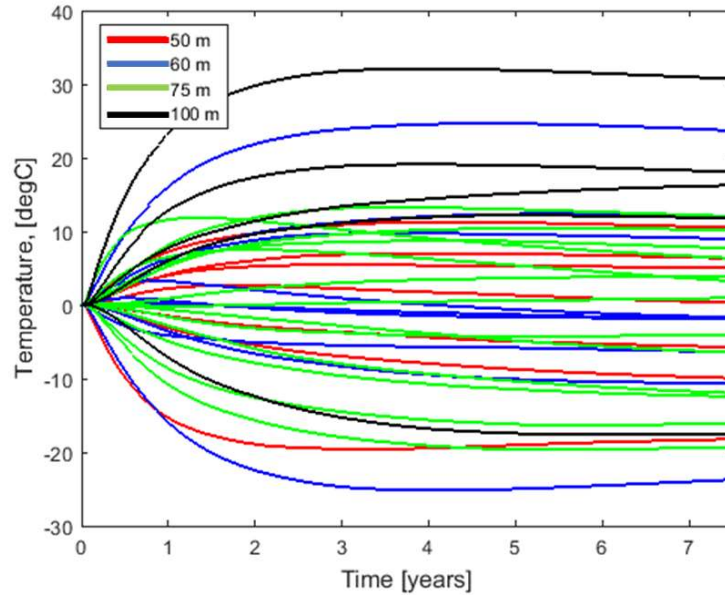


Figure 3.12: Temperature difference between the perpendicular and parallel flow directions for the different cases with geometric anisotropic ratio of 1.5. The difference is temperature profile in the perpendicular direction minus temperature profile in the parallel direction.

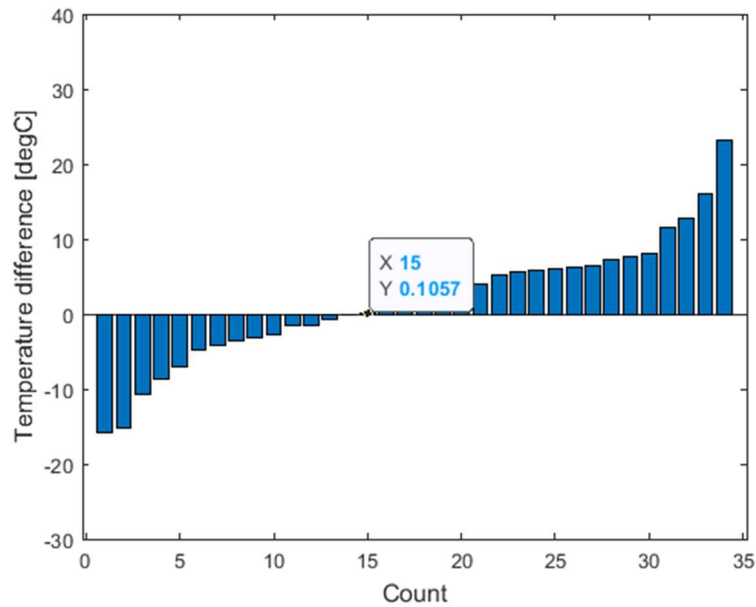


Figure 3.13: Temperature difference between the perpendicular and parallel flow directions for the different cases with geometric anisotropic ratio of 1.5. The difference is temperature profile in the perpendicular direction minus temperature profile in the parallel direction.

From Chapter 2, it was seen that the thermal drawdown was related to the fracture surface area contacted by fluid. In the field-scale cases shown here, the criterion for defining the flow wetted surface was to select the areas of the grids that had more than 10 m³/d of fluid flow. The filter was set within Petrel, the post-processing software, as shown in Figure 3.14.

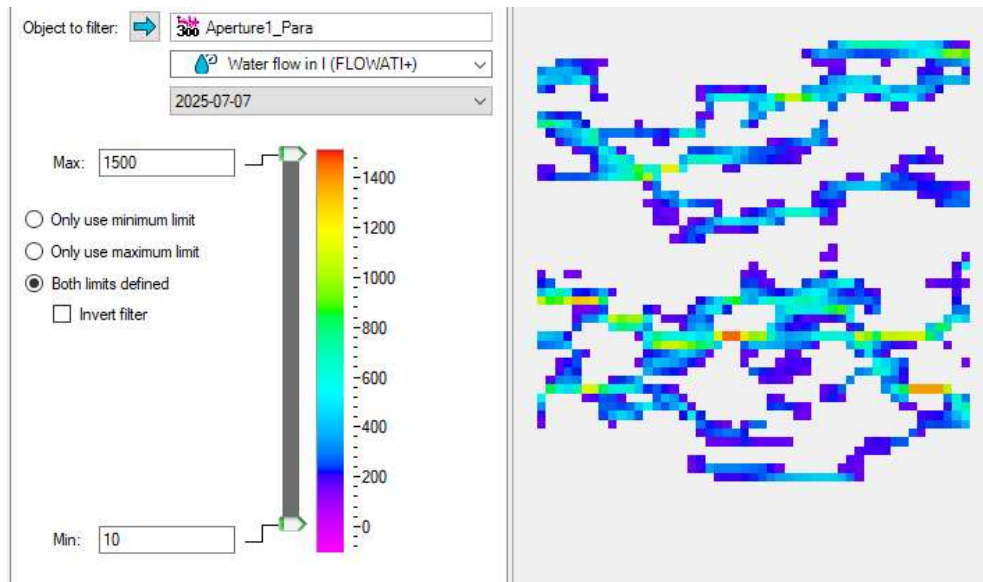


Figure 3.14: Setting the filter to determine the fracture surface area contacted by the flowing fluid.

The first aperture distribution selected for further analysis had a temperature difference of -15.3 °C between the perpendicular flow configuration and the parallel flow configuration. Subsequently, it will be referred to as Aperture 1. The range in the y-direction was 50 m, while the range in the x-direction was 75 m. Recall from Figure 3.5 that the aperture distributions with a geometric anisotropy ratio of 1.5 tend to be more distributed and appear isotropic. Figure 3.15 shows the flow maps and temperature maps for the parallel and perpendicular flow configurations of Aperture 1. Though both flows are channelized, the parallel flow configuration has more fluid flow paths (Figure 3.15a). On the other hand, the perpendicular flow configuration has few fluid flow paths with

relatively high flowrate within one preferential flow path (Figure 3.15b). The estimated flow wetted surface was 26.48% for the parallel flow configuration and 19.96% for the perpendicular flow direction. The parallel flow configuration appears to have a better thermal sweep than the perpendicular flow configuration (Figures 3.15 c and d). The higher flow wetted surface area in the parallel configuration is assumed to be a solid contributing factor to its better thermal sweep.

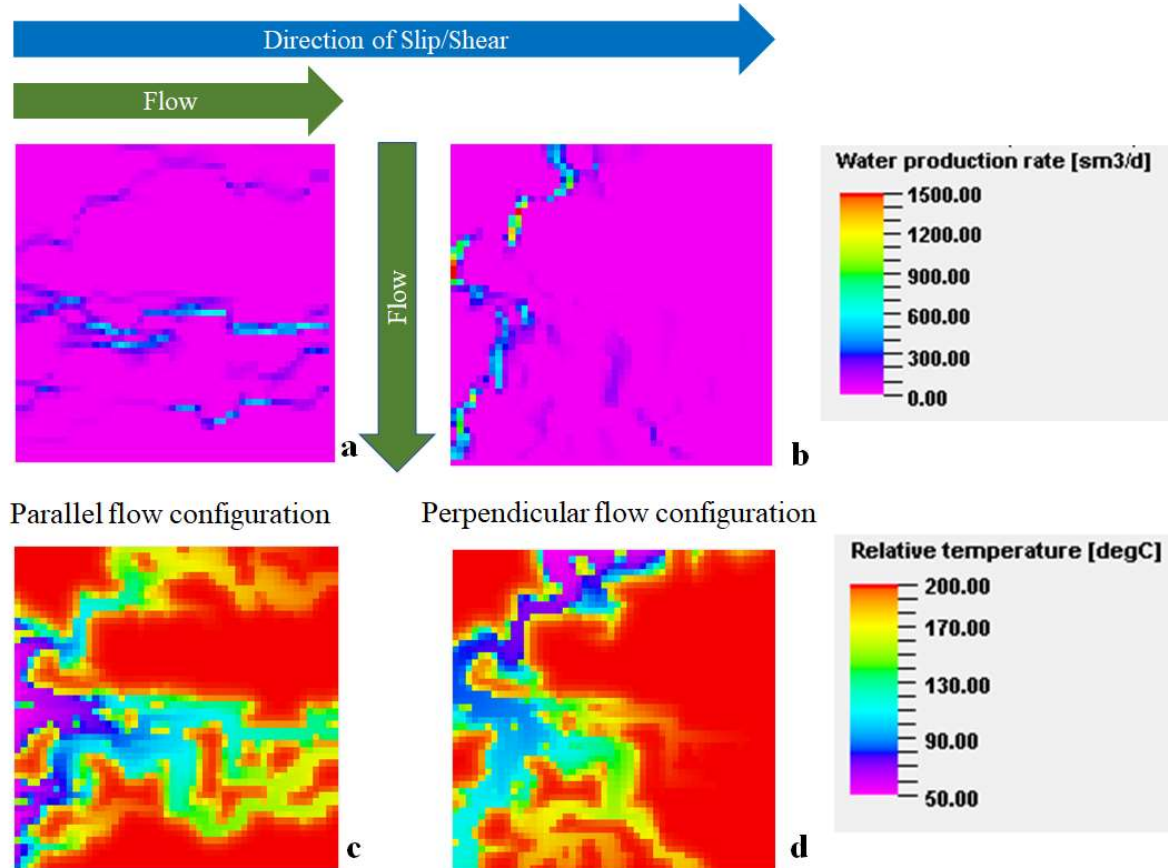


Figure 3.15: Fluid flow and heat transport on the fracture aperture after one year for Aperture 1.

Figure 3.16 shows the flow maps and temperature maps for the parallel and perpendicular flow configurations of Aperture 2, the second aperture distribution selected for further analysis. The range in the y-direction was 100 m, while the range in the x-direction was 150 m. This aperture distribution resulted in a 23.5 °C difference in temperature in favor of the perpendicular flow configuration than the parallel flow configuration. From the flow map of Figure 3.16, flow is seen to follow a straight path in the parallel flow configuration (Figure 3.16a). In contrast, flow is seen to follow a tortuous

path in the perpendicular flow configuration (Figure 3.16b). As a result, less area is contacted in the parallel flow configuration (21.5% flow wetted surface) than in the perpendicular flow configuration (29.1% flow wetted surface). From the temperature map, the unswept areas close to the initial reservoir temperature are more prominent in the parallel flow configuration (Figure 3.16c) than the perpendicular flow configuration, contributing to why more heat is extracted in the perpendicular flow configuration.

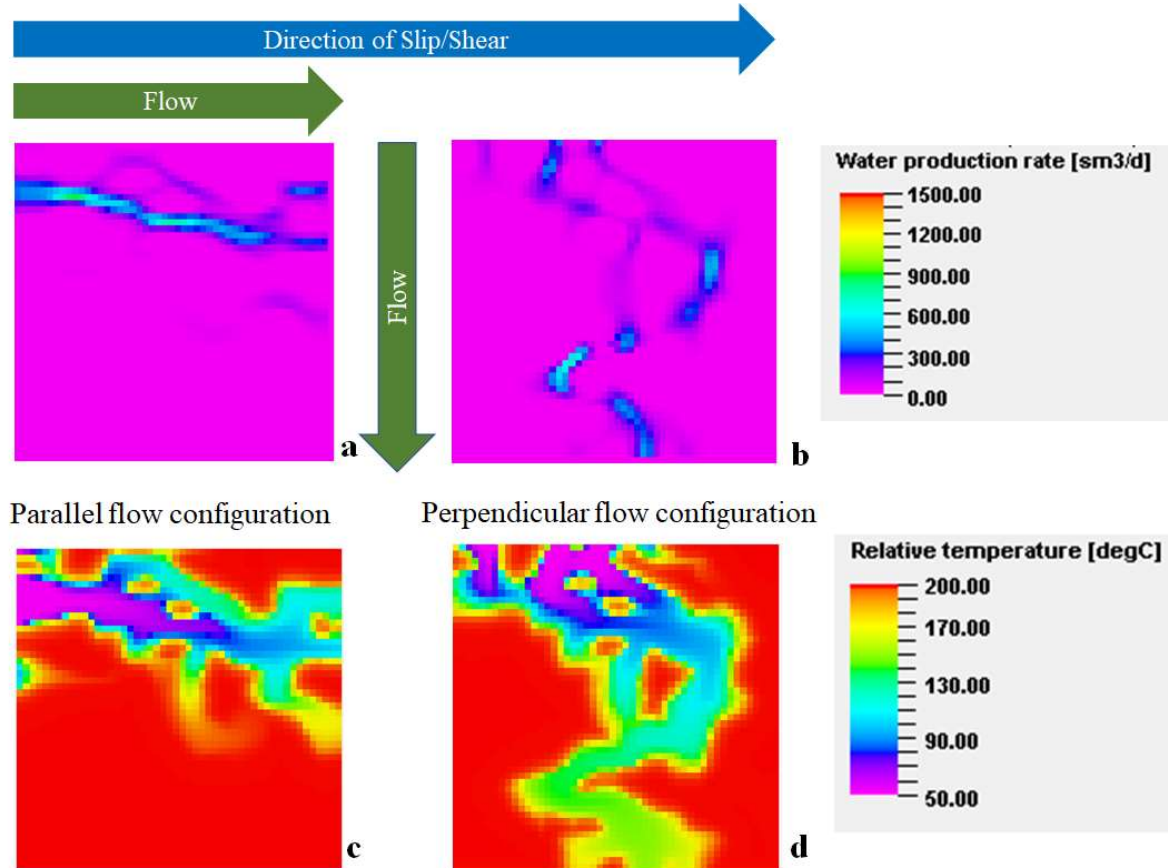


Figure 3.16: Fluid flow and heat transport on the fracture aperture after one year for Aperture 2.

3.7.3 Geometric Anisotropy Ratio of 2

For the geometric anisotropy ratio of 2, the y-direction range values of 50 m, 60 m, 75 m, and 100 m correspond to the x-direction range of 100 m, 120 m, 150 m, and 200 m. On analyzing the temperature difference between the perpendicular and parallel flow directions for the different ranges in the y-direction for this geometric anisotropic ratio, there was no evident preferred flow configuration from the plots (Figure 3.17). For the y-

direction range of 100 m, there was little difference in temperature between the perpendicular flow configuration and the parallel flow configuration. Figure 3.18 shows the sorted count of the temperature difference between the perpendicular and parallel flow directions for the different cases with geometric anisotropic ratio of 2 taken at one year into the simulation. This geometric anisotropy ratio had a total of 47 aperture distributions. For this geometric anisotropy ratio, about 70.2% of the aperture distributions favored the perpendicular flow configuration (Figure 3.18).

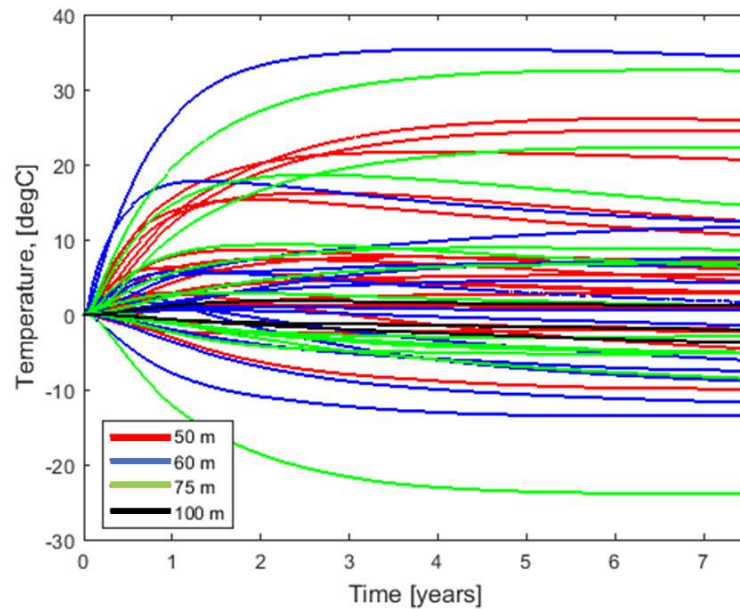


Figure 3.17: Temperature difference between the perpendicular and parallel flow directions for the different cases with geometric anisotropic ratio of 2. The difference is temperature profile in the perpendicular direction minus temperature profile in the parallel direction.

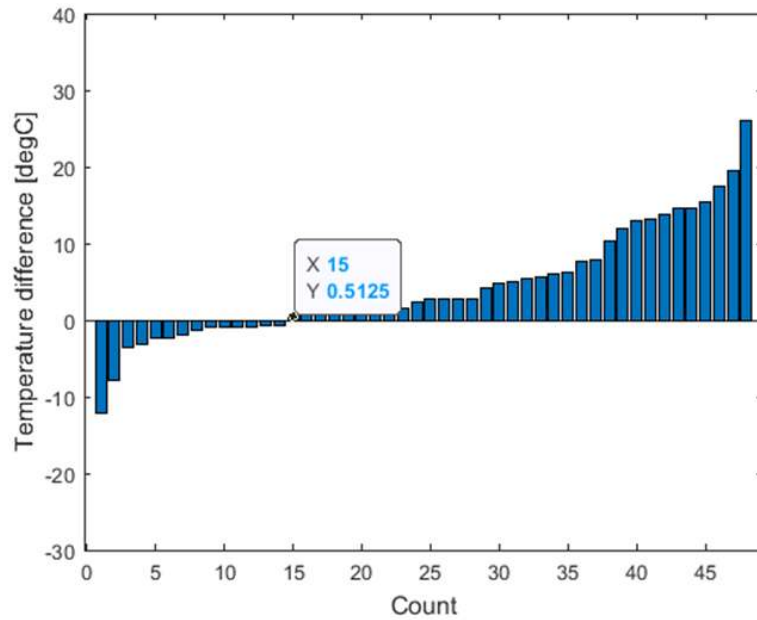


Figure 3.18: Temperature difference between the perpendicular and parallel flow directions for the different cases with geometric anisotropic ratio of 2. The difference is temperature profile in the perpendicular direction minus temperature profile in the parallel direction.

Recall from Figure 3.3 that the geometric anisotropy ratio of actual fractures was between 2 to 3. Thus, real fractures may have a 70% chance of having better thermal performance in the perpendicular flow configuration compared to the parallel flow configuration.

Similar to the procedure for a geometric anisotropy ratio of 1.5, two aperture distributions were selected for further analysis. The first had a temperature difference of -7.8 °C between the perpendicular flow configuration and the parallel flow configuration one year into the simulation. Henceforth, it will be referred to as Aperture 3. The second had a temperature difference of 26.2 °C between the perpendicular flow configuration and the parallel flow configuration one year into the simulation. From now, it will be referred to as Aperture 4. Both aperture distributions had the highest and lowest differences between the temperatures in the perpendicular and parallel flow configurations. Coincidentally, both had the y-direction range being 60 m, while the range in the x-direction was 120 m.

Figure 3.19 shows the flow maps and temperature maps for the parallel and perpendicular flow configurations of Aperture 3. From Figure 3.19a, the flow in the parallel direction seems to flow along several striations on the fracture. However, the perpendicular flow configuration (Figure 3.19b) has flow predominantly in one preferential path and fewer fluid flow paths than the parallel flow direction. The estimated flow wetted surface was 34.4% for the parallel flow configuration and 29.4% for the perpendicular flow direction. Figures 3.19c and 3.19d show the temperature maps for the two flow configurations of Aperture 3. There is evidence of thermal sweep in near-parallel paths across the fracture plane in the parallel flow configuration (Figure 3.19c). Several fluid flow paths in the parallel flow configuration allow for more heat extraction from the system than the perpendicular flow configuration, where the channelized flow is limited to one dominant flow path and few alternative fluid flow paths. Thus, the presence of interconnected flow paths leading to more flow wetted surface area contributed to making the parallel flow configuration yield higher temperatures measured at the producer than the perpendicular flow configuration.

The results for the aperture distribution with the highest difference in temperatures at one year into the simulation between perpendicular and flow configuration are presented in Figure 3.20. The aperture distribution is referred to as Aperture 4 hereafter. In both flow configurations, the flow was highly channelized within preferential paths (Figures 3.20a and 3.20b), leading to large areas of low heat extraction (Figures 3.20c and 3.20d).

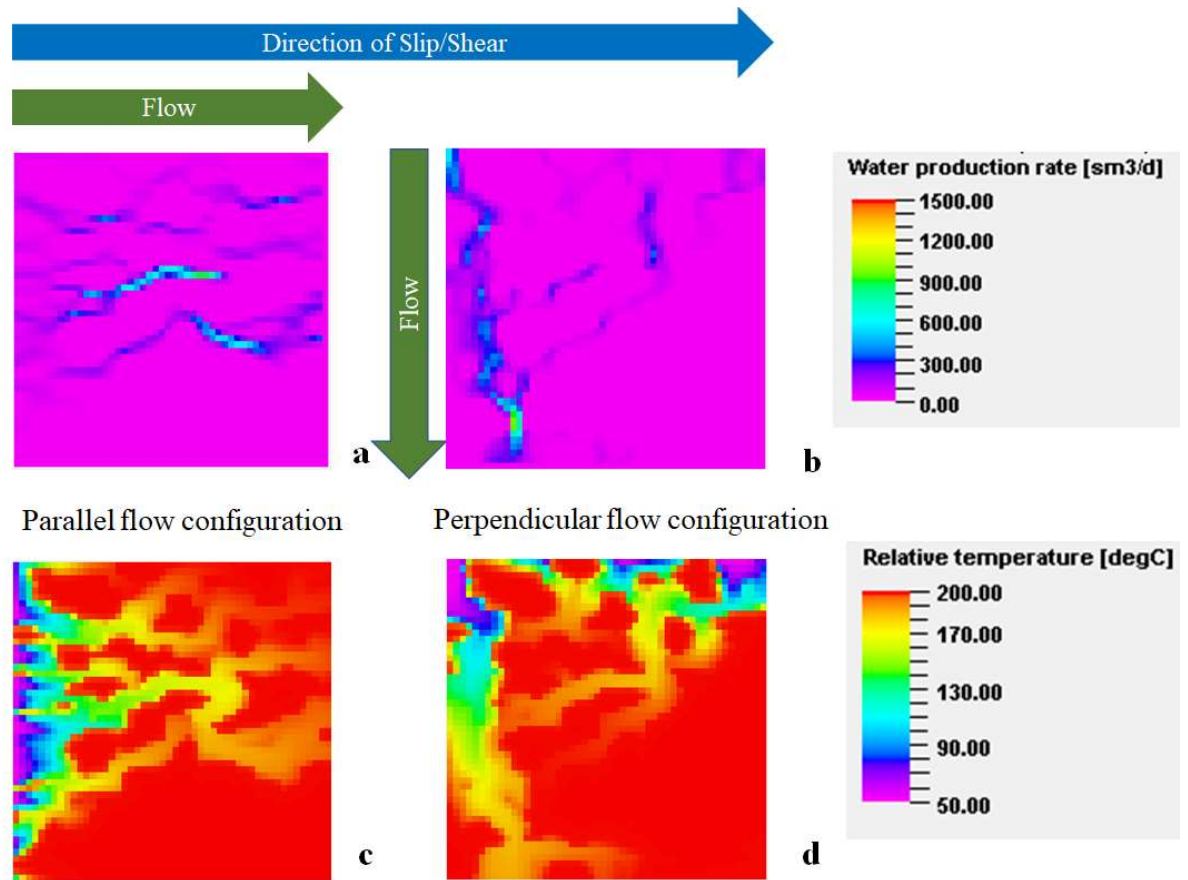


Figure 3.19: Fluid flow and heat transport on the fracture aperture after one year for Aperture 3.

The two flow configurations had low estimated values of percentage area contacted by fluid, with 13.6% in the parallel flow configuration and 20.2% in the perpendicular flow direction. However, with the perpendicular flow configuration, the fluid was able to move through tortuous flow paths enabling more contact with the fracture surface than the parallel flow configuration.

It was of interest to know why Aperture 4 led to highly channelized flow. Figure 3.21 shows the aperture distribution for Aperture 4 across the fracture plane with indications for perpendicular flow configuration and parallel flow configuration relative to the direction of slip/shear. The bottom part of the aperture distribution has areas of non zero aperture that are not connected. The apertures at the top part of the aperture distribution were connected, hence the channelized flow and heat transfer seen in Figure 3.20.

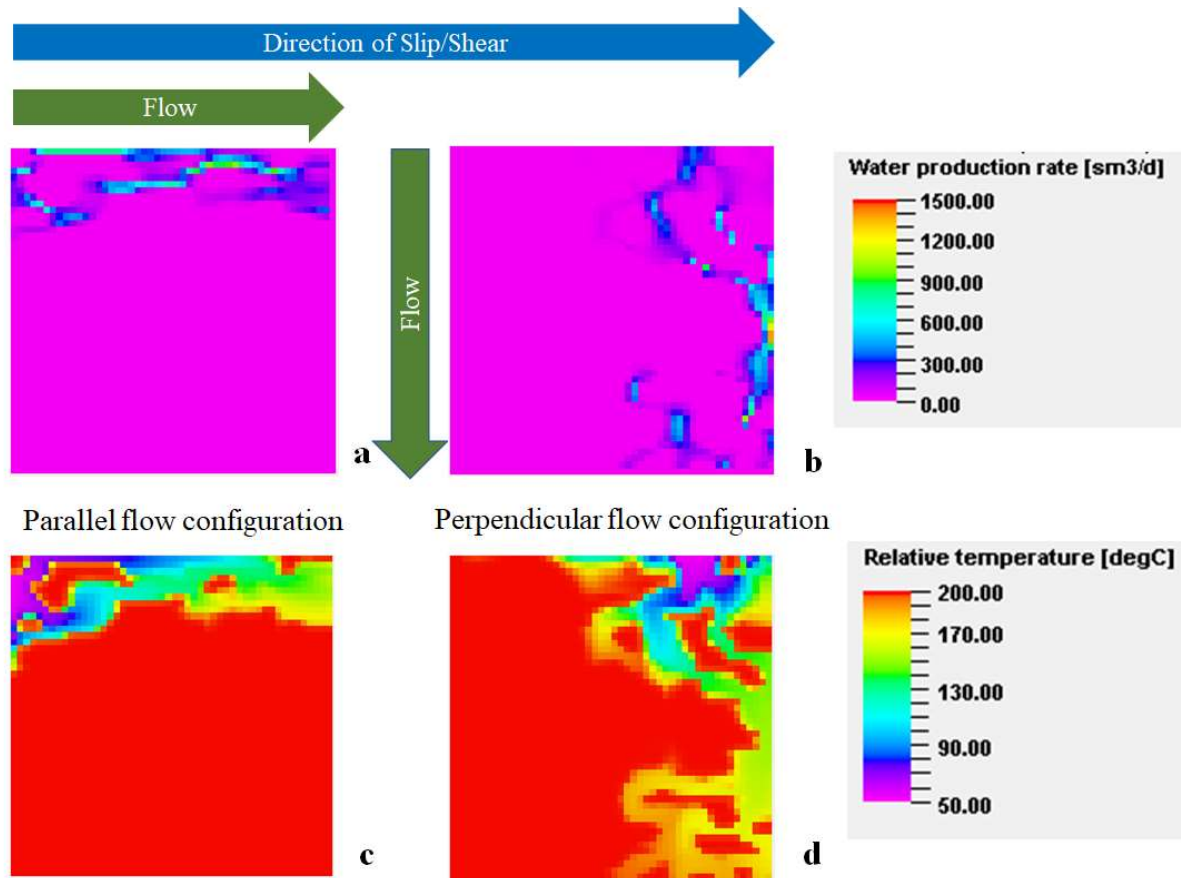


Figure 3.20: Fluid flow and heat transport on the fracture aperture after one year for Aperture 4.

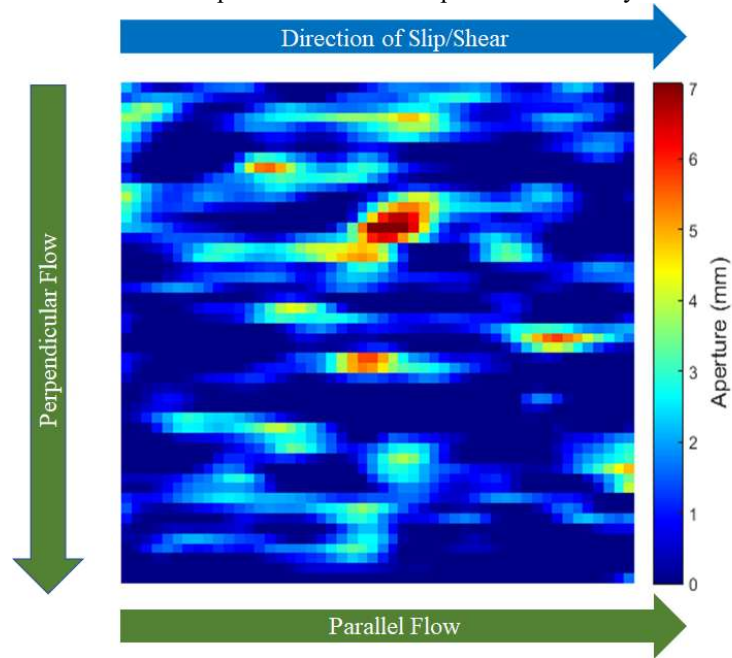


Figure 3.21: Fracture aperture distribution for Aperture 4.

3.7.4 Geometric Anisotropy Ratio of 3

The geometric anisotropy ratio of 3 implies an x-direction range of 150 m, 180 m, 225 m, and 300 m for the y-direction range values of 50 m, 60 m, 75 m, and 100 m.

Figure 3.22 is a display of the temperature difference between the perpendicular and parallel flow directions for the different ranges in the y-direction for the geometric anisotropic ratio of 3. Something striking about the plot is that most of the curves in favor of the perpendicular flow configuration result in a much higher temperature difference than the curves in favor of the parallel flow configuration. This high temperature difference in favor of the perpendicular flow direction is also seen in Figure 3.23, which shows the sorted count of the temperature difference between the perpendicular and parallel flow directions for the different cases with geometric anisotropic ratio of 3 taken at one year into the simulation. A total of 20 aperture distributions were studied for this geometric anisotropy ratio, for which about 60% of the aperture distributions favored the perpendicular flow configuration (Figure 3.23).

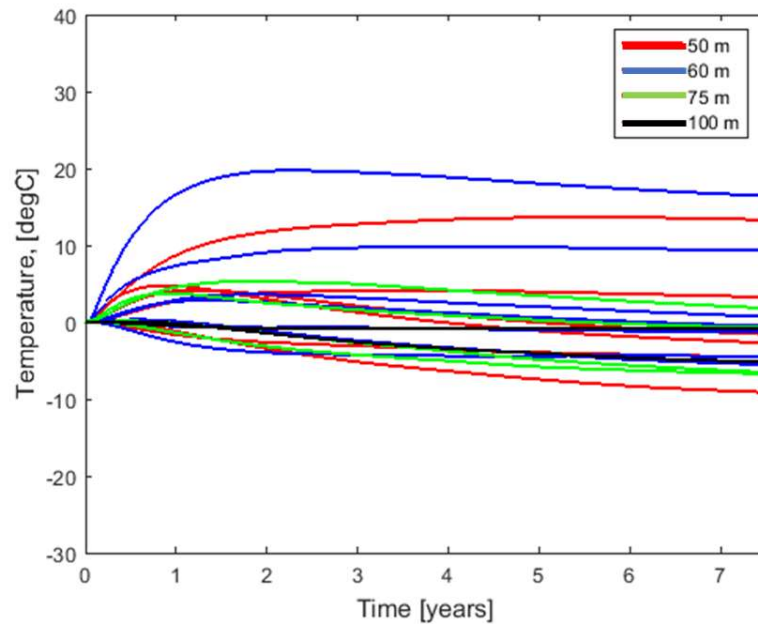


Figure 3.22: Temperature difference between the perpendicular and parallel flow directions for the different cases with geometric anisotropic ratio of 1.5. The difference is temperature profile in the perpendicular direction minus temperature profile in the parallel direction.

The fifth aperture distribution selected for further analysis had a temperature difference of $-2.6\text{ }^{\circ}\text{C}$ between the perpendicular flow configuration and the parallel flow configuration. In contrast, the sixth aperture distribution selected had a temperature difference of $16.5\text{ }^{\circ}\text{C}$. The aperture distributions will hereafter be referred to as Aperture 5 and Aperture 6, respectively. Their range in the y-direction was 60 m, while their range in the x-direction was 180 m. The aperture distributions with a geometric anisotropy ratio of 3, like those with a geometric anisotropy ratio of 4, have long striations in the parallel flow direction compared to their counterparts with geometric anisotropy ratios of 1.5 and 2 (Figure 3.5).

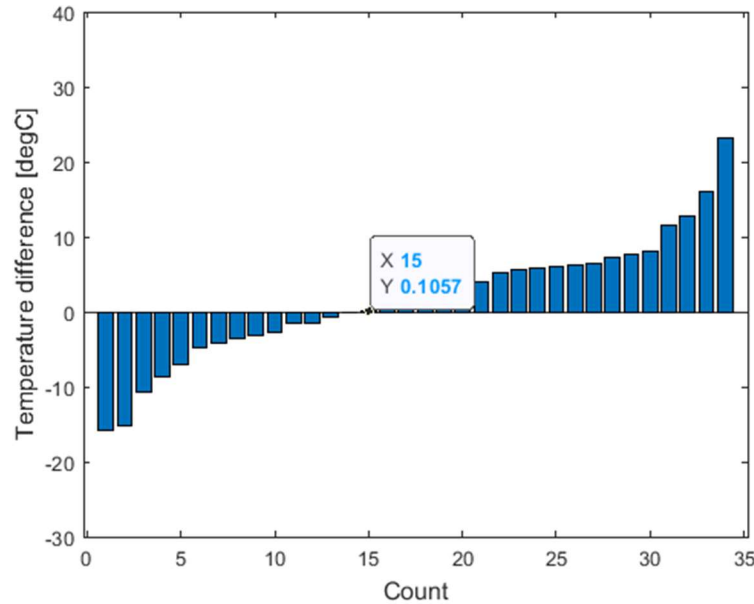


Figure 3.23: Temperature difference between the perpendicular and parallel flow directions for the different cases with geometric anisotropic ratio of 3. The difference is temperature profile in the perpendicular direction minus temperature profile in the parallel direction.

Figure 3:24 shows the flow maps and temperature maps for the parallel and perpendicular flow configurations of Aperture 5. Both flow configurations depict channelized flow. Figures 3.24a and 3.24b show that there is not much difference between the areas with dominant flow paths, which is confirmed by the estimate of 27.1% flow wetted surface area for the parallel flow configuration and 25.8% for the perpendicular flow direction. The difference in temperatures between the flow configurations was $2.6\text{ }^{\circ}\text{C}$ in favor of the parallel flow configurations, while the difference in the surface area

contacted by the fluid is 1.3%. Though estimates from the parallel flow configuration suggest that configuration to have a better thermal performance than the perpendicular flow configuration, the difference is not significant. Figures 3.24c and 3.24d, though they have different flow paths, do not significantly differ between the thermal sweep of the two flow configurations.

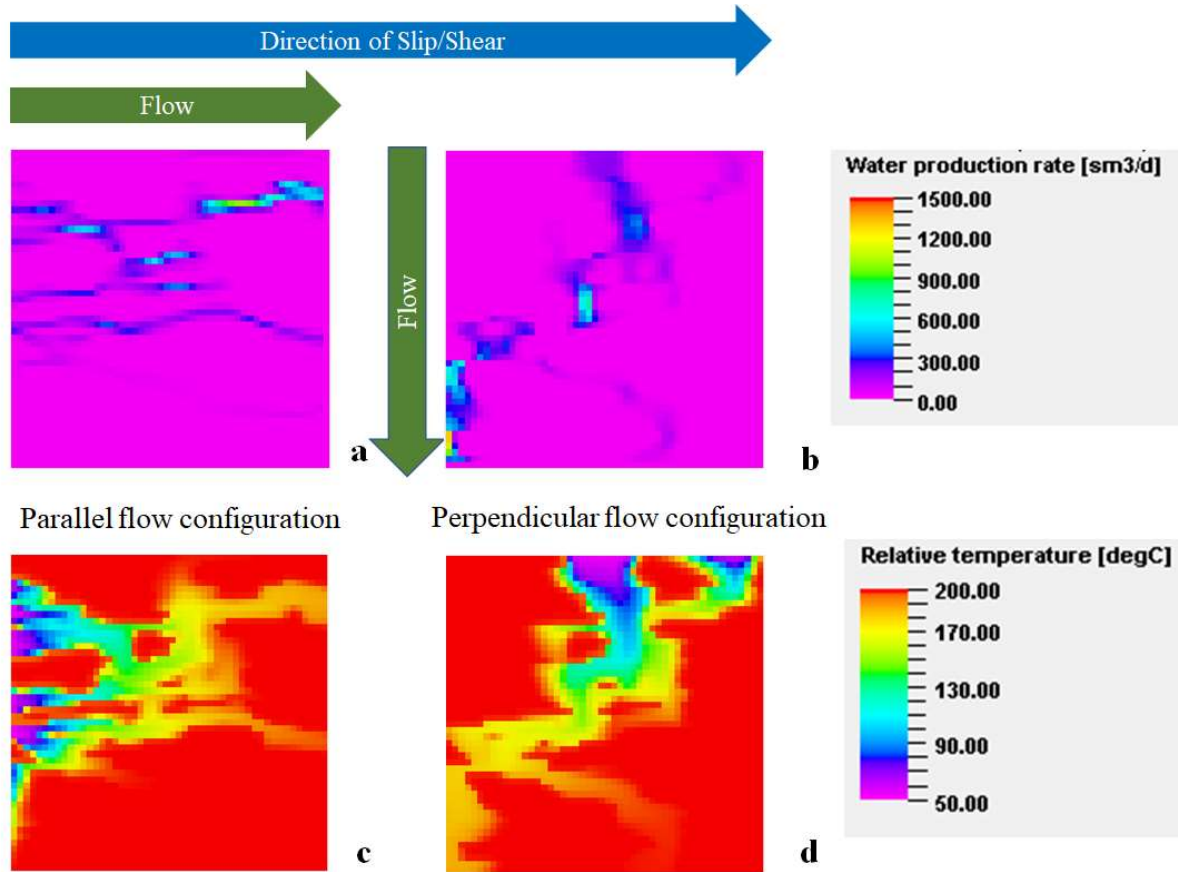


Figure 3.24: Fluid flow and heat transport on the fracture aperture after one year for Aperture 5.

The aperture distribution with the highest temperature difference between the flow configurations at one year into the simulation was also analyzed. This aperture distribution will subsequently be denoted as Aperture 6. Aperture 6 resulted in a 16.5 °C difference in temperature in favor of the perpendicular flow configuration than the parallel flow configuration. Its flow map and temperature map are shown in Figure 3.25.

From Figure 3.25a, the flow path of the parallel flow configuration appears dominant in one connected path with another minor channel. Contrastingly, flow in the

perpendicular flow configuration appears to follow tortuous paths (Figure 3.25b). Similar to other aperture distributions where the flow was tortuous in the perpendicular direction, more fracture surface area is contacted in the perpendicular flow configuration (25.1% flow wetted surface) than in the parallel flow configuration (21.6% flow wetted surface). The area cooled by injecting cold water through the fracture of the perpendicular flow configuration is larger than the swept areas of the parallel flow configuration (Figures 3.25c and 3.25d). This larger contact area demonstrates why more heat is extracted in the perpendicular flow configuration.

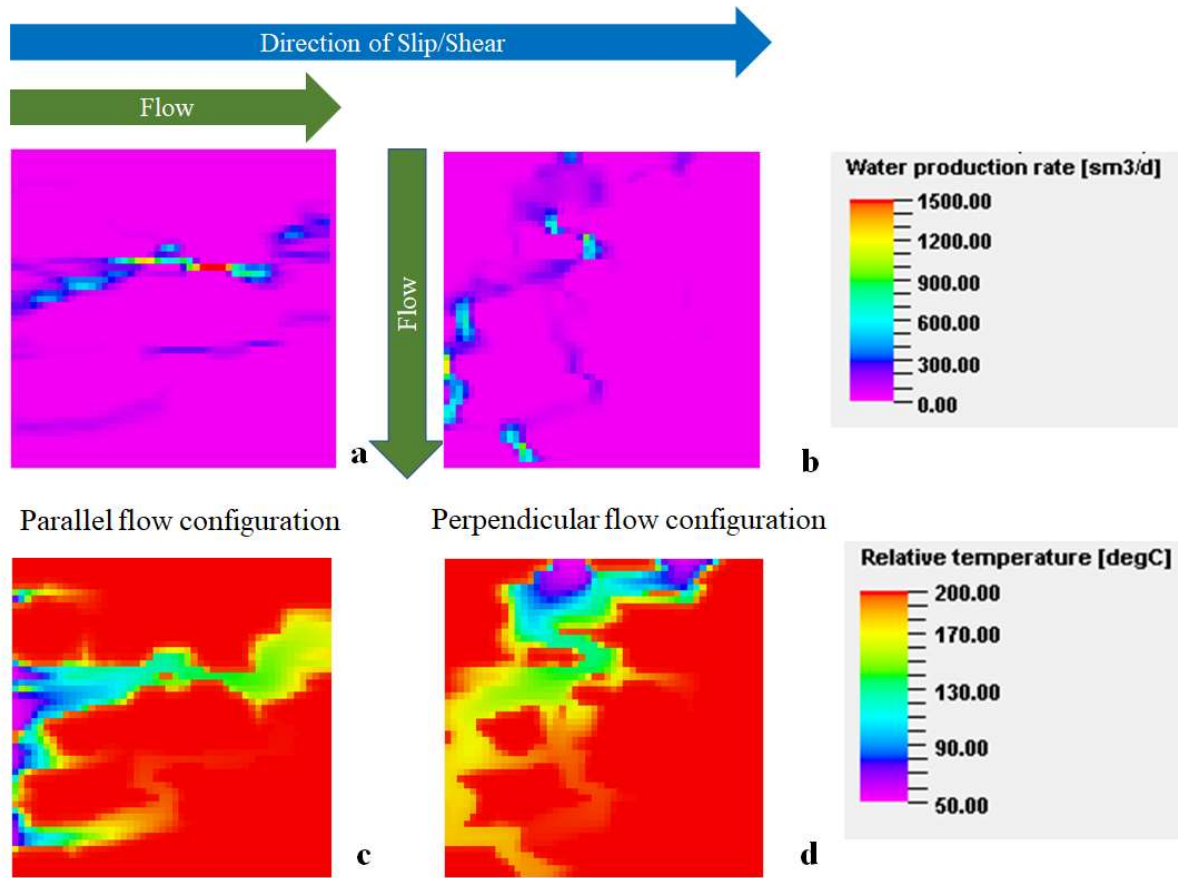


Figure 3.25: Fluid flow and heat transport on the fracture aperture after one year for Aperture 6.

3.7.5 Geometric Anisotropy Ratio of 4

The last set of aperture distributions contrasted by geometric anisotropy ratios had a geometric anisotropy ratio of 4. For the y-direction range values of 50 m, 60 m, 75 m, and 100 m, the x-direction ranges were 200 m, 240 m, 300 m, and 400 m.

The temperature difference between the perpendicular and parallel flow directions for the different cases with geometric anisotropic ratio of 4 is shown in Figure 3.26 for the simulation duration. Similar to the observations for the aperture distributions with a geometric anisotropy ratio of 3, there was not much temperature difference for the curves in favor of the parallel flow compared to the curves in favor of the perpendicular flow configuration.

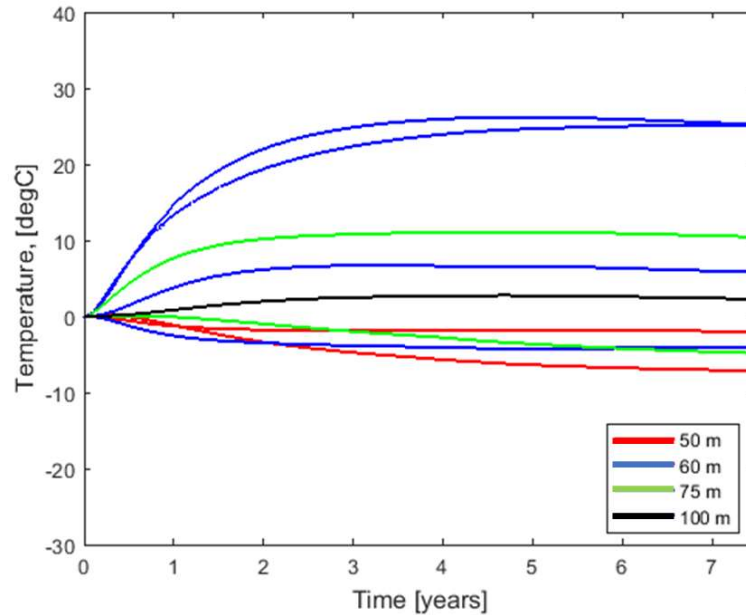


Figure 3.26: Temperature difference between the perpendicular and parallel flow directions for the different cases with geometric anisotropic ratio of 4. The difference is temperature profile in the perpendicular direction minus temperature profile in the parallel direction.

The sorted and counted data for the temperature difference between the perpendicular and parallel flow directions for the different cases with geometric anisotropic ratio of 4 are shown in Figure 3.27. This geometric anisotropy ratio had eight aperture distributions. For this geometric anisotropy ratio, about 62.5% of the aperture distributions favored the perpendicular flow configuration.

Further analysis was carried out on the aperture distributions with the highest temperature difference at one year into the simulation in favor of either flow configuration. The aperture distribution with the highest temperature difference in favor of the parallel flow configuration had a temperature difference of -1.2 °C. This distribution is hereafter

referred to as Aperture 7. On the other hand, the aperture distribution with the highest temperature difference in favor of the perpendicular flow configuration had a temperature difference of 14.6 °C. It will be denoted as Aperture 8. For Aperture 7, the range in the y-direction was 50 m, while the range in the x-direction was 200 m. For Aperture 8, the range in the y-direction was 60 m, and the range in the x-direction was 240 m.

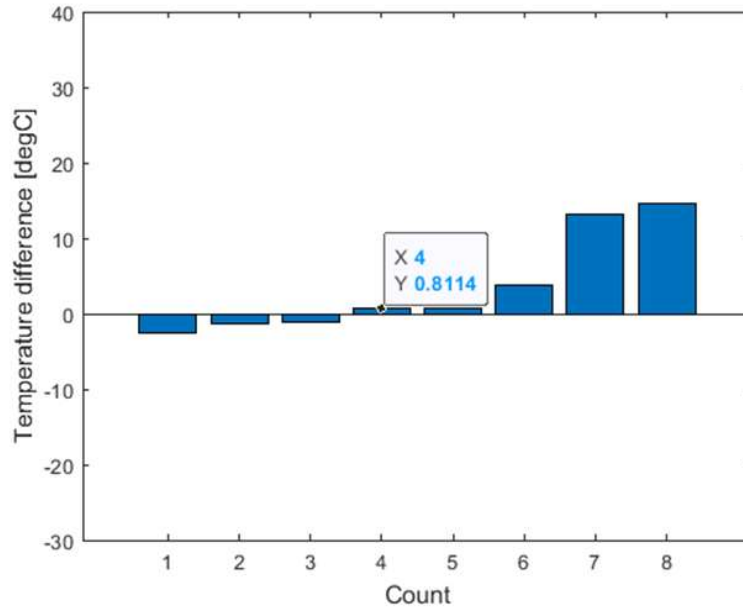


Figure 3.27: Temperature difference between the perpendicular and parallel flow directions for the different cases with geometric anisotropic ratio of 4. The difference is temperature profile in the perpendicular direction minus temperature profile in the parallel direction.

Figure 3.28 shows the flow maps and temperature maps for the parallel and perpendicular flow configurations of Aperture 7. Aperture 7 has several near-horizontal flow paths which support flow and consequently heat extraction along the striations for the parallel flow configuration (Figures 3.28a and 3.28c). The fluid flow path is tortuous for the perpendicular flow configuration, and the thermally swept area also follows a tortuous pattern (Figures 3.28b and 3.28d). The estimated flow wetted surface in the parallel flow configuration was 34.3%, while it was 28.3% for the perpendicular flow direction. With the relatively large difference in the fracture surface area contacted, it might be expected that the temperature difference between the flow configurations will be significant. The estimated temperature difference between flow configurations was 1.2 °C in favor of the parallel direction. Thus it was deduced that another factor contributing to

heat extraction for systems with spatial variations in fracture aperture was the local flow rate. It can be observed from Figure 3.28b that within the flow paths, the flow rate is in general higher than the flow rates seen in the flow map for the parallel flow configuration (Figure 3.28a). The higher flow rates in the perpendicular flow configuration suggest higher permeability in the flow path for that aperture distribution. The local flow rate may not be as significant in contributing to heat extraction as the flow wetted surface area.

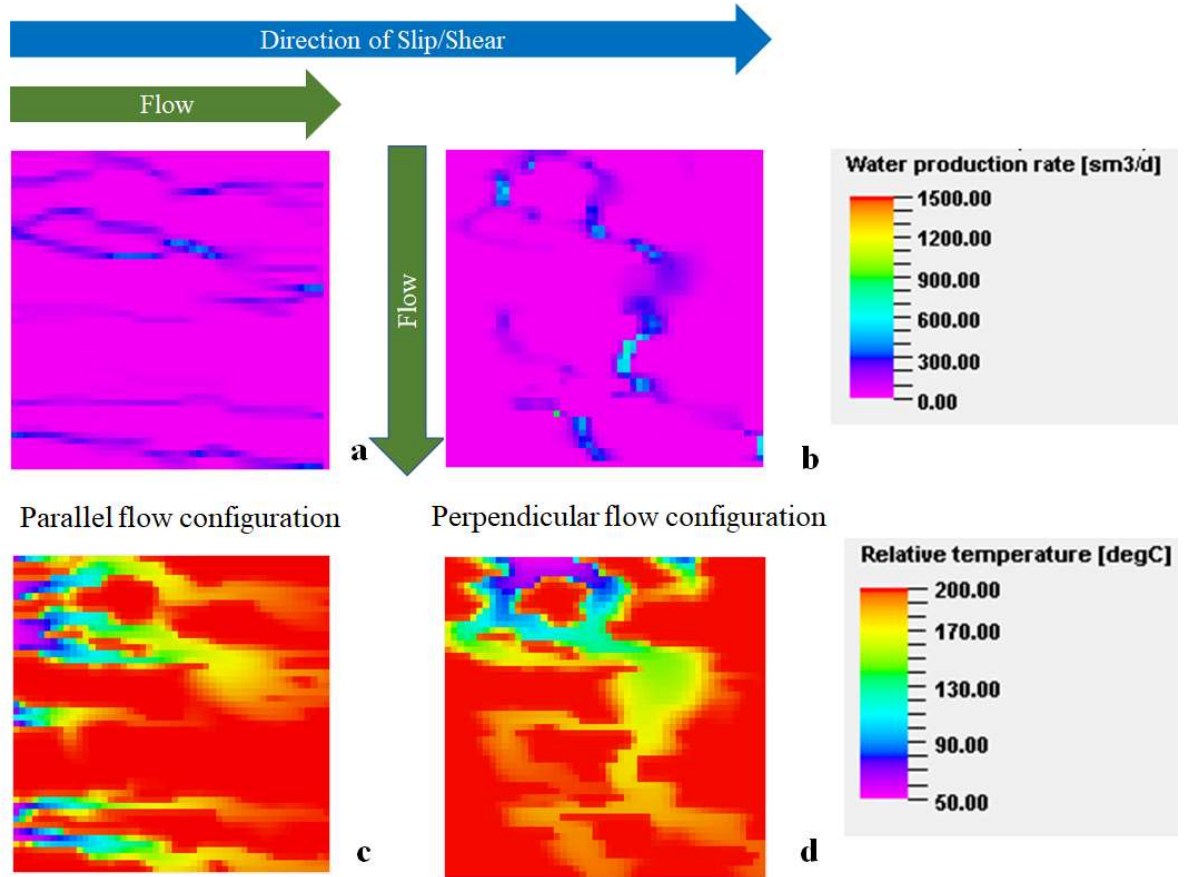


Figure 3.28: Fluid flow and heat transport on the fracture aperture after one year for Aperture 7.

Figure 3.29 shows the flow maps and temperature maps for the parallel and perpendicular flow configurations of Aperture 8. There are two dominant flow paths in the parallel flow configuration, as seen in Figure 3.29a. However, as with other cases of flow in the perpendicular flow configuration, the flow path is tortuous (Figure 3.29b). The estimated flow wetted surface area for the parallel flow configuration was 29.5%, while it was 31.4% for the perpendicular flow configuration. The perpendicular flow configuration temperature map shows more cooled areas, suggesting more heat was

extracted in that flow configuration (Figure 3.29d). For the parallel flow configuration, heat extraction appears to have occurred in the two predominant paths, with large amounts of reservoir surface uncontacted by the flowing fluid.

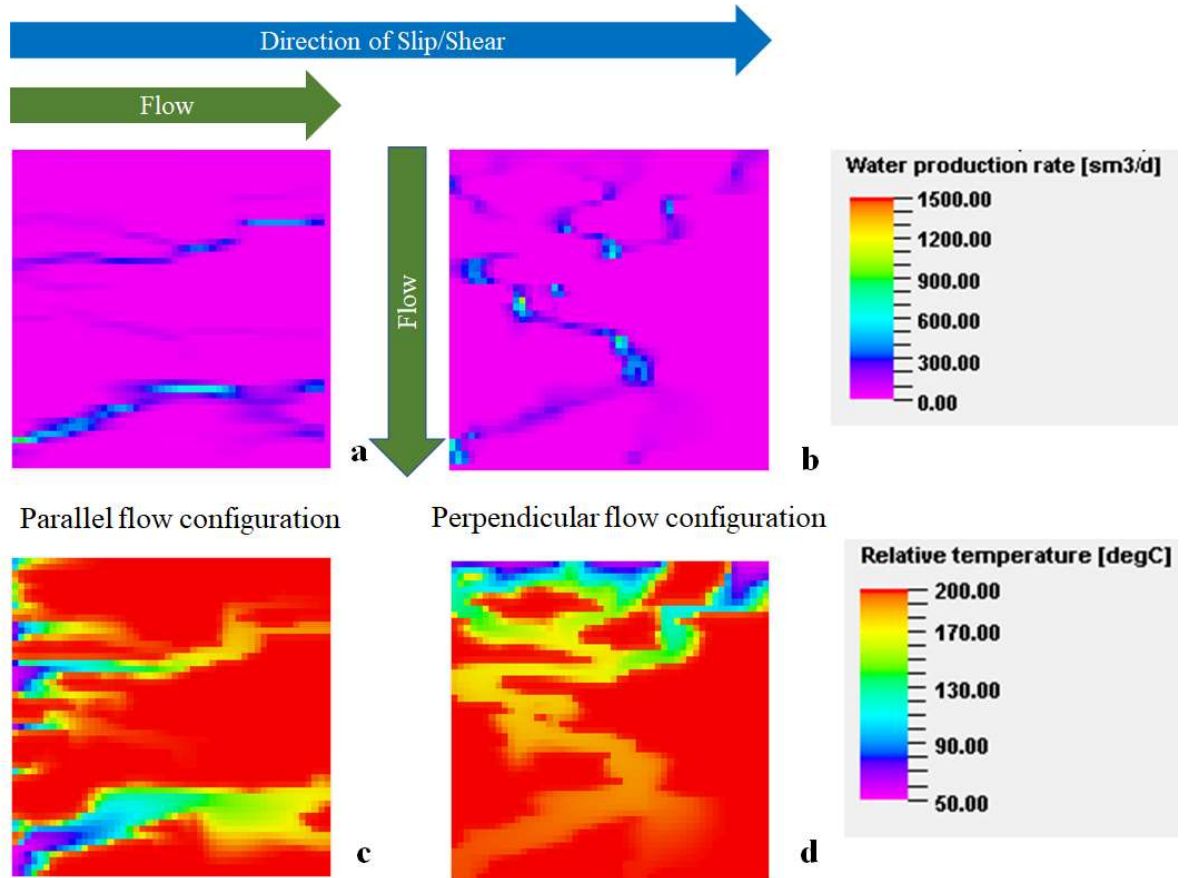


Figure 3.29: Fluid flow and heat transport on the fracture aperture after one year for Aperture 8.

3.7.6 Some Simulation Challenges

One can observe from the data in Table 3.1 that not all the geometric anisotropy ratios and ranges in the y-direction had the same number of aperture distributions presented. Though several aperture distributions were generated for each range in the y-direction and geometric anisotropy ratio, not all the generated distributions met the criterion of being in the limits in literature for Hurst coefficients of natural fractures. For example, when computing the Hurst coefficients for the geometric anisotropy ratio of 1.5, some aperture distributions had Hurst exponents below 0.5. On the other hand, for the geometric anisotropy ratios of 3 and 4, some aperture distributions had Hurst exponents

above 0.95 in the perpendicular direction. There were even Hurst exponents above 1 for the geometric anisotropy ratio of 4; thus, the aperture distributions were rejected. Figure 3.30 is a boxplot showing the ranges of the Hurst exponents for each of the geometric anisotropy ratios for the perpendicular and parallel directions. The cyan bar shows the range of $H_{\parallel} = 0.6$ measured from real faults and fractures. In the same vein, the magenta bar shows the range of $H_{\perp} = 0.8$ measured from real faults and fractures.

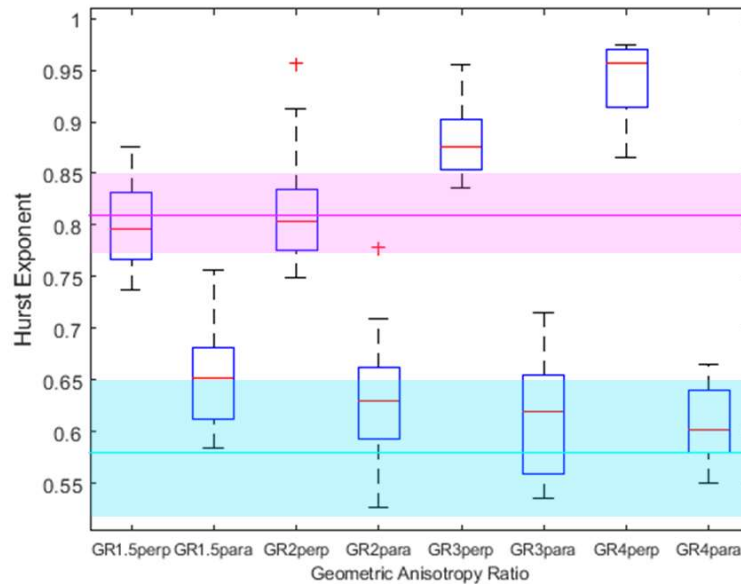


Figure 3.30: Boxplot of the Hurst Exponents for the different geometric anisotropy ratios.

The high Hurst exponent values explain why the latter two geometric anisotropy ratios have reduced aperture distributions. The geometric anisotropy ratio of 2 had most of its distribution with Hurst exponents within the cyan and magenta bars of Figure 3.30. Moreover, not all of the cases were able to run at the specified operating conditions of injection pressure of 150 bar, injection temperature of 40 °C, producer bottom hole pressure of 20 bar, and constant flow rate of 25 kg/s. They either required, in the perpendicular direction, higher injection pressures or lower fluid injection rates to ensure fluid flow, especially with the geometric anisotropy ratios of 3 and 4 where the striations cut across the fracture length in some cases. The higher injection pressures could exceed 220 bar, critical pressure of water, which was a simulation limit for this study.

In one case where 25 kg/s of flow was limited in the perpendicular flow direction but passed through without difficulty in the parallel direction, the flow rate was adjusted to model the circulation of 9 kg/s of water for both flow configurations. The results for that aperture distribution (denoted as Aperture 9) are shown in Figure 3.31. The range in the y-direction was 75 m, while the range in the x-direction was 300 m, corresponding to a geometric anisotropy ratio of 3.

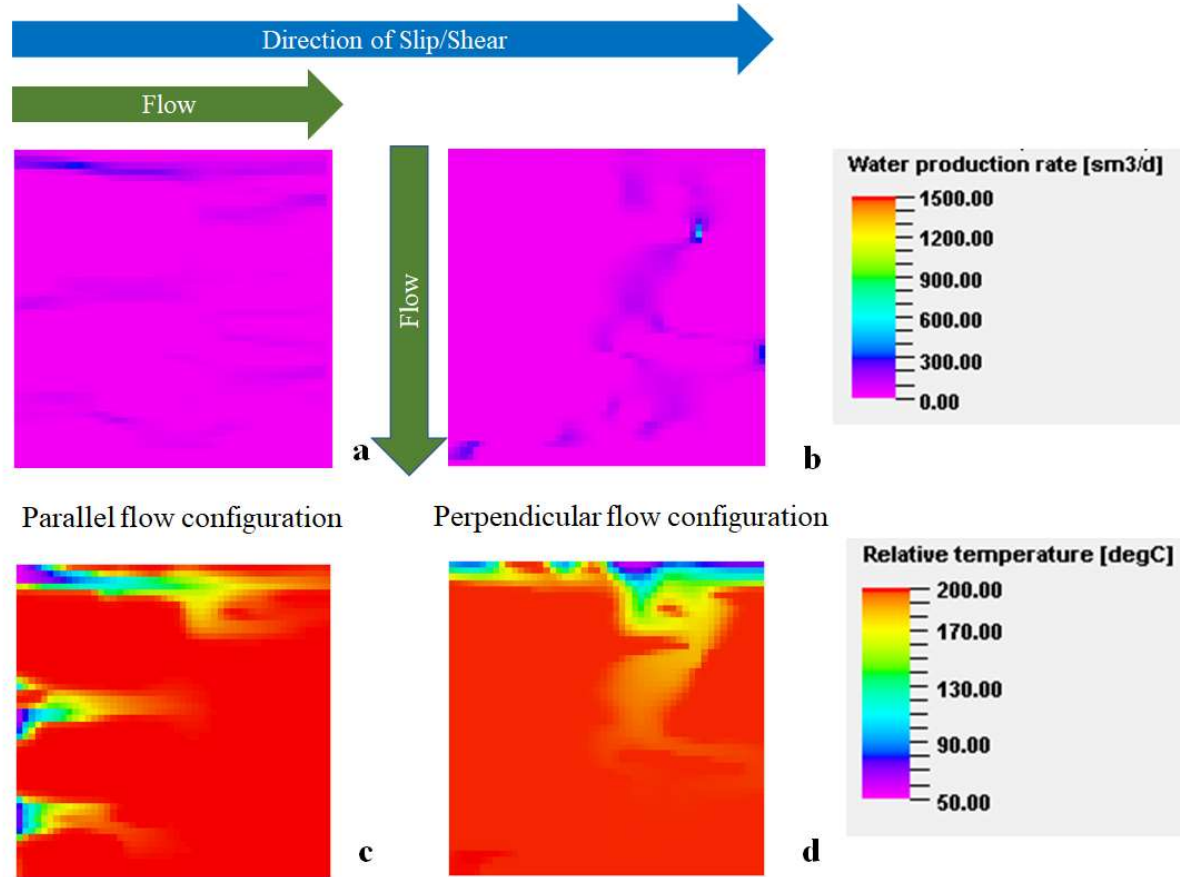


Figure 3.31: Fluid flow and heat transport on the fracture aperture after one year for Aperture 9.

The cumulative heat extracted from both flow configurations is shown in Figure 3.32. Though the flow rate was low, it was still possible to see a difference in heat extracted between the flow configurations. The perpendicular flow configuration resulted in higher energy extracted than the parallel flow configuration.

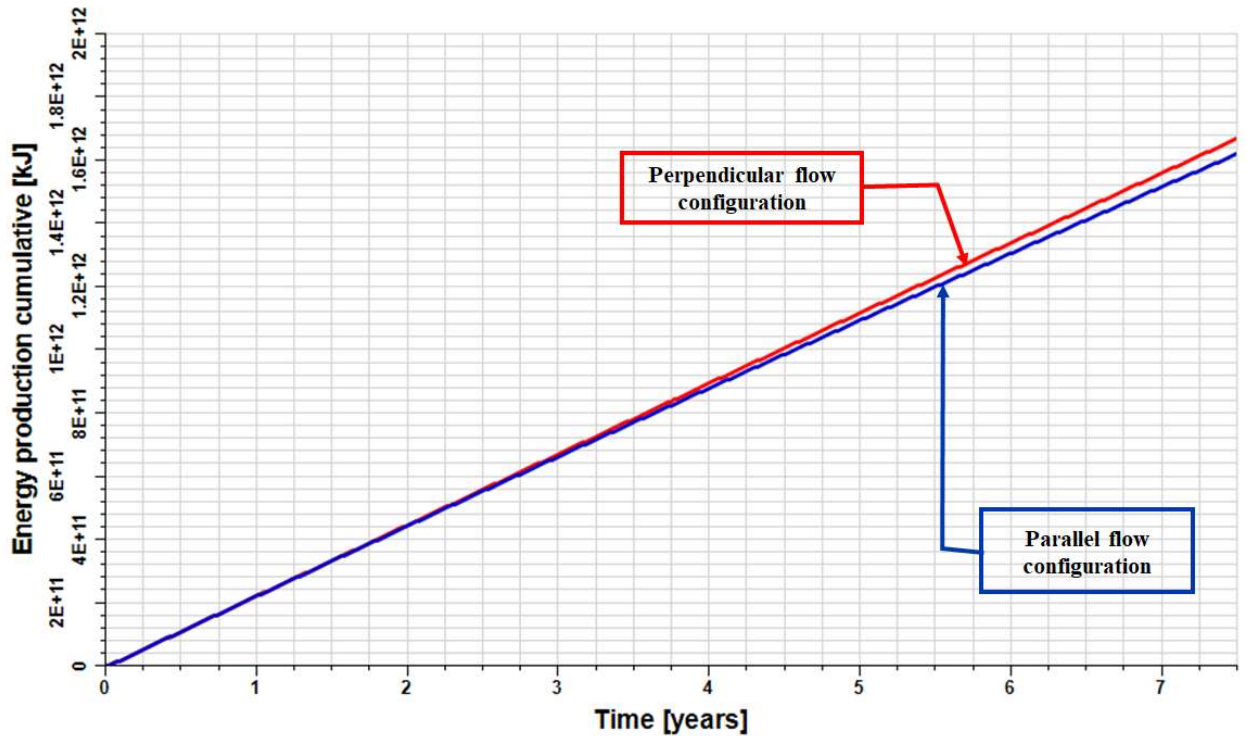


Figure 3.32: Cumulative Energy produced between the perpendicular and parallel flow directions for Aperture 9.

3.8 Summary

In this phase of the study, the thermal performance of a hypothetical Enhanced Geothermal System was investigated at field scale, taking into account anisotropic fracture aperture distributions. The fracture aperture distribution was treated as an autocorrelated random field with different ranges in the x- and y-directions. These ranges were defined by different geometric anisotropic ratios between 1.5 to 4. To ensure that realistic aperture distributions were modeled, the Hurst exponents of the aperture distributions were checked and compared with the typical values seen in the work by Candela et al. (2012).

A total of 110 synthetic aperture distributions were generated using the Sequential Gaussian Simulation method in SGeMS. The thermal drawdown between the perpendicular flow configuration and the parallel flow configuration was compared. The results showed, on average, a 60% chance that the perpendicular flow configuration will result in improved flow and heat transfer compared to the parallel flow configuration.

When investigating the thermal performance by geometric anisotropy ratios, it was seen that the aperture distributions with a geometric anisotropy ratio of 2 had about 70% of the aperture distribution with better thermal performance in favor of the perpendicular flow direction. This geometric anisotropy ratio also had most of its aperture distributions with Hurst exponents in the range found in natural faults and fractures. Thus, the results may be representative of the behavior of actual fractures.

As was seen in Chapter 2, the temperature correlated with the flow wetted surface. The higher the flow wetted surface, the higher the temperature and heat extracted, and the higher the difference between a given pair of flow directions. In all of the geometric anisotropic ratios, the perpendicular flow configuration resulted in improved thermal performance than the parallel flow configuration more than 58% of the time. For specific aperture distributions where this was not the case, the difference between the temperature difference was not very high for most of these aperture distributions.

The perpendicular flow configuration had tortuous flow paths, while the parallel flow direction mostly had flow in near-horizontal paths. The tortuous flow paths contributed to more fracture surface area being contacted by the flowing fluid, leading to improved thermal performance.

The results imply that it is beneficial to consider the direction of shear at the field scale when placing wells.

Having examined the impact of anisotropy on the thermal performance of lab-scale and field-scale simulations, a modeling assumption, constant viscosity, was investigated to see how it impacts the thermohydraulic modeling of EGS for fractures with spatial variations. A comparison between modeling with constant viscosity and temperature-dependent viscosity is the crux of Chapter 4.

Chapter 4

4 Temperature-Dependent Viscosity: Relevance to the Numerical Simulation of Enhanced Geothermal Systems

4.1 Introduction

Reservoir models are valuable tools to mimic the behavior of a reservoir, thus allowing for field development optimization and optimizing operation strategies. A reservoir model provides a means of answering questions such as “what is the most efficient well spacing?”, “when and how should the reservoir be exploited?” and “what will the long-term behavior of the reservoir be?” before wells are drilled and the field put into production. Hence, reservoir models are cheaper and time-saving alternatives to implementing field development strategies.

There are two techniques for solving mathematical reservoir models: analytical and numerical. The analytical methods offer the advantage of providing exact solutions, and those solutions are continuous throughout the system. However, analytical methods fall short when dealing with varying rock and fluid properties in the reservoir. Usually, to find an analytical solution to the reservoir model, the problem may be modified, sometimes drastically through several assumptions, to make it plausible to be handled analytically. On the other hand, numerical solutions involve discretizing or approximating the mathematical model, that is, using a numerical tool such that continuous forms of the partial differential equations governing the physical systems are written in a discrete form. The discretization process is performed not only on the partial differential equation but also on the physical systems. This implies that the physical system is divided into several subdomains that are coupled to one another. The numerical approach allows representative properties to be assigned to as many parts of the system as data are available

for. Complexities in reservoir models are better handled with numerical models. However, some measure of accuracy is lost in discretizing the partial differential equations and the physical system.

The fundamental equations governing the coupled heat, flow, and mass transport in Enhanced Geothermal Systems were described in Chapter 2. One assumption that is often made in analytical solutions and some numerical simulations is that the viscosity of the working fluid, water, is constant. For instance, in the analytical solutions by Bödvarsson & Tsang (1982), Kolditz (1995), Cheng et al. (2001), Ghassemi et al. (2003), and Fox et al. (2015), the viscosity was either assumed to be constant or not used in the governing equations. Similarly, in the numerical models by Bataillé et al. (2006), Jiang et al. (2014), and Guo, et al. (2016), the viscosity was also considered to be constant. It is known that the viscosity varies more markedly than the other thermophysical properties for most liquids (Wang et al., 2014). However, for water, the impact of temperature on viscosity is more evident than pressure (Figure 4.1). Assuming constant fluid viscosity when modeling Enhanced Geothermal Systems makes the computations simpler and faster (Jiang et al., 2014). However, neglecting the effects of viscosity as the temperature of the system changes with time may lead to inaccuracies in the model. Huang et al. (2019) compared the net power output of an EGS using a model with constant viscosity and a model with variable viscosity. They concluded that simulations with constant fluid viscosity assumed might not sufficiently predict the net electric power output of real EGS.

As seen in preceding chapters, real fractures have spatial variations in their apertures, leading to flow channeling, premature thermal breakthrough, and reduced energy extracted from the Enhanced Geothermal System. To properly model the system for better forecasting, the spatial variations in the fracture aperture and the impact of channeling need to be considered. Hence in this study, a numerical simulation model was built to account for two situations that may occur during heat extraction from an Enhanced Geothermal System. First, the viscosity of the working fluid (water for this study) varies with changes in the system's temperature. Second, the possibility that the fractures, the main flow conduits, may have asperities that could create channels and alter flow paths, affecting the amount and distribution of the surface area available for heat transfer.

This study aimed to investigate what impact the temperature dependency of water viscosity has on the numerical modeling of EGS thermal performance and identify under which conditions the fluid viscosity effects on heat transport modeling can be neglected with minimal impact on computational accuracy.

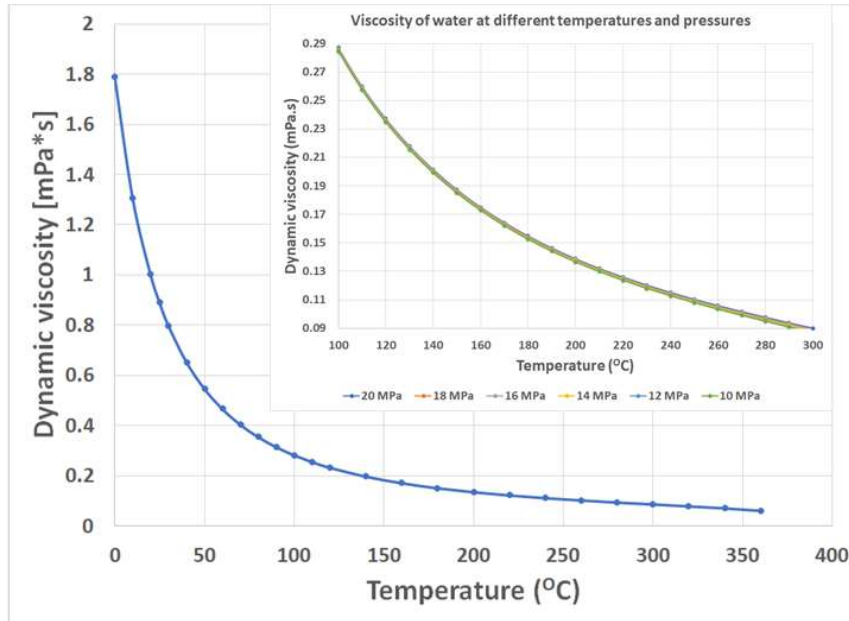


Figure 4.1: Variation of viscosity with temperature. The insert in the graph shows the trend at various pressures.

4.2 Methodology

4.2.1 Description of the Enhanced Geothermal System

A hypothetical EGS system was modeled as a horizontal single-fractured system with a horizontal injector and a horizontal producer. The system is low permeability except at the fracture, where the permeability is very high with spatial variations. The X-Y plane is a square of length L 1000 m. Water is injected at a mass flow rate \dot{m} of 40 kg/s. The thermophysical properties include rock thermal conductivity, $k_r = 2.8 \text{ W/(m } ^\circ\text{C)}$, rock density of 2600 kg/m^3 , and specific heat capacities of the rock and water, $c_r = 1000 \text{ J/(kg K)}$ and $c_w = 4200 \text{ J/(kg K)}$.

Different average initial reservoir temperatures were considered: 120 °C, 150 °C, 200 °C, and 250 °C. No effect of a geothermal gradient was considered during the simulation. Water injection temperatures of 20 °C, 40 °C, and 60 °C were also considered.

4.2.2 Relevant Temperature-Dependent Parameters

The governing equations and model assumptions are covered in Chapter 2, Sections 2.2.1 and 2.2.2, respectively. The fracture modeled in this study was horizontal, and thus the effect of gravity was not considered. The density of water is modeled as a function of pressure and temperature using the formation volume factor of water (B_w) as follows:

$$\rho_w = \frac{\rho_{ST}}{B_w} \quad (4.1)$$

where:

$$B_w = B_w(P_{ref}) \times (1 - X) \times (1 + C_{T1} \times (T - T_{ref}) + C_{T2} \times (T - T_{ref})^2) \quad (4.2)$$

$$X = C \times (T - T_{ref}) \quad (4.3)$$

$T_{ref} = 293.15$ K; $C_{T1} = 3.0 \times 10^{-4} \text{K}^{-1}$; $C_{T2} = 3.0 \times 10^{-6} \text{K}^{-2}$; C is the water compressibility, and $B_w(P_{ref})$ is the water formation volume factor at the reference pressure.

The water viscosity was input as a table showing the viscosity of water at temperatures ranging from 0 to 360 °C, taken from Engineering ToolBox (2004). The viscosity values used are shown in Table 4.1.

Table 4.1: Water viscosity at different temperatures at a pressure of 101.325 kPa

Temperature (°C)	0.01	10	20	40	60	80	100	120	140
Viscosity (cp)	1.79	1.30	1.00	0.65	0.46	0.35	0.28	0.23	0.19
	1	6	2	3	6	4	2	2	7

Temperature (°C)	160	180	200	220	240	260	280	300	360
Viscosity (cp)	0.17	0.15	0.13	0.12	0.11	0.10	0.09	0.08	0.06
	0	0	5	2	1	2	4	6	0

4.2.3 Determination of Aperture Distribution

The goal of this study was to investigate the effects of the temperature dependency of water viscosity on the numerical modeling of EGS thermal performance taking cognizance of spatial variations in the fracture aperture field. Three synthetic aperture distributions were derived using Sequential Gaussian simulation (SGSIM) within the Stanford Geostatistical Modeling Software (SGeMS) to characterize the fracture with spatial heterogeneity. The variogram and histogram data of the heterogeneous aperture field from Ishibashi et al. (2012) comprised the input to SGeMS, where SGSIM was used. Chapter 2 gives details on variogram modeling and how SGSIM can be used to determine the artificial aperture fields. In addition, a complete discussion on the SGSIM method and variogram models can be found in Goovaerts (1997).

4.2.3.1 Description of the aperture distributions

Three different aperture distributions were studied to investigate if there was any effect of fracture aperture variability on the thermal performance when comparing results from constant viscosity and temperature-dependent viscosity. Figure 4.2 shows these aperture distributions. The aperture distributions a, c, and e are the top views, while the diagrams below them (b, d, and f) are the respective isometric views. The flow direction is from top to bottom with respect to the aperture planes described by Figures 4.2 a, c, and e.

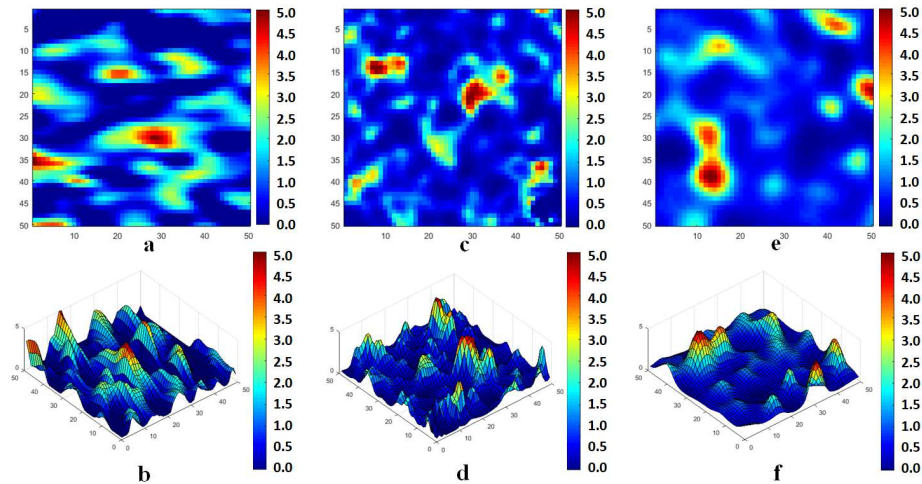


Figure 4.2: Description of the aperture distributions used in this study. The apertures range from 0 - 5 mm. The aperture distributions on top are the planar views, while the diagrams at the bottom are the isometric views.

Table 4.2 shows some statistics related to the different aperture distributions. The percentage of area with aperture > 0.1 mm provides a basis for comparing the area that may be available for flow and consequently heat transfer. The percentage of area with aperture > 2.5 mm gives some idea of how permeable the fracture may be. The mean is the average of the given aperture distribution, while the standard deviation indicates how distributed the aperture values may be, i.e., the lower the standard deviation, the more evenly distributed the aperture may be. The numbers 0.1 mm and 2.5 mm were chosen to have a uniform reference for comparing all aperture distributions.

Table 4.2: Statistics for the aperture distributions

	Aperture 1	Aperture 2	Aperture 3
Percentage of area with aperture > 0.1 mm (%)	70.00	94.28	97.16
Percentage of area with aperture > 2.5 mm (%)	7.60	6.28	6.92
Mean aperture (mm)	0.94	0.85	0.97
Standard deviation (mm)	0.312	0.306	0.282
Range x-direction (m)	300	50	200
Range y-direction (m)	100	50	200

Figures 4.2a and 4.2b depict an aperture distribution that is anisotropic with a geometric anisotropic ratio of 3 and ranges 100 m and 300 m. The aperture distribution is characterized by striations in the x-direction, i.e., the range in the x-direction is higher than the range in the y-direction. This distribution will be referred to as “Aperture 1” in subsequent discussions. Of the three aperture distributions, this has the least percentage of area with aperture distribution greater than 0.1 mm (Table 4.2), suggesting that it may have the least surface area available for flow. Moreover, Aperture 1 has the highest standard deviation, which may indicate the possibility of channeling as the areas with high permeability will result in preferential flow paths.

Figures 4.2c and 4.2d represent an aperture distribution that is isotropic with a range of 50 m. Though it has a high percentage of fracture surface with aperture > 0.1 mm,

it has the lowest mean aperture distribution of the three aperture distributions studied. This distribution will be referred to as “Aperture 2” in subsequent discussions.

Figures 4.2e and 4.2f are of an aperture distribution that is isotropic with a range of 200 m. Of the three aperture distributions, it has the highest percentage of fracture surface > 0.1 mm, the highest mean, and the lowest standard deviation. This distribution will be referred to as “Aperture 3” in subsequent discussions.

4.3 Simulation Model and Software used

ECLIPSE thermal compositional numerical simulator was used to model the coupled thermohydraulic process. ECLIPSE is a finite difference simulator. For this modeling, the simulator was run in fully implicit mode. Cartesian block-center geometry in three dimensions was used. The model is a 50 by 50 by 70 grid. In the X and Y directions, the individual cells are of uniform length of 20 m, while in the Z direction, the thicknesses are very fine around the fracture and become coarse away from the fracture. Figure 4.3 shows a snapshot of the reservoir simulation domain.

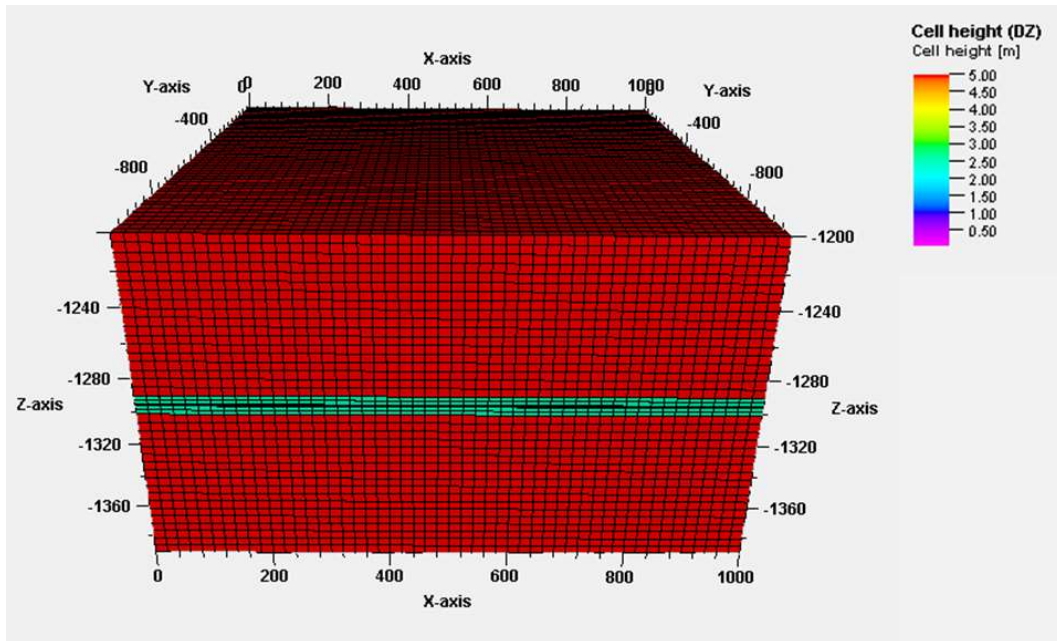


Figure 4.3: Reservoir simulation domain showing the grids used in the model. The height (Z-axis) is not drawn to scale.

The fracture aperture values had to be converted to permeability to use in the simulator. The fracture was treated as a porous medium with porosity set as 0.99, while the local cubic law defines the heterogeneous permeability for a fracture with spatial variations (Oron & Berkowitz, 1998), which is represented by Equation 4.4.

$$k_{f_{ij}} = \frac{b_{ij}^2}{12} \quad (4.4)$$

where k_f , i , j , and b are the effective permeability, grid number in the x-direction, grid number in the y-direction, and local fracture aperture.

4.4 Results and Discussion

4.4.1 Constant Viscosity vs. Temperature-Dependent Viscosity: Parallel Plate Fracture Model

For all the reservoir temperature and injection temperature pairs, scenarios were run using a smooth parallel plate model for the fracture. The permeability of the fracture was computed using Equation 4.4 but with a constant aperture value of 5 mm.

The constant viscosity used was 0.15 cp for a temperature of 180 °C (the average of 120 °C, 150 °C, 200 °C, and 250 °C – the temperatures modeled in this study) and pressure of 101.325 kPa. This case showed an insignificant difference between assuming a constant viscosity in the model and using a temperature-dependent viscosity in the model. This negligible difference is shown in Figures 4.4 and 4.6 based on results for reservoir temperatures of 200 °C and 120 °C, and injection water temperatures of 40 °C and 60 °C respectively. The differences between the thermal drawdown from a temperature-dependent viscosity model and a constant viscosity model are shown in Figures 4.5 and 4.7, as it is not apparent from Figures 4.4 and 4.6. Though the difference is negligible, the higher the difference between the reservoir temperature and injection temperature, the higher the difference between the results from assuming constant viscosity vs. temperature-dependent viscosity. Moreover, the higher the average temperature of the reservoir, the higher the absolute difference between the results from using constant

viscosity vs. using temperature-dependent viscosity in the model. Bataillé et al. (2006) also had a similar finding that the circulation of the fluid is not sensitive to viscosity variations with temperature.

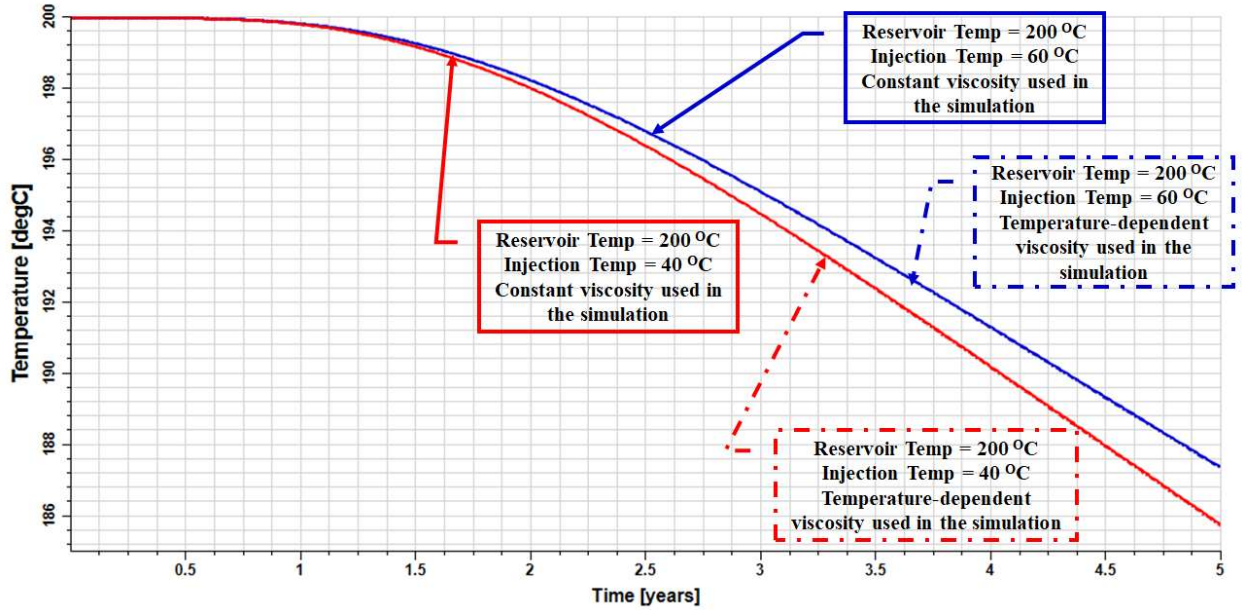


Figure 4.4: Comparison between the EGS thermal performance prediction using constant viscosity (bold lines) and temperature-dependent viscosity (dash lines) for reservoir temperature of 200 °C, assuming a parallel plate fracture model.

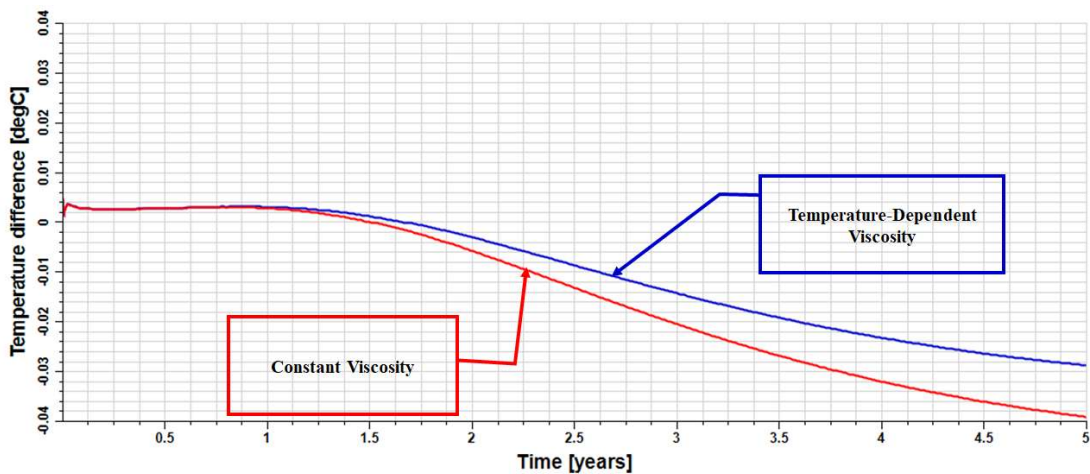


Figure 4.5: Temperature difference between the EGS thermal performance prediction using constant viscosity (red line) and temperature-dependent viscosity (blue line) for reservoir temperature of 200 °C and injection water temperature of 40 °C, assuming a parallel plate fracture model.

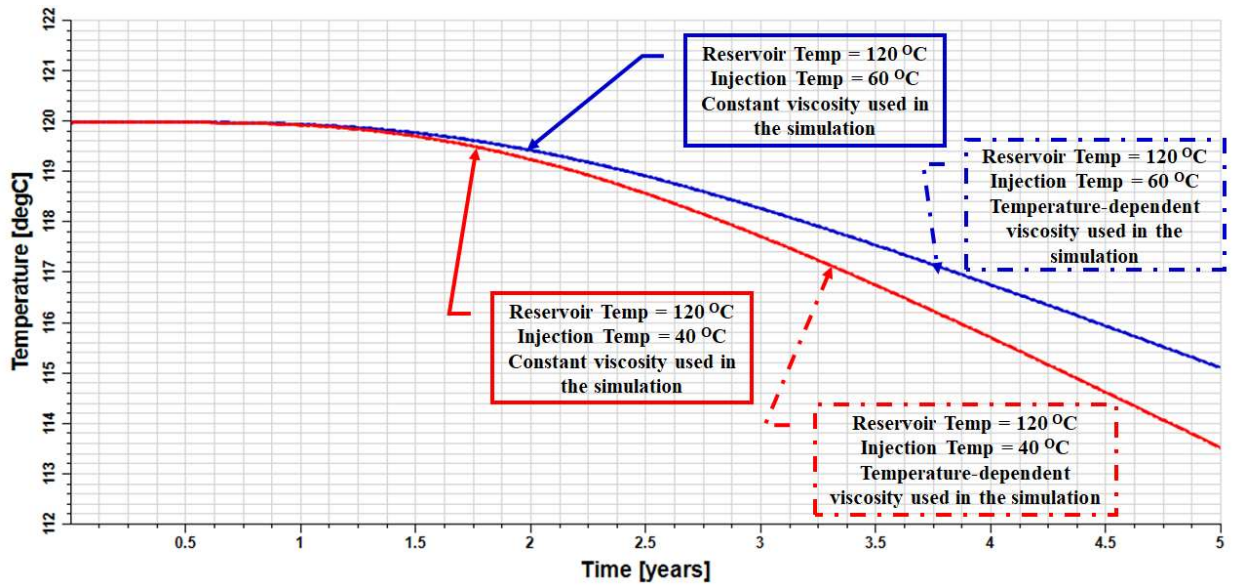


Figure 4.6: Comparison between the EGS thermal performance prediction using constant viscosity (bold lines) and temperature-dependent viscosity (dash lines) for reservoir temperature of 120 °C, assuming a parallel plate fracture model.

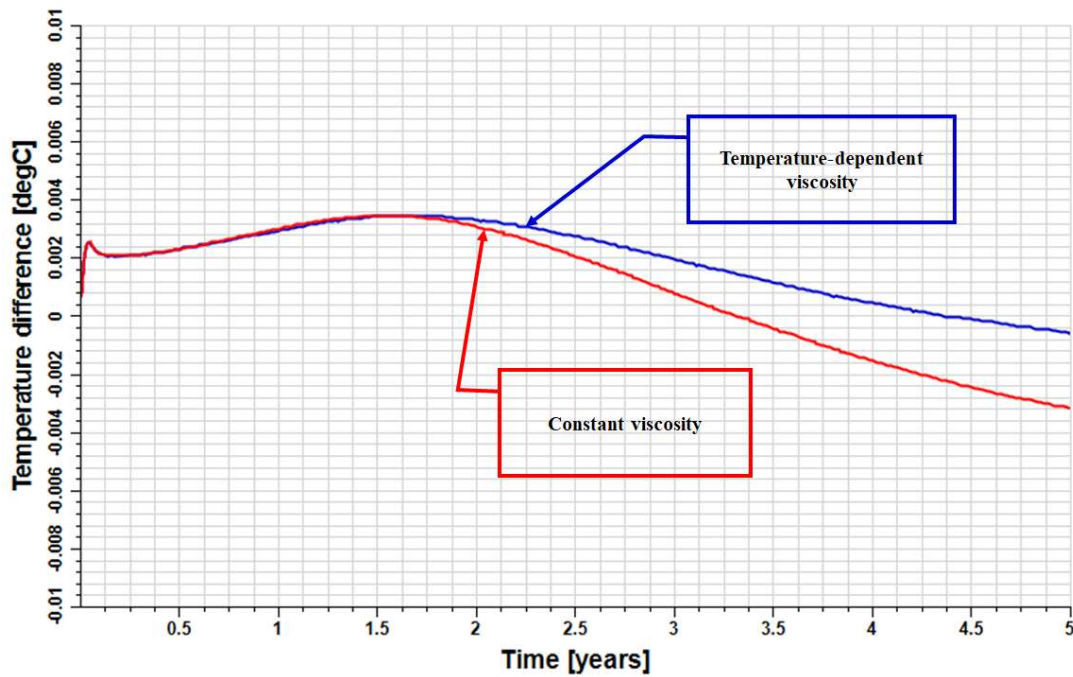


Figure 4.7: Temperature difference between the EGS thermal performance prediction using constant viscosity (red line) and temperature-dependent viscosity (blue line) for reservoir temperature of 120 °C and injection water temperature of 40 °C, assuming a parallel plate fracture model.

4.4.2 Constant Viscosity vs. Temperature-Dependent Viscosity: All Aperture Distributions

The temperature profile for all the aperture distributions at a reservoir temperature of 200 °C and injection water temperature of 40 °C are presented in Figure 4.8. The goal was to determine if the characteristics of the aperture had any impact on the differences between using a constant viscosity or a temperature-dependent viscosity in the simulation. It can be deduced that assuming a constant fracture aperture can lead to overly optimistic estimates of the thermal performance of EGS if the aperture field is indeed heterogeneous. Also, Aperture 1, which was anisotropic and had flow perpendicular to the striations, had the highest difference in temperature when comparing the model with a parallel plate fracture aperture and the fractures with spatial variations in aperture.

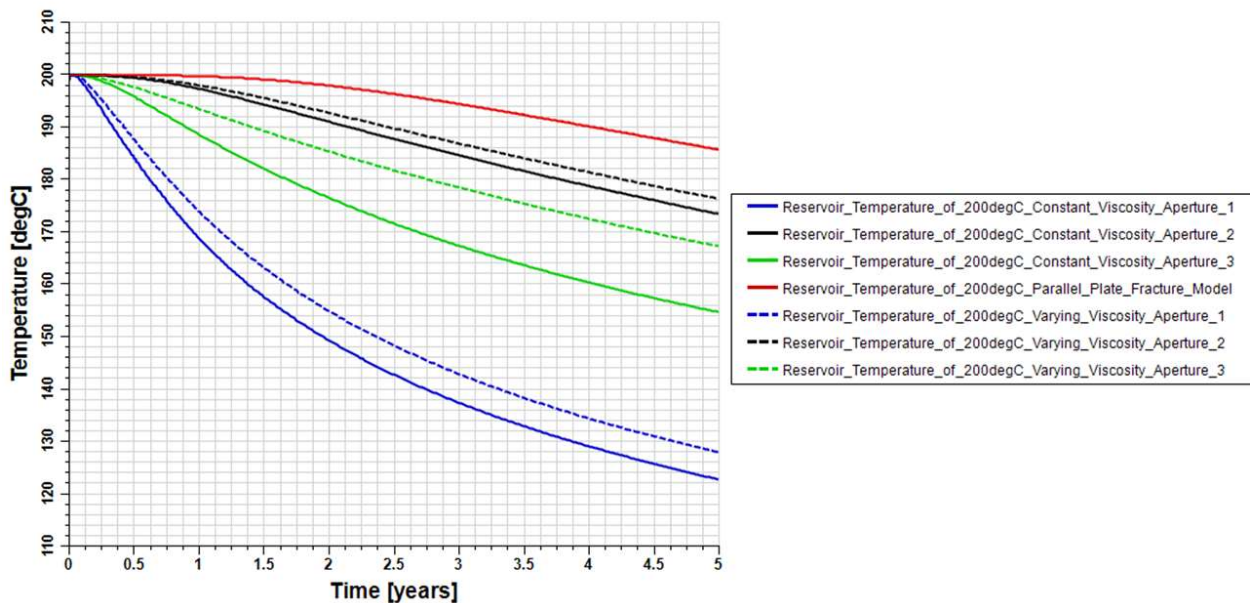


Figure 4.4: Temperature profile for all the aperture distributions at a reservoir temperature of 200 °C and injection water temperature of 40 °C.

The flow map (Figure 4.9) and the percentage of the surface area contacted by fluid (Figure 4.10) were used to help gain further insights into the results seen in Figure 4.8. The portion of the surface area contact by the fluid is tabulated in Table 4.3. Analysis of the flow maps (Figure 4.9) reveals that Aperture 1 has flow dominant in one section of the fracture surface, Aperture 2 has a more distributed flow, and Aperture 3 also has flow

dominant in one area of the fracture surface. However, from Figure 4.10, it can be deduced that the fracture for Aperture 3 is permeable overall and has low flow rates covering most of the surface area.

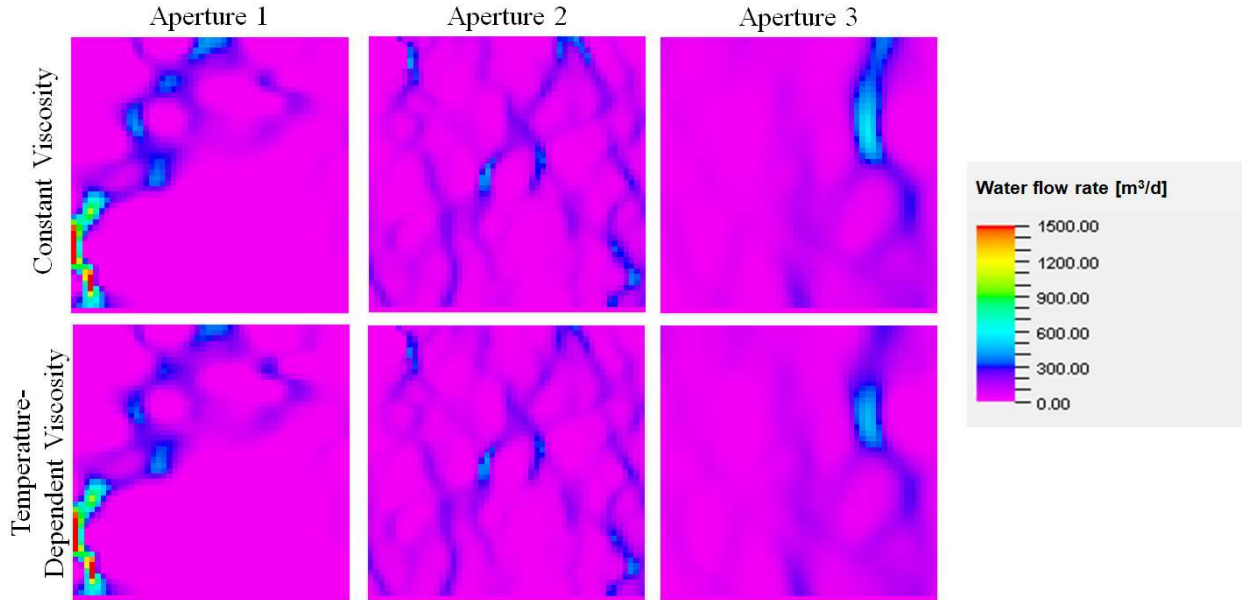


Figure 4.5: Flow maps for all the aperture distributions at a reservoir temperature of 200 °C and injection water temperature of 40 °C.

Aperture 1 also has the lowest flow wetted surface of the three aperture distributions (Table 4.3). This low contact surface area suggests channelized flow and explains why the thermal drawdown for Aperture 1 is very high irrespective of the viscosity model being used. On the other hand, Aperture 3 has the highest contact surface area of the three aperture distributions. One would expect that it would have the least thermal drawdown as a result. This one was not the case, and this can be attributed to the apparent channelized flow characterized by a high flow rate in one section of the fracture surface.

Table 4.3: Percentage of flow wetted surface for the aperture distributions

	Aperture 1	Aperture 2	Aperture 3
Constant Viscosity	38.72 (%)	82.68 (%)	84.36 (%)
Temperature-Dependent Viscosity	39.92 (%)	84.36 (%)	86.96 (%)
Difference in number of grid cells contacted by fluid	30	42	65

The difference between the number of grid cells on the fracture surface contacted by the fluid in the constant viscosity model and the temperature-dependent viscosity model should indicate the difference in the thermal drawdown between the two viscosity models. For Aperture 3 with the highest contrast, it was the case that the temperature-dependent viscosity model resulted in less thermal drawdown than the model using constant viscosity. For Aperture 1, which had the smallest difference in the number of grid cells contacted by the fluid, the difference in the thermal drawdown between the constant viscosity model and the temperature-dependent viscosity model was not the smallest of the three aperture distributions being studied. This is because the aperture distribution is prone to channeling, and there are alternative flow paths where fluid can flow to extract heat from the rock.

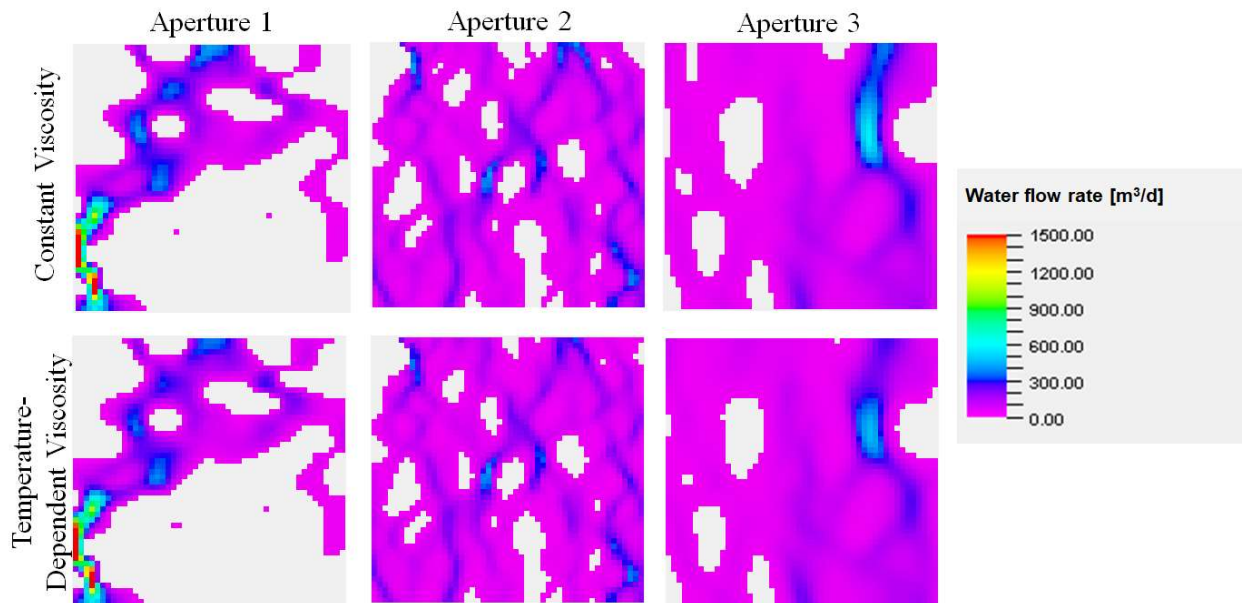


Figure 4.6: Flow map for all the aperture distributions showing the area contacted by the flowing fluid at a reservoir temperature of 200 °C and injection water temperature of 40 °C.

Having taken a look at the results in general for all the fracture aperture distributions, it is relevant to see how the models compare for different injection and average reservoir temperatures for each aperture distribution.

4.4.3 Constant Viscosity vs. Temperature-Dependent Viscosity: Aperture 1

Figure 4.11 shows the thermal performance of the hypothetical EGS at the producer on Aperture 1 assuming constant viscosity compared with temperature-dependent viscosity for different reservoir temperatures and injection temperature of 40 °C. The solid lines represent the temperature profile at the producer if the fracture were assumed to be of constant aperture. It can be observed that as the difference between the reservoir temperature and injection water temperature increases (going from the curves at the bottom to the curves at the top), the difference between the temperature profile of constant viscosity and temperature-dependent viscosity increases.

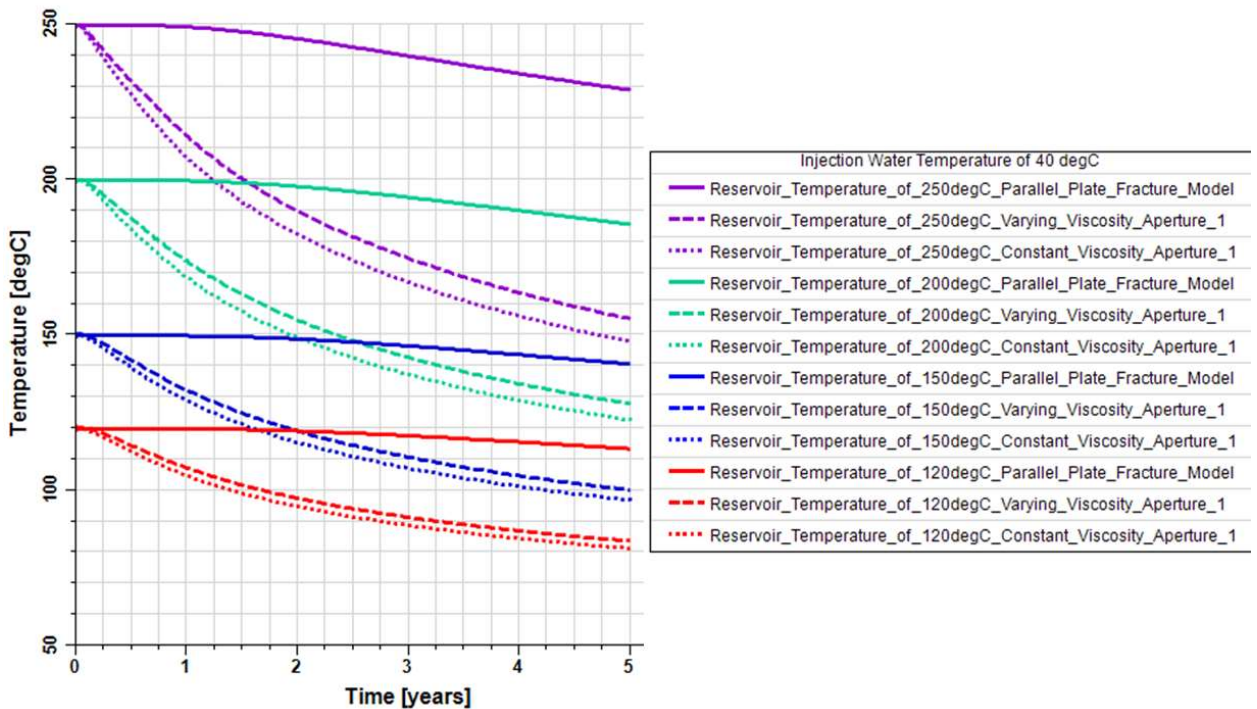


Figure 4.7: Temperature profile at the producer on Aperture 1 assuming constant viscosity and temperature-dependent viscosity for different reservoir temperatures and injection temperature of 40 °C.

A similar trend is seen when the injection water temperature is 60 °C as shown in Figure 4.12. However, in Figure 4.12, the difference between temperature profiles of the constant viscosity model and the temperature-dependent viscosity model, for a given reservoir temperature, reduces with the increase in injection water temperature. Almost

no difference is seen between the results of constant viscosity and temperature-dependent viscosity at low reservoir temperatures and injection water temperature of 60 °C.

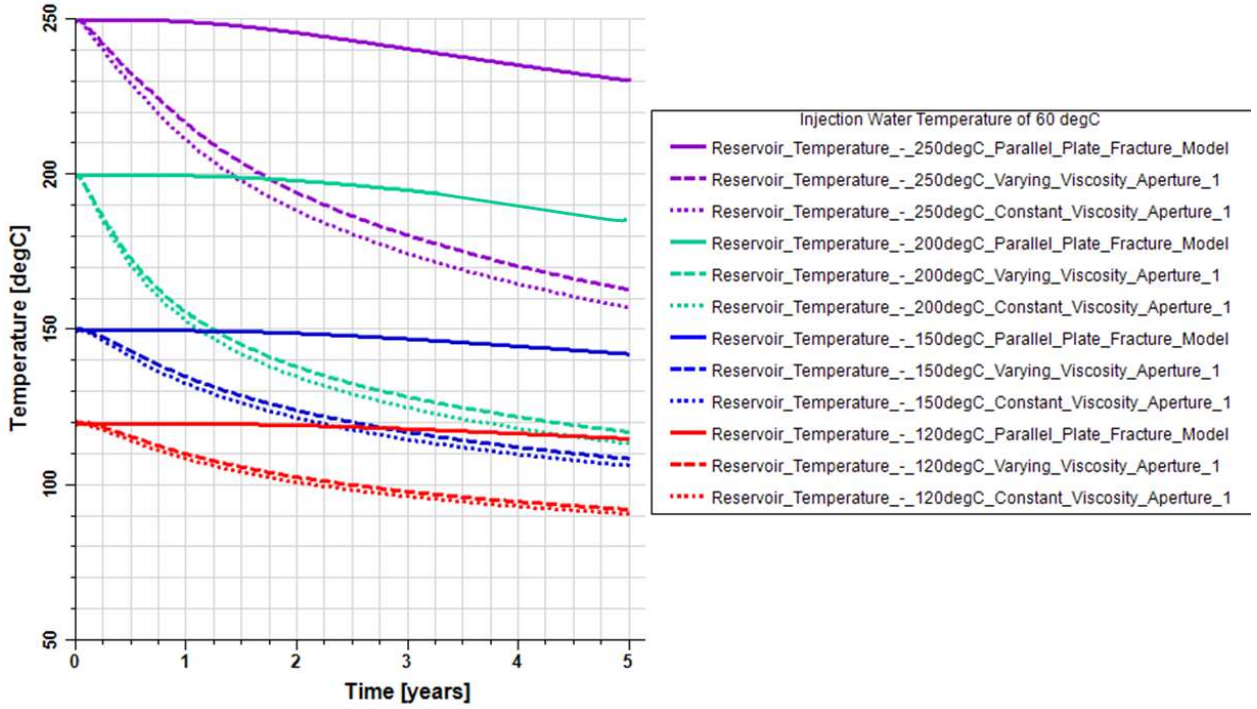


Figure 4.8: Temperature profile at the producer on Aperture 1 assuming constant viscosity, temperature-dependent viscosity for different reservoir temperatures, and injection temperature of 60 °C.

The differences seen between the temperature profiles of the constant viscosity model and the temperature-dependent model can be linked to the mobility term in Darcy’s law (Equation 4.5).

From Darcy’s law, the fluid velocity vector is given by:

$$\vec{v} = -\frac{k}{\mu}(\nabla P) \quad (4.5)$$

where k is the intrinsic permeability tensor of the rock matrix; μ is the fluid’s dynamic viscosity; and P is one of the independent variables, pressure. The mobility term is $\frac{k}{\mu}$. For a fixed flow rate (velocity \times area), an increase in the fluid’s viscosity in the system due to the reducing temperature of the rock would mean a decrease in velocity. Thus, to maintain the flow rate, more area is required. The reduced fluid mobility due to the increased

viscosity from rock temperature decrease leads to the fluid flowing in other paths of least resistance. Figure 4.13 shows the temperature of the aperture in the X-Y plane for the scenario of constant viscosity and temperature viscosity for a reservoir temperature of 200 °C and injection water temperature of 40 °C after five years of continuous fluid circulation. In Figure 4.13b, the circulating fluid can contact additional areas of the rock not contacted by the circulating fluid in the constant viscosity model. The ellipse on Figure 4.13b shows areas with extra thermal sweep due to alternative paths transversed by the liquid in the temperature-dependent viscosity model.

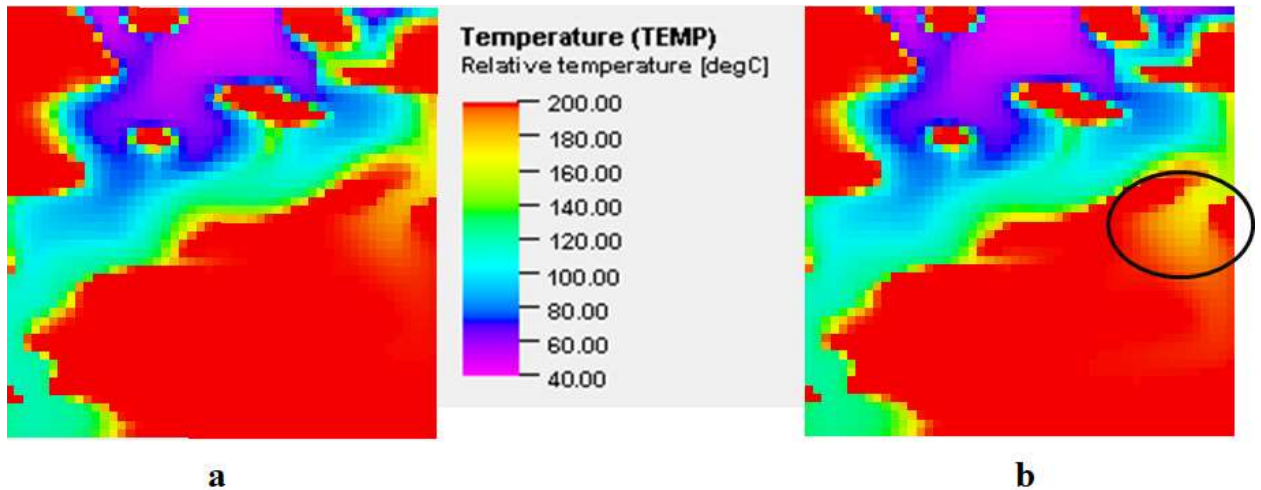


Figure 4.9: Temperature distribution at the fracture after five years in the X-Y plane. 13a is for constant viscosity, while 13b is for temperature-dependent viscosity. The reservoir temperature is 200 °C, while the injection water temperature is 40 °C.

4.4.4 Constant Viscosity vs. Temperature-Dependent Viscosity: Aperture 2

Figure 4.14 shows the thermal performance of the hypothetical EGS at the producer on Aperture 2 assuming constant viscosity and temperature-dependent viscosity for different reservoir temperatures and injection temperature of 40 °C. Compared to Aperture 1, due to the more distributed nature of the Aperture 2 fracture, the constant viscosity and temperature-dependent viscosity plots do not differ significantly from the results of assuming a smooth fracture. Again, it can be seen that as the difference between the reservoir temperature and injection water temperature reduces, the difference between the temperature profile of constant viscosity and temperature-dependent viscosity reduces.

Moreover, it can also be observed that at lower temperatures, the temperature profiles of the cases with varying spatial aperture are close to the temperature profile of the case assuming a constant aperture. For this reason, a similar plot for 60 °C was not shared as there were minimal differences between the results from the constant viscosity model and the temperature-dependent viscosity model.

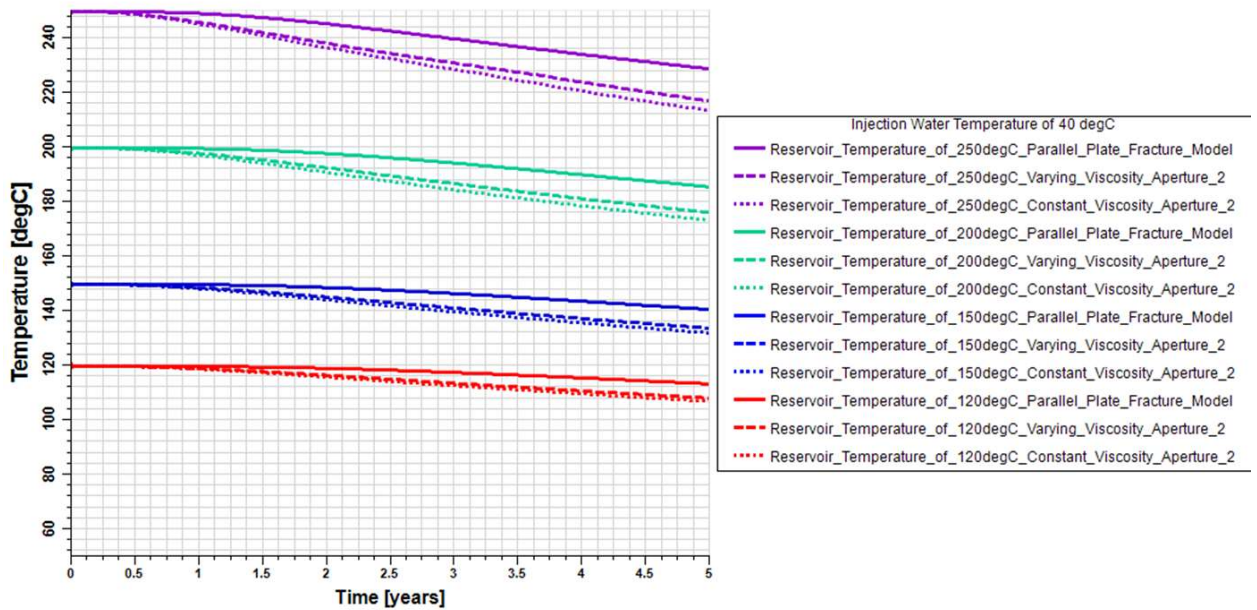


Figure 4.10: Temperature profile at the producer on Aperture 2 assuming constant viscosity and temperature-dependent viscosity for different reservoir temperatures and injection temperature of 40 °C.

The temperature distribution of the fracture on the X-Y plane for Aperture 2 after five years is shown in Figure 4.15. It reveals that a lot of rock area has been contacted by the fluid, which will lead to more heat extraction. Also, due to the more evenly distributed aperture, there is minimal difference seen between the temperature maps for the constant viscosity scenario and temperature-dependent viscosity scenario.

4.4.5 Constant Viscosity vs. Temperature-Dependent Viscosity: Aperture 3

Figure 4.16 shows the thermal performance of the hypothetical EGS at the producer for Aperture 3, assuming constant viscosity and temperature-dependent viscosity

for different reservoir temperatures and injection temperature of 40 °C. As in the previous cases, as the difference between the reservoir temperature and injection water temperature increases, the difference between the temperature profile of constant viscosity and temperature-dependent viscosity increases, and vice versa. However, the differences seen for this aperture are much more than were seen for Aperture 1 and Aperture 2.

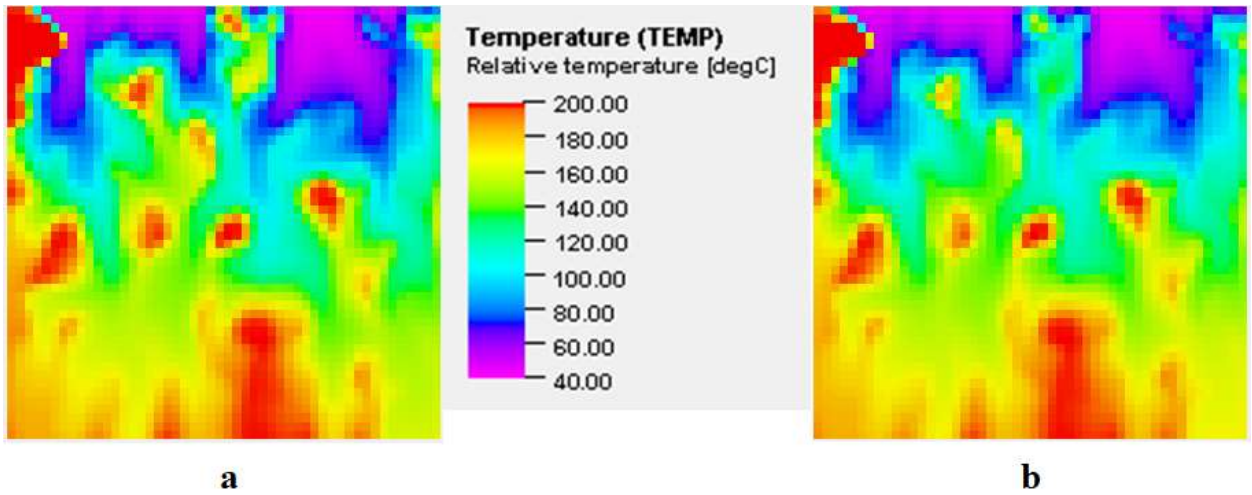


Figure 4.11: Temperature distribution at the fracture after five years in the X-Y plane. 15a is for constant viscosity, while 15b is for temperature-dependent viscosity.

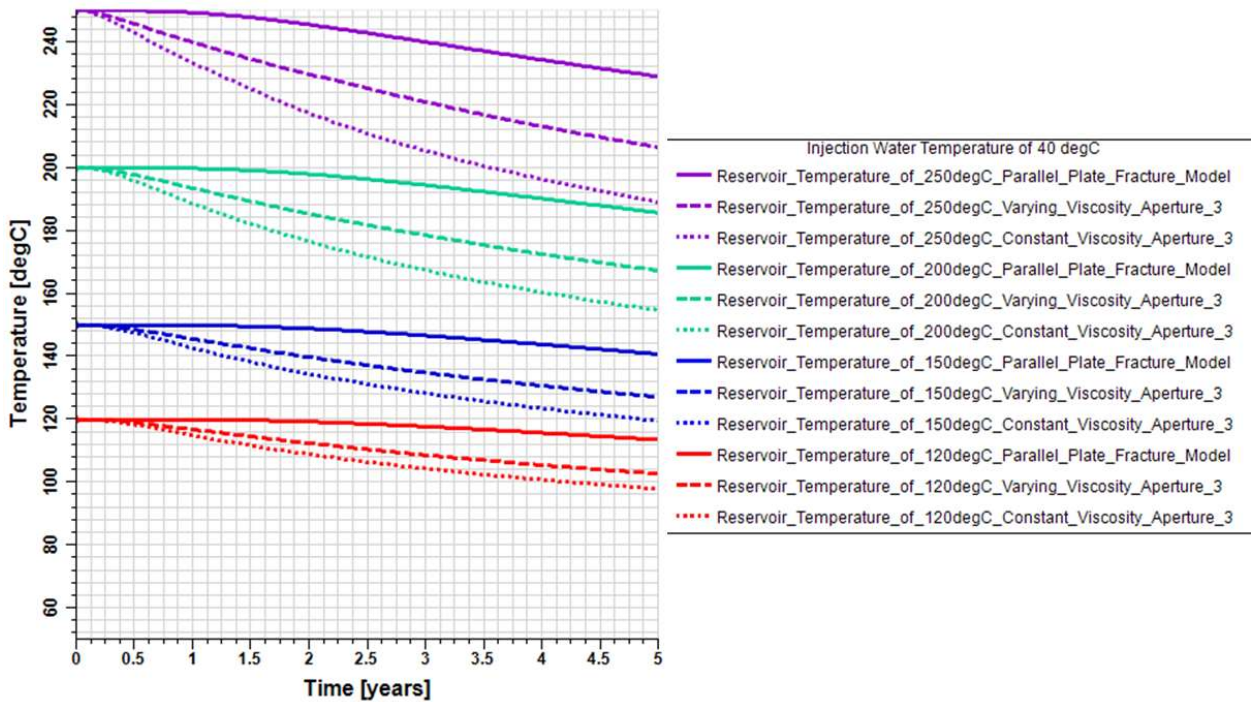


Figure 4.12: Temperature profile at the producer on Aperture 3 assuming constant viscosity, temperature-dependent viscosity for different reservoir temperatures, and injection temperature of 40 °C.

Aperture 3 is characterized by isotropic ranges of 200 m. The range indicates the length beyond which the spatial properties of the fracture would change. Thus, when modeling with constant viscosity, the fluid appears to remain predominantly within a specific portion of the fracture (Figure 4.10), leading to heat extraction concentrated on that region and thus higher thermal drawdown. This situation where fluid flow is predominantly in a section of the fracture is in contrast with Aperture 2 that has a smaller range allowing for more distributed flow. On the other hand, with the temperature-dependent viscosity scenario, as the mobility of the fluid reduces due to reduced temperature in the system, alternative preferential paths of least resistance are taken. Hence more heat is extracted from the rock resulting in a lower thermal drawdown than the model using constant viscosity.

Figure 4.17 shows the temperature at the aperture in the X-Y plane for the scenario of constant viscosity and temperature viscosity for a reservoir temperature of 200 °C and injection water temperature of 40 °C after five years of continuous fluid circulation for Aperture 3. As shown in Figure 4.17b, there is a better thermal sweep across the fracture

plane compared to Figure 4.17a (constant viscosity model). The right portion of Figure 4.17a is more cooled than the right side of Figure 4.17b, demonstrating that the fluid appeared to have taken alternative paths in areas that were not cooled, leading to higher temperatures at the producer.

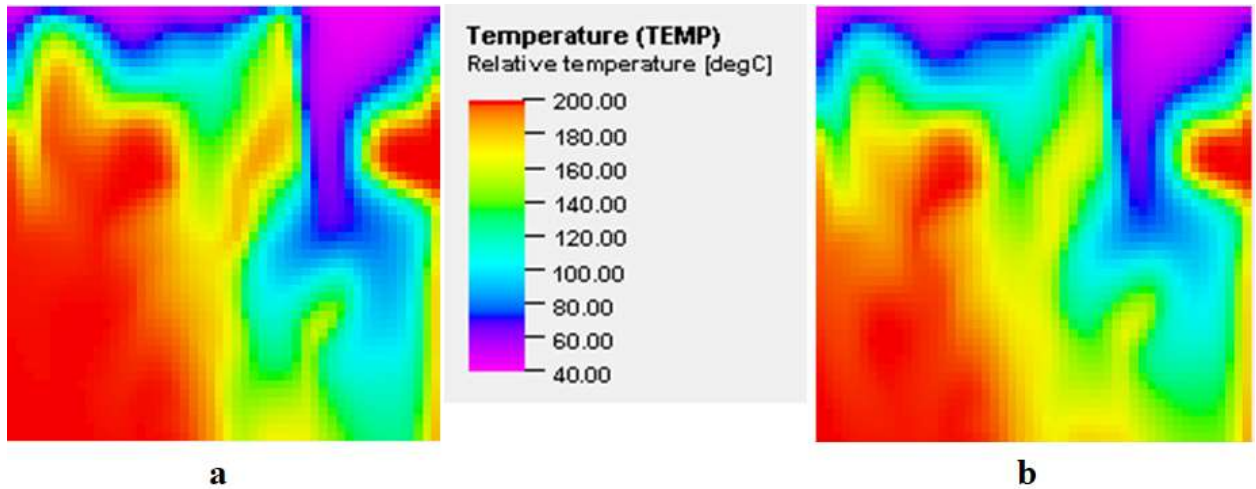


Figure 4.13: Temperature distribution at the fracture after five years in the X-Y plane. 17a is for constant viscosity, while 17b is for temperature-dependent viscosity.

A similar trend is seen when the injection water temperature is 60 °C as shown in Figure 4.18. As with Aperture 1, with a higher injection water temperature and lower difference between the reservoir temperature and injected water temperature, the difference between the profiles of the constant viscosity and temperature-dependent viscosity reduces.

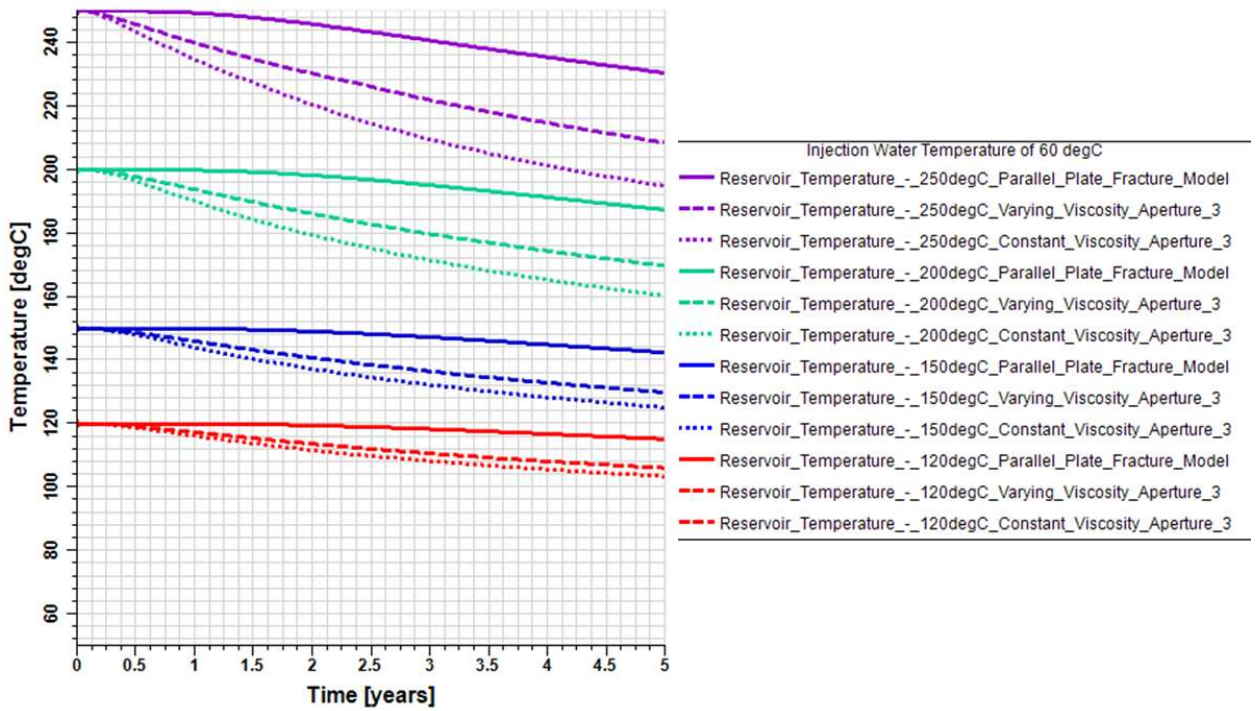


Figure 4.14: Temperature profile at the producer on Aperture 3 assuming constant viscosity and temperature-dependent viscosity for different reservoir temperatures and injection temperature of 60 °C.

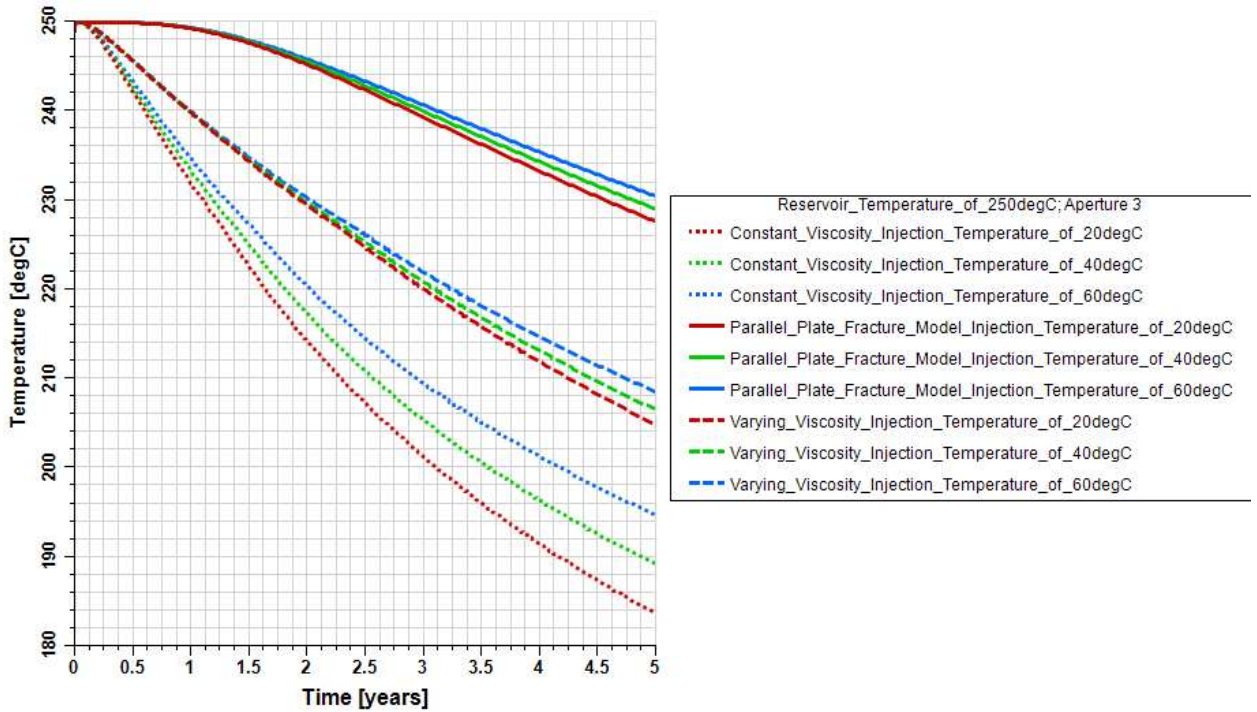


Figure 4.15: Temperature profile at the producer for Aperture 3 assuming constant viscosity and temperature-dependent viscosity for different injection temperatures and reservoir temperature of 250 °C.

The trend, including an injection water temperature of 20 °C is shown in Figure 4.19. In this case, only the reservoir temperature of 250 °C was considered. With lower injection water temperatures, the difference between the constant viscosity results and temperature-dependent viscosity results becomes amplified. This difference is shown in Figure 4.20. Also, as time elapses, the difference between the results from the constant viscosity model and the temperature-dependent viscosity model increases.

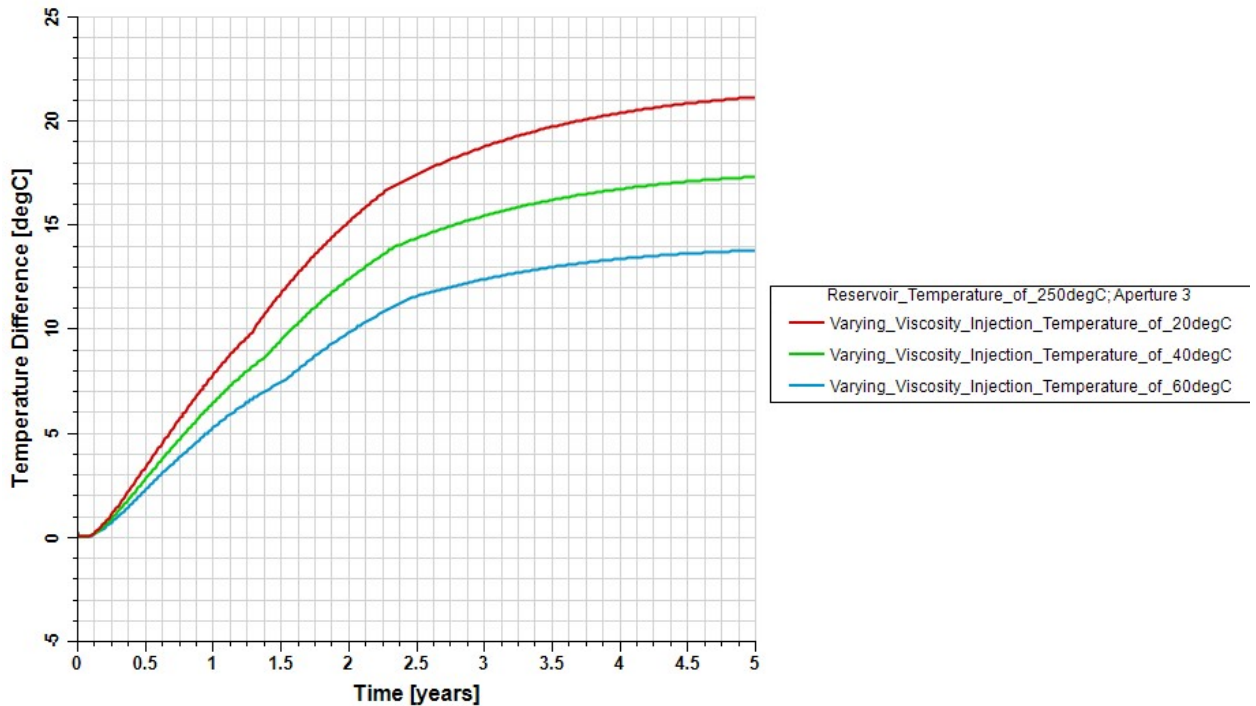


Figure 4.16: Difference between temperature profiles for constant viscosity and temperature-dependent viscosity models for different injection temperatures and reservoir temperature of 250 °C.

4.5 Summary

This study examined the impact of using a temperature-dependent viscosity in modeling the thermal behavior of injecting cold water into a single-fracture, hot, low-permeability system representing a hypothetical EGS. Different fracture aperture fields were analyzed using a thermohydraulic model. Average reservoir temperatures that ranged from 120 °C to 250 °C and water injection temperatures of 20 °C and 60 °C were considered. The results were compared with a model that uses constant viscosity.

The following were deduced from this study: -

- If the fracture aperture is considered to be uniform, there is a negligible difference between using constant viscosity and temperature-viscosity in the model. However, because actual fractures have spatial variations in their aperture, assuming a constant fracture aperture may result in an optimistic thermal performance prediction.
- Fracture apertures with spatial variations show lower thermal performance than a fracture aperture that is considered uniform. A higher degree of channeling and consequently lower area available for flow and heat transfer result in a higher difference between the thermal performance of a uniform aperture field and an aperture field with spatial variations. A higher degree of channeling was seen in the fracture with anisotropic aperture distribution.
- Fractures with lower ranges have more distributed flow than fractures with higher ranges. Consequently, there is a lower difference between the model with constant viscosity and the model with temperature-dependent viscosity for smaller ranges.
- The difference between the reservoir temperature and the injection water temperature is also a contributing factor to how much the results of a constant viscosity model would differ from a temperature-dependent viscosity model. The higher the temperature difference, the greater the results of the two models will differ.
- In general, for low reservoir temperatures, there is a slight difference between the constant viscosity model and a temperature-dependent viscosity model. On the other hand, reservoirs with high average temperatures show marked differences between the constant viscosity model and a temperature-dependent viscosity model.

The preceding conclusions imply that if an Enhanced Geothermal System is known to be channelized (perhaps through tracer tests) and the temperature difference between the reservoir and the injected fluid is high, then the temperature-dependent viscosity would be necessary for modeling the system to simulate its thermal performance better. On the other hand, if the aperture distribution of the Enhanced Geothermal System is evenly

distributed, a constant viscosity may suffice in simulating the process. Moreover, if the temperature difference between the reservoir and the injected fluid is low, a constant viscosity can be used in the model without significantly impacting computational accuracy. Overall a high correlation length leading to an increased area of preferential flow paths presents the most significant effect contributing to the differences seen between modeling with a constant viscosity or a temperature-dependent viscosity.

Chapter 5

5 Thermohydromechanical Modeling of Enhanced Geothermal Systems

5.1 Introduction

In the preceding chapters, one assumption made in the governing equations was that thermal stresses and changes in aperture due to cold water injection through hot rock were negligible. However, studies (Benson et al. (1987), Stefánsson (1997), Kaya et al. (2011), and Koh et al. (2011)) have shown that in systems where cold water is injected into hot rocks, some degree of thermal stress occurs impacting the fracture aperture and permeability. Hence, a rigorous approach to modeling the Enhanced Geothermal System will involve a thermohydromechanical modeling of the system.

Benson et al. (1987) observed permeability increase in a reservoir during cold-water reinjection. They analyzed the transient well injectivity data of three wells to understand the increase in permeability within the reservoir. Their analysis suggested that the observed permeability increase was due to thermal contraction and thermal stress cracking of the formation resulting from coldwater injection. Injectivity increase phenomena near the coldwater injector were also observed in geothermal reservoirs studied by Stefánsson (1997) and Kaya et al. (2011).

McDermott et al. (2006) investigated the influence of thermohydromechanical (THM) coupling on the heat extraction from fractured crystalline rocks using an experimentally validated geomechanical model. Their study indicated that preferential fluid flow paths might develop, depending on the mechanical and thermal stress releases that occur during intense exploitation of these systems.

Ghassemi and Govindarajan (2007) studied thermally-induced aperture changes in a one-dimensional system. They investigated the temporal variation of fracture aperture in response to the individual and combined effects of thermal stress and silica

dissolution/precipitation. The aperture change of a single fracture within an infinitely large reservoir was calculated and compared with numerical results in their work. The results showed that, for lower initial fracture apertures, the significant increase in fracture permeability and the associated pressure drop at the injection point were mainly attributable to thermoelastic effects. In contrast, the increase in fracture aperture near the production well was mainly due to silica dissolution. On the other hand, for larger initial apertures, silica precipitation/dissolution effects were minimal, and thermoelastic effects were prevalent.

Ghassemi et al. (2008) used analytical methods to investigate porothermoelastic effects of heat extraction on fracture aperture. Their study indicated that fracture aperture increases near the injection point due to thermally induced stresses and causes a reduction in fluid injection pressure. The thermoelastic effects dominated near the injection point compared to those of poroelasticity.

Pandey et al. (2017) investigated the effect of mechanical deformation on a typical Enhanced Geothermal System using a numerical approach where the fracture was treated as a thin porous layer. They observed that the injection of cold water into the hot rock resulted in the thermal contraction of the rock, which resulted in the reduction of the vertical compressive stress on the fracture wall. Hence, the fracture aperture increased. They also noted that the compressive stress outside the zone being cooled by the injected water experienced rebalancing of the weight of the overburden rock, hence in some areas of the fracture, there was fracture closure.

Liu, et al. (2019) carried out the thermohydromechanical modeling of a geothermal reservoir where permeability heterogeneities were considered. They determined that the injection of cold water into the reservoir caused the contraction of the permeable pathways, leading to channeling within the reservoir.

Several studies (e.g., Abelin, et al., 1991; Hakami and Larsson, 1996; Tsang and Neretnieks, 1998; Tester et al., 2006; Watanabe et al., 2008; Mattson et al., 2018; Co et al., 2017, Hawkins et al., 2017) indicate that there are spatial variations of fracture surfaces across different scales, and have demonstrated that varying fracture aperture can lead to flow channeling. The studies mentioned above on thermohydromechanical coupling in

Enhanced Geothermal Systems have not considered the spatial variations in fracture aperture.

Guo et al. (2016) developed a numerical model that fully couples the thermohydromechanical processes during heat production and quantitatively investigated nonuniform (i.e., heterogeneous) effects aperture on flow channeling in a single planar fracture. The aperture was treated as an autocorrelated random field across the fracture plane. They used a horizontal penny-shaped fracture in a large body of low-permeability hot crystalline rock. Fluid density and viscosity were assumed to be constant. Their study suggests that thermal breakthrough occurs earlier when accounting for thermal stresses. They also studied the effects of the correlation length and mean value of the aperture field on the thermal performance of EGS. They demonstrated that large spatial correlation lengths induced flow channeling.

The studies on thermohydromechanical modeling demonstrate that the thermomechanical influences on EGS are not negligible. Thus a rigorous approach to modeling Enhanced Geothermal Systems needs to consider the thermoelastic effects as part of the physical processes occurring within the system. The review of related literature demonstrates that there is limited knowledge on the quantitative effects of spatially heterogeneous fracture aperture on flow channeling. Consequently, in this chapter, the objective was to perform a thermohydromechanical modeling of a hypothetical Enhanced Geothermal System. The fracture was considered to have an anisotropic aperture distribution. First, the thermohydromechanical model was verified against an analytical model. Then the model was applied to study the short-term thermoelastic effect on a mesoscale analog Enhanced Geothermal System. Subsequently, the model was applied to a case with an anisotropic heterogeneous aperture to determine if accounting for thermomechanical influences would change how favorable a flow configuration would be towards the thermal performance of an Enhanced Geothermal System.

5.2 Methodology

5.2.1 Formulation of the problem

A combination of thermal (T), hydraulic (H), and mechanical (M) physical processes are expected to influence the energy extraction from the system consisting of a low permeability rock having significant temperature difference between the injectate and the rock as fluid flows within a single fracture.

The transport mechanism in the system involves heat conduction by contact between the rock and fluid, advection, and also mass transport in the fluid. The conductive heat exchange between the injected water and the impermeable rock, and the convective heat transfer as the injected water flows within the fracture, results in some thermal stress on the system. The changes in the effective stress as water is injected results in changes in the fracture aperture.

The following assumptions were considered in setting up the system to be modeled: -

- The fluid circulating throughout the system is single phase and remains in the liquid state throughout the duration of the simulation.
- Fluid flow is in the laminar regime, with Reynold's number low enough to allow the application of Darcy's law.
- There is no gas trapped in the rock fracture.
- Fluid-rock interaction such as chemical dissolution/deposition is minimal and can be ignored.

The overall process is summarized in the flow chart in Figure 5.1.

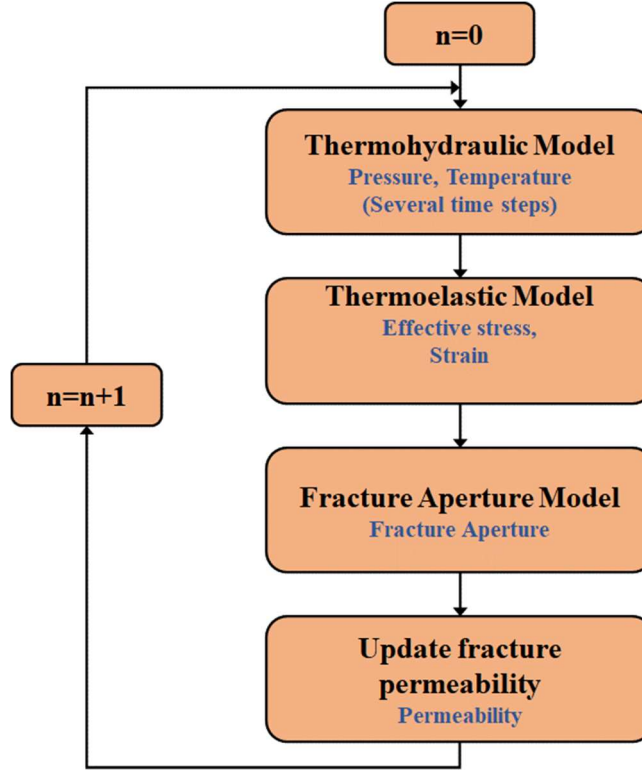


Figure 5.1: Thermohydromechanical workflow used in this study.

5.2.2 Relevant Equations for the Coupled Thermohydromechanical Process

This section deals with the relevant equations related to the coupled thermohydromechanical process taken from the work by Shao (1997) and implemented in VISAGE, the software used for this aspect of the study.

5.2.2.1 Governing Equations

The equation for mechanical equilibrium is given by:

$$\text{div}(\sigma) = 0 \quad (5.1)$$

where σ is the stress tensor.

The fluid diffusivity equation is given by:

$$\frac{k}{\mu} \nabla^2 p = \frac{1}{M} \frac{\partial p}{\partial t} + b \frac{\partial \epsilon_{kk}}{\partial t} - 3\alpha_m \frac{\partial T}{\partial t} \quad (5.2)$$

where k is the permeability of the porous medium, μ is the fluid viscosity, M is Biot's modulus, p is pressure, t is time, b is known as Biot's coefficient, ϵ_{kk} is the volumetric strain, α_m is the drained isochoric thermal fluid mass change coefficient, and T is the temperature.

The heat diffusivity equation is given by:

$$\lambda \nabla^2 T = C_\epsilon^0 \frac{\partial T}{\partial t} - 3\alpha_m T_0 \frac{\partial p}{\partial t} + 3\alpha_0 K_0 T_0 \frac{\partial \epsilon_{kk}}{\partial t} - \frac{k C_p}{\mu} \bar{\nabla} p \cdot \bar{\nabla} T \quad (5.3)$$

where λ is the thermal conductivity of the rock, C_ϵ^0 is the drained isochoric heat capacity of the porous medium, α_0 is the drained thermal expansion coefficient of the porous medium, K_0 is the bulk modulus of the equivalent material, T_0 is the initial temperature, and C_p is the specific heat capacity of the fluid.

5.2.2.2 Constitutive Equations

The constitutive equations are based on simple linear thermoporoelasticity theory.

$$\sigma - \sigma_0 = D^0 : \epsilon - b(p - p_0)I - 3\alpha_0 K_0 (T - T_0)I \quad (5.4)$$

$$p - p_0 = M \left[-b\epsilon_{kk} + \frac{m}{\rho_0^f} \right] + 3\alpha_m M (T - T_0) \quad (5.5)$$

$$s - s_0 = 3\alpha K \epsilon_{kk} + \frac{C_\epsilon}{T_0} (T - T_0) + \left[s_m^0 + \frac{3\alpha_m M}{\rho_0^f} \right] m \quad (5.6)$$

where $\sigma - \sigma_0$ is the change in stress, $p - p_0$ is the change in pore pressure, $s - s_0$ is the variation of entropy of the porous system, α is the undrained linear thermal expansivity of the porous system, C_ϵ is the undrained isochoric heat capacity of the porous medium, s_m^0 is the fluid entropy at initial conditions, m is the relative fluid mass change per unit volume, ρ_0^f is the initial fluid density, and D^0 represents the drained elastic stiffness matrix given by Equation 5.7.

$$D^0 = \frac{E}{(1+\nu)(1-2\nu)} \begin{bmatrix} (1-\nu) & \nu & \nu & & & \\ \nu & (1-\nu) & \nu & & & \\ \nu & \nu & (1-\nu) & & & \\ & & & (1-2\nu) & & \\ & & & & (1-2\nu) & \\ & & & & & (1-2\nu) \end{bmatrix} \quad (5.7)$$

with the independent parameters being Young's Modulus E and Poisson's Ratio ν . The shear modulus G for the material is then given by:

$$G = \frac{E}{2(1+\nu)} \quad (5.8)$$

The coupling parameters include:

$$b = 1.0 - \frac{K_0}{K_m} \quad (5.9)$$

$$\frac{1}{M} = \frac{b-\phi}{K_m} - \frac{\phi}{K_f} \quad (5.10)$$

$$\alpha_m = (b - \phi)\alpha_0 + \phi\alpha_f \quad (5.11)$$

where K_m is the bulk modulus of the solid phase, K_f is the bulk modulus of the fluid, ϕ is porosity, and α_f is the thermal expansion coefficient of the fluid.

The compatibility equations relate the strain to displacements by:

$$\epsilon_{ij} = \frac{1}{2}(u_{i,j} + u_{j,i}) \quad (5.12)$$

where u denotes the displacement.

The boundary Γ is divided into two parts — traction and displacement boundaries.

$$u_i = \bar{u}_i, \quad \text{on } \Gamma_u \text{ (displacement condition)} \quad (5.13)$$

$$t_i = \bar{t}_i, \quad \text{on } \Gamma_\sigma \text{ (traction condition) (where traction } t_i = \sigma_{ij}n_j) \quad (5.14)$$

Solving the constitutive, compatibility, and equilibrium equations with the boundary conditions will provide the stress, strain, and displacement fields. For the software used in this study (VISAGE), these are solved using the Galerkin finite element method.

5.3 Software used

In the previous chapters, heat transport and fluid flow were coupled in a thermohydraulic model. To account for porothermoelasticity, the thermohydraulic process was coupled with a geomechanical process. This coupling was achieved using ECLIPSE and VISAGE numerical engines with a user interface and post-processor provided by PETREL software. The thermohydraulic process of EGS heat extraction was modeled using ECLIPSE thermal compositional numerical simulator. ECLIPSE is a finite-difference simulator and is run in the fully implicit mode.

VISAGE is a general solver for finite-element geomechanics. A sequential coupling methodology is used between the two software. When fluid flows through the ECLIPSE grid, the pore pressure and temperature changes computed from ECLIPSE result in the deformation of cells in VISAGE, which affects pore volumes, pressure, and temperature. This coupling methodology, which is two-way, allows several timesteps to be run in ECLIPSE for each step in VISAGE because the fluid flow occurs a lot faster than the geomechanical and thermoelastic deformation.

At a given coupled time step, the rock strain state will determine the aperture. Then the effective permeability is computed using the updated aperture results from VISAGE. Figure 5.2 shows the interaction between the different components of the thermohydromechanical process.

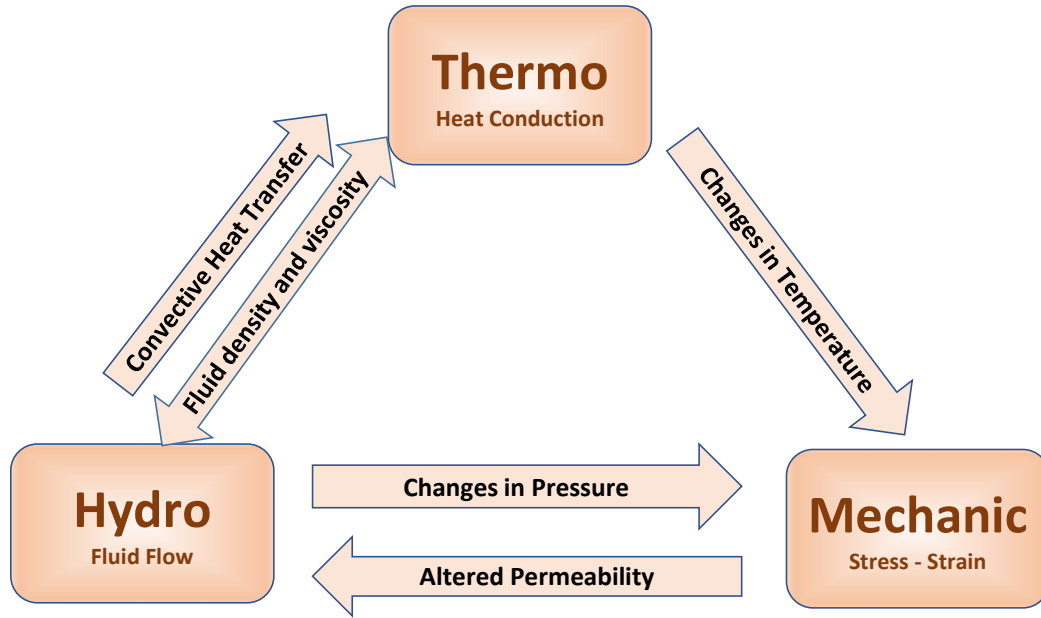


Figure 5.2: Interaction between the different processes in the two-way thermohydraulic coupling between ECLIPSE (thermohydraulic model) and VISAGE (geomechanical model).

The fracture is characterized as a porous medium with porosity set as 0.99, while the heterogeneous permeability is defined by the local cubic law, which is represented by equation 5.15.

$$k_{fij} = \frac{b_{ij}^2}{12} \quad (5.15)$$

where k_f , i , j , and b , are the effective permeability, grid number in the x-direction, grid number in the y-direction, and local fracture aperture.

5.4 Permeability Updating

For a body restricted from deformation, thermal stresses are generated due to the change in temperature of the rock as the fluid is being injected. The rock will change its shape or volume due to the temperature change. This change is the thermal strain, which occurs due to the thermal stresses, will develop in sections where the body is not restricted from deformation. The rock is constrained from expansion or contraction at the fixed boundaries. Three-dimensional strain is computed within the software. However, the net

strain in the x- and y-direction are much less than in the z-direction. Thus, the change in rock thickness resulting from the temperature difference between the rock and injectate is assumed to occur in the z-direction. Moreover, since no displacement occurs at the boundaries of the rock, any elongation or reduction in height is also assumed to occur at the fracture since the rock is not restricted from deformation at that end. An expansion of the rock will reduce the aperture, while a contraction of the rock will increase the aperture. The expansion or reduction in aperture is explained in Figure 5.3. Once the new fracture aperture is determined for each time step, the fracture permeability is updated using Equation 5.15 and used in the next time step.

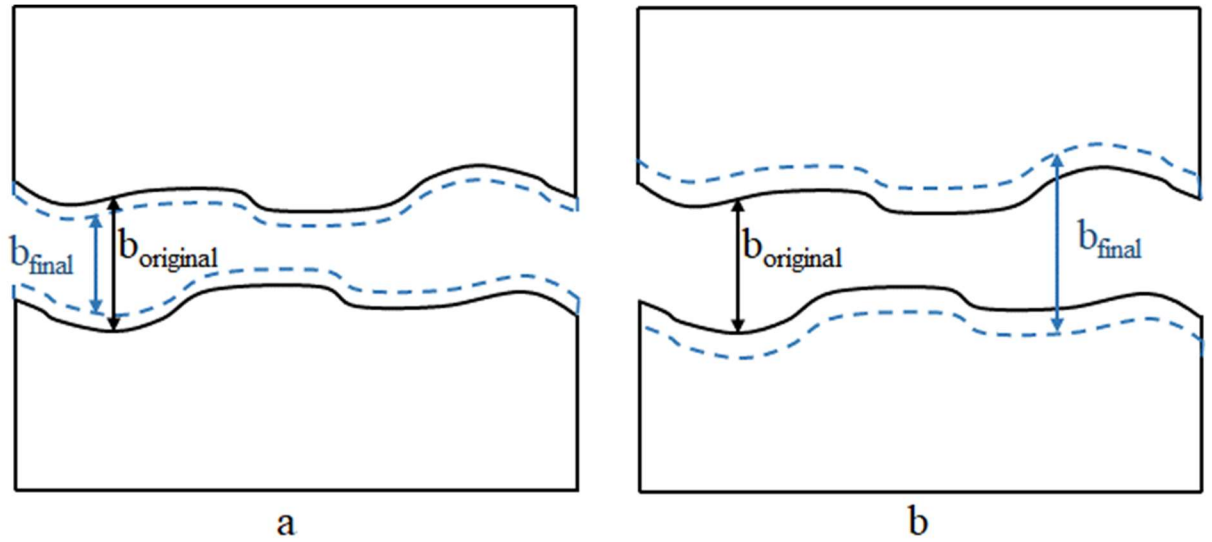


Figure 5.3: Schematic of how the aperture is assumed to change with changes in strain. In Figure 5.3a, the rock is expanding; hence the aperture is reducing. In Figure 5.3b, the rock is contracting, leading to an increase in the aperture.

The fracture aperture under applied stress is also dependent on the fracture stiffness. According to Bai & Elsworth (1994), the change in hydraulic conductivity, K , of a single fracture set that accounts for the solid deformation of the matrix and stiffness of the fracture is given by:

$$\Delta K = \frac{\rho g b^3}{12z\mu} \left[1 + \Delta\epsilon \left(\frac{K_n b}{E} + \frac{b}{z} \right)^{-1} \right]^3 \quad (5.16)$$

where K_n is the stiffness of the matrix, b is the fracture aperture and z is the thickness of the matrix block. Though the ratio K_n/E varies, studies that a value of 0.1/cm is a reasonable value to use (Bai & Elsworth, 1994). Equation 5.16 is used to update the permeability considering the fracture stiffness.

5.5 Verification

Before applying the thermohydromechanical model to the case studies, the model was verified against the numerical model in the work by Guo et al. (2016). Table 5.1 shows the parameters used in the model. The model in the work by Guo et al. (2016) had a penny-shaped fracture, whereas the fracture was rectangular in the model used for this study. Guo et al. investigated how thermal drawdown can induce channeling in Enhanced Geothermal Systems, where they simulated fractures with several heterogeneous aperture distributions and the impact of thermohydromechanical modeling on channeling. Their study had a case of a homogeneous fracture plane. Figure 5.4 shows their results of the homogeneous fracture plane with results of a heterogeneous fracture plane. The verification exercise was done against the homogeneous fracture plane, and results were compared for five years. The initial pore pressure in the study was 34 MPa. At the boundaries, the vertical stress (which was the minimum principal stress) was 64 MPa, the minimum horizontal stress was 70 MPa, and the maximum horizontal stress was 100 MPa at the fracture depth.

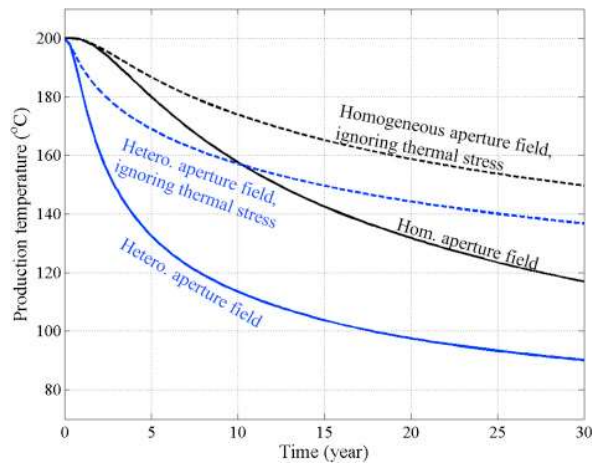


Figure 5.4: Comparing the thermohydraulic and thermohydromechanical models for a single fracture with homogeneous and heterogeneous apertures (Guo et al., 2016).

Table 5.1: Parameters used in the thermohydrromechanical model verification

Symbol	Description	Value	Units
φ	Porosity of the formation	0.01	-
k	Permeability of the formation matrix	1×10^{-20}	m^2
q_o	Constant injection rate	12.5	m^2/s
w_0	Initial aperture	0.00024	m
ν	Poisson's Ratio	0.25	-
α_T	Linear thermal expansion coefficient of rock matrix	8×10^{-6}	1/K
T^Δ	Temperature difference between the rock and the injected fluid	150	K
K_r	Thermal conductivity of rock	3.5	W/m/K
ρ_r	Rock solid density	2500	kg/m^3
ρ_f	Fluid density	887.2	kg/m^3
p_r	Reference pressure for fluid density	34	MPa
T_r	Reference temperature for fluid density	200	degC
C_r	Specific heat capacity of rock	790	J/kg/K
C_f	Specific heat capacity of fluid	4460	J/kg/K
μ	Dynamic fluid viscosity	1.42×10^{-4}	$\text{Pa}\cdot\text{s}$
α_f	Volumetric thermal expansion coefficient of fluid	7.66×10^{-4}	1/K
β_f	Fluid compressibility	5.11×10^{-10}	Pa^{-1}
G	Rock shear modulus	20	GPa

5.1 Application of Thermohydrromechanical Modeling to the Altona Field Laboratory

In an investigation by Hawkins et al. (2020), the spatial distribution of groundwater fluid flow paths in a mesoscale field laboratory (Altona Field Laboratory) was identified by combining principal component analysis, machine learning (genetic algorithm), and joint pressure-tracer calibration. The resulting nonuniform fracture aperture distribution was subsequently employed in a thermohydraulic model to forecast the thermal evolution of the production well. These predictions were then compared to the actual, measured values

previously reported in Hawkins et al. (2017a, 2018). The resulting nonuniform aperture field predicted a 4 °C rise in production well temperature after roughly 26 to 40 h of continuous reservoir heating, whereas measured thermal breakthrough occurred after seven hours. For comparison, a uniform fracture aperture predicts thermal breakthrough in about two months.

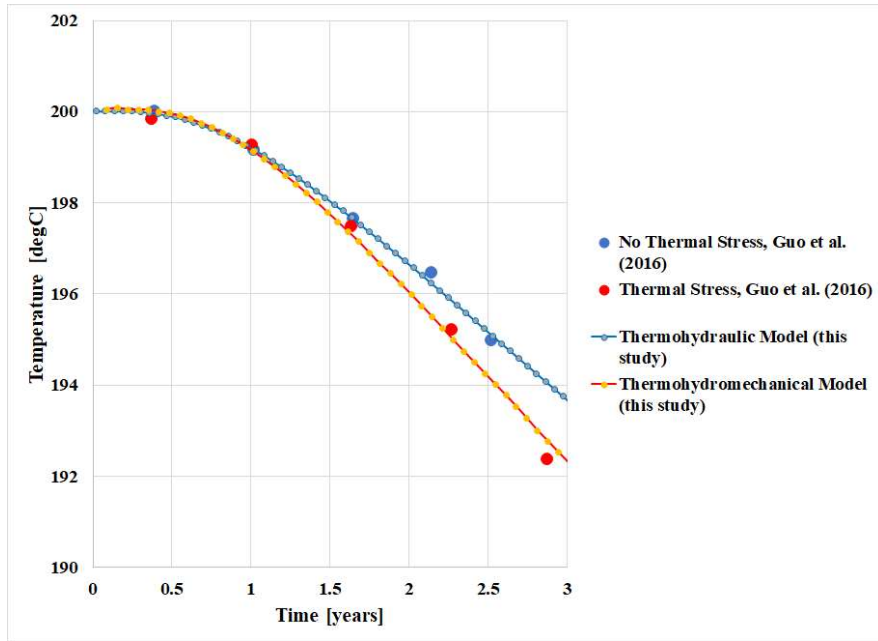


Figure 5.5: Comparing the results of this study with the results from Guo et al. (2016) for three years.

As the experiment progressed, the temperatures measured were increasingly different from the predicted temperatures. According to Hawkins et al. (2018), possible causes for the deviation include uncertainty in the adsorption reaction parameters; mismatch in the tracer return curves; accuracy of the tracer sampling and analysis instrument; or thermal-mechanical influences which may have caused the flow path to change due to the fracture closing upon heating the reservoir.

The objective of this section of the study was to investigate if accounting for thermal-mechanical influences could explain the differences between the measured and predicted temperatures of the analog mesoscale EGS experiment. The system was modeled as a coupled thermohydromechanical (THM) system where a thermal reservoir simulator was used in combination with a geomechanical simulator.

5.1.1 The Analog Geothermal Reservoir - Altona Field Laboratory

The Altona Field Laboratory (AFL) is a mesoscale site located in northeastern New York State near the USA/Canadian border. The formation is the Potsdam Sandstone, which is a well-cemented sandstone of nearly pure quartz. Since the first five wells were drilled in 2004, the 10 m x 10 m five-spot well configuration has been the target of numerous investigations on flow channeling in sparsely-spaced fracture planes (Figure 5.6). The target fracture was a subhorizontal bedding plane located roughly 7.6 m below ground surface (Hawkins et al., 2017). Based on the combined results of numerical models, adsorbing tracer tests, Ground Penetrating Radar (GPR) surveys, and Fiber-Optic Distributed Temperature Sensing (FO-DTS), a narrow channel roughly 1-2 m wide spans the 14.1 m distance between well 204 to the west and well 304 to the east. A tracer test was performed in 2016 using inert carbon-cored nanoparticles (Hawkins et al., 2017), and the tracer return curve matched the expectation of the flow channel that was deduced from the study. Also, a heat exchange experiment was conducted in 2015 (Hawkins et al., 2017, 2018), which is described below.

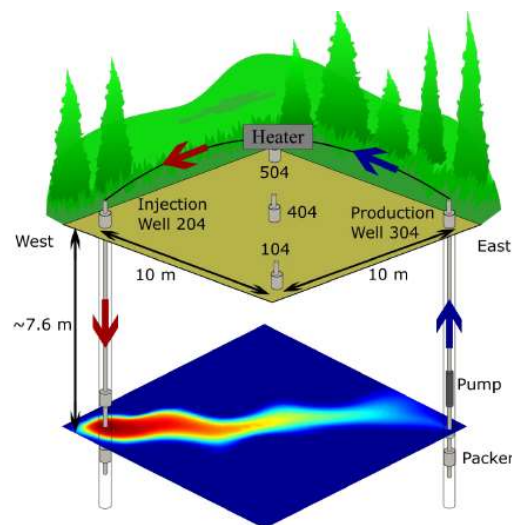


Figure 5.6: Three-dimensional schematic of the Altona Field Laboratory (AFL) showing the spatial configuration of injection well 204 and production well 304 and three monitoring wells (104, 404, and 504) (Hawkins et al., 2017).

5.1.2 The Altona Field Heat Transport Experiment

In the fall of 2015, the Altona field site served as an analog mesoscale geothermal reservoir. For six days, hot injection water (74 °C) was circulated at a flow rate of 5.7 L/min through the cold ambient formation (11.7 °C) between the injection well (204) and production well (304) separated by 14.1 m (Figure 5.6). During reservoir heating, thermal sensors measured temperature rise at the production well and three monitoring wells. Temperature rise was also measured in 10 dry observation wells in the rock above the fracture equipped with a fiber-optic cable network and a Fiber-Optic Distributed Temperature Sensor (FODTS) (Hawkins et al., 2017).

After six days, the fracture fluid temperature rise ranged from 0.9 °C to 31.1 °C within the 10 m × 10 m field. The thermal sensor network recorded the largest temperature rise in the direct path between the injector and producer. A thermohydraulic model was used to estimate the temperature rise of the fluid at the production well. As the experiment progressed, the production well temperatures measured were increasingly greater than the predicted temperatures (Figure 5.7). By the end of the 6-day experiment, production well temperature rose to a final temperature of 29.1 °C. According to Hawkins et al. (2018), possible causes for the deviation include uncertainty in the adsorption reaction parameters; mismatch in the tracer return curves; accuracy of the tracer sampling and analysis instrument; or thermal-mechanical influences which may have caused the flow path to change due to the fracture closing upon heating the reservoir.

The numerical simulation model was a 50 × 50 × 70 grid representing the x, y, and z axes for this study. While each cell measure 0.32 m X 0.32 m in area, the thickness differed across the model ranging from 0.005 (at the fracture) to 5m far away from the fracture. Figure 5.8 shows the mesh for the thermohydraulic model. The model includes a single injector/producer well-pair with working fluid circulation through a single fracture within the cold, impermeable rock. Hot water is cooled by the surrounding rock and then recovered at the production well. Thermal stresses are assumed to accumulate as the target fracture experiences nonuniform heating induced by circulation through the heterogeneous plane.

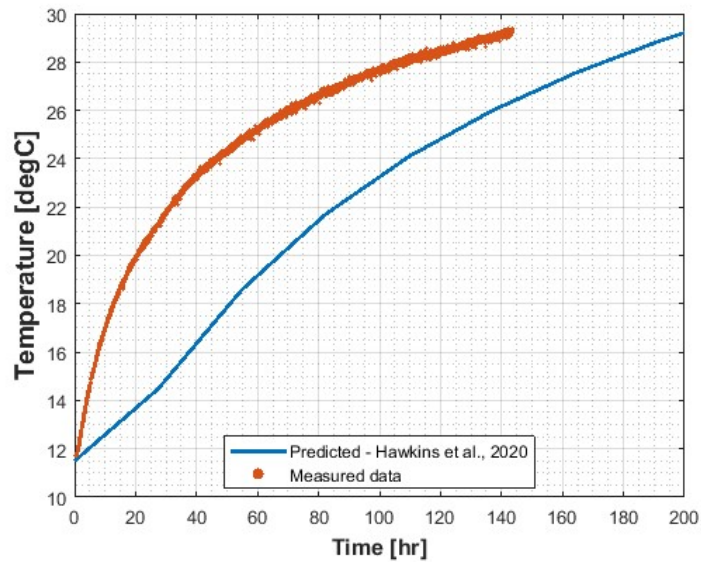


Figure 5.7: Comparison between the predicted data and the observed data for the Altona Field Heat Transport Experiment (Hawkins et al., 2020).

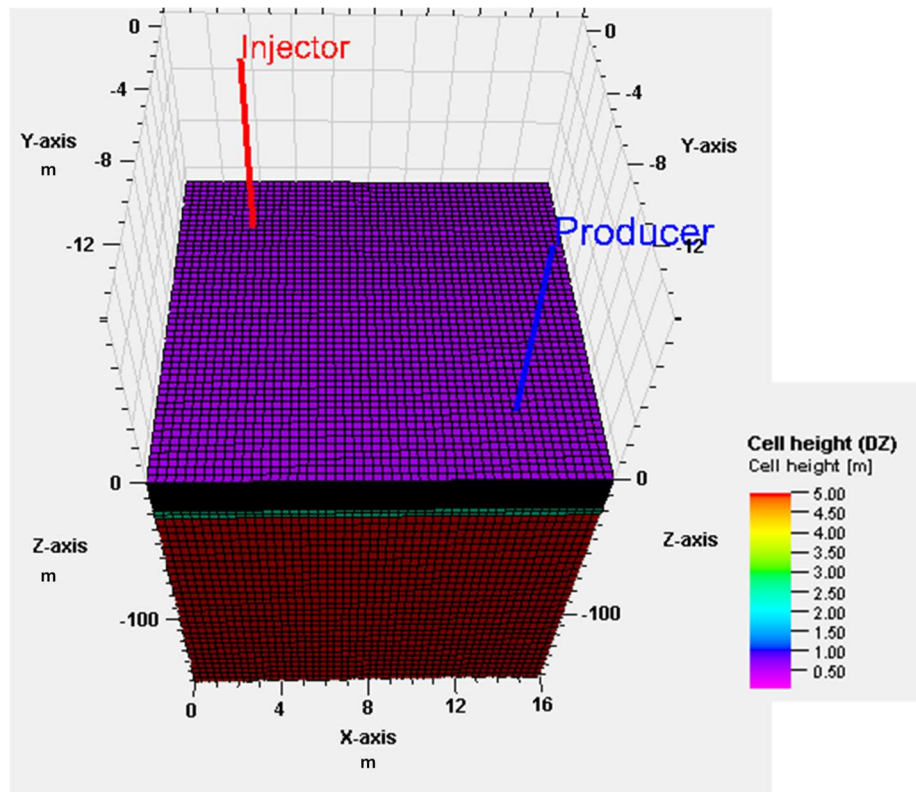


Figure 5.8: Three-dimensional mesh for the thermohydraulic model representing the Altona Field Laboratory (AFL).

5.1.3 Determination of the aperture distribution

The permeability distribution adopted in the current study resulted from a machine learning algorithm that used a joint pressure-tracer calibration to identify the spatial distribution of fracture aperture at the Altona Field Laboratory (AFL) (Hawkins et al., 2020). Here, the employed aperture distribution is the aperture distribution reported in Hawkins et al. (2020) that best fits three data sets. These data sets include (1) inert tracer breakthrough curve using C-Dot nanoparticles; (2) inter-well frictional pressure loss between the injector and producer; and (3) temperature rise at the production well as a function of reservoir heating. Figure 5.9 shows the thermohydraulic model with the permeability distribution on the fracture plane.

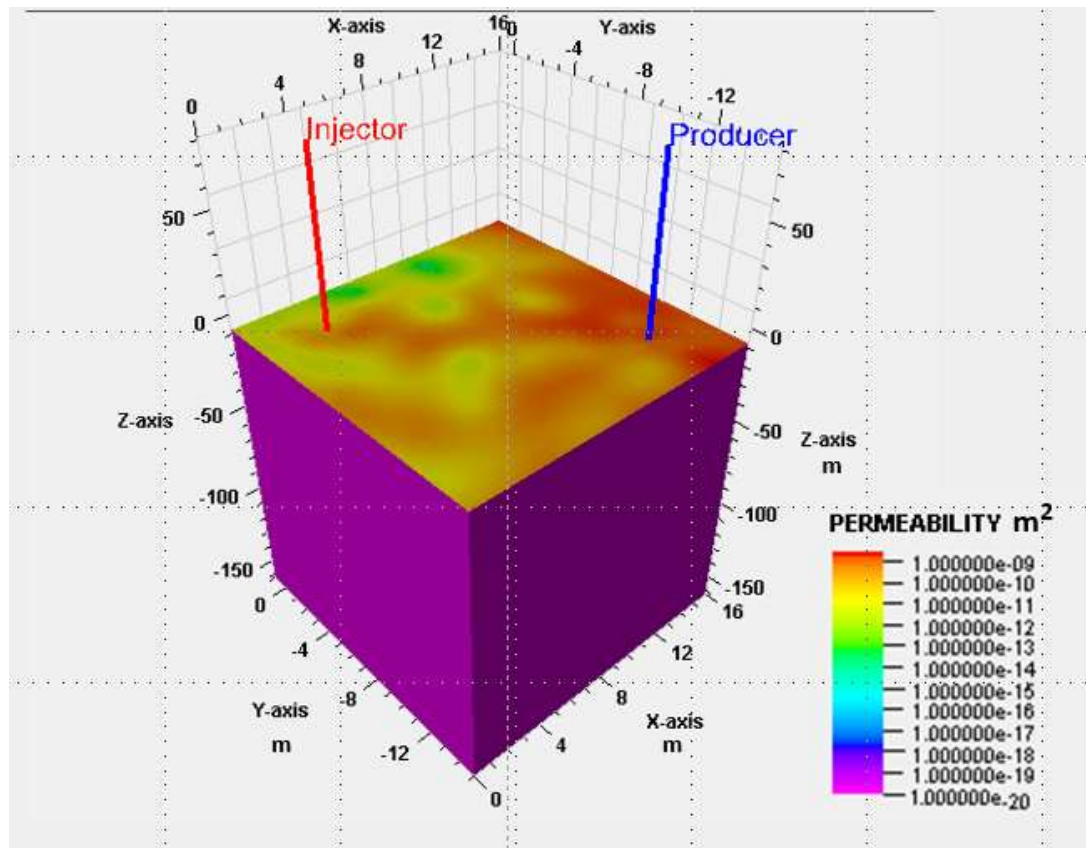


Figure 5.9: Schematic of the thermohydraulic model with the fracture plan exposed to show the heterogeneous permeability distribution.

5.1.4 Modeling with Temperature-Dependent Viscosity

One of the assumptions in the model by Hawkins et al. (2020) was that the viscosity was constant throughout the simulation. However, as shown in Chapter 4, when there are spatial variations in the fracture aperture and a significant difference between the injection temperature and the reservoir temperature, the effects of using constant viscosity may not be negligible. Consequently, before performing the thermohydraulic modeling, the thermohydraulic model was rerun with temperature-dependent viscosity.

From the plot in Figure 5.10, though the curve from the model with temperature-dependent viscosity is close to the observed at later times, it does not account for the early thermal breakthrough seen in the measured data. Both the constant viscosity and temperature-dependent viscosity thermal drawdown curves do not match the early time behavior of the observed data.

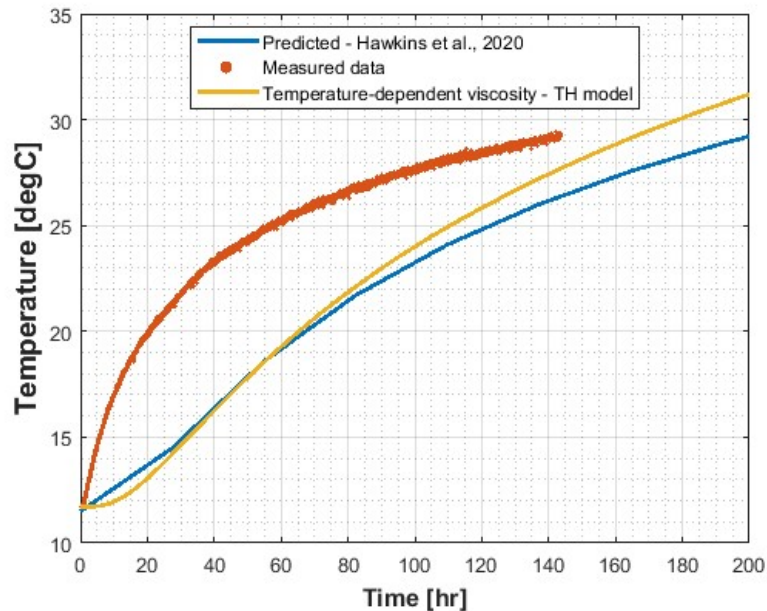


Figure 5.10: Plot of the thermal drawdown using temperature-dependent viscosity in the model along with the observed and predicted data for the Altona Heat Transport Experiment.

5.1.5 Geomechanical Model Description and simulation domain

The thermohydraulic model was embedded within the geomechanical simulation domain. The geomechanical model had geometrically gridded cells out from the reservoir model,

i.e., the mesh became progressively coarser at locations farther from the fracture. The dimensions of the coupled simulation domain are approximately $125\text{ m} \times 125\text{ m} \times 200\text{ m}$. This grid dimension is much larger than the domain in which heat transfer was determined to have occurred at the Altona Field Laboratory. Thus, this domain is considered adequate to simulate the constraints of the Altona far-field. The simulation domain is shown in Figure 5.11. The computational domain consists of approximately 414,720 elements.

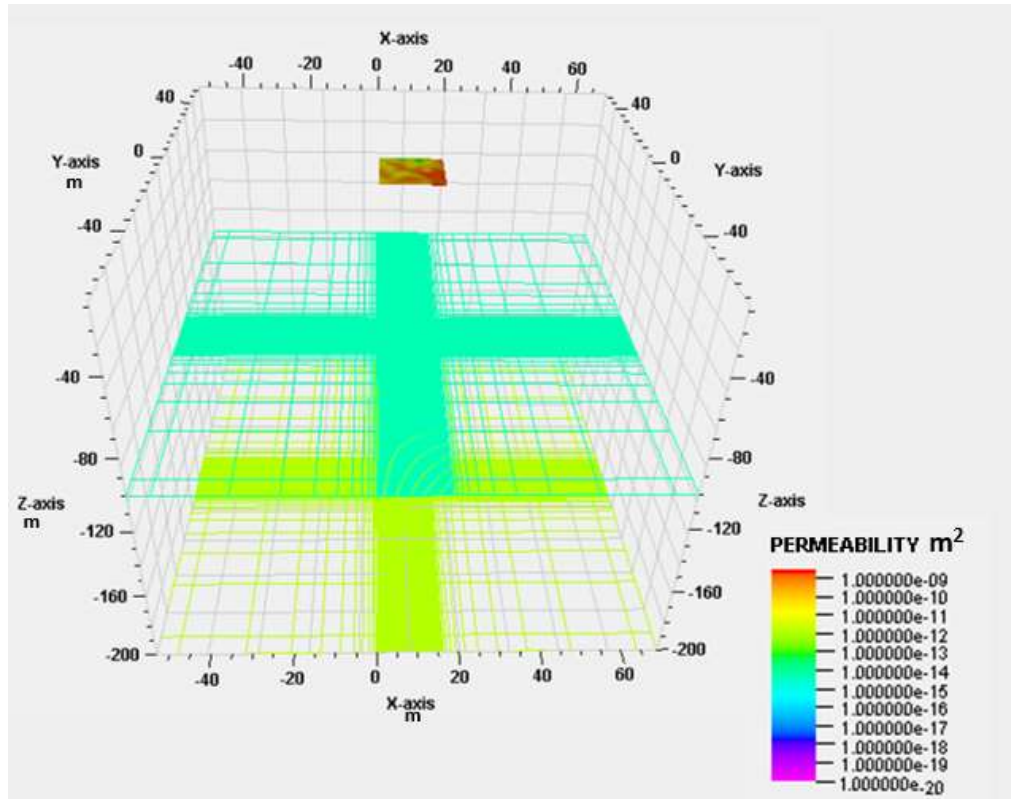


Figure 5.11: Fracture from the thermohydraulic (TH) model embedded within the geomechanical model. The dark color shows the degree of refinement of the model. The grids become coarser away from the TH model for the geomechanical model.

The principal stresses imposed on the model and referenced for the fracture depth of 7.6 m include 0.29 MPa for the vertical stress (using an overburden of 0.025 MPa/m and surface pressure of 0.101325 MPa); 0.48 MPa for the minimum horizontal stress (two times the minimum principal stress); and 0.67 MPa for the maximum horizontal stress (three times the minimum principal stress). Pore pressure was determined using a normal hydrostatic gradient of freshwater at 0.01 MPa/m resulting in 0.177 MPa at the fracture depth. The maximum water injection pressure was 0.185 MPa, and throughout the

simulation, the fluid pressure remained below the minimum principal stress. These parameters were chosen to ensure a subhorizontal fracture was mimicked, and the fracture did not propagate during the simulation. Additional rock and fluid properties used in the simulations are presented in Table 5.2, taken from Hawkins et al. (2018) and Merxhani (2016).

Table 5.2: Rock and fluid properties, and other parameters used for the Altona Field Laboratory Case Study

Symbol	Description	Value	Units
ϕ	Porosity of the formation	0.01	-
k	Permeability of the formation matrix	1×10^{-20}	m^2
	Rock solid density	2500	kg/m^3
E	Rock Young's Modulus	50	GPa
ν	Poisson's Ratio	0.25	-
Kr	Thermal Conductivity of rock	7.6	W/m/K
Cr	Specific heat capacity of rock	1000	J/kg/K
α	Linear thermal expansion coefficient of rock matrix	1.3E-05	1/K
μ	Dynamic Fluid viscosity (constant case)	0.0001	Pa*s
P	Reference pressure for constant fluid viscosity	101.325	KPa
T	Reference temperature for constant fluid viscosity	74	$^{\circ}\text{C}$
Cp	Specific heat capacity of fluid	4200	J/kg/K
β	Volumetric thermal expansion coefficient of fluid	0.00077	1/K
ρ	Reference fluid density	1000	kg/m^3
P	Reference pressure for fluid density	101.325	KPa
T	Reference temperature for fluid density	15.6	$^{\circ}\text{C}$

5.1.6 Results and Discussion

5.1.6.1 Spatial Results

The results for six days of continuous fluid circulation are presented and discussed here. Figure 5.12 shows the spatial distributions of the fracture aperture, thermal stress, and energy flow paths based on the thermohydromechanical model. Figure 5.12 also includes

the temperature map at the fracture plane for the thermohydraulic model and the thermohydronechanical model. The time stamps presented are eight hours into the experiment and one day and five days of continuous fluid circulation. For results interpretation, it should be noted that compressive stresses are taken as positive while tensile stresses are negative.

With sustained hot water injected, the heating up of the rock results in the expansion of the rock in the regions in contact with the hot water. The expansion of the rock causes a reduction in the fracture aperture. As time progresses, the aperture reduces further in the region near the injection well. This reduction in aperture is seen in Figure 5.12 in the row for apertures, where the location of the injector is dark blue.

The changes in the fracture aperture are a direct consequence of the changes in thermal stress due to hot water injection. Figure 5.12 in the row for thermal stress shows that there is increased compressive thermal stress in the region where there is flow of energy as a result of the hot water injected into the cold rock. There are also some regions of increased tensile stress around the compressive thermal stress regions caused by redistribution of the vertical stress within the rock body. The compressive thermal stress reduces the aperture. Thus, nearer the injection well where the compressive thermal stress is highest, the aperture is reduced more.

A comparison of the temperature maps of the thermohydraulic model and the thermohydronechanical model shows minimal differences. In the case of the thermohydronechanical model, near the injection point, the area that is heated up reduces with time compared to the thermohydraulic model. This slight temperature difference is not sufficient to cause a significant change in the thermal breakthrough curve, as seen in Figure 5.13, despite the increase in compressive thermal stress and reduction in fracture aperture. Possible reasons for the negligible impact of thermoelasticity in the Altona field include the low fluid injection rate, which is not sufficient to cause considerable differences in heat exchange though there are changes in the fracture aperture; and with the fracture aperture reduction near the injection point, the fluid moves further in the preferential path (which should cause channelized flow) but also contacts cooler rock in the areas of increased tensile stress, which counteracts the effect of channelized flow.

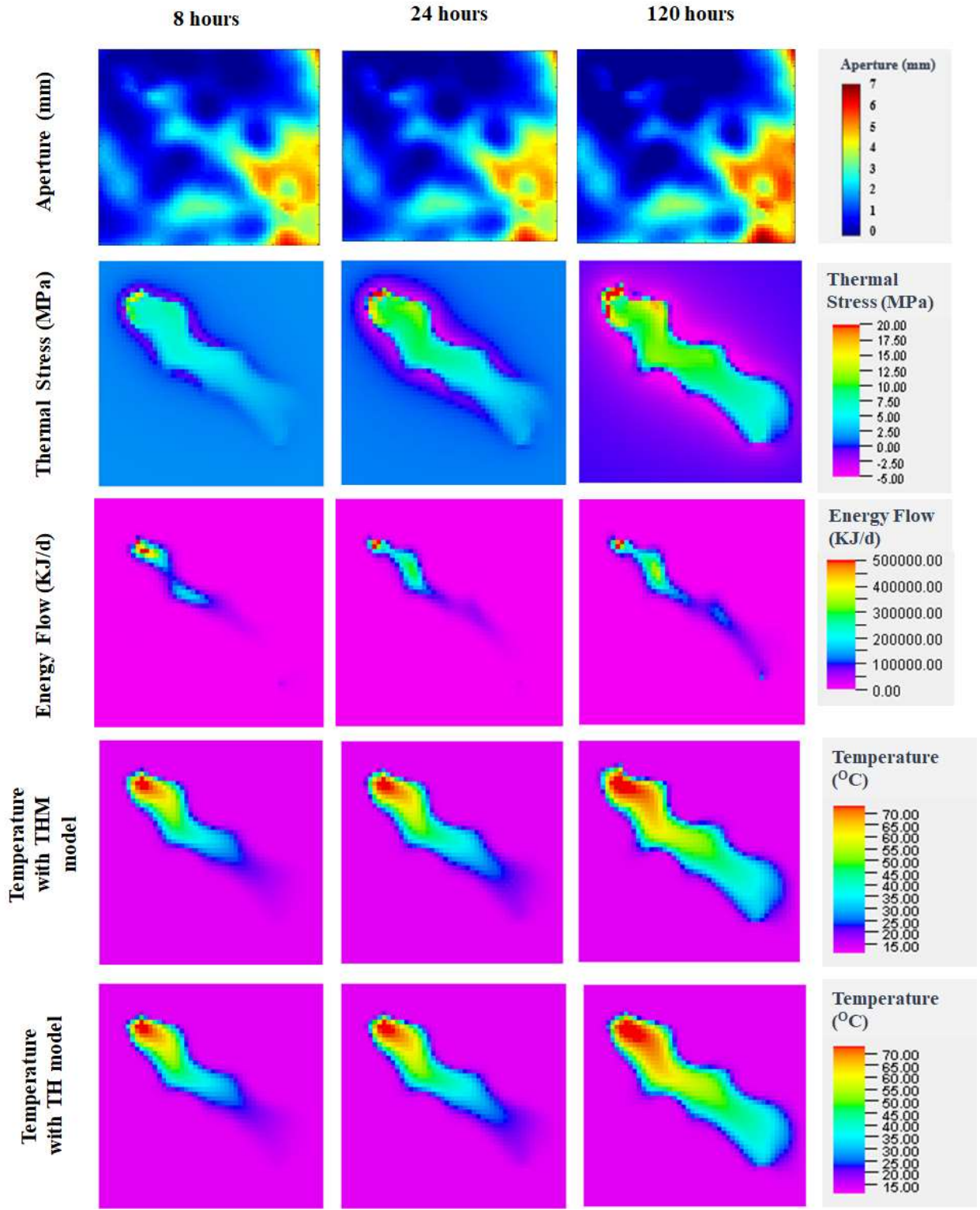


Figure 5.12: Evolution of fracture aperture distribution, thermal stress, energy flow paths, and the temperature distribution for the Altona field case study. The “THM model” includes the thermoelastic effects the “TH model” does not include thermoelastic effects.

5.1.6.2 Summary of findings on the application of thermohydraulic modeling in the Altona Field Laboratory

An analog mesoscale Enhanced Geothermal System has been modeled. The injection of hot water into the cold rock has been demonstrated to lead to the creation of thermal stresses within the rock body. In this field, the fracture was characterized by spatial variations, and the presence of thermal stress led to the reduction of fracture aperture.

The thermohydraulic model could not account for the differences in measured temperature from the predicted temperature. Similarly, the thermohydraulic model did not match the observed data, including the early breakthrough time seen in the observed data. Though there were thermal-mechanical effects, they were insufficient to cause significant changes to the thermal drawdown curves, perhaps due to the low injection rate or minor scale of the reservoir.

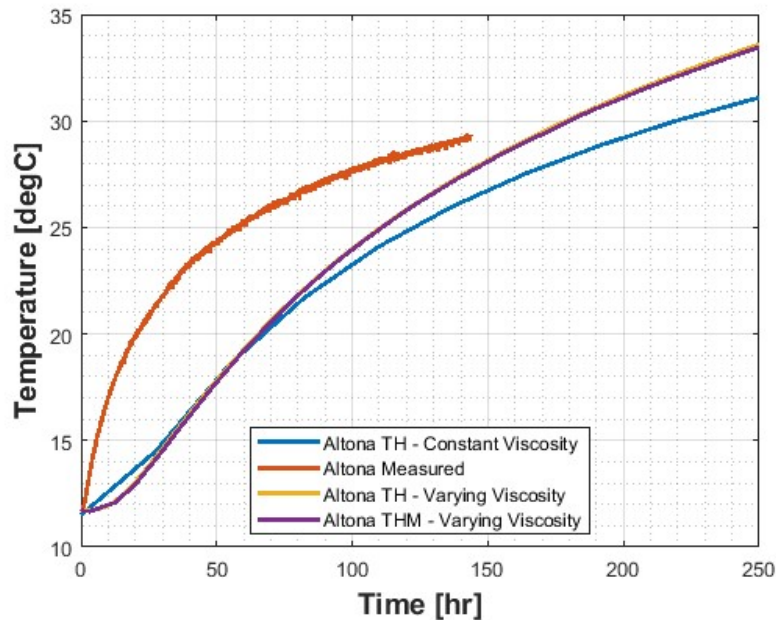


Figure 5.13: Production well fluid temperature for the thermohydraulic (THM) model and the thermohydraulic (TH) model along with the measured data at the Altona Field Laboratory.

5.2 Application of Thermohydronechanical Modeling to Anisotropic Aperture Distributions

The study on the Altona Field Laboratory demonstrated how thermal stresses could lead to changes in the fracture aperture. In this section, an investigation was carried out to determine how flow channeling is impacted by thermoelasticity on anisotropic fracture surfaces.

Two aperture distributions were studied in this section based on the hypothetical Enhanced Geothermal System modeled in Chapter 3. The first was one of the anisotropic distributions where the flow was favorable in the perpendicular flow configuration. The aperture distribution had a geometric anisotropy ratio of 2, with the range in the y-direction being 60 m and the range in the x-direction being 120 m. The temperature difference between the perpendicular flow configuration and the parallel flow configuration one year into the simulation was 26.2 °C.

The second aperture distribution was favorable in the parallel flow direction. The geometric anisotropy ratio was 4. The ranges in the y- and x- directions were 60 m and 240 m. The temperature difference between the flow configurations was -3.56 °C at one year into the simulation. In addition to modeling the scenario with horizontal wells, a case of the same aperture distribution with vertical wells and the horizontal fracture was included. This inclusion of vertical wells scenario was because in literature, most studies investigating the impact of thermohydronechanical coupling on single fractures, especially with spatial variations, have used the vertical wells – horizontal fracture configuration (example, Guo et al., 2016; Pandey et al., 2017).

Additional parameters were required to couple the thermohydraulic model to the geomechanical model. These parameters are documented in Table 5.3 and were taken for typical values of a granitic rock.

The geomechanical grid measured 4000 m by 4000 m by 2600 m with the thermohydraulic model embedded at its center. The areas close to the thermohydraulic model were gridded finely, while locations far from the thermohydraulic model were coarse to manage computational time. Figure 5.14 shows the grid and model extent.

Because a reverse faulting regime is being mimicked, at the reservoir depth of 1200 m, the vertical stress was 400 bar, the minimum horizontal stress was 600 bar, and the maximum horizontal stress was 700 bar.

Table 5.3: Additional parameters required for the thermohydrmechanical model

Symbol	Description	Value	Units
ν	Poisson's Ratio	0.25	-
α_T	Linear thermal expansion coefficient of rock matrix	8×10^{-6}	1/K
E	Rock Young's modulus	50	GPa

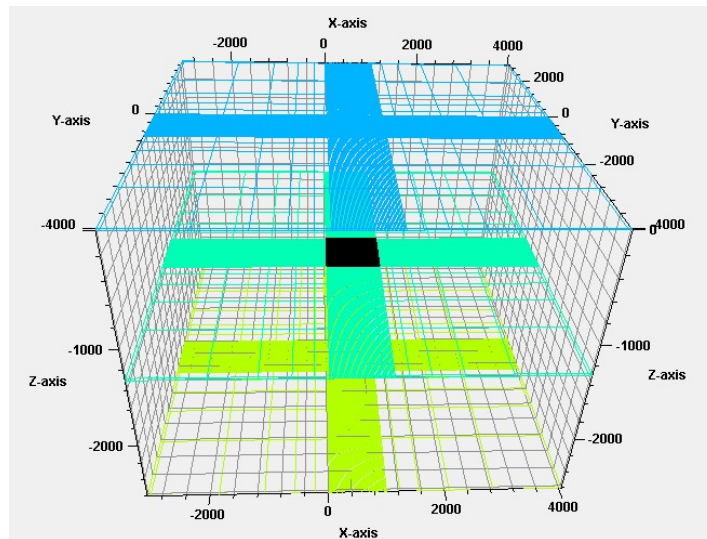


Figure 5.14: Grid of the thermohydrmechanical model. The area colored in black shows the location of the fracture embedded within the grid.

5.2.1 Results and Discussion

5.2.1.1 Thermohydrmechanical modeling for the aperture distribution with thermal drawdown in favor of the perpendicular flow configuration

Figure 5.15 shows the original aperture distribution of the first case that was studied for thermohydrmechanical effects. The thermal drawdown curves for both flow configurations using a thermohydraulic model and a thermohydrmechanical model are

presented in Figure 5.16. The curves of the thermohydromechanical model show higher temperatures compared to the curves of the thermohydraulic models. This is true for both flow configurations. However, the thermal drawdown is less with the thermohydromechanical model in the parallel flow configuration.

Evaluating the flow and temperature maps help to understand the trend seen in Figure 5.16. Figure 5.17 is the aperture distribution, flow map, and temperature map one month into the simulation. A similar figure is given in Figure 5.18 for one year into the simulation.

Figures 5.17 and 5.18 show that with the injection of cold water into the hot rock, the rock contracts and the aperture increases in areas contacted by the fluid. The opening up of the aperture allows the fluid to contact more areas of the rock initially closed due to mismatched asperities. This is more prominent in the parallel flow configuration, where higher flow rates are seen in the flow maps and more area is cooled in the temperature map, suggesting more heat extraction. While this occurs in the perpendicular flow direction, it is not as much as in the parallel case due to the high degree of tortuosity and channeling in the perpendicular flow configuration.

This analysis suggests that if thermoelasticity is considered in the modeling, for cases where there is a marginal difference in thermal drawdown between the perpendicular flow and parallel flow in the thermohydraulic model, the final result may be that there is still not much difference between the two flow configurations.

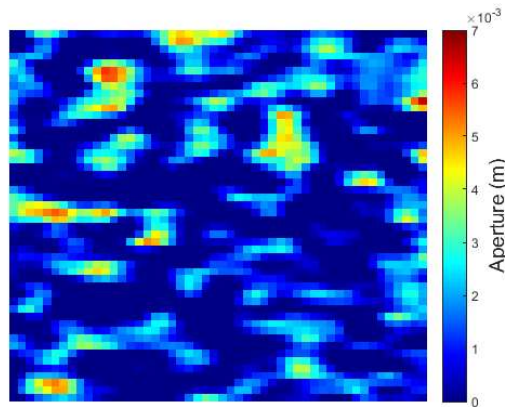


Figure 5.15: Original aperture distribution used for the thermohydromechanical model where thermal drawdown was in favor of the perpendicular flow configuration.

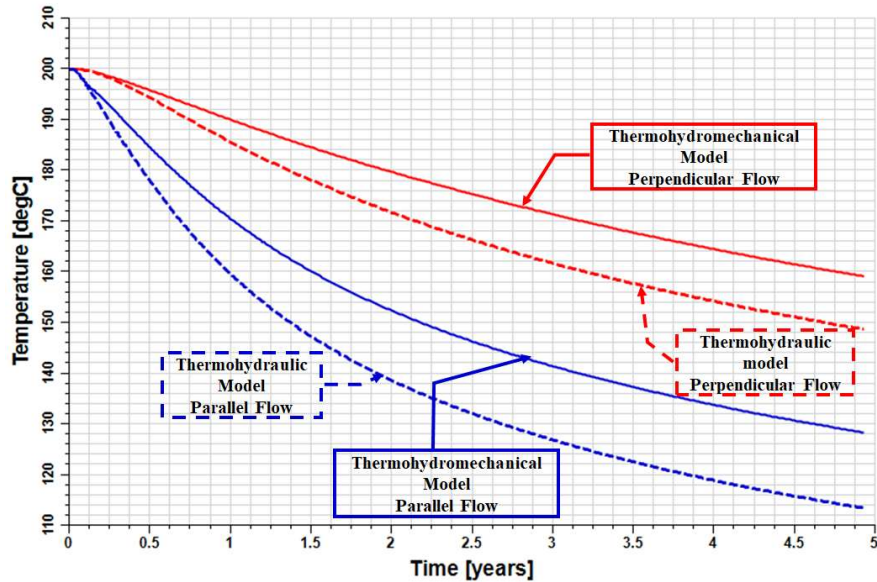


Figure 5.16: Thermal drawdown curves of the thermohydraulic and thermohydromechanical models for the perpendicular and parallel flow configuration.

5.2.1.2 Thermohydromechanical modeling for the aperture distribution with thermal drawdown in favor of the parallel flow configuration

For the second case in which thermohydromechanical effects were studied, the original aperture distribution as shown in Figure 5.19 is the original aperture distribution. Because an additional case with vertical wells was investigated, Figure 5.20 shows the location of the vertical wells as well as the location of the horizontal wells for a perpendicular flow configuration. The vertical wells were placed 465 m apart in a zone of good connectivity between the wells. The thermal drawdown curves for the flow configurations and the vertical well using a thermohydraulic model and a thermohydromechanical model are presented in Figure 5.21.

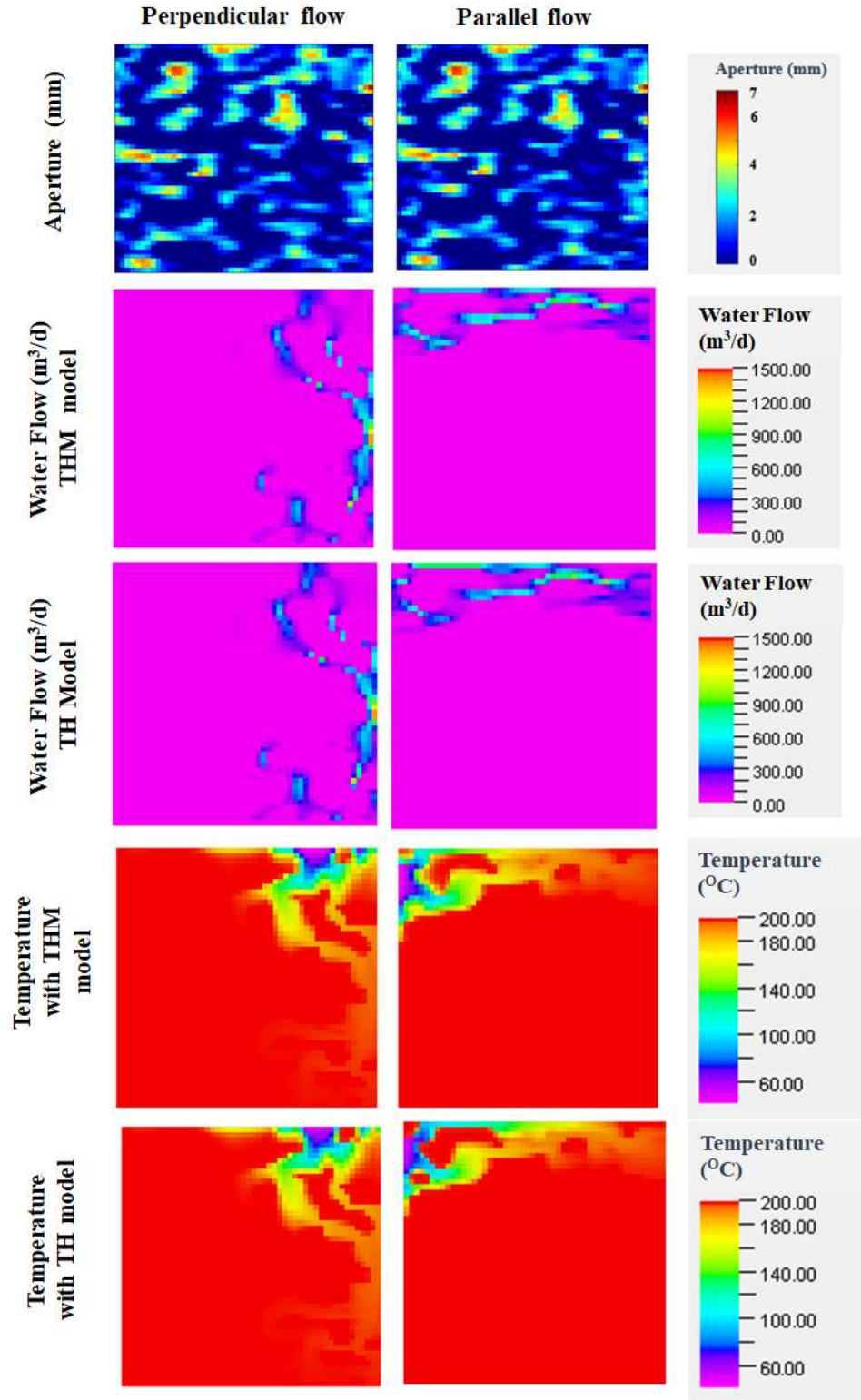


Figure 5.17: Comparison between the aperture, temperature, and flow maps for the thermohydraulic and thermohydromechanical model one month into the simulation – Perpendicular and Parallel flow configurations.

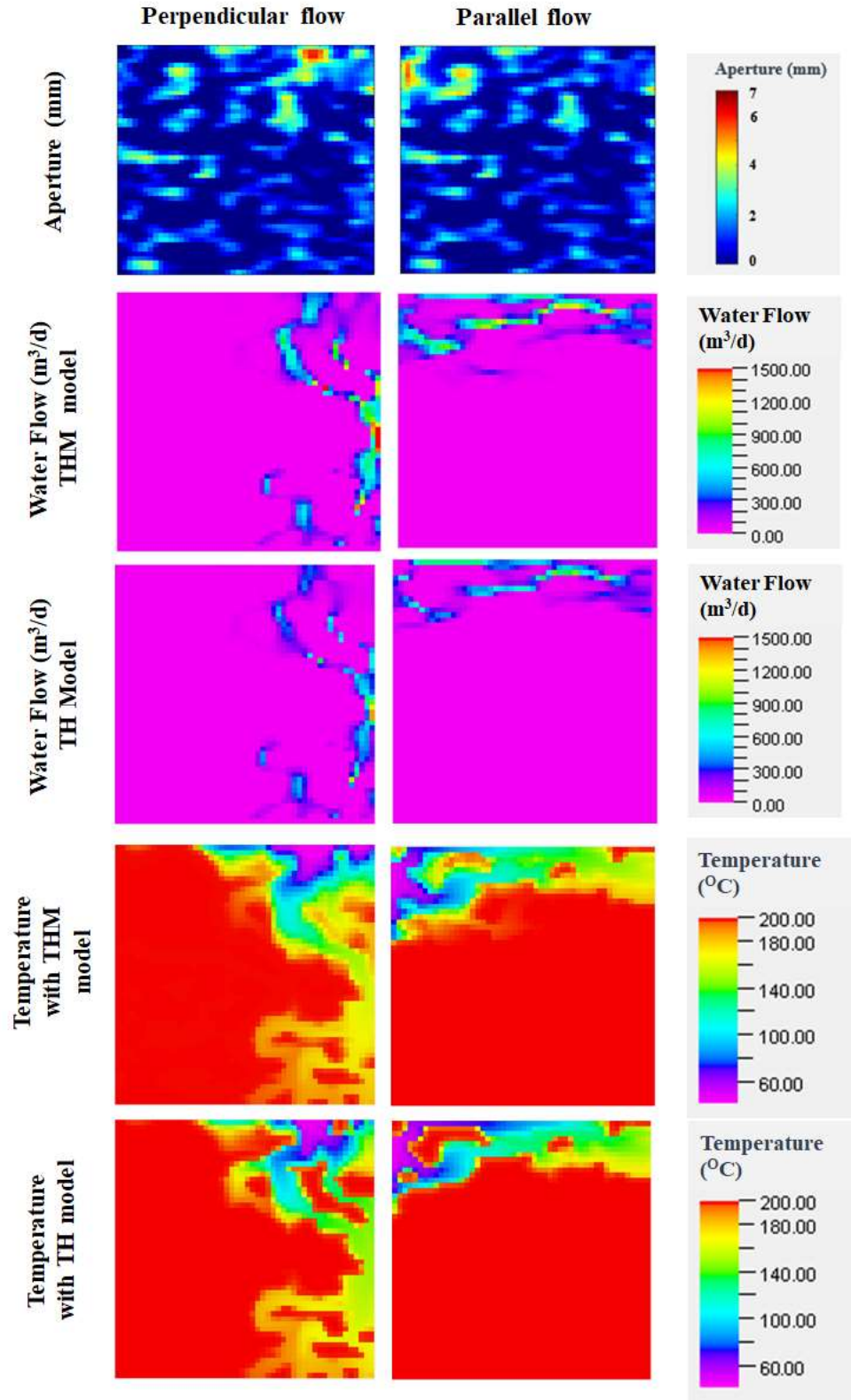


Figure 5.18: Comparison between the aperture, temperature, and flow maps for the thermohydraulic and thermohydromechanical model one year into the simulation – Perpendicular and Parallel flow configurations.

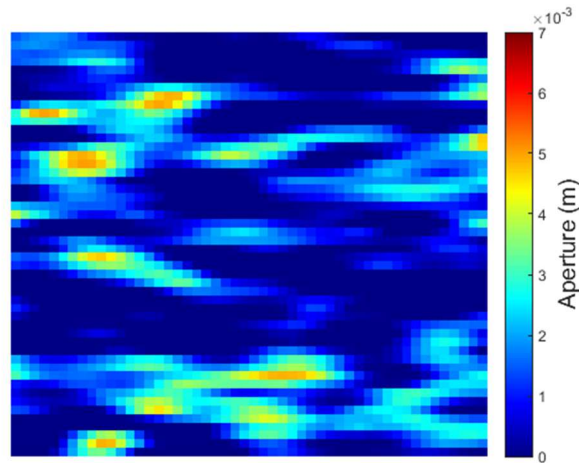


Figure 5.19: Original aperture distribution used for the thermohydraulic model where thermal drawdown was in favor of the parallel flow configuration.

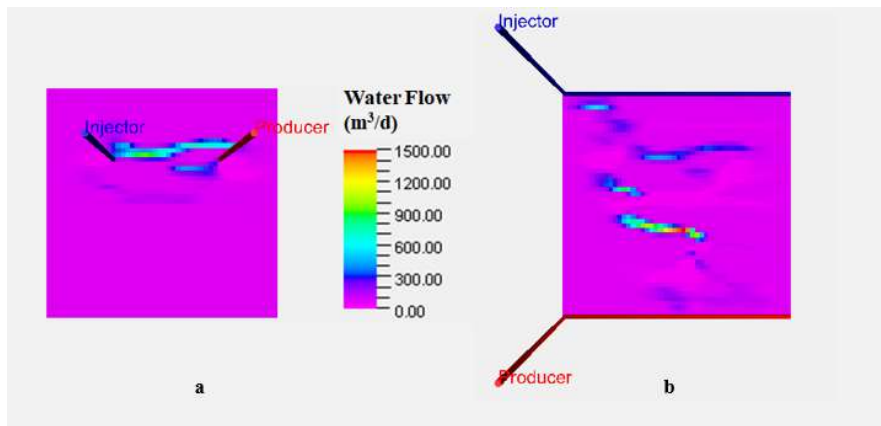


Figure 5.20: Location of the vertical wells (a) along the fracture compared to the location of the horizontal wells (b) in a perpendicular flow configuration.

For this aperture distribution which had a geometric anisotropy ratio of 4, implying that the connected features in the direction of slip were four times longer than the features in the direction perpendicular to slip, the results of the thermohydraulic model were different from what was seen in the previous case with geometric anisotropy ratio of 2.

This aperture distribution is characterized by long striations (about 240 m) in the x-direction. As seen from the flow map of Figure 5.23, there are several flow paths in the parallel flow direction contributing to more contact of the fluid with the rock and hence improved heat extraction. Fluid flow in the perpendicular flow configuration is through a

channel with a tortuous path. For this aperture distribution, the difference in the thermal drawdown curves between the flow configurations is small, more so negligible in the parallel direction, as can be seen in Figures 5.21 and 5.22.

In the case of the perpendicular flow configuration, injection of cold water causes the rock to contract leading to an opening of the aperture. Due to the large distance between connected features on the fracture surface, the opening of the aperture does not go beyond the existing flow path hence the fluid remains within the preferential flow path, leading to more channeling. Thus, the thermal drawdown is increased in the perpendicular flow configuration. The same response is seen with the vertical well configuration where flow remains within a flow path, leading to more channeling. Though a similar response is seen in the parallel flow configuration, the average temperature measured at the producer does not differ much between the thermohydraulic model and the thermohydromechanical model. The distance between connected features in the parallel flow configuration is small and hence the effect of channeling is almost counteracted by the opening up of nearby rock in that flow configuration.

In Figure 5.23, the areas highlighted with black circles indicate changes in the fracture aperture for the different flow configurations. The flow and temperature maps of the thermohydromechanical models across the perpendicular, parallel, and vertical well configuration show the areas where the impact of the changes in the fracture aperture was more significant.

The results from this case demonstrate that there are scenarios where injection of cold water into hot rock would lead to reduced thermal performance for fractures with spatial variations, which is different from the results seen in the previous case.

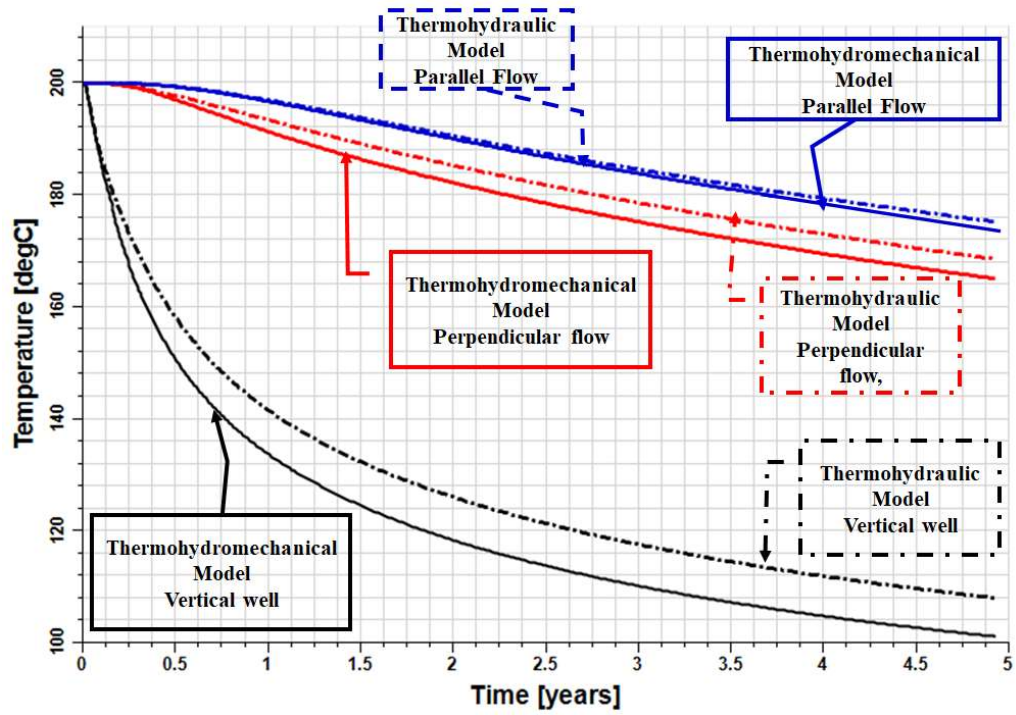


Figure 5.21: Thermal drawdown curves of the thermohydraulic and thermohydromechanical models for the perpendicular and parallel flow configuration and the vertical well.

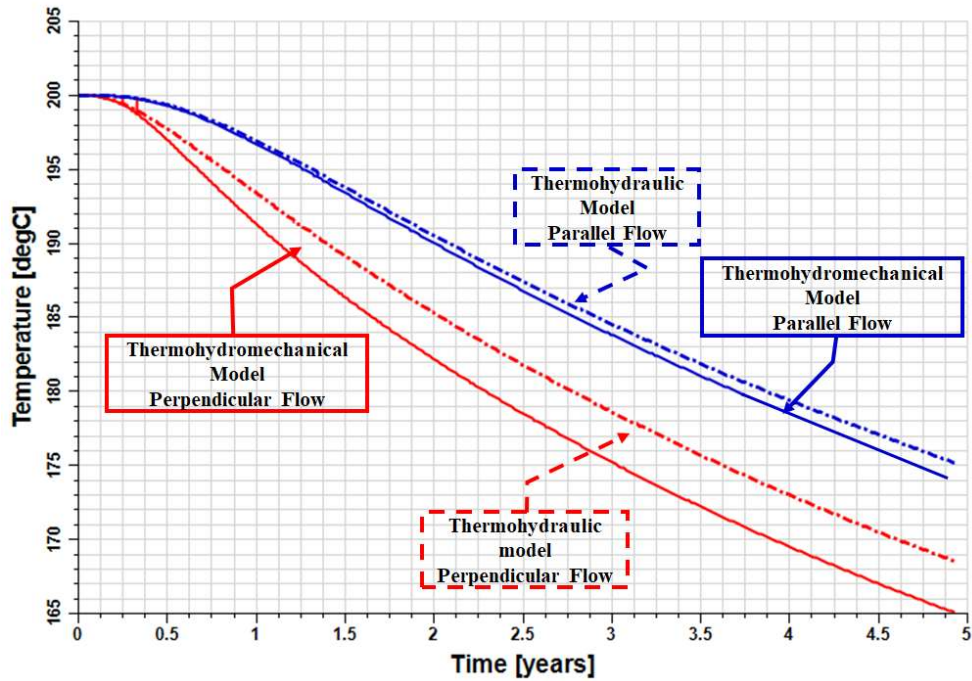


Figure 5.22: Thermal drawdown curves of the thermohydraulic and thermohydromechanical models for the perpendicular and parallel flow configuration only.

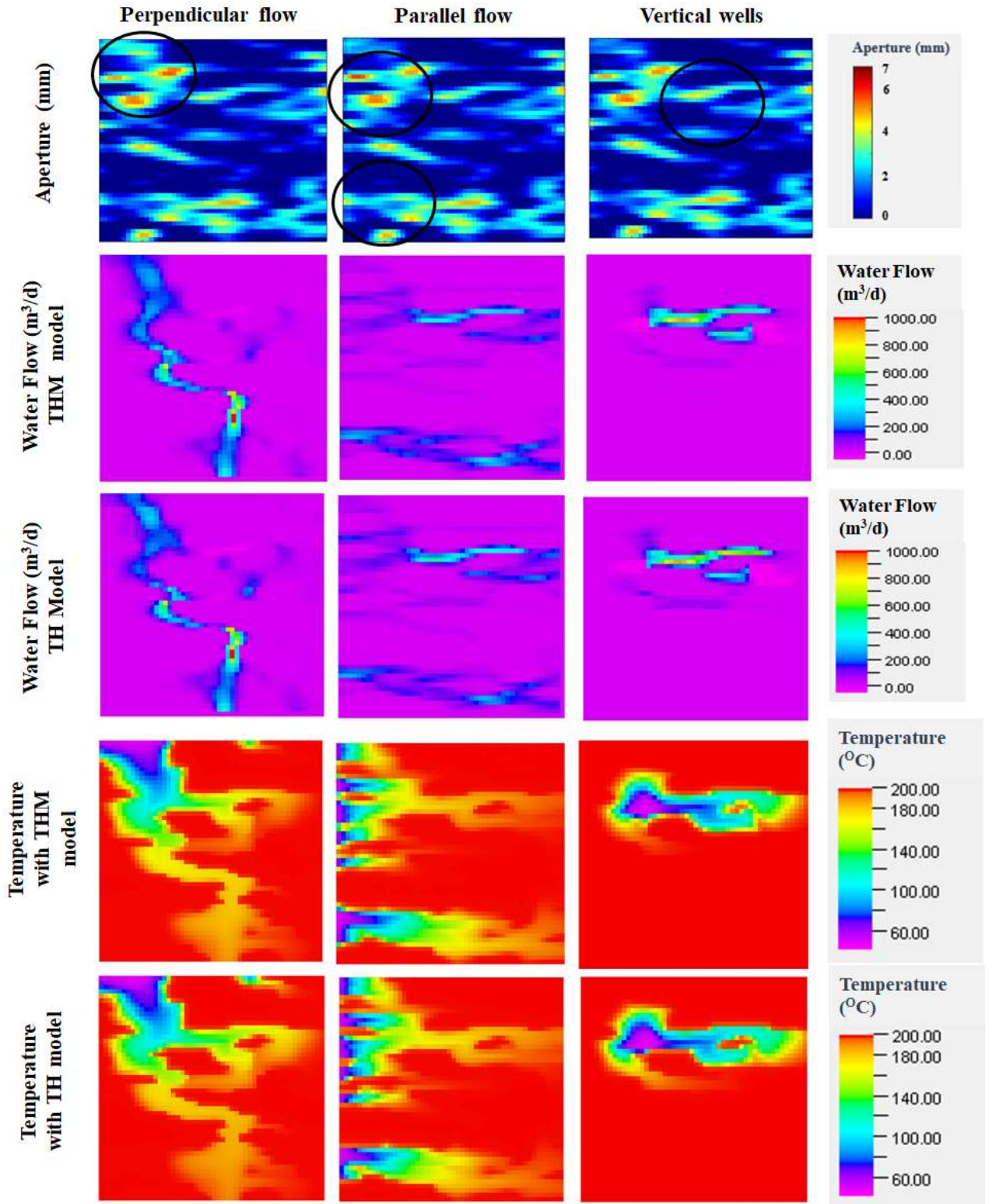


Figure 5.23: Comparison between the aperture, temperature, and flow maps for the thermohydraulic and thermohydromechanical model one year into the simulation – Perpendicular, Parallel and vertical flow configurations.

5.3 Summary

This study investigated the application of thermoelasticity in the modeling of systems with nonisothermal effects. First, an analog EGS with spatially varying aperture distribution was modeled. It was demonstrated that the injection of hot water into a cold reservoir could lead to thermal stresses and changes in the aperture distribution. These changes, however, were not sufficient to cause a significant change in the temperature measured at the extraction well for the system being modeled.

Subsequently, the impact of incorporating thermoelasticity in modeling a hypothetical EGS with anisotropic aperture distribution was investigated. Two cases with different geometric anisotropy ratios were studied. The results showed that cold water injection into hot rock could either lead to improved thermal drawdown or reduced thermal drawdown. The fracture aperture distribution with a geometric anisotropy ratio of 2 had improved thermal drawdown for the two flow configurations. The improved thermal drawdown could be attributed to the contraction of the rock, opening up more areas for flow. On the other hand, the aperture distribution with a geometric anisotropy ratio of 4 had a deteriorating thermal drawdown. The parallel flow configuration was minimally affected by channeling due to the many flow paths in that flow configuration and counteracting effects of fracture aperture opening in favor of the flow configuration.

Chapter 6

6 Comparing CO₂ and Water as Enhanced Geothermal System Working Fluids

6.1 Introduction

Enhanced or Engineered Geothermal Systems (EGS) have the potential to increase the geothermal capacity in the US (Tester et al., 2006) and consequently expand the reach to locations without natural geothermal resources. Although piloted over many years, Enhanced Geothermal Systems are still in the research and small or early demonstration phases. Most studies and field tests on EGS have used water as the working fluid. However, Brown (2000) suggested a novel renewable energy concept wherein supercritical CO₂ could be used in place of water for both reservoir creation and heat extraction. Brown (2000) highlighted the advantageous properties of CO₂ over water, including a higher density-to-viscosity ratio, a more significant buoyancy force, and lower salt solubility. Since then, several studies have built on the work of Brown (2000) to investigate the viability of a CO₂-EGS system.

Pruess (2006) considered a five-spot well configuration with three orthogonal fracture sets spaced 50 m apart through which the injected working fluids extract heat by conduction from the matrix blocks. The reservoir conditions were 200 °C and 500 bar, and injection conditions were 20 °C and 510 bar. From their investigation, they deduced that the heat extraction rates of CO₂ were about 50% more than water, leading to substantially accelerated energy recovery.

Luo et al. (2014) modeled a doublet CO₂-EGS system and considered the variation of CO₂ and the fluid turbulence within the wellbore. They concluded that CO₂ was better than water as the working fluid, and for a long life of the EGS, a CO₂ injection rate of 10 kg/s was favorable.

Pan et al. (2017) compared the geochemical impacts of CO₂-EGS to H₂O-EGS using a numerical model of the St. John's Dome CO₂-EGS site research site in Arizona. In the course of their study, they also found out that the net heat extraction and the mass flow production rates for CO₂-EGS were more considerable compared to H₂O-EGS.

Wang et al. (2018) simulated the heat extraction and simultaneous CO₂ sequestration in an enhanced geothermal system. They considered the influence of surrounding formation permeability, geothermal gradients, and different reservoir permeability parameters. The objective was to compare a CO₂-based EGS with a water-based EGS. The system modeled was an EGS doublet. They demonstrated the relevance of considering fluid losses from the reservoir to the surrounding formation. As with the studies mentioned earlier, Wang et al. (2018) also concluded that the CO₂-based EGS has greater heat extraction than the water-based EGS.

Huang et al. (2019) carried out a field-scale investigation of the heat extraction performances of water and supercritical CO₂ as EGS working fluids. A five-spot well pattern was used. A fixed pressure drop was specified between the injection well and four production wells. They determined that supercritical CO₂ had a higher mass flow rate, higher heat extraction rate, a shorter field life, and approximately the same cumulative heat extraction compared with water for the given pressure drop.

On the other hand, Pritchett (2009) considered multiphase flow effects during the heat mining and CO₂ sequestration process and found that heat sweep effectiveness can be maximized if water is used as a working fluid in place of CO₂. This heat sweep effectiveness when using water was explained as due to the development of an unstable material interface between the low-viscosity injected CO₂ and more viscous native water, resulting in the more mobile CO₂ bypassing the relatively higher viscosity regions and reducing the overall thermal sweep efficiency.

Fractures are usually the primary flow conduit in EGS, predominantly created through hydroshearing (Gischig and Preisig, 2015). Hydroshearing leads to fractures that are self-propped due to mismatched asperities across the two fracture surfaces. Several studies (e.g., Abelin et al., 1991; Hakami and Larsson, 1996; Tsang and Neretnieks, 1998; Tester et al., 2006; Watanabe et al., 2008; Co, Pollard and Horne, 2017, Mattson, et al., 2018; Hawkins et al., 2018) have demonstrated at various scales that variation in fracture aperture can lead to flow channeling where the fluid moves along a preferential flow path. In an EGS, cold injectate is circulated through one or more fractures in the hot rock reservoir, and fluid collection at one or more producers returns the heated working fluid to the ground surface. Therefore, heat is recovered only across the effective heat transfer area available between injectors and producers. Under channeled flow conditions, a relatively reduced heat transfer area can lead to inadequate heat transfer efficiency (e.g., Neuville et al., 2010) and, consequently, cause premature thermal breakthrough and reduced energy recovery (Co, 2017; Hawkins et al., 2017; 2018).

The studies mentioned above that have investigated the impact of channeling on mass and heat transport have considered water as the injected fluid. There are few studies describing the behavior of CO₂ as a working fluid in the presence of fractures with spatial variations. Moreover, several studies investigating the suitability of CO₂ as an EGS working fluid have not considered the possible spatial variations in fracture aperture.

Zhang et al. (2017) carried out a laboratory scale investigation comparing the heat transfer behavior of supercritical CO₂ on a fracture with aperture variability and a smooth fracture at different mass flow rates and different rock temperatures. The study showed that heat transfer through the fracture with aperture variability was hindered by channeling effects. However, their study did not compare how water would perform in a similar situation. Furthermore, the behavior of fluids varies with factors such as temperature and pressure, and lab-scale studies may not adequately model realistic durations for which there are changes in temperatures and pressures seen in the field. Hence it is of interest to understand how the heat transfer on both varying-aperture and smooth fractures compares for CO₂ and water on the field scale, considering in situ conditions and field-scale durations.

Because channeling and short-circuiting are common occurrences with water as a working fluid for EGS, this study contrasted the performance of CO₂ with water, and evaluated the behavior of the fluids in the presence of fractures with spatial variations in aperture. The operating conditions modeled in this study ensured that CO₂ remained in the supercritical state.

6.2 Methods

6.2.1 Governing Equations and Model Assumptions

The system modeled is a hypothetical EGS doublet consisting of a single injector/producer well-pair circulating the working fluid through a single fracture contained within a hot, impermeable rock. Relatively cold injectate is heated by the surrounding rock and then recovered at the production well. The fracture is horizontal, and hence gravity is not considered in the flow equation within the fracture.

The governing equations and model assumptions are the same as those in Chapter 2, Sections 2.2.1 and 2.2.2. Here, the fluid can either be water or CO₂.

For CO₂, the following additional assumptions were made:

- The CO₂ is injected at supercritical conditions and remains above critical temperature and pressure through the flow duration.
- When displacing water, the CO₂ is partially miscible according to the Spycher and Pruess equation of state (Spycher and Pruess, 2009).

6.2.2 Model Description

The hypothetical EGS doublet has a horizontal fracture measuring 1000 m x 1000 m at a depth of 1295.5 m below ground surface and is embedded within the relatively impermeable bulk rock matrix. Horizontal wells, one injection and one production, are placed at the edges of the fracture. The model is a 50 by 50 by 70 grid. In the horizontal x and y directions, the individual cells are of uniform length of 20 m, while in the vertical z-direction, the cell thicknesses are very fine around the fracture and become coarser away from the fracture. Figure 6.1 shows a snapshot of the reservoir simulation domain.

The coupled flow and heat transport mechanism was modeled with a three-dimensional compositional numerical simulator – ECLIPSE (Schlumberger, 2016).

For this study, the thermal performance of the EGS using water and CO₂ was compared. The reservoir fluid was considered to be water, and due to the low porosity and permeability of the matrix, CO₂ was not stored. For the case of water as the working fluid, the Thermal option of the simulator was used. The formulation of equations used to describe thermal processes can be found in Schlumberger (2016) and has three essential differences from a general compositional simulator: the addition of an energy variable and an energy equation; the presence of a water component in the gas phase as well as the water phase; and temperature dependence of properties. The thermodynamic properties of water are based on the International Association for the Properties of Water and Steam (IAPWS-IF97) (Wagner et al., 2000) using the keyword: THSTT97. For the case of CO₂ as the injected fluid, the Thermal CO2STORE option was used. The fluid properties are defined similarly to a standard thermal case, but the CO₂ component is allowed to dissolve in the aqueous phase. The CO₂: H₂O phase splitting, activity coefficient models, and CO₂ density follow the procedure given by Spycher and Pruess (2005) and Spycher and Pruess (2009). CO₂ viscosity is calculated by the procedure outlined in Fenghour et al. (1998). Other rock and fluid properties used in the model are presented in Table 6.1.

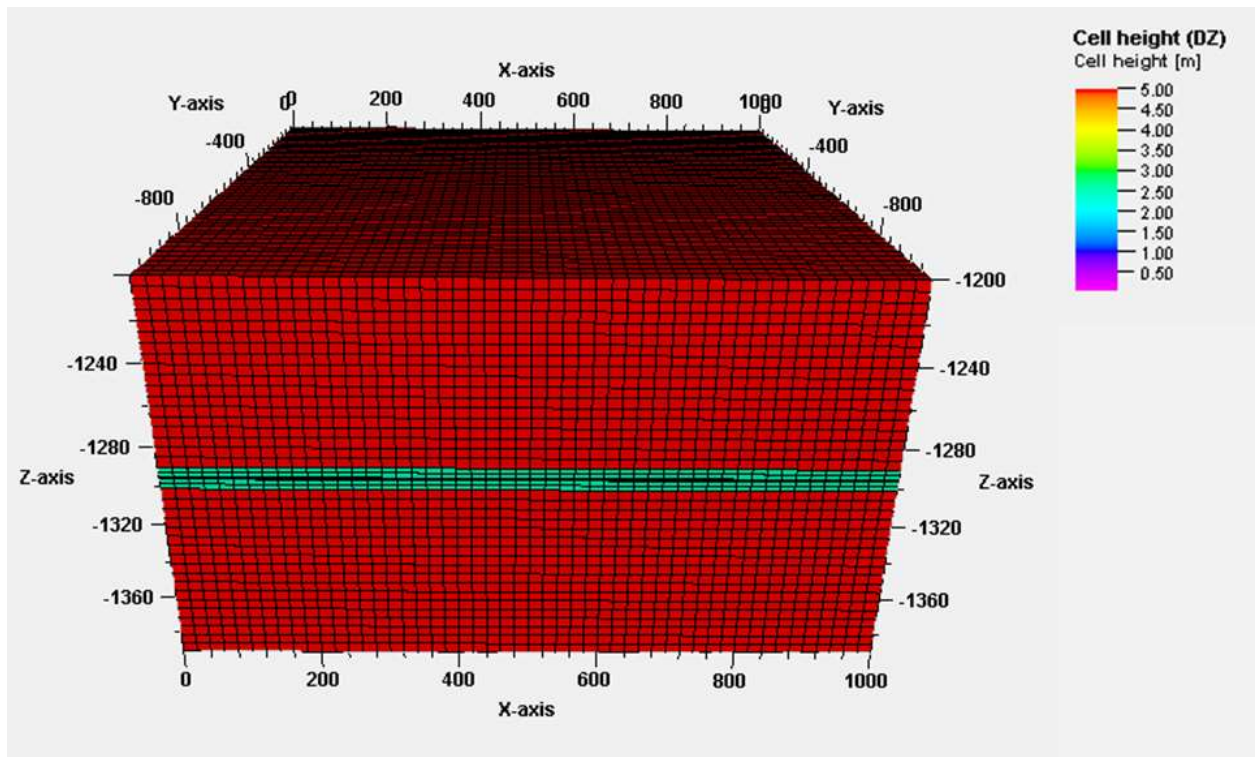


Figure 6.1: The hypothetical EGS model showing the grids. The height (Z-axis) is not to scale.

The initial reservoir conditions are 200 °C and 120 bar (12 MPa), while the injection conditions are 40 °C and 150 bar (15 MPa) at the bottomhole. At these conditions, water is a single-phase liquid. For CO₂, the bottomhole pressure of the producer does not go below 74 bar (7.4 MPa) throughout the simulation duration to ensure the fluid in the reservoir remains in supercritical condition. Temperature and pressure losses within the wellbores were not modeled in this study.

6.2.3 Relevant Properties of Water and CO₂

Because the thermal performance of water and CO₂ would be compared, it was essential to understand their state as working fluids and their relevant thermophysical properties.

Figure 6.2 shows the phase behavior of water. The blue circle shows the injection pressure and temperature, while the blue star shows the reservoir conditions modeled in this study. The critical point for water is defined by a temperature of 373.95 °C and 220.64 bar (22.064 MPa). Thus, water is a single-phase liquid at both the injection and reservoir conditions.

Table 6.1: Rock and fluid properties, and other parameters used in the model for comparing CO₂ and Water as EGS working fluids

Symbol	Description	Value	Units
φ	Porosity of the formation	0.01	-
k	Permeability of the formation matrix	$9.87 * 10^{-21}$	m ²
K_r	Thermal conductivity of rock	2.8	W/m/K
C_r	Specific heat capacity of rock	1000	J/kg/K
ρ_r	Density of the rock	2600	kg/m ³
μ	Dynamic fluid viscosity	0.0001303	Pa*s
P	Reference pressure for fluid viscosity	101.325	kPa
T	Reference temperature for fluid viscosity	200	°C
C_w	Specific heat capacity of fluid	4200	J/kg/K
ρ_{ST}	Reference fluid density	1000	kg/m ³
P_{ref}	Reference pressure for fluid density	101.325	kPa
T_{ref}	Reference temperature for fluid density	15.6	°C
C	Fluid compressibility	$5.00 * 10^{-10}$	Pa ⁻¹

The phase behavior of CO₂ is shown in Figure 6.3. The injection pressure and temperature are highlighted with a red circle, while a red star denotes the reservoir condition. The critical point for CO₂ is defined by a temperature of 31.0 °C and 73.8 bar (7.83 MPa). CO₂ behaves like a supercritical fluid at the injection condition – having gas-like viscosity and expansivity but with a density like that of a liquid.

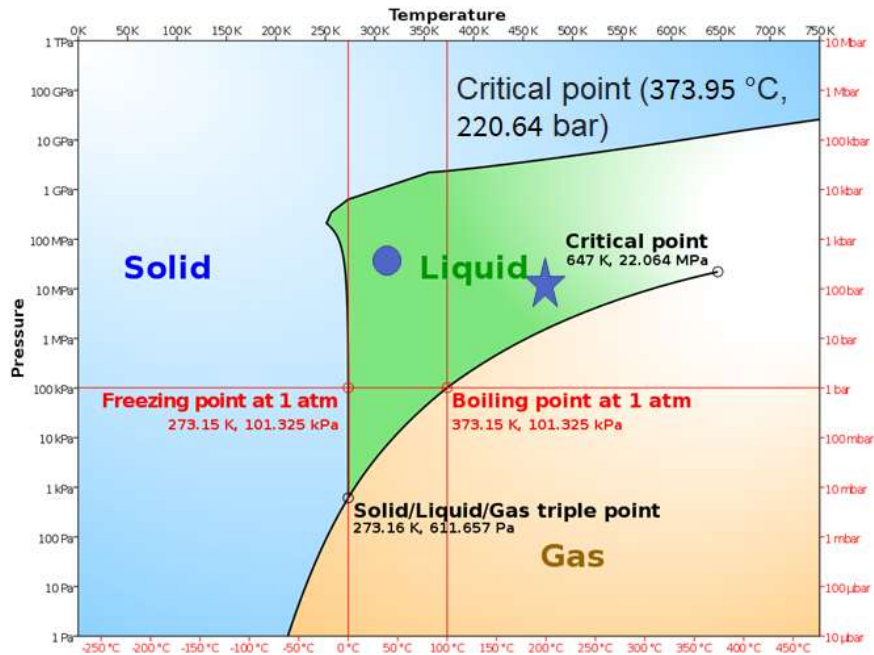


Figure 6.2: Phase behavior of water. The blue circle shows the injection conditions, while the blue star shows the reservoir conditions (Wikipedia, 2021b).

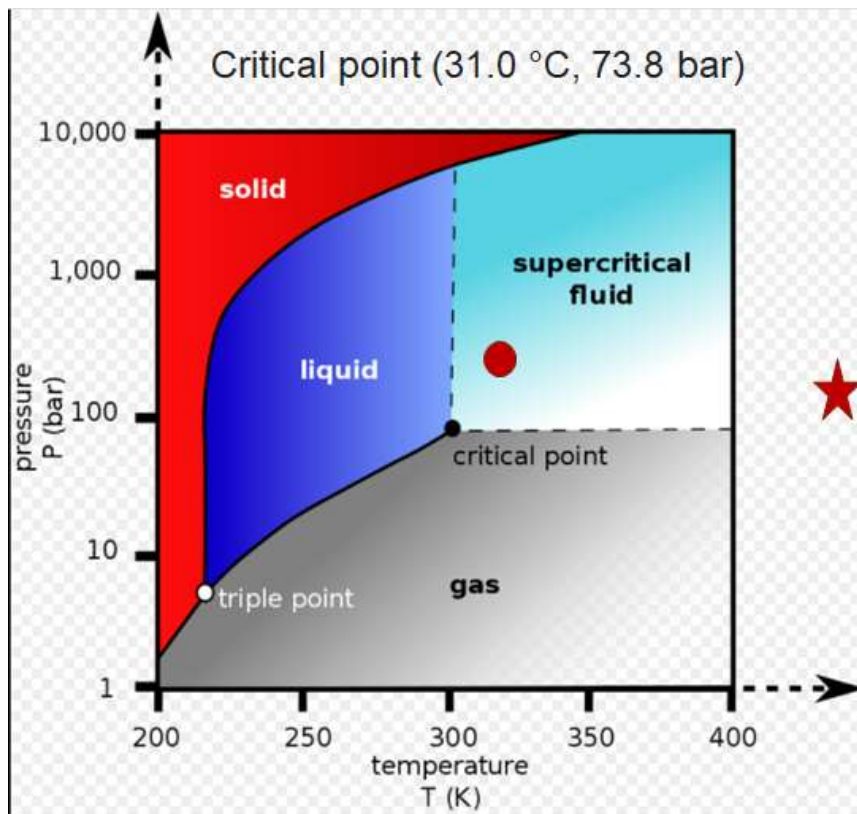


Figure 6.3: Phase diagram for CO₂. The red circle shows the injection conditions, while the red star shows the reservoir conditions (Wikipedia, 2021c).

The thermophysical properties of CO₂ and water have different behavior at various temperatures and pressures. Figure 6.4 shows fundamental thermophysical properties of water and CO₂ as a function of temperature and pressure. These are the density, viscosity, specific heat capacity, and thermal conductivity of the fluids.

The specific heat capacity and thermal conductivity of water were treated as constants in the numerical model. All other thermophysical properties of CO₂ and water were modeled as temperature- and pressure-dependent.

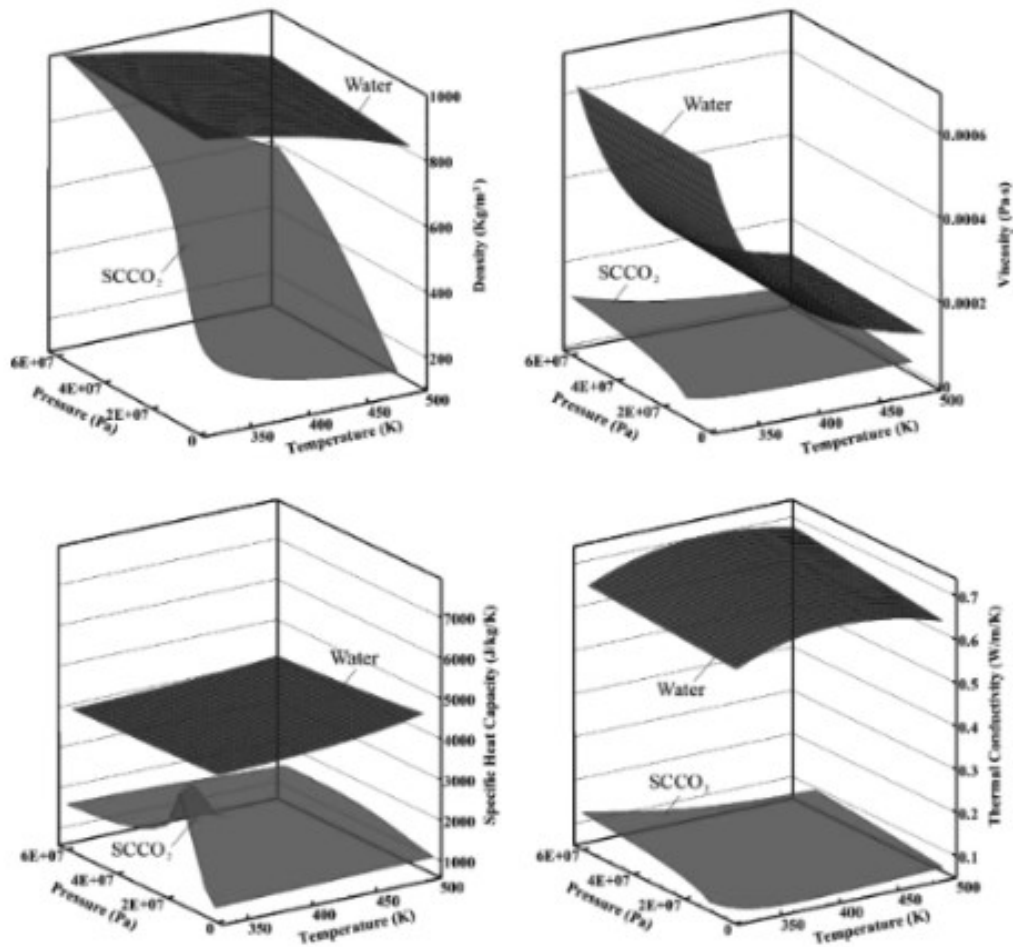


Figure 6.4: Thermophysical properties of water and CO₂ as a function of temperature and pressure (Huang et al., 2019).

The relevant thermophysical properties of CO₂ and water are presented in Table 6.2. The compressibility ratio in the table is the ratio of the compressibility of CO₂ to the compressibility of water. The data presented for that ratio is an estimate.

Table 6.2: Thermophysical properties of CO₂ and water at the injection and reservoir conditions

Property	Injection Conditions		Reservoir Conditions	
	Water	CO ₂	Water	CO ₂
Density (kg/m ³)	998.65	780.23	872	148.77
Viscosity (cp)	0.65	0.067	0.13	0.025
Density/Viscosity Ratio	1536.38	11645.22	6707.69	5950.80
Compressibility Ratio* (CO ₂ to Water)	50		125	
Heat Capacity (kJ/(kg.K))	4.14	2.67	4.42	1.22
Specific Enthalpy (kJ/kg)	180.77	285.48	856.67	625.17

6.2.4 Fracture characterization

In this study, a comparison was made between the performance of a fracture that is parallel walled to a fracture that is considered to have spatial variations. In the model, the fracture is treated as a porous medium with porosity set as 0.99. At the same time, the local cubic law defines the heterogeneous permeability for a fracture with spatial variations (Oron & Berkowitz, 1998), which is represented by Equation 6.1. When computing the value for a homogeneous permeability field (i.e., smooth parallel-plate fracture), the aperture value was constant at 5 mm.

$$k_{f_{ij}} = \frac{b_{ij}^2}{12} \quad (6.1)$$

where k_f , i , j , and b are the effective permeability, grid number in the x-direction, grid number in the y-direction, and local fracture aperture, respectively.

6.2.5 Determination of the spatially varying fracture aperture distributions

The aperture distributions used in this study were represented statistically by a spatially autocorrelated random field. The apertures were generated using the method of sequential Gaussian simulation (SGSIM) within the Stanford Geostatistical Modeling Software (SGeMS) (Remy et al., 2009). A complete discussion on the SGSIM method and variogram modeling can be found in Goovaerts (1997) and Section 2.2.5.3. The spatial autocorrelation characteristics were described by the variogram model and the correlation length λ of the apertures. The distribution of the fracture aperture was lognormal. A Gaussian variogram model was used for all the aperture distributions in this study. The variogram was treated as spatially isotropic on the fracture, with a nugget of zero.

According to Tsang and Tsang (1987) and Tsang et al. (1988), the ratio of correlation length λ to the characteristic flow length of a system L , is usually between 0.05 and 0.40 for typical hydrological applications. The system is modeled with a characteristic flow length of 1000 m, translating to correlation lengths between 50 m to 400 m. Hence for this study, three different aperture distributions were generated for each of the correlation lengths of 50 m, 100 m, 200 m, and 400 m. Figure 6.5 shows a snapshot of selected aperture distributions across the different correlation lengths.

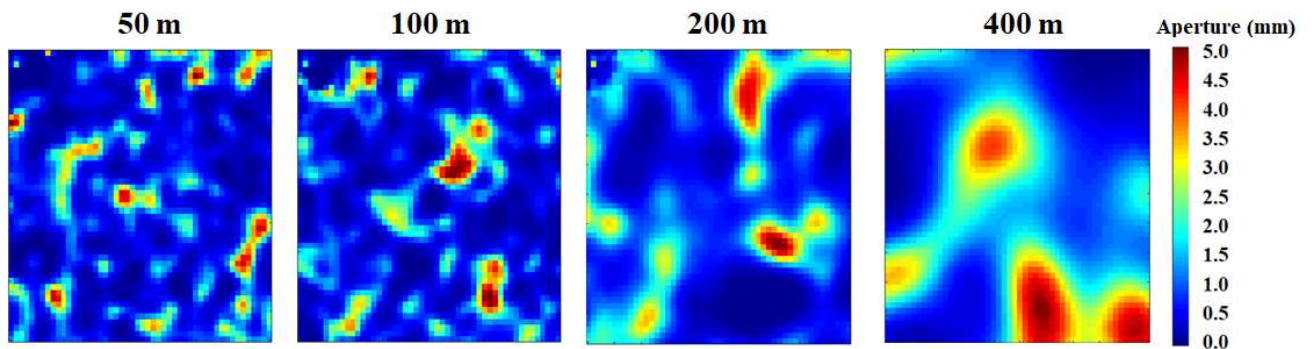


Figure 6.5: Heterogeneous fracture aperture distribution for correlation lengths of 50 m, 100 m, 200 m, and 400 m.

6.2.6 Workflow and Metrics for Evaluation

To understand the value of CO₂ and water as working fluids, the numerical simulation was performed at the same injection pressure and temperature for a smooth fracture. Different mass flow rates were used, ranging from 10 kg/s to 280 kg/s. The produced energy, energy production rate, and Carnot efficiency were metrics for analyzing the data.

Subsequently, a specific CO₂ injection rate was chosen to match the input energy of water at 40 kg/s. Using the same energy input for both fluids, a comparison of thermal output was made between the thermal performance of CO₂ and water for a smooth fracture and fractures with spatial variations with apertures of different correlation lengths. The cumulative produced energy and energy production rate were analyzed to deduce the performance of the fluids over the simulated time.

Finally, the impact of different injection rates (20 kg/s, 40 kg/s, 60 kg/s, and 80 kg/s of water) was evaluated using a fracture with heterogeneous aperture distribution defined by a correlation length of 200 m.

6.3 Results and Discussion

6.3.1 Heat Extraction at Different Mass Flow rates – Smooth Fracture Evaluation

Presented here are the cumulative heat produced and net heat extracted after two years of circulating CO₂ or water. For the given initial reservoir conditions and injection conditions, water gives a higher heat produced and heat extracted at each mass flow rate. This higher heat extracted compared to CO₂ is shown in Figure 6.6. However, using the mass flow rate is not a suitable equivalent metric for comparing the heat extraction performance of CO₂ and water. The reason for the same mass flow rate not being suitable for comparison is the significant difference between their heat capacities of the fluids and the differences in thermophysical properties at different temperatures and pressures. From Figure 6.6, the red lines indicate that the mass flow rate of CO₂ needs to be about five times that of water

to generate the same produced energy at the selected time under the given injection and reservoir conditions.

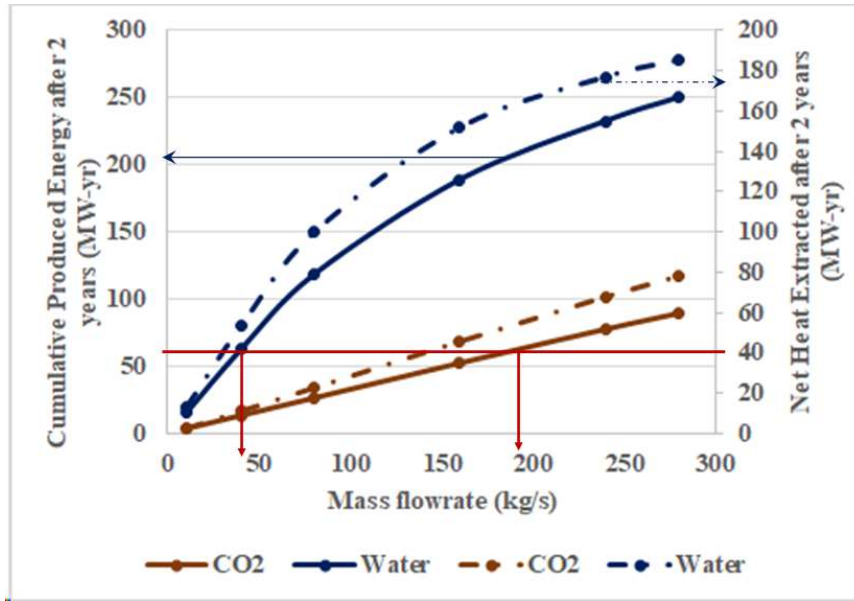


Figure 6.6: Cumulative energy produced (bold lines) and net heat extracted (dashed lines) for CO₂ and water at different mass flow rates after two years of continuous fluid circulation, smooth fracture case.

From Figure 6.6, it can be seen that the net heat extracted for water does not follow a linear trend. Hence the mass flow rate for heat extraction from EGS needs to be selected optimally. Figure 6.7 shows the heat production rate and the net heat rate measured after two years. The net heat extraction rate (in dashed lines) appears to plateau for water at high mass flow rates, supporting the need for optimal selection of injected mass flow rates. The CO₂ curves do not show a similar trend, although this may be because the presented mass flow rates are too low to give the equivalent behavior of water at the same rates.

The Carnot efficiency, which is the maximum theoretical efficiency of a hypothetical engine, is computed using the expression:

$$\eta = 1 - \frac{T_C}{T_H} \quad (6.2)$$

where T_C is the ambient temperature, 15.6 °C, while T_H is the exit temperature of the fluid from the production well. The values were taken after two years of continuous fluid circulation and are presented in Table 3. Figure 8 is a plot of the Carnot efficiencies of a hypothetical power plant for the different fluids at different mass flow rates.

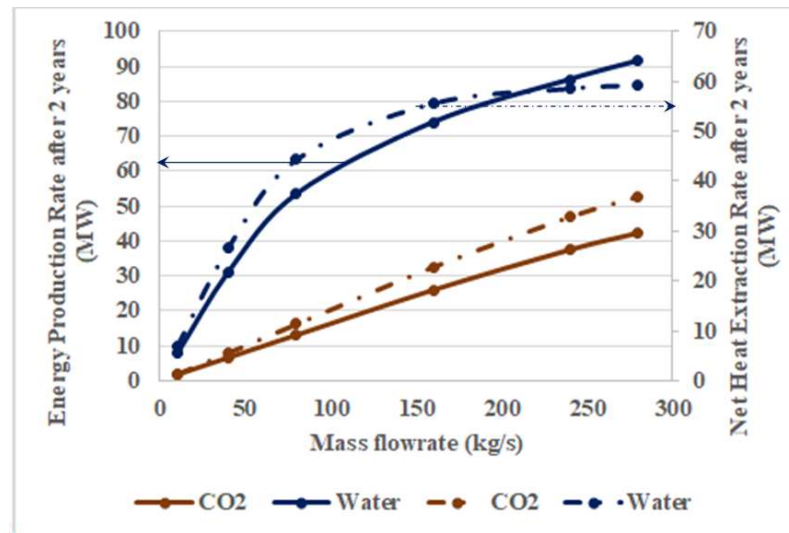


Figure 6.7: Energy production rate (bold lines) and net heat extraction rate (dashed lines) for CO₂ and water at different mass flow rates after two years of continuous fluid circulation.

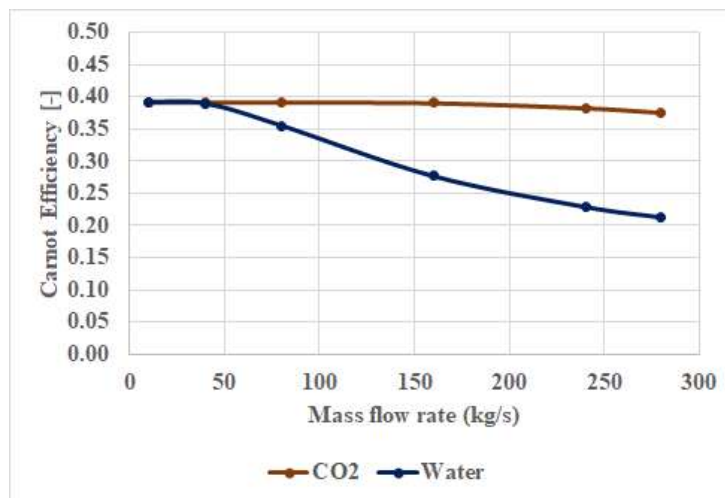


Figure 6.8: Carnot efficiencies for CO₂ and water at different mass flow rates after two years of continuous fluid circulation, smooth fracture case.

Table 6.3: Exit Temperature of the fluid from the production well

Exit Temperature after 2 years (°C)						
	10kg/s	40kg/s	80kg/s	160kg/s	240kg/s	280kg/s
CO ₂	200.0	200.0	200.0	199.3	193.3	188.0
Water	200.0	198.1	173.2	125.1	100.6	92.9

6.3.2 Heat Extraction at a Fixed Energy Input – Smooth Fracture

In order to appropriately compare the performance of CO₂ and water as EGS working fluids, the volumetric throughput for water at 40 kg/s was matched with a CO₂ mass flow rate of 235 kg/s which gave the same input energy required to push the fluids through the system at the specified injection conditions. The fracture was still treated as a smooth, parallel-walled fracture.

Figure 6.9 shows the cumulative input energy and cumulative produced energy of the fluids over seven years. For the same energy input, CO₂ gives a higher energy output over the simulated life of the reservoir. This higher energy output is consistent with the findings of previous works referenced earlier in this chapter.

Having established the CO₂ mass flow rate that would give the same energy input for water at 40 kg/s, the thermal performance was evaluated for a fracture with heterogeneous aperture distributions defined by different correlation lengths.

6.3.3 Heat Extraction at a Fixed Energy Input – Fracture with spatial variations, different correlation lengths

The correlation length is the distance beyond which the statistical variance minus the covariance of the apertures does not change significantly with further increase in distance. There would be larger distances between areas of high aperture and areas of low aperture with higher correlation lengths. Thus, the contact area with a high correlation length would be less than the contact area with a low correlation length, leading to possible channeling.

Figure 6.10 shows the difference between the cumulative energy produced from CO₂ and water, measured over time. This analysis was done for the different aperture

distributions of each correlation length. However, due to the similarity in results, only results of one aperture distribution for each correlation length are presented. CO₂ starts out extracting more energy from the system for all correlation lengths compared to water. As time progresses, with higher correlation length, energy extraction using CO₂ reduces. Also, for both water and CO₂, the cumulative energy extracted reduces with an increase in correlation length.

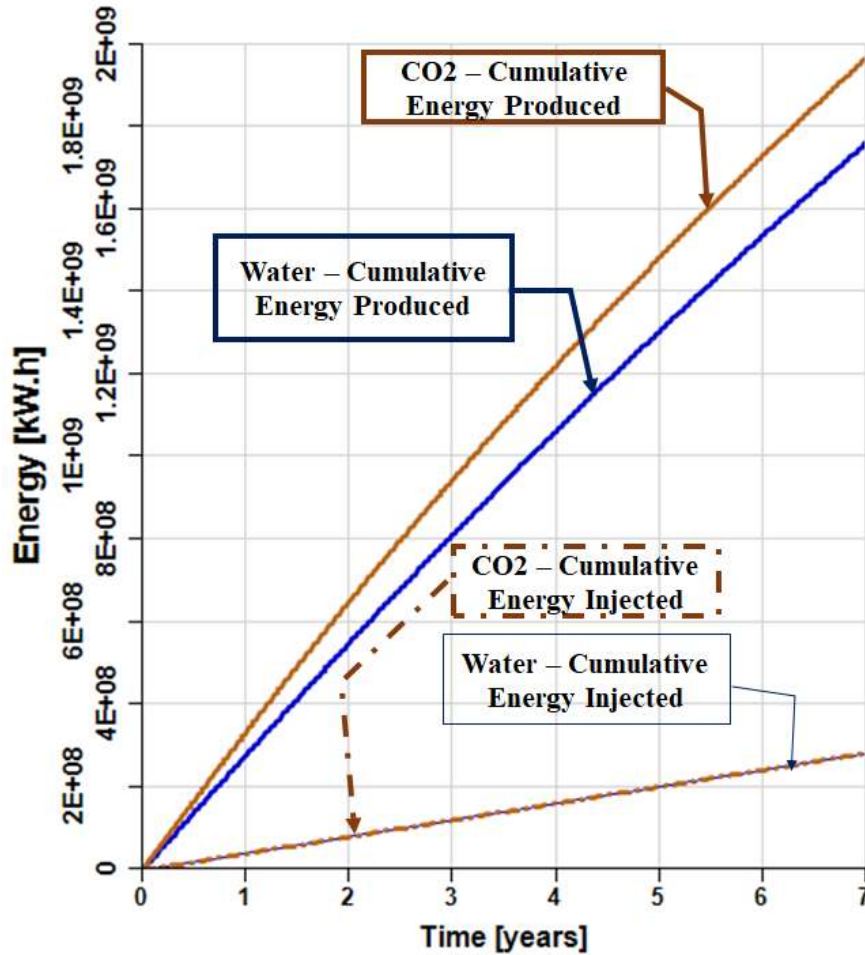


Figure 6.9: Cumulative energy produced vs. cumulative energy injected for CO₂ and water over seven years in a smooth fracture.

Figure 6.11 shows the temperature profile of the fracture plane for selected correlation lengths. It was assumed that the fluid in the fracture has the same temperature as the rock it is in contact with. In general, it appears that water has a greater contact area with the fracture surface than CO₂.

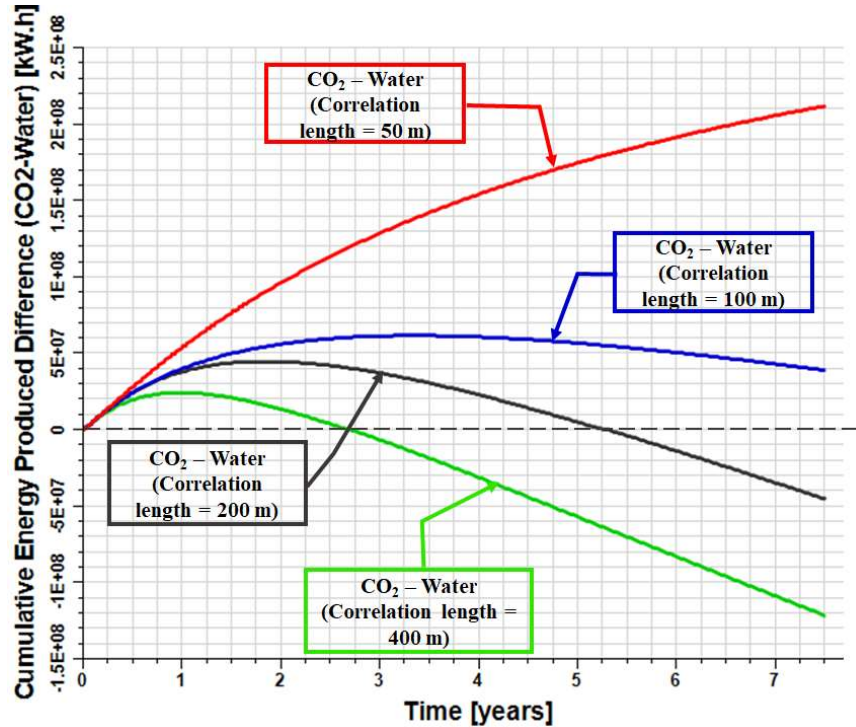


Figure 6.10: Difference between cumulative energy produced for CO₂ and water over time for different fracture aperture correlation lengths.

As the reservoir temperature drops with continuous fluid circulation, water becomes more viscous, and its mobility is reduced. In contrast, a similar temperature drop has only a negligible effect on the mobility of CO₂. There is a stable contact interface between the injected water and the in-situ water, which allows for a better thermal sweep efficiency. The higher viscosity of the water on the cooler paths diverts the water to move through alternative flow paths. Over time, the water will contact a larger area of the rock, as the mobility changes act to create a more balanced sweep. The CO₂, however, has much higher initial mobility, and as a pathway cools, it remains high mobility relative to alternative pathways. Hence the CO₂ flow from injector to producer tends to remain in the more permeable paths, and there appear to be by-passed areas due to heterogeneity of the fracture aperture.

The thermal drawdown of CO₂ is a lot more than that of water for all correlation lengths. This high thermal drawdown of CO₂ can be seen in Figure 6.12, where the

difference between the temperature measured at the producer for CO₂ is less than the temperature measured for water, resulting in all the temperature difference curves being less than zero (0). However, as correlation length increases, the thermal drawdown increases.

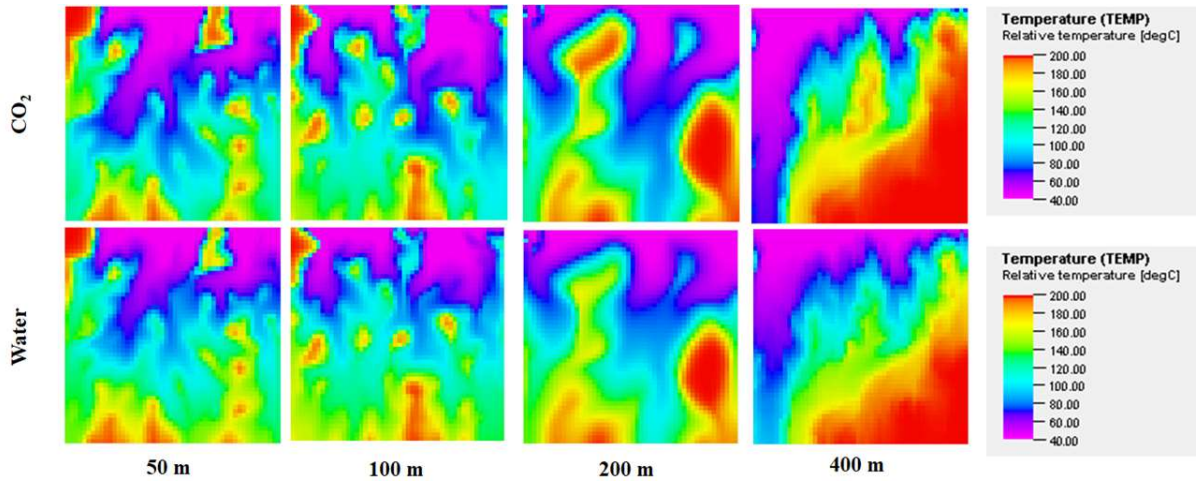


Figure 6.11: Temperature map at the fracture for CO₂ and water at seven years for different fracture aperture correlation lengths.

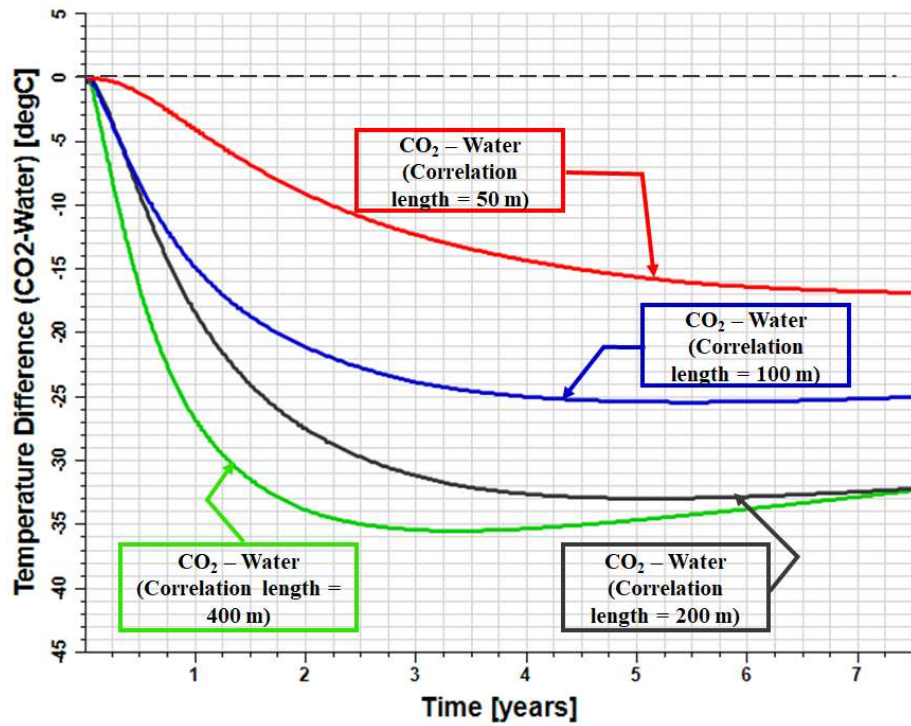


Figure 6.12: Temperature difference measured at the producer for CO₂ and water over time for different fracture aperture correlation lengths.

6.3.4 Heat Extraction at a Fixed Equivalent Energy Input – Fracture with spatial variations, different flow rates

For one realization of the aperture distributions with a correlation length of 100 m, different rates for CO₂ and water were modeled to investigate the impact of flow rate on heat extraction while accounting for aperture spatial variations. The rates modeled were 20 kg/s, 40 kg/s, 60 kg/s and 80 kg/s for water with equivalent mass flow rates that would generate same energy input as water of 117 kg/s, 234 kg/s, 351 kg/s and 468 kg/s respectively for CO₂. Figure 6.13 shows the difference in cumulative energy produced between CO₂ and water for the different flow rates.

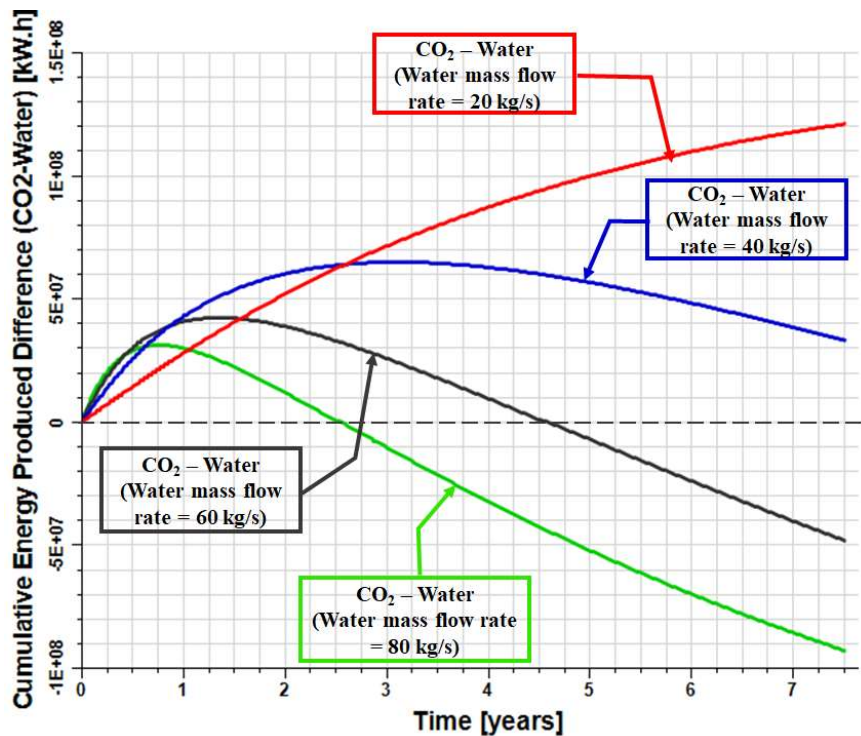


Figure 6.13: Difference in cumulative energy produced for CO₂ and water at different mass flow rates for a selected fracture with aperture variability with a correlation length of 200 m.

With increasing mass flow rate, the difference between the energy produced by using CO₂ over water reduces. From Figure 6.13, the point where the curve crosses the zero (0) line indicates the time when water begins to extract more energy from the system than CO₂ does. This time reduces with an increase in mass flow rate. A similar trend was

seen for the other fractures with variability in the aperture distributions, though the results are not presented here.

Figure 6.14 shows the temperature status of the fracture plane after seven years of continuous fluid circulation. More heat is extracted from the EGS for both fluids with a higher mass flow rate. However, there is evidence of more channeling with CO₂ than water, which is more evident at higher rates, with more bypassed areas when CO₂ is compared with water.

The temperature difference curves between CO₂ and water indicate a higher thermal drawdown for CO₂ than water, as shown in Figure 6.15. For higher mass flow rates, there is a turning point in the curves, which demonstrates that after some time, the difference in thermal drawdown between CO₂ and water is reducing, and may reach the point where the difference is zero, perhaps when sufficient heat has been extracted from the rock.

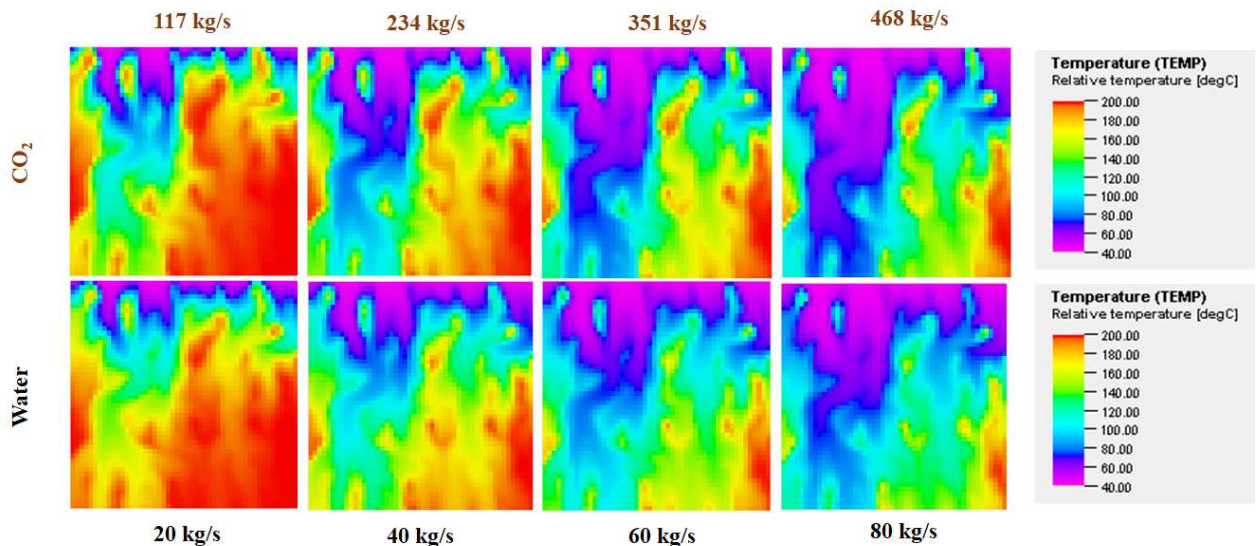


Figure 6.14: Evolution of the temperature distribution at the fracture plane for CO₂ and water for the different mass flow rates.

6.3.5 Heat Extraction at a Fixed Energy Input – Fracture with spatial variations, comparison with a smooth fracture at a fixed rate, and fixed aperture distribution correlation length

A comparison was made between CO₂ and water, assuming the fracture was smooth (parallel-walled) and with aperture spatial variation of 200 m correlation length at 40 kg/s of water mass flow rate. For the fracture with aperture variability, the thermal drawdown of CO₂ is disproportionately more prominent than that of water, as shown in Figure 6.16. It is not only the high mass flow rate that contributes to the thermal drawdown. The low viscosity of CO₂ and consequently its higher mobility compared to water make it more susceptible to channeling.

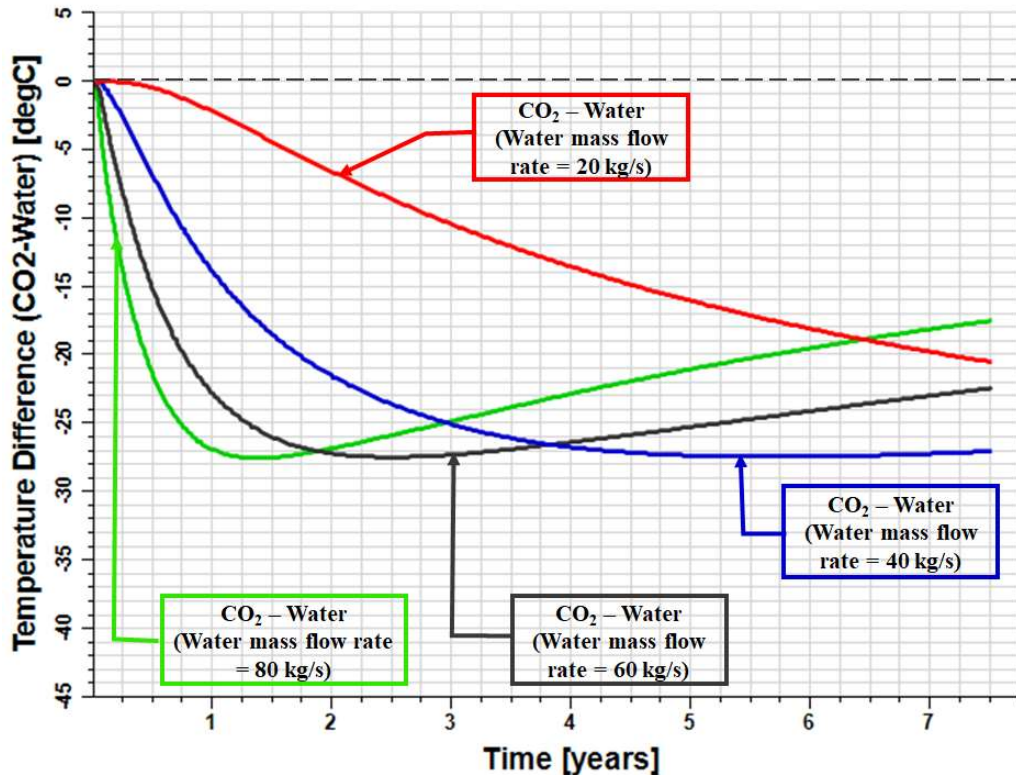


Figure 6.15: Temperature difference measured at the producer for CO₂ and water over time for different mass flow rates.

Although the energy input remains the same for the smooth fracture and the fracture with aperture variability, the energy extracted is reduced with the fracture having aperture variability. This reduced energy extracted occurs for both the water and CO₂ injection fluids and is due to channeling of the flow by the heterogeneity of the fracture aperture. Figure 6.17 shows the energy extracted for CO₂ and water when used over a smooth fracture and a fracture having aperture variability. Despite the high mass flow rate of CO₂, it is more impacted by channeling, which causes the heat extracted to become less than that of water after about two years. As shown in Figure 6.18, the energy extraction rate reduces rapidly with time compared to water. Hence, CO₂ may not be beneficial in the long term with a heat mining strategy of continuous CO₂ circulation where fractures have spatial variations in their apertures.

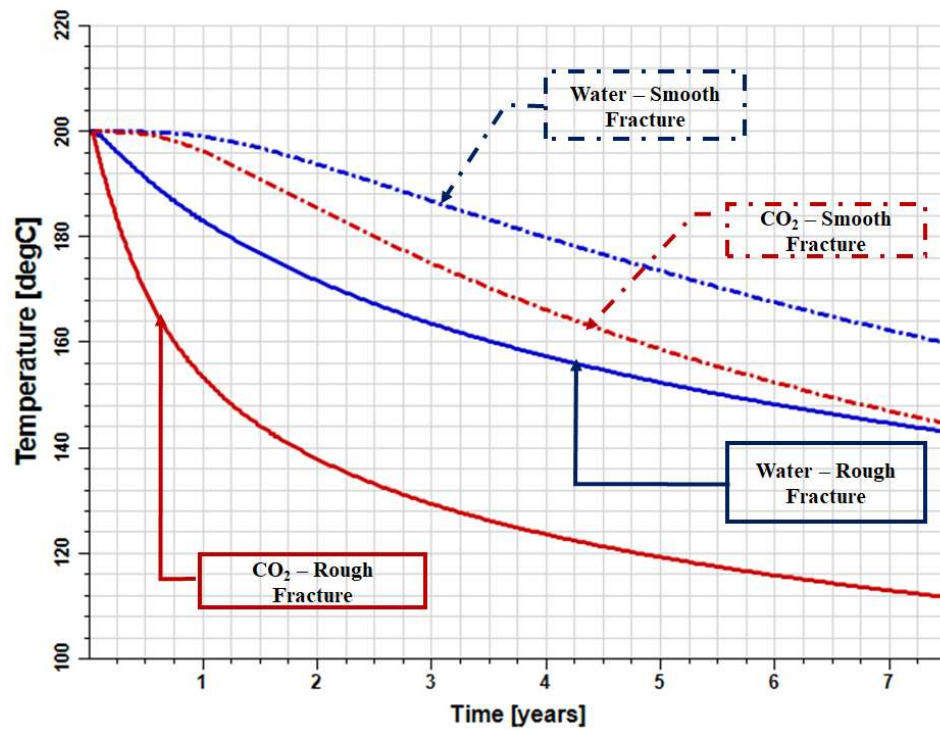


Figure 6.16: Temperature difference measured at the producer for CO₂ and water as a function of time for 40 kg/s of water and 200 m fracture aperture correlation length.

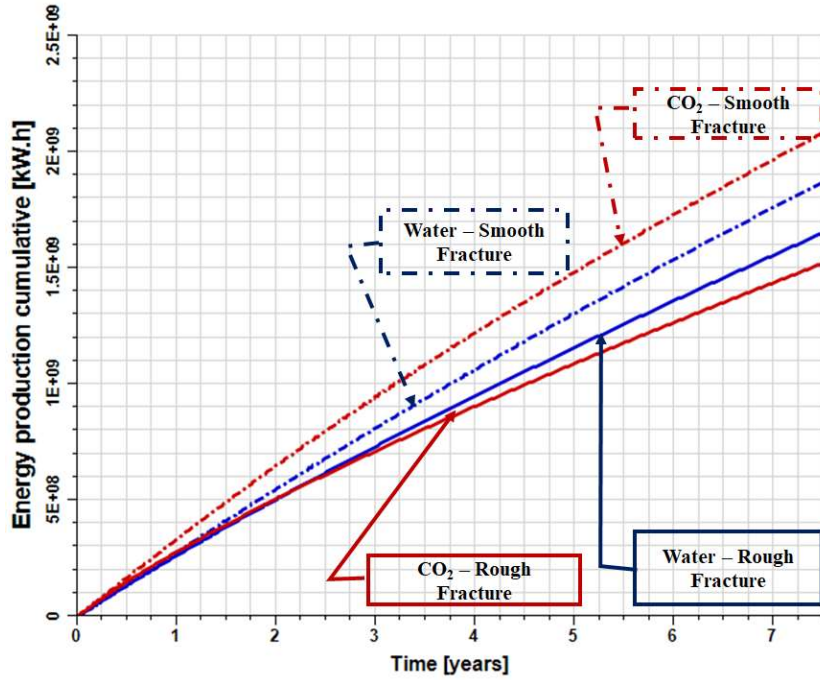


Figure 6.17: Cumulative energy extracted for CO₂ and water over time for smooth fracture and fracture with spatial variations.

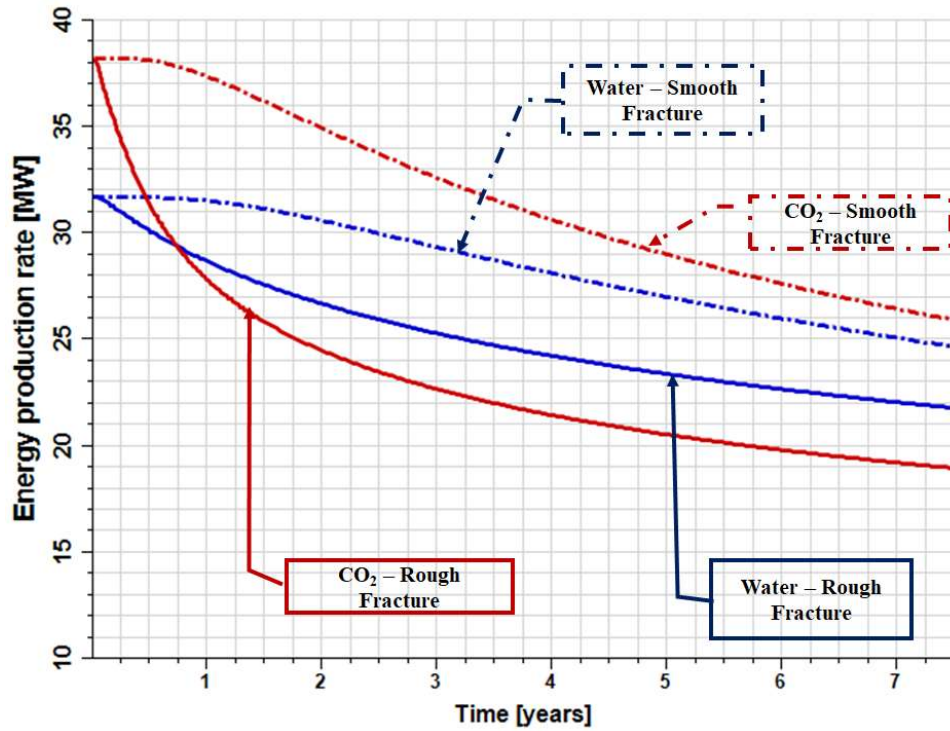


Figure 6.18: Energy extraction rate for CO₂ and water over time for smooth fracture and fracture with spatial variations.

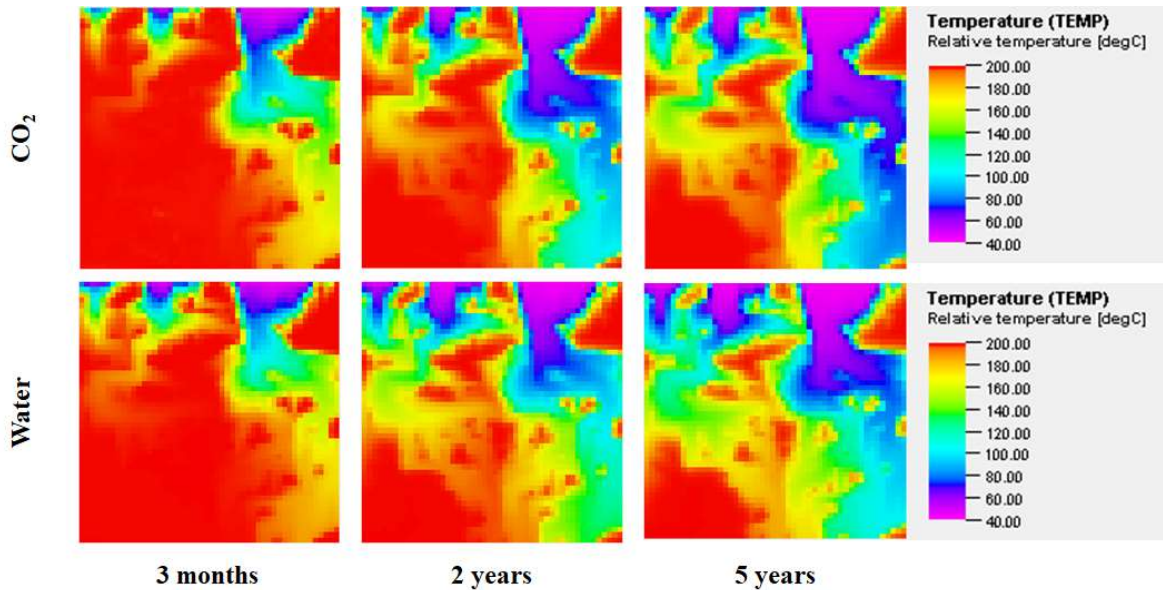


Figure 6.19: Temperature map for CO₂ and water over time for a fracture with spatial variations.

6.4 Summary

An investigation of CO₂ as an alternative working fluid to water for enhanced geothermal systems has been performed. Various thermal performance metrics have been evaluated for different mass flow rates of CO₂ and water. It has been demonstrated that using the same mass flow rate is not necessarily an appropriate metric for evaluating the thermal performance of CO₂ compared to water. Based on the same mass flow rate, water will appear to give superior thermal performance. This superior thermal performance is due to water being delivered through the system in a liquid state and does not account for the energy required to do this. Because the phase behavior of CO₂ and water differ at varying temperatures and pressures, the energy input was used as the metric for evaluating the thermal performance of the working fluids.

CO₂ at the injected condition of 40 °C and 150 bars, and at the reservoir condition of 200 °C and 120 bars, is a supercritical fluid with thermophysical properties that make it quite attractive for heat mining. On comparing it with water for the same energy input and assuming a smooth fracture, the use of CO₂ resulted in more energy extracted.

However, the gas-like viscosity of CO₂ is a disadvantage when the flow and heat extraction is modeled with a heterogeneous fracture aperture and over realistic periods for heat extraction. CO₂ is affected by channeling due to viscous fingering and fracture aperture heterogeneity. At high correlation lengths and high mass flow rates, the channels persist over time, leading to a very inefficient thermal sweep. Water at low temperatures is more viscous than the background reservoir water. So cooler pathways become less preferential, and the sweep contacts a larger area of the rock over time. Thus, the energy extracted from the reservoir using water exceeds that of CO₂ for aperture distributions with high correlation lengths and at high equivalent mass flow rates.

CO₂ results in higher thermal drawdown than water, though it initially extracts more heat from the reservoir. For fractures with spatial variations, the heat extraction rate reduces with time. Thus, in the long term, the cumulative energy extracted from the reservoir may be surpassed by a system where water is used, especially at high flow rates and if the fracture aperture has high correlation lengths.

This study spurs questions for future investigators. What might be an optimal strategy for harnessing heat from an enhanced geothermal system? Would a water alternating supercritical CO₂ injection cycle give an advantage when extracting heat through fractures with heterogeneous apertures? For example, using the water to vary the sweep pattern and then using CO₂ at the same injected energy rate to exploit that sweep efficiently until it cools.

Chapter 7

7 Conclusions and Recommendations

Adequate modeling of Enhanced Geothermal Systems requires sufficiently capturing the physical processes that occur during the heat extraction process. Faults and fractures are the main flow conduits in Enhanced Geothermal Systems. Accounting for the fracture morphology in modeling the system would make for a better understanding of optimal ways to harness heat from the system, result in better history matching and forecasting.

In this study, it has been demonstrated that actual fractures have spatial variations in their aperture, and the fracture aperture variability exhibits anisotropy, which has implications for heat transport. By modeling the coupled flow and heat process at the lab scale, it was demonstrated that flow perpendicular to the lateral direction of fracture shear offset often results in a better thermal performance than flow parallel to the lateral direction of fracture shear offset. Metrics for evaluating the thermal performance include the thermal drawdown, contact surface area, and the energy extracted. It was seen that 70% of the fracture aperture distributions analyzed resulted in lower thermal drawdown, more contact surface area, and more energy extract when the flow was in the perpendicular flow configuration.

A similar analysis was done for field-scale fractures. Artificially generated aperture distributions characterized by anisotropy were modeled for different geometric anisotropy ratios and different correlation lengths. The results from the thermohydraulic model indicated that about 60% of the fracture aperture distributions had lower thermal drawdown and higher heat extracted in the direction perpendicular to slip or shear. The findings suggest that there may be optimum well configurations relative to fracture shear that could improve the thermal performance of enhanced geothermal systems.

One assumption that is often made in analytical solutions and some numerical simulations is that the viscosity of the working fluid, water, is constant. In reality, water viscosity is significantly impacted by the temperature of the enhanced geothermal system.

In this study, a comparison was made between an EGS model built with constant water viscosity and an EGS model built with temperature-dependent viscosity. Different injector and reservoir temperatures were investigated. In addition, three aperture distributions were studied. It was found out that if an Enhanced Geothermal System is known to be channelized (perhaps through tracer tests) and the temperature difference between the reservoir and the injected fluid is high, then temperature-dependent viscosity would be necessary for modeling the system to simulate its thermal performance better. On the other hand, if the aperture distribution of the Enhanced Geothermal System is evenly distributed, a constant viscosity may suffice in simulating the process. Moreover, if the temperature difference between the reservoir and the injected fluid is low, a constant viscosity can be used in the model without significantly impacting computational accuracy. Overall a high correlation length leading to an increased area of preferential flow paths presents the most significant effect that contributes to the differences seen between modeling with a constant viscosity or a temperature-dependent viscosity.

The impact of thermal stresses was also investigated in this study. A thermohydrromechanical model was applied to the Altona Field Laboratory experiments. Though there was evidence of thermal stress and aperture changes, these did not significantly change the thermal breakthrough output curves. Thermohydrromechanical modeling was also applied to a hypothetical EGS with an anisotropic fracture aperture distribution. It was shown that the presence of spatial variations do not always result in deteriorating thermal performance, but thermal drawdown could be improved by the injection of cold water into the hot rock.

Supercritical CO₂ was investigated as an alternative working fluid for EGS while considering spatial variations in fracture aperture. It was established that for a smooth fracture and the same energy input, CO₂ resulted in more energy extracted from the reservoir than water. However, the gas-like viscosity of CO₂ is a disadvantage when the flow and heat extraction is modeled with a heterogeneous fracture aperture and over realistic periods for heat extraction. CO₂ is affected by channeling due to viscous fingering and fracture aperture heterogeneity. At high correlation lengths and high mass flow rates, the channels persist over time, leading to a very inefficient thermal sweep. Water at low

temperatures is more viscous than the background reservoir water. So cooler pathways become less preferential, and the sweep contacts a larger area of the rock over time. Thus, the energy extracted from the reservoir using water exceeds that of CO₂ for aperture distributions with high correlation lengths and at high equivalent mass flow rates. CO₂ results in higher thermal drawdown than water, though it initially extracts more heat from the reservoir. For fractures with spatial variations, the heat extraction rate reduces with time. Thus, in the long term, the cumulative energy extracted from the reservoir may be surpassed by a system where water is used, especially at high flow rates and if the fracture aperture has high correlation lengths.

The study contributes the following to the body of knowledge: First the impact of fracture aperture variability anisotropy on heat transfer has been evaluated. There is information about how heat transport is impacted by the geometric anisotropy of the fracture surface on the lab-scale and the field scale. The impact of fracture aperture variability anisotropy on heat transfer is relevant for optimizing well placement relative to the fracture shear or slip direction in Enhanced Geothermal Systems.

Secondly, the conditions under which a constant viscosity can be used in modeling EGS were determined, especially since analytical models and some numerical models do not account for the dependence of viscosity on temperature. If the fractures are known to be smooth, have low correlation lengths, or have distributed surface areas, a constant viscosity can be used in the model, especially if the difference between the reservoir temperature and the injection water temperature is small. However, for anisotropic fracture surfaces, surfaces with high correlations lengths or high tortuosity, and when the difference between the reservoir temperature and injection water temperature is large, the use of constant viscosity could result in significant computational errors from the actual.

Thirdly, it has been shown that when thermoelasticity is considered, some fractures with spatial variations can have improved thermal drawdown due to opening up of pathways when the rock contracts on injecting cold water. Finally, this work shows the first comparison between CO₂ and water at a field scale considering fracture surface aperture variability.

This study has opened up room for further investigations. For future work, it will be great to perform field tests that evaluate fracture surface anisotropy with the flow configuration. The numerical study can be expanded to multiple fractures and discrete fracture networks, accounting for surface aperture variability, to determine if there is a minimum number of fractures to counteract the effect of channeling or a network configuration that would improve thermal performance.

Vertical fractures with vertical wells can also be modeled to see how the fracture anisotropy impacts convective flow and has significant consequences for heat transport. Furthermore, in modeling water and CO₂ at high flow rates, non-Darcy effects can be considered in the model.

The modeling of geothermal systems involving complex physical processes requires much computational effort. With advances in artificial intelligence algorithms, developing proxy models that can replicate thermohydraulic and thermohydromechanical simulations would be valuable.

Bibliography

- Abbasi, M., Mansouri, M., Daryasafar, A., & Sharifi, M. (2019). Analytical model for heat transfer between vertical fractures in fractured geothermal reservoirs during water injection. *Renewable Energy*, *130*, 73-86. doi:10.1016/j.renene.2018.06.043
- Abelin, H., Birgersson, L., Gidlund, J., & Neretnieks, I. (1991). A large-scale flow and tracer experiment in granite: 1. experimental design and flow distribution. *Water Resources Research*, *27*(12), 3107-3117.
- Augustine, C. (2011). *Updated U.S. Geothermal Supply Characterization and Representation for Market Penetration Model Input*. Golden: NREL/TP-6A2-47459.
- Augustine, C. (2016). Update to Enhanced Geothermal System Resource Potential Estimate. *40th GRC Annual Meeting*, (pp. 1-7). Sacramento, California.
- Bai, B., He, Y., Li, X., Li, J., Huang, X., & Zhu, J. (2017). Experimental and analytical study of the overall heat transfer coefficient of water flowing through a single fracture in a granite core. *Applied Thermal Engineering*, 79-90.
- Bai, M., & Elsworth, D. (1994). Modeling of Subsidence and Stress-Dependent Hydraulic Conductivity for Intact and Fractured Porous Media. *Rock Mech. Rock Engng.* , 209-234.
- Barton, N., & Choubey, V. (1977). The shear strength of rock joints in theory and practice. *Rock Mechanics*, *10*, 1-54. Retrieved from <https://doi.org/10.1007/BF01261801>
- Barton, N., Bandis, S., & Bakhtar, K. (1985). Strength, deformation and conductivity coupling of rock joints. *International Journal of Rock Mechanics and Mining Sciences & Geomechanics Abstracts*, *22*, 121-140.
- Bataillé, A., Genthon, P., Rabinowicz, M., & Fritz, B. (2006). Modeling the coupling between free and forced convection in a vertical permeable slot: Implications for the heat production of an Enhanced Geothermal System. *Geothermics*, *35*(5-6), 654-682. doi:10.1016/j.geothermics.2006.11.008
- Bendat, J. S., & Piersol, A. G. (1971). *Random Data: Analysis and Measurement Procedures*. New York: Wiley-Interscience.
- Benson, S. M., Daggett, J., Iglesias, E., Arellano, V., & Ortiz-Ramirez, J. (1987). Analysis of Thermally Induced Permeability Enhancement in Geothermal Injection Wells. *Proceedings, Twelfth Workshop on Geothermal Reservoir Engineering*. Stanford, California: Stanford University.

- Biswas, A., & Si, B. C. (2013). Model Averaging for Semivariogram Model Parameters. In *Advances in Agrophysical Research*. Rijeka, Croatia: InTech.
- Bödvarsson, G. S., & Tsang, C. F. (1982). Injection and Thermal Breakthrough in Fractured Geothermal Reservoirs. *Journal of Geophysical Research: Solid Earth*, 87(B2). doi:10.1029/JB087iB02p01031
- Brown, D. W. (2000). A hot dry rock geothermal energy concept utilizing supercritical CO₂ instead of water. *PROCEEDINGS, Twenty-Fifth Workshop on Geothermal Reservoir Engineering*. Stanford: Stanford University.
- Brown, S. R. (1987). Fluid flow through rock joints: the effect of surface roughness. *Journal of Geophysical Research: Solid Earth*, 92(B2), 1337-1347. doi:10.1029/JB092iB02p01337
- Brown, S. R. (1989). Transport of fluid and electric current through a single fracture. *J. Geophysic. Res.*, 94, 9429-9438.
- Bruel, D. (2007). Using the migration of induced seismicity as a constraint for fractured Hot Dry Rock reservoir modelling. *International Journal of Rock Mechanics and Mining Sciences*, 44, 1106-1117. doi:10.1016/j.ijrmms.2007.07.001
- Candela, T., Renard, F., Bouchon, M., Brouste, A., Marsan, D., Schmittbuhl, J., & Voisin, C. (2009). Characterization of Fault Roughness at Various Scales: Implications of Three-Dimensional High Resolution Topography Measurements. *Pure and Applied Geophysics*, 1817–1851.
- Candela, T., Renard, F., Klinger, Y., Mair, K., Schmittbuhl, J., & Brodsky, E. E. (2012). Roughness of fault surfaces over nine decades of length scales. *Journal of Geophysical Research*, 117(B8).
- Cheng, A. H.-D., Ghassemi, A., & Detournay, E. (2001). Integral equation solution of heat extraction from a fracture in hot dry rock. *Int. J. Numer. Anal. Meth. Geomech*, 25, 1327-1338. doi:DOI: 10.1002/nag.182
- Cladouhos, T., Clyne, M., Nichols, M., Petty, S., Osborn, W., & Nofziger, L. (2011). Newberry Volcano EGS demonstration stimulation modeling. *Transactions - Geothermal Resources Council*, 35, pp. 317-322.
- Co, C. (2017). *Modeling and Characterization of Fracture Roughness and Its Impact on Mass Transport*. Stanford: Stanford University.
- Co, C. K., Pollard, D. D., & Horne, R. N. (2017). Towards a better understanding of the impact of fracture roughness on permeability-stress relationships using first principles. *42nd Stanford Geothermal Workshop Proceedings*. Stanford, California.
- Develi, K., & Babadagli, T. (2015). Experimental and visual analysis of single-phase flow through rough fracture replicas. *Int. J. Rock Mech. Min. Sci.*, 139-155.

- Dezayes, C., Genter, A., & Valley, B. (2010). Overview of the fracture network at different scales within the granite reservoir of the EGS Soultz site (Alsace, France). *World Geothermal Congress*. Bali, Indonesia. Retrieved from <http://www.geothermal-energy.org/pdf/IGAstandard/WGC/2010/3116.pdf>
- Evans, K. F. (2005). Permeability creation and damage due to massive fluid injections into granite at 3.5 km at Soultz: 2. Critical stress and. *Journal of Geophysical Research*, *110*(B4). doi:10.1029/2004JB003169
- Feng, G., Xu, T., Gherardi, F., Jiang, Z., & Bellani, S. (2017). Geothermal assessment of the Pisa plain, Italy: Coupled thermal and hydraulic modeling. *Renewable Energy*, *111*, 416-427. doi:10.1016/j.renene.2017.04.034
- Fenghour, A., Wakeham, W. A., & Vesovic, V. (1998). The Viscosity of Carbon Dioxide. *Journal of Physical and Chemical Reference Data*, *27*(1), 31-44.
- Fox, D. B., Koch, D. L., & Tester, J. W. (2015, October 28). The effect of spatial aperture variations on the thermal performance of discretely fractured geothermal reservoirs. *Geothermal Energy*, *3*(21). doi:10.1186/s40517-015-0039-z
- Gao, X., Zhang, Y., Hu, Z., & Huang, Y. (2021). Numerical Investigation on the Influence of Surface Flow Direction on the Heat Transfer Characteristics in a Granite Single Fracture. *Applied Sciences*, *11*(2), 751.
- Ge, Y., Kulatilake, P., Tang, H., & Xiong, C. (2014). Investigation of natural rock joint roughness. *Comput Geotech*, 290-305.
- Ghassemi, A., & Govindarajan, S. K. (2007). Changes in fracture aperture and fluid pressure due to thermal stress and silica dissolution/precipitation induced by heat extraction from subsurface rocks. *Geothermics*, *36*, 115-140. doi:10.1016/j.geothermics.2006.10.001
- Ghassemi, A., Tarasovs, S., & Cheng, A. H.-D. (2003). An integral equation solution for three-dimensional heat extraction from planar fracture in hot dry rock. *International Journal for Numerical and Analytical Methods in Geomechanics*, *27*, 989-1004. doi:10.1002/nag.308
- Gischig, V., & Preisig, G. (2015). Hydro-Fracturing versus Hydro-Shearing: A Critical Assessment of two Distinct Reservoir Stimulation Mechanisms. *13th International Congress of Rock Mechanics* (p. 12). Montréal, Canada: ISRM. doi: 10.13140/RG.2.1.4924.3041
- Goovaerts, P. (1997). *Geostatistics for Natural Resources Evaluation*. New York: Oxford University Press.
- Gringarten, A. C., & Sauty, J. P. (1975). A theoretical study of heat extraction from aquifers with uniform regional flow. *Journal of Geophysical Research*, *80*(35), 1121-1124.

- Gringarten, A. C., Witherspoon, P. A., & Ohnishi, Y. (1975, March 10). Theory of Heat Extraction From Fractured Hot Dry Rock. *Journal of Geophysical Research*, *80*(8), 1120-1124.
- Guo, B., Fu, P., Hao, Y., Peters, C. A., & R.Carrigana, C. (2016). Thermal drawdown-induced flow channeling in a single fracture in EGS. *Geothermics*, *61*, 46-62. doi:10.1016/j.geothermics.2016.01.004
- Hakami, E., & Larsson, E. (1996). Aperture measurements and flow experiments on a single natural fracture. *International Journal of Rock Mechanics and Mining Sciences & Geomechanics Abstracts*, *33*(4), 395-404. doi:10.1016/0148-9062(95)00070-4
- Hawkins, A. J., & Becker, M. W. (2012). MEASUREMENT OF THE SPATIAL DISTRIBUTION OF HEAT EXCHANGE IN A GEOTHERMAL ANALOG BEDROCK SITE USING FIBER OPTIC DISTRIBUTED TEMPERATURE SENSING. *PROCEEDINGS, Thirty-Seventh Workshop on Geothermal Reservoir Engineering*. Stanford, California: Stanford University.
- Hawkins, A. J., Becker, M. W., & Tester, J. W. (2018). Inert and adsorptive tracer tests for field measurement of flow-wetted-surface area. *Water Resources Research*, *54*, 5341-5358.
- Hawkins, A. J., Fox, D. B., & Becker, M. W. (2017). Measurement and simulation of heat exchange in fractured bedrock using inert and thermally degrading tracers. *Water Resources Research*, *53*, 1210-1230.
- Hawkins, A. J., Fox, D. B., Koch, D. L., Becker, M. W., & Tester, J. W. (2020). Predictive inverse model for advective heat transfer in a short-circuited fracture: Dimensional analysis, machine learning, and field demonstration. *Water Resources Research*. doi:https://doi.org/10.1029/2020WR027065
- Heinze, T., Frank, S., & Wohnlich, S. (2021). FSAT – A fracture surface analysis toolbox in MATLAB to compare 2D and 3D surface measures. *Computers and Geotechnics*, *132*. Retrieved from https://doi.org/10.1016/j.compgeo.2020.103997
- Huang, W., Cao, W., Wei, G., Jin, Y., & Jiang, F. (2019). Modeling Thermohydraulic Process in Enhanced Geothermal System Based on Two-Equation Thermal Model for Porous Media. In M. Yasser, H. Kamel, & V. Kambiz (Eds.), *Convective Heat Transfer in Porous Media* (pp. 203-226). Boca Raton: CRC Press.
- Huang, X., Zhu, J., Li, J., Bai, B., & Zhang, G. (2016). Fluid friction and heat transfer through a single rough fracture in granitic rock under confining pressure. *International Communications in Heat and Mass Transfer*, *75*, 78-85.
- Isaka, B. L., & Ranjith, P. G. (2019). The use of super-critical carbon dioxide as the working fluid in enhanced geothermal systems (EGSs): A review study.

Sustainable Energy Technologies and Assessments, 36.
doi:<https://doi.org/10.1016/j.seta.2019.100547>

- Ishibashi, T., Watanabe, N., Hirano, N., Okamoto, A., & Noriyoshi, T. (2012). Upgrading of aperture model based on surface geometry of natural fracture for evaluating channeling flow. *GRC Transactions*, 36, 481- 486.
- Ito, H. (2003). Inferred role of natural fractures, veins, and breccias in development of the artificial geothermal reservoir at the Ogachi Hot Dry Rock site, Japan. *Journal of Geophysical Research*, 109-118. doi:10.1029/2001JB001671
- Ito, T., & Hayashi, K. (2003). Role of stress-controlled flow pathways in HDR geothermal reservoirs. *Pure and Applied Geophysics*, 1103-1124. doi:10.1007/PL00012563
- Iwano, M., & Einstein, H. (1993). Stochastic Analysis of Surface Roughness, Aperture And Flow In a Single Fracture. *Geology*.
- Jiang, F., Chen, J., Huang, W., & Luo, L. (2014). A three-dimensional transient model for EGS subsurface thermo-hydraulic process. *Energy*, 72, 300-310. doi:10.1016/j.energy.2014.05.038
- Kaya, E., Zarrouk, S. J., & O'Sullivan, M. J. (2011). Reinjection in geothermal fields: A review of worldwide experience. *Renewable and Sustainable Energy Reviews*, 15(1), 47-68. doi:10.1016/j.rser.2010.07.032
- Kigobe, M., & Kizza, M. (2006). Dealing With Spatial Variability Under Limited Hydrogeological Data. Case Study: Hydrological Parameter Estimation in Mpigi-Wakiso. In J. A. Mwakali, & G. Taban-Wani (Eds.), *Advances in Engineering and Technology* (pp. 211-220). Uganda: Elsevier Science.
- Kohl, T., & Mégel, T. (2007). Predictive modeling of reservoir response to hydraulic stimulations at the European EGS site Soultz-sous-Forêts. *International Journal of Rock Mechanics and Mining Sciences*, 44, 1118-1131. doi:10.1016/j.ijrmms.2007.07.022
- Kolditz, O. (1995). Modelling flow and heat transfer in fractured rocks: Dimensional effect of matrix heat diffusion. *Geothermics*, 24(3), 421-437.
- Kolditz, O., & Clauser, C. (1998). Numerical simulation of flow and heat transfer in fractured crystalline rocks: application to the hot dry rock site in Rosemanowes (U.K.). *Geothermics*, 1-23.
- Lee, H., & Cho, T. (2002). Hydraulic characteristics of rough fractures in linear flow under normal and shear load. *Rock Mechanics and Rock Engineering*, 35(4), 299-318.
- Li, W., Yost, K., & Sousa, R. (2013). Heat Transfer Between Fluid Flow and Fractured Rocks. *GRC Transactions*, 37, 165-172.

- Liu, G., Pu, H., Zhao, Z., & Liu, Y. (2019). Coupled thermo-hydro-mechanical modeling on well pairs in heterogeneous porous geothermal reservoirs. *Energy*, 631-653.
- Luo, F., Xu, R.-N., & Jiang, P.-X. (2014, January). Numerical investigation of fluid flow and heat transfer in a doublet enhanced geothermal system with CO₂ as the working fluid (CO₂-EGS). *Energy*, 64, 307-322.
- Luo, S., Zhao, Z., Peng, H., & Pu, H. (2016). The role of fracture surface roughness in macroscopic fluid flow and heat transfer in fractured rocks. *International Journal of Rock Mechanics and Mining Sciences*, 87, 29-38.
- Ma, Y., Zhang, Y., Hu, Z., Yu, Z., Huang, Y., & Zhang, C. (2019). Experimental study of the heat transfer by water in rough fractures and the effect of fracture surface roughness on the heat transfer characteristics. *Geothermics*, 235-242.
- Malinverno, A. (1990). A simple method to estimate the fractal dimension of a self-affine series. *Geophys. Res. Lett.*, 1953-1956.
- Mandelbrot, B. B. (1983). *The Fractal Geometry of Nature*. New York: Freeman.
- Martínez, Á. R., Roubinet, D., & Tartakovsky, D. M. (2013). Analytical models of heat conduction in fractured rocks. *Journal of Geophysical Research: Solid Earth*, 119(1). doi:10.1002/2012JB010016
- Mattson, E., White, M., Zhang, Y., Johnston, B., Hawkins, A., & team, t. E. (2018). Collab Fracture Characterization: Preliminary Results from the Modeling and Flow Testing of Experiment 1. *GRC Transactions*, 42, 756-765.
- McClure, M., & Horne, R. (2014). Characterizing Hydraulic Fracturing With a Tendency-for-Shear-Stimulation Test. *SPE Reservoir Evaluation & Engineering*, 17, 233-243. doi:10.2118/166332-PA
- McDermott, C. I., Randriamanjatoa, A. R., Tenzer, H., & Kolditz, O. (2006). Simulation of heat extraction from crystalline rocks: The influence of coupled processes on differential reservoir cooling. *Geothermics*, 35(3), 321-344. Retrieved from <https://doi.org/10.1016/j.geothermics.2006.05.002>
- Meakin, P. (1998). *Fractals: Scaling and Growth far From Equilibrium*. New York: Cambridge Univ. Press.
- Méheust, Y., & Schmittbuhl, J. (2001). Geometrical heterogeneities and permeability anisotropy of rough fractures. *Journal of Geophysical Research: Solid Earth*, 106(B2). doi:10.1029/2000JB900306
- Méheust, Y., & Schmittbuhl, J. (2001). Geometrical Heterogeneities and Permeability Anisotropy of Rough Fractures. *J. Geophys. Res.*, 2089–2102.

- Murphy, H. D., & Fehler, M. C. (1986). Hydraulic fracturing of jointed formations. *International Meeting on Petroleum Engineering*. Beijing, China: Society of Petroleum Engineers. doi:10.2118/14088-MS
- National Renewable Energy Laboratory. (2009). *Geothermal Resource of the United States*. Retrieved October 31, 2018, from National Renewable Energy Laboratory: https://www.nrel.gov/gis/images/geothermal_resource2009-final.jpg
- Neuville, A., Toussaint, R., & Schmittbuhl, J. (2010). Fracture roughness and thermal exchange: A case study at Soultz-sous-Forêts. *Comptes Rendus Geoscience*, 342, 616-625. doi:10.1016/j.crte.2009.03.006
- Office of Energy Efficiency and Renewable Energy. (2014). *How an Enhanced Geothermal System Works*. Retrieved October 25, 2018, from <https://www.energy.gov/eere/geothermal/how-enhanced-geothermal-system-works>
- Olson, J. E. (2003). Sublinear scaling of fracture aperture versus length: an exception or the rule? *Journal of Geophysical Research: Solid Earth*, 1978-2012.
- Olson, J. E., & Schultz, R. A. (2011). Comment on a note on the scaling relations for opening mode fractures in rock by CH Scholz. *Journal of Structural Geology*, 1523-1524.
- Oron, A. P., & Berkowitz, B. (1998). Flow in rock fractures: The local cubic law assumption reexamined. *Water Resources Research*, 34(0043-1397). doi:10.1029/98WR02285
- Pan, F., McPherson, B., & Kaszuba, J. (2017). Evaluation of CO₂-fluid-rock interaction in enhanced geothermal systems: field-scale geochemical simulations. *Geofluids*.
- Pandey, S. N., Chaudhuri, A., & Kelkar, S. (2017). A coupled thermo-hydro-mechanical modeling of fracture aperture alteration and reservoir deformation during heat extraction from a geothermal reservoir. *Geothermics*, 17–31.
- Peitgen, H., & Saupe, D. (1988). *The Science of Fractal Images*. New York: Springer-Verlag.
- Peitgen, H., & Saupe, D. (1988). *The Science of Fractal Images*. New York: Springer-Verlag.
- Petty, S., Nordin, Y., Glassley, W., Cladouhos, T. T., & Swyer, M. (2013). Improving Geothermal Project Economics with Multi-zone Stimulation: Results from the Newberry Volcano EGS Demonstration. *Thirty-Eighth Workshop on Geothermal Reservoir Engineering*. Stanford.
- Pine, R., & Batchelor, A. (1984). Downward migration of shearing in jointed rock during hydraulic injection. *International Journal of Rock Mechanics and Mining*

Sciences & Geomechanics Abstracts. 21, pp. 249-263. Great Britain: Elsevier.
doi:10.1016/0148-9062(84)92681-0

- Plouraboué, F., Kurowski, P., Boffa, J.-M., Hulin, J.-P., & Roux, S. (2000). Experimental study of the transport properties of rough self-affine fractures. *Journal of Contaminant Hydrology*, 295-318.
- Pollack, H. N., Hurter, S. J., & Johnson, J. R. (1993). Heat flow from the Earth's interior: Analysis of the global data set. *Reviews of Geophysics*, 31(3), 267-280. Retrieved from <https://doi.org/10.1029/93RG01249>
- Pritchett, J. W. (2009). On the relative effectiveness of H₂O and CO₂ as reservoir working fluids for EGS heat mining. *Trans Geotherm Resour Counc.* , 33, pp. 235–243.
- Pruess, K. (2006). Enhanced geothermal systems (EGS) using CO₂ as working fluid—A novel approach for generating renewable energy with simultaneous sequestration of carbon. *Geothermics*, 35(4), 351-367.
doi:<https://doi.org/10.1016/j.geothermics.2006.08.002>
- Pruess, K., & Narasimhan, T. N. (2012). On fluid reserves and the production of superheated steam from fractured, vapor-dominated geothermal reservoirs. *Journal of Geophysical Research: Solid Earth*, 87(B11), 9329-9339.
- Pyrak-Nolte, L. J., Montemagno, C. D., & Nolte, D. D. (1997). Volumetric imaging of aperture distributions in connected fracture networks. *Geophysical Research Letters*, 24(18), 2343-2346.
- Raleigh, C. B., Witherspoon, P. A., Gringarten, A. C., & Onishi, Y. (1974). Multiple hydraulic fracturing for the recovery of geothermal energy. 426. EOS, Trans. AGU.
- Remy, N., Boucher, A., & Wu, J. (2009). *Applied Geostatistics with SGeMS: a User's Guide*. Cambridge University Press. doi:doi:10.1017/CBO9781139150019
- REN21. (2020). *Renewables 2020 Global Status Report*. Paris: REN21 Secretariat.
- Sanyal, S., & Butler, S. (2005). An Analysis of Power Generation Prospects from Enhanced Geothermal Systems. *Proceedings World*. Antalya, Turkey. Retrieved from http://repository.stategeothermaldata.org/metadata/record/98ddf901b9782a25982e01af3b082759/file/an_analysis_of_power_generation_prospects_from_enhanced_geothermal_systems_-_by_subir_sanyal_and_steven_butler_wgc2005.pdf
- Schlumberger. (2016). *ECLIPSE Technical Description*. Version 2016.2.
- Schmittbuhl, J., Steyer, A., Jouriaux, L., & Toussaint, R. (2008). Fracture morphology and viscous transport. *Int J Rock Mech Min*, 422-430.

- Scholz, C. H. (2010). A note on the scaling relations for opening mode fractures in rock. *Journal of Structural Geology*, 1485-1487.
- Shao, J. F. (1997). A Numerical Solution for a Thermo-hydro-mechanical Coupling Problem with heat Convection. *Int. J. Rock Mech. Min. Sci.*, 34(1), 163-166.
- Spycher, N., & Pruess, K. (2005). CO₂-H₂O mixtures in the geological sequestration of CO₂.II. Partitioning in chloride brines at 12-100 C and up to 600 bar. *Geochimica et Cosmochimica Acta*, 69(13), 3309-3320.
- Spycher, N., & Pruess, K. (2009). A Phase-Partitioning Model for CO₂-Brine Mixtures at Elevated Temperatures and Pressures: Application to CO₂-Enhanced Geothermal Systems. *Transport Porous Media* , 82(1), 173-196.
- Stacey, R., & Williams, M. J. (2017). Validation of ECLIPSE Reservoir Simulator for Geothermal Problems. *GRC Transactions*, 41.
- Stefánsson, V. (1997). Geothermal Reinjection Experience. *Geothermics*, 26, 99-139. doi:10.1016/S0375-6505(96)00035-1
- Tester, J., Anderson, B. J., Batchelor, A. S., Blackwell, D. D., DiPippo, R., M., D. E., . . . al., e. (2006). *The Future of Geothermal Energy*. Massachusetts Institute of Technology. Retrieved from <https://energy.mit.edu/wp-content/uploads/2006/11/MITEI-The-Future-of-Geothermal-Energy.pdf>
- Thompson, M. E., & Brown, S. R. (1991). The Effect of Anisotropic Surface Roughness on Flow and Transport in Fractures. *Journal of Geophysical Research*, 96(B13), 21,923 - 21,932.
- Tsang, C.-F., & Neretnieks, I. (1998). Flow Channeling in Heterogeneous Fractured Rocks. *Reviews of Geophysics*, 36(2), 275-298. doi:10.1029/97RG03319
- Tsang, Y. W., & Tsang, C. F. (1989). Flow channeling in a single fracture as a two-dimensional strongly heterogeneous permeable medium. *Water Resources Research*, 25(9), 2076-208. doi:10.1029/WR025i009p02076
- Tsang, Y. W., Tsang, C. F., Neretnieks, I., & Moreno, L. (1988). Flow and tracer transport in fractured media: a variable aperture channel model and its properties. *Water Resources Research*, 24(12), 2049-2060.
- Tse, R., & Cruden, D. M. (1979). Estimating joint roughness coefficients. *International Journal of Rock Mechanics and Mining Sciences & Geomechanics Abstracts*, 303-307.
- U. S. Energy Information Administration. (2018). *Annual Energy Outlook 2018*. Annual Energy Outlook. Retrieved from <https://www.eia.gov/outlooks/aeo/>
- Vermilye, J. M., & Scholz, C. H. (1995). Relation between vein length and aperture. *Journal of Structural Geology*, 423-434.

- Voss, R. F. (1985). *Scaling Phenomena in Disorder Systems*. Plenum: New York.
- Wagner, W., Cooper, J. R., Dittmann, A., Kijima, J., Kretzschmar, H.-J., Kruse, A., . . . Willkommen, T. (2000). The IAPWS Industrial Formulation 1997 for the Thermodynamic Properties of Water and Steam. *Transactions of the ASME*, 122, pp. 150-182. ASME.
- Wang, C., Cheng, W., Nian, L., Han, B., & Liu, M. (2018). Simulation of heat extraction from CO₂-based enhanced geothermal systems considering CO₂ sequestration. *Energy*, 157-167.
- Wang, C., Liu, S., Wu, J., & Li, Z. (2014). Effects of temperature-dependent viscosity on fluid flow and heat transfer in a helical rectangular duct with a finite pitch. *Brazilian Journal of Chemical Engineering*, 31(3), 787-797. Retrieved from <https://dx.doi.org/10.1590/0104-6632.20140313s00002676>
- Watanabe, K., & Takahashi, H. (1995). Fractal geometry characterization of geothermal reservoir fracture networks. *J. Geophys. Res.*, 100(B1), 521-528.
- Watanabe, N., Hirano, N., & Tsuchiya, N. (2008). Determination of aperture structure and fluid flow in a rock fracture by high-resolution numerical modeling on the basis of a flow-through experiment under confining pressure. *Water Resources Research*, 44(6). doi:W06412
- Wikipedia. (2021, March). *Phase diagram*. Retrieved from https://en.wikipedia.org/w/index.php?title=Phase_diagram&oldid=1012868127
- Wikipedia. (2021, February 23). *Self-Similarity*. Retrieved from <https://en.wikipedia.org/w/index.php?title=Self-similarity&oldid=1008404278>
- Wikipedia. (2021, January). *Supercritical carbon dioxide*. Retrieved from https://en.wikipedia.org/w/index.php?title=Supercritical_carbon_dioxide&oldid=997626129
- Witherspoon, P. A., Wang, J. S., Iwai, K., & Gale, J. E. (1980). Validity of Cubic Law for Fluid Flow in a Deformable Rock Fracture. *Water Resources Research*, 16(6), 1016-1024.
- Wu, Y., & Li, P. (2020). The potential of coupled carbon storage and geothermal extraction in a CO₂-enhanced geothermal system: a review. *Geothermal Energy*. doi:<https://doi.org/10.1186/s40517-020-00173-w>
- Xing, H., Liu, Y., Gao, J., & Chen, S. (2015). Recent development in numerical simulation of enhanced geothermal reservoirs. *Journal of Earth Science*, 26(1), 28–36.
- Yang, S.-Y., & Yeh, H.-D. (2009). Modeling heat extraction from hot dry rock in a multi-well system. *Applied Thermal Engineering*, 1676-1681. doi:10.1016/j.applthermaleng.2008.07.020

- Yao, C., Shao, Y., & Yang, J. (2018). Numerical Investigation on the Influence of Areal Flow on EGS Thermal Exploitation Based on the 3-D T-H Single Fracture Model. *Energies*, 11(11). doi:10.3390/en11113026
- Zhang, L., Jiang, P., Wang, Z., & Xu, R. (2017). Convective heat transfer of supercritical CO₂ in a rock fracture for enhanced geothermal systems. *Applied Thermal Engineering*, 115, 923-936.
doi:<https://doi.org/10.1016/j.applthermaleng.2017.01.013>.
- Zhang, X., Wang, Z., Sun, Y., Zhu, C., Xiong, F., & Tang, Q. (2020). Numerical Simulation on Heat Transfer Characteristics of Water Flowing through the Fracture of High-Temperature Rock. *Geofluids*, 14.
- Zhao, J., & Tso, C. P. (1993). Heat transfer by water flow in rock fractures and the application to hot dry rock geothermal systems. *International Journal of Rock Mechanics and Mining Sciences & Geomechanics Abstracts*, 30(6), 633-641.
- Zimmerman, R. W., Chen, D.-W., & Cook, N. G. (1992). The effect of contact area on the permeability of fractures. *Journal of Hydrology*, 139(1-4), 79-96.
doi:10.1016/0022-1694(92)90196-3